



**HAL**  
open science

# Investigation of Plasma Surface Interactions using Mueller Polarimetry

Elmar Slikboer

► **To cite this version:**

Elmar Slikboer. Investigation of Plasma Surface Interactions using Mueller Polarimetry. Plasma Physics [physics.plasm-ph]. Université Paris Saclay (COMUE); Technische hogeschool (Eindhoven, Pays-Bas), 2018. English. NNT: 2018SACLX093 . tel-01951739

**HAL Id: tel-01951739**

**<https://pastel.hal.science/tel-01951739>**

Submitted on 11 Dec 2018

**HAL** is a multi-disciplinary open access archive for the deposit and dissemination of scientific research documents, whether they are published or not. The documents may come from teaching and research institutions in France or abroad, or from public or private research centers.

L'archive ouverte pluridisciplinaire **HAL**, est destinée au dépôt et à la diffusion de documents scientifiques de niveau recherche, publiés ou non, émanant des établissements d'enseignement et de recherche français ou étrangers, des laboratoires publics ou privés.

# Investigation of Plasma Surface Interactions using Mueller Polarimetry

Thèse de doctorat de l'Université Paris-Saclay  
préparée à l'École Polytechnique

Ecole doctorale n°572 Ondes et Matières (EDOM)  
Spécialité de doctorat : Physique des Plasmas

Thèse présentée et soutenue à Eindhoven, Pays-Bas, le 26-11-2018, par

**ELMAR THEODORUS SLIKBOER**

Composition du Jury :

prof.dr.ir. E.J.E. Cottaar Université de technologie d'Eindhoven	Président
prof.dr.ir. W.M.M. Kessels Université de technologie d'Eindhoven (PMP)	Rapporteur
prof.dr. F. Goudail Institut d'optique Graduate School (SPIM)	Rapporteur
Univ.-Prof.Dr.rer.nat.habil. R. Brandenburg Universität Rostock	Rapporteur
prof.dr.ir. G.M.W. Kroesen Université de technologie d'Eindhoven (EPG)	Directeur de thèse
dr.Dipl.-Ing A. Sobota Université de technologie d'Eindhoven (EPG)	Co-directeur de thèse
dr. O.Y.N. Guaitella École Polytechnique (LPP)	Co-directeur de thèse
dr. E. Garcia-Caurel École Polytechnique (LPICM)	Co-directeur de thèse

---

# Investigation of Plasma Surface Interactions using Mueller Polarimetry

PROEFSCHRIFT

ter verkrijging van de graad van doctor aan de Technische Universiteit  
Eindhoven, op gezag van de rector magnificus prof.dr.ir. F.P.T. Baaijens, voor een  
commissie aangewezen door het College voor Promoties, in het openbaar te  
verdedigen op maandag 26 november 2018 om 13:30 uur

door

Elmar Theodorus Slikboer

geboren te Schijndel

Dit proefschrift is goedgekeurd door de promotoren en de samenstelling van de promotiecommissie is als volgt:

voorzitter: prof.dr.ir. E.J.E. Cottaar  
1e promotor: prof.dr.ir. G.M.W. Kroesen  
copromotoren: dr.Dipl.-Ing. A. Sobota  
dr. O.Y.N. Guaitella (École Polytechnique)  
dr. E. Garcia-Caurel (École Polytechnique)  
leden: prof.dr.ir. W.M.M. Kessels  
prof.dr. F. Goudail (Institut d'optique Graduate School)  
Univ.-Prof.Dr.rer.nat.habil. R. Brandenburg (Universität Rostock)

Het onderzoek dat in dit proefschrift wordt beschreven is uitgevoerd in overeenstemming met de TU/e Gedragscode Wetenschapsbeoefening.

The work in this project has been funded by the “*Chaire Énergie Durable*” at École Polytechnique under the reference EXXI with the financial aid from the EDF foundation. Additional funding was received within the LABEX Plas@par project and from financial state aid managed by the Agence Nationale de la Recherche under the reference ANR-11-IDEX-0004-02.



Chaire Energie Durable  
 **FONDATION EDF**  
Science - Enseignement  
en partenariat avec l'Institut de France



A catalogue record is available from the Eindhoven University of Technology Library

ISBN: 978-90-386-4634-3



# Contents

<b>Summary (EN)</b>	<b>i</b>
<b>Résumé (FR)</b>	<b>iii</b>
<b>Samenvatting (NL)</b>	<b>v</b>
<b>List of Symbols and Abbreviations</b>	<b>vii</b>
<b>1 Global Introduction</b>	<b>1</b>
1.1 Plasma Surface Interaction . . . . .	2
1.1.1 Introduction . . . . .	2
1.1.2 Approaches to Study Plasma Surface Interactions . . . . .	4
1.1.3 Our Approach: Optically Active Targets . . . . .	5
1.2 Introduction of Polarized Light and Mueller Polarimetry . . . . .	8
1.2.1 Description of Polarization . . . . .	9
1.2.2 Polarization Interaction with Materials . . . . .	11
1.2.3 Polarization Diagnostics . . . . .	13
1.3 Non-Thermal Atmospheric Pressure Plasmas . . . . .	15
1.3.1 Plasma Jet Design and Basic Operation . . . . .	18
1.3.2 Investigation of Guided Ionization Waves . . . . .	19
1.3.3 Interaction with Dielectric Materials . . . . .	20
1.4 Outline of this PhD Thesis . . . . .	24
References . . . . .	26
<b>2 Experimental Setup and Measurement Procedure</b>	<b>33</b>
2.1 The Mueller Polarimeter . . . . .	34
2.1.1 Setup Design . . . . .	34
2.1.2 Choice of the Orientations of the Liquid Crystals . . . . .	37
2.2 Measurement Procedure and Calibration . . . . .	41
2.2.1 Calibration Procedure . . . . .	41
2.3 Analyses of the Mueller Matrix . . . . .	43
2.3.1 Optically Active Targets . . . . .	44
2.3.2 Logarithmic (Differential) Decomposition . . . . .	45
2.3.3 Homogeneous Elliptical Retarder Model . . . . .	47
References . . . . .	49

---

<b>3</b>	<b>Electro-Optic Properties of <math>\text{Bi}_{12}\text{SiO}_{20}</math></b>	<b>51</b>
3.1	Introduction of BSO . . . . .	52
3.2	Relation between Birefringence and Electric Field . . . . .	53
3.2.1	Index Ellipsoid . . . . .	55
3.2.2	Light Propagation . . . . .	56
3.3	DC Electric Fields Applied to BSO . . . . .	60
3.3.1	Logarithmic Decomposition . . . . .	61
3.3.2	Homogeneous Elliptical Retarder Model . . . . .	71
3.4	Summary and Perspectives . . . . .	74
	References . . . . .	75
<b>4</b>	<b>Electric Field Patterns Induced by Plasma at <math>45^\circ</math> Incidence</b>	<b>77</b>
4.1	Investigating Electric Fields Induced by Plasma . . . . .	78
4.2	Measuring Axial Electric Fields . . . . .	79
4.2.1	BSO examined at Normal Incidence . . . . .	79
4.2.2	Measurement Example with the AC Jet at $45^\circ$ . . . . .	80
4.3	Measuring Radial Electric Fields . . . . .	87
4.3.1	Electro-Optic $\text{Fe}:\text{LiNbO}_3$ . . . . .	87
4.3.2	Measurement Example using Felinbo . . . . .	89
4.4	Electric Field Patterns . . . . .	90
4.4.1	AC Plasma Jet . . . . .	90
4.4.2	Influence of a Controlled Environment . . . . .	98
4.4.3	Time-Resolved Investigation of a Pulsed Plasma Jet in Air . . . . .	106
4.5	Summary and Perspectives . . . . .	117
	References . . . . .	119
<b>5</b>	<b>Study of a Plasma Target Interaction at Normal Incidence</b>	<b>123</b>
5.1	Measuring the Plasma Jet Dynamics Impacting on a Target . . . . .	124
5.1.1	Imaging of Ionization Wave Propagation . . . . .	124
5.1.2	Adapting the Measurement Procedure for Electric Field Investigation . . . . .	129
5.1.3	Time-Resolved Plasma Impact on BSO . . . . .	131
5.2	Time-Resolved Electric Field Patterns . . . . .	135
5.2.1	Electric Field Patterns during Interaction . . . . .	140
5.2.2	Comparison with a Numerical Fluid Model . . . . .	142
5.2.3	Variation of Voltage Amplitude . . . . .	148
5.3	Summary and Perspectives . . . . .	154
	References . . . . .	156

<b>6</b>	<b>Temperature Induced By Plasma Jet Interaction</b>	<b>159</b>
6.1	Optical Effects Induced by Temperature . . . . .	160
6.1.1	The Background Structure . . . . .	160
6.1.2	The Photo-Elastic Effect . . . . .	161
6.1.3	Temperature Induced Strain . . . . .	163
6.2	Calibration of the Coupling Constants . . . . .	164
6.2.1	Procedure to Retrieve the Temperature Pattern . . . . .	166
6.2.2	Calibration through Variation of Applied Voltage . . . . .	168
6.3	Summary and Perspectives . . . . .	175
	References . . . . .	176
<b>7</b>	<b>Simultaneous Investigation of Temperature and Electric Field</b>	<b>177</b>
7.1	Relevance for Plasma Target Interaction . . . . .	178
7.2	Increase Temperature and Electric Field . . . . .	179
7.2.1	Dependency on the Operating Frequency of the Jet . . . . .	179
7.2.2	Gas Flow Dynamics . . . . .	183
7.3	Background Images from Previous Measurements . . . . .	185
7.3.1	Influence of a Controlled Environment with the AC-driven Plasma Jet . . . . .	186
7.3.2	Voltage Amplitude of the Pulsed Plasma Jet . . . . .	189
7.4	Summary and Perspectives . . . . .	191
	References . . . . .	192
<b>8</b>	<b>Investigation of Plasma Interacting with a Complex Surface</b>	<b>195</b>
8.1	Complex Plasma Surface Interactions . . . . .	196
8.1.1	Test Case: Plasma Impact on Onion Cells . . . . .	197
8.1.2	Experimental Setup and Procedure . . . . .	198
8.2	Material Evolution during Target Interaction . . . . .	202
8.2.1	Dewetting by Plasma Impact . . . . .	202
8.2.2	Mapping Before and After Exposure . . . . .	204
8.2.3	Electric Field Through Onion Cells . . . . .	208
8.2.4	Outlook and Discussion . . . . .	218
8.3	Summary and Perspectives . . . . .	220
	References . . . . .	221
	<b>General Conclusions and Perspectives</b>	<b>223</b>
<b>A</b>	<b>Time Resolved Individual Electric Field Components</b>	<b>I</b>
<b>B</b>	<b>Additional Figures from Complex Surface Interactions</b>	<b>VII</b>
	<b>Curriculum Vitae</b>	<b>XIX</b>
	<b>Acknowledgements</b>	<b>XXIII</b>



# Investigation of Plasma Surface Interactions using Mueller Polarimetry

## Summary

In this thesis, a new diagnostic method called Mueller Polarimetry is examined for the investigation of plasma-surface interactions. This imaging technique allows the time-resolved optical characterization of targets under plasma exposure. The measured Mueller matrices are analyzed by using the logarithmic decomposition providing polarimetric data on diattenuation, depolarization, and birefringence. The latter is used by examining materials that possess optically active behavior to identify specific aspects of the plasma interaction, e.g. electric fields or temperature.

This work focusses on electro-optic targets, which primarily enables the detection of electric fields induced by surface charge deposited during the interaction. The birefringence is coupled to the externally induced electric field by analytically relating the phase retardance for the probing polarized light beam to the perturbed index ellipsoid, according to the Pockels effect. Through this analytical approach, materials with specific electro-optic properties can be chosen in such a way – together with the orientation of the Mueller polarimeter itself – that all the individual electric field components (axial and radial) induced inside the sample are imaged separately. This has never been done before and allows to better understand the plasma dynamics in the vicinity of a dielectric surface.

It is used to investigate the surface impact by guided ionization waves generated by a kHz-driven atmospheric pressure plasma jet. These non-thermal filamentary discharges are generally applied to various samples for e.g. surface

---

functionalization of polymers or biomedical treatment of organic tissues. However, available diagnostic tools are limited to study these interactions. Imaging Mueller polarimetry applied to electro-optic targets examines the axial and radial field patterns in terms of amplitude (3-6 kV/cm), spatial scales ( $\leq 1$ mm axial and  $\leq 1$ cm radial), and timescales ( $\leq 1\mu$ s pulsed and  $\leq 10\mu$ s AC) for various operating parameters of the jet, for example voltage amplitude and surrounding gas.

Simultaneous with the transient birefringence induced by the electric field, a constant background pattern is also observed. This results from strain induced by temperature gradients inside the targeted material. An analytical relation is obtained following the photo-elastic effect, which allowed a fitting procedure to be designed to retrieve the temperature pattern. This procedure is used after calibration to show that the temperature of the sample can vary up to 25 degrees relative to room conditions – while changes in the electric field are seen as well – depending on the operating frequency of the AC driven plasma jet. The accurate determination of the temperature is important since most applications involve temperature sensitive samples.

Lastly, this work shows how complex samples (in terms of surface geometry and/or chemical composition) can be examined during a plasma-surface interaction. This is done by combining them with the electro-optic targets. Due to the addition of a (thin) complex sample, depolarization is added to the system through scattering of the polarized light beam. In-situ observed changes of depolarization relate to the evolution of the complex sample during the plasma treatment. This, coupled with the simultaneously monitored electric field patterns, provides a unique diagnostic tool to examine the plasma-surface interactions. This has been applied for a test case where a single layer of onion cells is exposed to the ionization waves generated by the non-thermal plasma jet.

# L'Étude des Interactions Plasma-Surface en utilisant la Polarimétrie de Mueller

## Résumé

Cette thèse examine une nouvelle méthode de diagnostic, appelée Polarimétrie de Mueller, pour l'étude des interactions plasma-surface. Cette technique d'imagerie permet la caractérisation optique résolue en temps des cibles exposées au plasma. Les matrices de Mueller mesurées sont analysées en utilisant la décomposition logarithmique donnant des informations polarimétriques sur la diatténuation, la dépolariation et la biréfringence. Cette dernière est exploitée en examinant des matériaux optiquement actifs afin d'identifier des aspects spécifiques de l'interaction avec le plasma, tels que les champs électriques ou la température de surface.

Ce travail se concentre sur les cibles électro-optiques, qui permettent principalement la détection de champs électriques induits par la charge de surface déposée lors de l'interaction. La biréfringence est couplée analytiquement au champ électrique induit extérieurement, en rapportant le retard de phase du faisceau sonde de lumière polarisée, à l'ellipsoïde d'index perturbé suivant l'effet Pockels. Grâce à cette approche analytique, les matériaux ayant des propriétés électro-optiques spécifiques peuvent être choisis de telle manière – selon l'orientation du polarimètre de Mueller lui-même – que toutes les composantes individuelles de champ électrique (axiales et radiales) induites à l'intérieur de l'échantillon soient imagées séparément. Pour la première fois les composantes du champ électriques peuvent être découplées permettant de mieux comprendre la dynamique du plasma proche d'une surface diélectrique.

---

Cette technique est utilisée pour étudier l'impact d'ondes d'ionisation sur des surfaces. Ces décharges, générées par un jet de plasma à pression atmosphérique dans la gamme kHz, sont des plasmas froids filamentaires généralement utilisés pour des applications diverses telles que la fonctionnalisation de surface de polymères ou des traitements biomédicaux, mais les méthodes de diagnostic disponibles pour étudier les effets induits sur les surfaces sont limités. L'imagerie de polarimétrie Mueller appliquée aux cibles électro-optiques permet d'examiner les champs axiaux et radiaux en termes d'amplitude (3-6 kV/cm), d'échelles spatiales ( $\leq 1$ mm axiales and  $\leq 1$ cm radiales) et d'échelles temporelles ( $\leq 1\mu$ s pulsée and  $\leq 10\mu$ s CA) pour divers paramètres de fonctionnement du jet, e.g. amplitude de tension et gaz environnant.

Simultanément à la biréfringence transitoire induite par le champ électrique, un signal de fond constant est également observé. Il est induit par la contrainte résultante du gradient de température induit à l'intérieur du matériau ciblé. Une relation analytique est obtenue en utilisant l'effet photo-élastique, permettant de développer une procédure de fitting pour retrouver la distribution de température. Cette procédure est utilisée, après calibration, pour montrer que la température de l'échantillon peut varier jusqu'à 25 degrés par rapport aux conditions ambiantes – tandis que les changements dans le champ électrique sont également mesurés – et dépend de la fréquence de la tension d'alimentation AC du jet de plasma. La détermination précise de la température induite dans les cibles est importante car la plupart des applications visent des échantillons thermo-sensibles.

Enfin, ce travail montre comment des échantillons complexes (aussi bien en terme d'état de surface que de composition chimique) peuvent être examinés lors d'une interaction plasma-surface, en les combinant avec une cible électro-optique. En raison de l'ajout d'un échantillon complexe (mince), une composante de dépolarisation est ajoutée due à la diffusion du faisceau lumineux polarisé. Les changements de dépolarisation sont liés à l'évolution de l'échantillon complexe au cours du traitement par plasma. Ceux-ci, couplés aux champs électriques mesurés simultanément, fournissent un outil de diagnostic unique pour examiner les interactions plasma-surface. Cela a été appliqué à un cas test où une seule couche de cellules d'oignon est exposée aux ondes d'ionisation générées par le jet de plasma froid.

# Onderzoek naar Plasma-Oppervlakte Interacties met behulp van Mueller Polarimetrie

## Samenvatting

In dit proefschrift wordt een nieuwe diagnostische methode, genaamd Mueller polarimetrie, bestudeerd voor het onderzoek naar plasma-oppervlakte-interacties. Deze visualisatietechniek maakt tijdsopgeloste optische karakterisatie van materiaaloppervlakken onder plasmablootstelling mogelijk. De gemeten Mueller-matrices worden geanalyseerd door gebruik te maken van de logaritmische decompositie, waardoor polarimetrische informatie verkregen wordt over dichroïsme, depolarisatie en dubbelbreking. Laatstgenoemde is van belang voor materialen die optisch actief gedrag vertonen waardoor deze gebruikt kunnen worden om specifieke aspecten, zoals elektrische velden en temperatuur, van een plasma-interactie te onderzoeken.

Dit werk richt zich op elektro-optische materialen die in de eerste plaats de mogelijkheid bieden elektrische velden te detecteren. Deze zijn veroorzaakt door gedeponeerde oppervlakteladingen tijdens de interactie. De dubbelbreking kan worden gerelateerd aan het extern geïnduceerde elektrische veld, door de fasevertraging van de uitgezonden gepolariseerde lichtbundel volgens het Pockels effect te koppelen aan de verstoorde index-ellipsoïde. Via deze analytische benadering zijn materialen met specifieke elektro-optische eigenschappen en de oriëntatie van de Mueller polarimeter gekozen zodat alle individuele componenten (axiaal en radiëel) van het geïnduceerd elektrische veld apart gevisualiseerd worden. Dit is nog nooit eerder gedaan en biedt de mogelijkheid om de dynamiek van plasma's in de nabijheid van diëlektrische materialen te bestuderen.

---

Deze methode is toegepast om de oppervlakte-inslag van aangestuurde ionisatiegolven te onderzoeken, gegenereerd door een met kHz aangedreven plasma jet op atmosferische druk. Deze koude filamentaire ontladingen worden in het algemeen toegepast op verschillende monsters, voor bijvoorbeeld oppervlakte-functionaliseren van polymeren of biomedische behandeling van organische weefsels. Beschikbare diagnostische hulpmiddelen zijn echter beperkt beschikbaar voor de bestudering hiervan. Met beeldvormings Mueller polarimetrie toegepast op elektro-optische doelen worden de axiale en radiële elektrische velden onderzocht met betrekking tot amplitude (3-6 kV/cm), lengteschalen ( $\leq 1$  mm axiaal en  $\leq 1$  cm radiëel) en tijdschalen ( $\leq 1 \mu\text{s}$  gepulseerd en  $\leq 10 \mu\text{s}$  AC) voor verschillende operationele parameters van de jet, zoals spanningsamplitude en omgevingsgas.

Tegelijkertijd met de kortstondige dubbelbreking als gevolg van het elektrische veld is er ook een constant achtergrond patroon geobserveerd. Dit wordt veroorzaakt door mechanische spanning binnen het blootgestelde materiaal door geïnduceerde temperatuursgradiënten vanwege een inhomogene temperatuursverdeling. Een analytische relatie is verkregen via het foto-elastisch effect, dat het mogelijk maakt om via een numeriek algoritme de temperatuursverdeling te verkrijgen. Dit algoritme is gebruikt, na kalibratie, om aan te tonen dat de temperatuur van het monster tot 25 graden kan variëren ten opzichte van de kameromstandigheden afhankelijk van de frequentie waarop de AC-aangestuurde plasma jet aangedreven wordt. Ook veranderingen in het geïnduceerde elektrische veld zijn tegelijk zichtbaar. Een nauwkeurige bepaling van de temperatuur is belangrijk omdat de meeste toepassingen betrekking hebben op temperatuursgevoelige monsters.

Ten slotte laat dit werk zien hoe complexe monsters kunnen worden onderzocht tijdens een plasma-oppervlakte interactie. Dit wordt gedaan door ze aan te brengen op de elektro-optische materialen. Vanwege de toevoeging van een (dunne) complexe interactie wordt depolarisatie aan het systeem toegevoegd door verstrooiing van de gepolariseerde lichtbundel. In-situ waargenomen veranderingen van depolarisatie hebben betrekking op de toestandsevolutie van het blootgestelde complexe materiaal tijdens de plasmabehandeling. Dit, gekoppeld aan de gelijktijdig geobserveerde elektrische velden, biedt een uniek diagnostisch hulpmiddel voor het onderzoek naar plasma-oppervlakte interacties. Deze diagnostiek is toegepast voor een testcase waarbij een enkele cellaag van een ui is blootgesteld aan de ionisatiegolven die worden gegenereerd door de plasma jet.

# List of Symbols and Abbreviations

$\vec{k}$	wave vector, indicating the propagation direction of the light
$\vec{E}$	electric field
$\vec{B}$	magnetic field
$\epsilon_0$	vacuum permittivity
$\mu_0$	vacuum permeability
$\vec{\Pi}$	Poynting vector
$k, \omega$ and $\lambda$	wave number, frequency and wavelength
$\varphi_x$	relative phase of the x-component
$\vec{J}_P$	Jones vector
$\vec{S}_P$	Stokes vector
$P_{0/90}$	amount of linearly polarized light in the 0/90 degree coordinate system
$P_{45/135}$	amount of linearly polarized light in the diagonal 45/135 degree coordinate system
$P_{l/r}$	amount of circularly polarized light
$\rho_P$	degree of polarization
$M_J$	Jones matrix
$M_S$	Mueller matrix, used for Stokes vectors
$\rho$	change of polarization
$\Psi$	change in amplitude of polarization intensity
$\Delta$	change in phase retardance
$PSG$	Polarization State Generator
$PSA$	Polarization State Analyzer
$B$	$4 \times 4$ intensity matrix
$M$	$4 \times 4$ Mueller matrix
$I$	intensity element of the $B$ matrix
$QWP$	Liquid crystal named after quarter wave plate
$HWP$	Liquid crystal named after half wave plate
$\alpha_{i,pos}$	orientation of liquid crystal $i$ in positive state
$\alpha_{i,neg}$	orientation of liquid crystal $i$ in negative state
$\Delta\alpha_i$	change in orientation of liquid crystal $i$
$i$	indication of the liquid crystal, $i = 1, 2, 3$ or $4$

---

$\Lambda_i$	orientations of the liquid crystals within their mount
$W$	Mueller matrix of the PSG
$A$	Mueller matrix of the PSA
$ECM$	Eigenvalue Calibration Method
$B_0$	calibration intensity matrix (air)
$B_1$	calibration intensity matrix (vertical linear polarizer)
$B_2$	calibration intensity matrix (horizontal linear polarizer)
$B_3$	calibration intensity matrix (wave retarder)
$C_j, D_j, N_j$ and $H_j$	mathematical matrices constructed during the ECM
$\varphi_j$	orientation of the calibration sample $j$
$j$	indication of the calibration sample, $j = 0, 1, 2$ or $3$
$L$	logarithm of Mueller matrix $M$
$L_m$	diattenuation and birefringent properties extracted from $L$
$L_u$	depolarization and uncertainties extracted from $L$
$m$	$4 \times 4$ differential matrix, containing $\psi$ and $\gamma$
$\psi_{l/r}, \psi_{0/90}, \psi_{45/135}$	differential diattenuation: circular polarization and linear polarization properties along the 0/90 or 45/135 degree coordinate system
$\gamma_{l/r}, \gamma_{0/90}, \gamma_{45/135}$	differential birefringent properties
$G$	$4 \times 4$ Minkowski metric
$\Psi_{l/r}, \Psi_{0/90}, \Psi_{45/135}$	integrated diattenuation: circular polarization and linear polarization properties along the 0/90 or 45/135 degree coordinate system
$\Gamma_{l/r}$	integrated circular birefringent properties
$\Gamma_{0/90}$ and $\Gamma_{45/135}$	integrated linear birefringent properties
$HER$ -model	homogeneous elliptical retarder model
$LB$	linear birefringence (0/90 deg coordinate system)
$LB'$	linear birefringence (45/135 deg coordinate system)
$CB$	circular birefringence
$\{2, 3\}$	indication of matrix element, e.g. row 2 and column 3
$BSO$	electro-optic material $\text{Bi}_{12}\text{SiO}_{20}$
$Felinbo$	electro-optic material $\text{Fe:LiNbO}_3$
$d$	material thickness
$n_{0/90}$	refractive index, e.g. in the 0/90 degree system
$A_\varepsilon$	impermeability tensor
$\Delta\eta_i$	anisotropy terms deforming the index ellipsoid
$\bar{T}$	electro-optic $6 \times 3$ tensor with elements $r_{ij}$
$\bar{P}$	photo-elastic $6 \times 6$ tensor with elements $p_{ij}$
$\vec{S}$	strain vector
$\vec{u}$	displacement vector
$t_d$	time delay relative to an external trigger event
$T$	temperature
$\gamma_{1,2,3}$	calibration factors for temperature fitting procedure

Chapter **1**

# Global Introduction

## Contents

---

<b>1.1 Plasma Surface Interaction</b> . . . . .	<b>2</b>
1.1.1 Introduction . . . . .	2
1.1.2 Approaches to Study Plasma Surface Interactions . . . . .	4
1.1.3 Our Approach: Optically Active Targets . . . . .	5
<b>1.2 Introduction of Polarized Light and Mueller Polarimetry</b> . . . . .	<b>8</b>
1.2.1 Description of Polarization . . . . .	9
1.2.2 Polarization Interaction with Materials . . . . .	11
1.2.3 Polarization Diagnostics . . . . .	13
<b>1.3 Non-Thermal Atmospheric Pressure Plasmas</b> . . . . .	<b>15</b>
1.3.1 Plasma Jet Design and Basic Operation . . . . .	18
1.3.2 Investigation of Guided Ionization Waves . . . . .	19
1.3.3 Interaction with Dielectric Materials . . . . .	20
<b>1.4 Outline of this PhD Thesis</b> . . . . .	<b>24</b>
<b>References</b> . . . . .	<b>26</b>

---

## 1.1 Plasma Surface Interaction

From the title of this thesis, “Investigation of Plasma Surface Interactions using Mueller Polarimetry”, the two main subjects cannot be missed. However, despite being the obvious themes throughout this work, both *plasma surface interactions* and *Mueller polarimetry* are vast topics that need further clarification and specification. This introduction starts with a global picture of plasma surface interactions. Then it focuses on Mueller polarimetry and finally on the plasma that is investigated throughout the work. The last part of this chapter will give an outline of this thesis.

In general, the main goal of this thesis is to introduce a new optical diagnostic method (Mueller polarimetry) and examine how it can be used to study plasmas interacting with surfaces. It therefore brings together optics and plasma physics. The various subjects of this thesis show how to apply Mueller polarimetry to investigate plasma surface interactions, gain information about plasma processes at the surface and couple this to surface effects observed in the materials that are under plasma exposure.

### 1.1.1 Introduction

The framework of this thesis follows the question of how plasma surface interactions can be studied in a new way. This is not a new research topic, nor is it something that had no relevance in the past. In fact, one could say that plasma surface interactions as a theme is one of the most recurring areas within plasma research. This is simply because every plasma or gas discharge created in a laboratory will eventually interact with a surface on its path. The type of interaction can be classified depending on whether this surface is present to act as one of the electrodes, it is confining the discharge within a chamber or it is a sample that is interacting towards a specific goal for a certain application. In any case, the resulting interaction cannot be overlooked. The scope of interest for this work lies with the latter type of interaction and not the first two. The classification will be further elaborated depending on the application.

The application of the plasma is further divided depending on the desired goal of the surface interaction, which can either be to *design*, *modify*, *treat* or *assist* in any way. This will be further discussed below. The division is naturally not very strict and meant more to indicate the vast variety of applications that exist for which the investigation of plasma surface interactions are important.

The simple reason why plasma surface interactions have been studied frequently in the past and remain an important item today is because both the plasmas that are generated and the surfaces that they encounter change continuously. In the past, the type of interactions that were studied was determined greatly by the semiconductor industry and their interest in chip manufacturing. Industrial

size plasmas were and are applied to surfaces to *recreate* and *design* simple metalloids like silicon into comprehensive devices at a nanoscale.<sup>1</sup> Etching processes<sup>2</sup> and atomic layer deposition,<sup>3</sup> applied for thin film growth, are perhaps the most investigated interactions between any plasma and any surface up to this day.<sup>4</sup>

However, the interaction between a plasma and a target exceeds the interest of the semiconductor industry alone. Industrial size plasmas have been applied to e.g. glasses or plastics as well.<sup>5,6</sup> In this case, the goal of the interaction is not to design a comprehensive device through etching or deposition, but rather to change or *modify* surface properties e.g. wettability or adsorption.

These temperature sensitive surface modifications, for coating or surface functionalization, can be done at reduced pressure, but due to cost-saving developments the focus lies more with atmospheric pressure plasmas.<sup>7</sup> This deviates from the plasmas that are used for etching and atomic layer depositions which are mostly generated at low pressures. At lower pressure the plasma sheath is stable and not very collisional. This allows for stable control of the desired processes. At elevated or atmospheric pressure this is not the case since in general smaller plasmas are generated that consequently have a more heterogeneous and filamentary nature. Still a predefined goal is present but the necessary interactions are different. Etching processes and atomic layer deposition are less controllable, while e.g. charge transfer, species transport and electric field generation are of more interest.<sup>8,9</sup> The use of a dielectric barrier or pulsing to generate these discharges prevents them from becoming a thermal discharge. The interaction of thermal discharges with materials, e.g. welding applications or fusion wall interactions, is outside the scope of this work.

At atmospheric pressure the relatively small sized non-thermal discharges have been used for a third category of applications in which the purpose is to *treat* a surface, instead of *designing* or *modifying* a material. This is because the non-thermal behavior of these plasmas allows for the interaction with e.g. living tissues for biomedical applications<sup>10-12</sup> or bacteria and viruses for decontamination.<sup>13-15</sup>

---

<sup>1</sup>R. G. POULSEN *J. Vac. Sci. Technol.* 1977 **14**: 266–274

<sup>2</sup>J. W. COBURN and H. F. WINTERS *J. Vac. Sci. Technol.* 1979 **16**: 391–403

<sup>3</sup>H. B. PROFIJT et al. *J. Vac. Sci. Technol. A Vacuum, Surfaces, Film.* 2011 **29**: 050801

<sup>4</sup>M. A. LIEBERMAN and A. J. LICHTENBERG 2005 ISBN: 9780471724254

<sup>5</sup>E. LISTON et al. *J. Adhes. Sci. Technol.* 1993 **7**: 1091–1127

<sup>6</sup>D. L. FLAMM and O. AUCIELLO 1990 ISBN: 978-0-12-200430-8

<sup>7</sup>F. FANELLI and F. FRACASSI *Surf. Coatings Technol.* 2017 **322**: 174–201

<sup>8</sup>M. LAROSSI and F. LEIPOLD *Int. J. Mass Spectrom.* 2004 **233**: 81–86

<sup>9</sup>E. C. NEYTS *Plasma Chem. Plasma Process.* 2016 **36**: 185–212

<sup>10</sup>G. FRIDMAN et al. *Plasma Process. Polym.* 2008 **5**: 503–533

<sup>11</sup>M. G. KONG et al. *New J. Phys.* 2009 **11**: 115012

<sup>12</sup>K.-D. WELTMANN et al. *Contrib. to Plasma Phys.* 2009 **49**: 631–640

<sup>13</sup>E STOFFELS et al. *Plasma Sources Sci. Technol.* 2002 **11**: 383–388

<sup>14</sup>Y. S. SEO et al. *IEEE Trans. Plasma Sci.* 2010 **38**: 2954–2962

<sup>15</sup>J. EHLBECK et al. *J. Phys. D. Appl. Phys.* 2011 **44**: 013002

Consequently, the interaction is not only restricted to solid materials but to liquids as well. Lastly, a surface can be introduced to interact with the discharge to assist and amplify certain plasma processes, e.g. with powders for catalytic purposes.<sup>9,16</sup> This is not just to enhance or amplify a process, but can also be applied to influence or change the chemistry (pathways) in the plasma.

### 1.1.2 Approaches to Study Plasma Surface Interactions

The simplest way to investigate the plasma surface interactions occurring for these applications is to examine whether the desired goal for the material has been met after the interaction. In other words, did the plasma manage to decontaminate the food packaging for unwanted bacteria and viruses? Did the vitality or mortality of the treated cells change due to the plasma interaction? Or, has the wettability of the surface been altered? However, unfortunately this approach does not give more than a confirmation and some indication of how “strong” the interaction has been. When more detailed information about the specific interaction is required, more challenging diagnostics have to be used.

In general, three global strategies can be followed to investigate plasma surface interactions: plasma diagnostics applied to the discharge with a surface present; diagnosing the surface under plasma exposure; or using a numerical approach focusing again either more in detail on the discharge or on the target.

To study the discharge to which the surface is exposed to – in terms of fluxes, densities, and temperatures of species, electric fields that are generated and gas flow dynamics – plasma diagnostics are necessary. It goes without saying that certain goals for target treatment, modification or design cannot be met when the plasma does not have the proper “ingredients” with regard to energy levels, production of species and transport capabilities. A specific diagnostic can be designed to focus on an individual aspect of the plasma surface interaction. Examples for non-thermal plasma jet applications are the determination of electric field using Stark spectroscopy,<sup>17</sup> the helium metastable densities through laser absorption spectroscopy<sup>18</sup> or OH radical densities using laser-induced fluorescence.<sup>19</sup> Numerical approaches have the capabilities to examine, monitor and predict several aspects of the interaction. However, naturally, they rely on experiments for both input and validation.

The last approach is not to diagnose the plasma, but rather the surface that is under exposure. This can focus on e.g. surface analyses, global examination of the targeted material or chemical changes in liquid targets. Examples

---

<sup>16</sup>O. GUAITELLA et al. *J. Phys. D. Appl. Phys.* 2006 **39**: 2964–2972

<sup>17</sup>G. B. SRETENVIĆ et al. *Appl. Phys. Lett.* 2011 **99**: 161502

<sup>18</sup>T. DARNY et al. *Plasma Sources Sci. Technol.* 2017 **26**: 045008

<sup>19</sup>S. YONEMORI et al. *J. Phys. D. Appl. Phys.* 2012 **45**: 225202

related again for non-thermal jets focus on etch rates on polymers,<sup>20</sup> changes in materials' surface energy / wettability<sup>21</sup> and induced cellular changes or bacterial decontamination.<sup>22</sup>

Usually, only information on half of the problem relating plasma surface interactions is obtained when one of the experimental approaches is chosen and used. It is often not possible to simultaneously examine the discharge and the material using a combination of two diagnostics, because of the usual size and complexity of those diagnostics. Consequently, the most difficult thing is to couple the obtained plasma parameters from the plasma diagnostics to the observed material changes extracted from the surface examination. The two previous approaches are lacking essential information to really understand the total interaction mechanism, which only *in-situ* surface diagnostics can provide. These diagnostics are however very limited due to both the complexity of the samples and the discharges that are interacting with them. An example of an *in-situ* diagnostic to examine surface charge and electric fields experienced by the sample uses a series of capacitive probes coupled to segmented electrodes applied for surface dielectric barrier discharges (DBDs).<sup>23,24</sup> Our approach presented in this thesis could also be used to investigate *in-situ* the electric field that samples experience under plasma exposure but is not limited to surface DBDs. In addition, the optical diagnostic technique opens a wide variety of examinations that can be done, not only limited to electric field or surface charge.

### 1.1.3 Our Approach: Optically Active Targets

This work investigates Mueller polarimetry as a diagnostic for plasma surface interactions, as the title announced. In general, what Mueller polarimetry allows is the optical investigation of materials by measuring their Mueller matrix using polarized light. From the Mueller matrix, materials can be analyzed regarding their optical properties in terms of diattenuation, birefringence and depolarization.<sup>25</sup> As a result, the approach taken to investigate plasma surface interactions seems to have the focus on the material side.

However, the materials under investigation will be specifically chosen because of their dependence on external exposure. In other words, materials that for instance change due to external electric field or temperature are examined to identify exactly which electric fields and temperatures are obtained inside a target under a certain plasma exposure. Although this means that the examined materi-

---

<sup>20</sup>K. FRICKE et al. *Plasma Process. Polym.* 2011 **8**: 51–58

<sup>21</sup>R. FOEST et al. *Plasma Phys. Control. Fusion* 2005 **47**: B525–B536

<sup>22</sup>E STOFFELS et al. *Plasma Sources Sci. Technol.* 2006 **15**: S169–S180

<sup>23</sup>C. L. ENLOE et al. *AIAA J.* 2008 **46**: 2730–2740

<sup>24</sup>V. R. SOLOVIEV et al. *Phys. Plasmas* 2017 **24**: 103528

<sup>25</sup>J. GIL and R. OSSIKOVSKI 2016 ISBN: 9781482251555

als are not the ones used for applications, it does allow to bridge the gap between exclusive diagnostics that focus on only the discharge or on the material.

The targets that are chosen for our approach are used because of their dependence on external exposure. Their refractive index can be influenced, creating a birefringence (also called anisotropy) that can be detected with Mueller polarimetry. This is ideal for the investigation of plasma surface interactions since the changes in the (refractive index of the) materials are directly coupled to the plasma to which they are exposed. The type of interaction that is studied can be chosen depending on which *optical effect* is exploited.

The refractive index of a material can be altered by many different factors.<sup>26</sup> The *photoelastic* effect (also called *elasto-optic* effect) describes changes in the refractive index due to external mechanical strain or stress. This is easily observed in plastics that are deformed but occurs in many other materials as well. When the index of refraction is influenced by a temperature field the effect is named *thermo-optic*. Similarly, magnetic fields can cause anisotropies inside a material, according to the *magneto-optic* effect (also called the Cotton-Mouton effect or Voigt Effect depending on the type of material). The *photorefractive* effect describes changes in refractive index and absorption coefficient due to light exposure on materials.

For the purpose of this thesis to show the use of Mueller polarimetry to investigate plasma surface interactions, the *electro-optic* effect is mostly focused upon since it describes changes in a material due to surface charges and induced electric fields. Electric fields inside a plasma are relevant for numerous other plasma parameters regarding the discharge propagation and production, temperature, and fluxes of species. The surface charging of a material is as important since it influences the surface dynamics of the discharge and as such the plasma surface interactions. The knowledge of the electric field to which targets are exposed to is essential for the coupling of the observed changes in treated samples to the plasma that has caused them. Electric fields (generated without a plasma) influence cellular tissues through electroporation<sup>27,28</sup> and induce transport of dispersed particles through dielectrophoresis.<sup>29,30</sup>

The electro-optic effect occurs in all materials as a second-order influence of the electric field to the refractive index, scaling quadratically according to the *Kerr* effect.<sup>31</sup> For some materials, i.e. crystals that lack an inversion symmetry, there is also a first-order linear dependence on the electric field, called the *Pockels* effect,<sup>32</sup> which is generally much stronger than the *Kerr* effect. When electro-optic targets are exposed to electric fields (e.g. induced during a plasma surface interaction)

---

<sup>26</sup>M.-J. J. WU 1995 ISBN: 978-1-4615-2273-7

<sup>27</sup>E NEUMANN et al. *EMBO J.* 1982 **1**: 841–5

<sup>28</sup>J. C. WEAVER *J. Cell. Biochem.* 1993 **51**: 426–435

<sup>29</sup>R. PETHIG et al. *J. Phys. D. Appl. Phys.* 1992 **25**: 881–888

<sup>30</sup>P. R. C. GASCOYNE and J. VYKOUKAL *Electrophoresis* 2002 **23**: 1973–83

<sup>31</sup>J. KERR *London, Edinburgh, Dublin Philos. Mag. J. Sci.* 1875 **50**: 337–348

<sup>32</sup>F. POCKELS 1894

they become birefringent, which can be investigated with Mueller polarimetry.

The goal of the work presented in this thesis is to show how Mueller polarimetry can be used as a diagnostic to examine plasma surface interactions. Targets are investigated optically by measuring their Mueller matrix and analyzing their optical properties, as will be introduced below. This opens a wide range of possibilities since different optically active target can be used to examine the effect of exposure – of e.g. electric fields, temperature, mechanical stress, magnetic fields, radiation – induced during the interaction *inside* the targeted material. In addition, since depolarization is part of the optical investigation, it offers ways to examine the surface state of the targeted materials since polarized light is scattered as it propagates through it. This offers the possibility to do a unique investigation where surface changes are monitored (captured within depolarization) simultaneously with the external factors causing it, e.g. electric field induced inside the electro-optic materials (captured within the birefringence).

One of the main challenges for the use of Mueller polarimetry as a plasma diagnostic is to make measurements in a dynamic environment. Normally, only static samples are optically examined using the technique, but this will not offer the *in-situ* demands needed to investigate the transient plasma surface interaction. Therefore, a unique imaging Mueller polarimetry setup is built which allows for the time-resolved measurement of the Mueller matrix of a sample.

In the first place, this work focuses on examining electro-optic targets under plasma exposure. This allows for the detection of electric fields experienced during the interaction. The experimental procedure and method of analyses are crucial for these new examinations and are therefore highlighted in the thesis. Different approaches are examined to measure and identify all the individual electric field components separately. This offers new ways to examine surface discharge dynamics. The research is extended afterwards to simultaneously investigate also the temperature induced in the targeted materials.

Lastly, the thesis will show how “complete” *in-situ* investigations are performed using Mueller polarimetry by simultaneously investigating depolarization and birefringence. This allows seeing changes in a complex targeted sample while the optically active material (to which the sample is attached to) allows for the determination of the parameters that has possibly caused the changes of the sample.

The examples that will be shown for the application of Mueller polarimetry as a plasma surface diagnostic are only the start of the possibilities offered by the technique, which has never been used for this purpose before. The explanation of the build / design of the setup, analysis of the measurements, analytical description of optically active targets and the resulting investigated examples, allow others to follow our approach to investigate plasma surface interactions using Mueller polarimetry. An introduction will be given first of the optical technique and of polarized light.

## 1.2 Introduction of Polarized Light and Mueller Polarimetry

Mueller polarimetry is an optical examination of materials by measuring the Mueller matrix using polarized light. By using polarized light the characteristics of the electro-magnetic behavior of light are exploited. Described by Maxwell's equations, the propagation of light can be represented as a transverse electro-magnetic wave where the wave vector  $\vec{k}$  gives the propagation direction of the light, see figure 1.1(a). Both the electric and the magnetic field components (rel.  $\vec{E}$  and  $\vec{B}$ ) are oscillating in a plane normal to this wave vector, governed by the wave equations which are derived directly from Maxwell's equations:

$$\nabla^2 \vec{E} = \varepsilon_0 \mu_0 \frac{\partial^2 \vec{E}}{\partial t^2} \quad (1.1)$$

$$\nabla^2 \vec{B} = \varepsilon_0 \mu_0 \frac{\partial^2 \vec{B}}{\partial t^2} \quad (1.2)$$

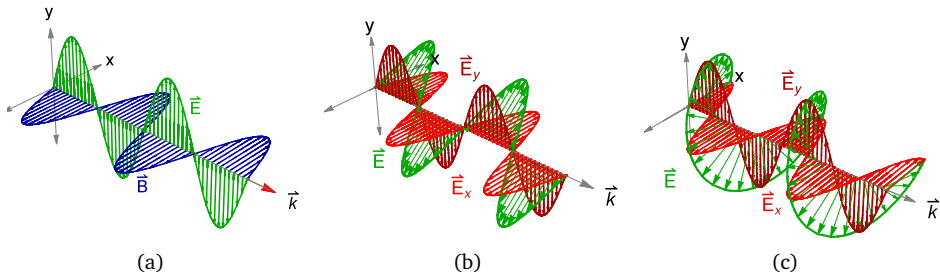


Figure 1.1: The propagation of light in direction  $\vec{k}$  is described by the oscillations of the electric (green) and magnetic (blue) field components in the plane normal to  $\vec{k}$ , see e.g. in figure 1.1(a). For the polarization of the beam the direction and relative phase of the electric field components (red) is considered, referred to as linearly polarized (figure 1.1(b)) or circularly polarized (figure 1.1(c)).

The Poynting vector  $\vec{\Pi}$  is parallel to the propagation direction of the light, described by the wave vector  $\vec{k}$ , and its magnitude relates to the energy flux transported by the light. It can therefore be related to the intensity of the light. The magnetic field component is always perpendicular to the electric field and consequently its behavior can be described using the electric field, by following Maxwell's equations. Thereby it is appropriate and sufficient to focus solely on the electric field components to describe the polarization of light, since interaction of light with magnetic materials or with nanostructures is not included.

$$\vec{\Pi} = \frac{1}{\mu_0} \vec{E} \times \vec{B} \quad (1.3)$$

When the electric field component of a radiation beam oscillates in a defined way within the plane normal to the propagation direction, the beam is said to be fully polarized. For polarized light where the orientation of the electric field oscillations does not change along the propagation, the polarization is specified as linear. In cases where the orientation rotates in time it is called elliptical, see figures 1.1(b) and 1.1(c).

The general solution to the electro-magnetic wave equations is given by equations (1.4) and (1.5), describing the electric and magnetic field components as a function of space,  $\vec{r} = (x, y, z)$  in Cartesian coordinates, and time  $t$ . The axis of propagation of the light is chosen as the  $z$ -axis and therefore  $\vec{E}$  and  $\vec{B}$  oscillate in the  $XY$ -plane. The scalar  $k$  is the wavenumber defined as the frequency  $\omega$  divided by the speed of light  $c$ . Both the magnitude of the individual vector components, i.e.  $E_x$  and  $E_y$ , and the relative phase,  $\varphi_x$  and  $\varphi_y$ , determine the state of polarization of the electric field component of the light.

$$\vec{E}(\vec{r}, t) = \begin{pmatrix} E_x \exp(i(kz - \omega t) + \varphi_x) \\ E_y \exp(i(kz - \omega t) + \varphi_y) \end{pmatrix} \quad (1.4)$$

$$\vec{B}(\vec{r}, t) = \begin{pmatrix} B_x \exp(i(kz - \omega t) + \varphi_x + \pi/2) \\ B_y \exp(i(kz - \omega t) + \varphi_y + \pi/2) \end{pmatrix} \quad (1.5)$$

As light interacts with materials – i.e. with solids, liquids or particles in gases – its polarization state or its degree of polarization can change. Mathematically the polarization of light can either be described using Jones calculus or Stokes calculus. These will be introduced below. While the Jones formalism is adequate to treat fully polarized beams, the Stokes formalism is more general and can be used to describe beams which can be either fully or partially polarized. As a result there are two different diagnostics using polarized light to investigate materials, called ellipsometry and Mueller polarimetry. An introduction will be given of both with a comparison and reasoning why in this work the latter is researched for new applications to investigate plasma surface interactions.

### 1.2.1 Description of Polarization

The state of polarization is defined by the orientation of the electric field oscillations within the propagation of the light, as shown with two examples in figure 1.1. The most general state of polarization of light is the elliptical one. The rotation of oscillations of  $\vec{E}$  follow an elliptical path seen from the moving frame / plane perpendicular to  $\vec{k}$ , see figure 1.2. This ellipse is characterized by its eccentricity

and angle  $\Psi$ , which can describe any polarization state, including the linear and circular ones. These are considered as particular cases of elliptical polarization, with an eccentricity of respectively 1 and 0.

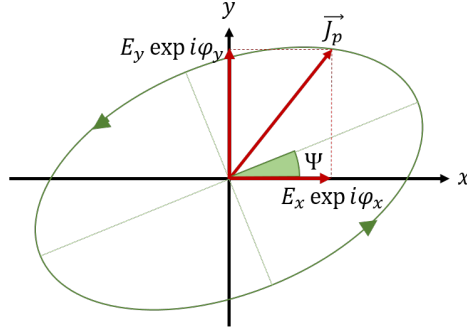


Figure 1.2: Visualization of a polarization state (red) using an ellipse. This shows the rotating orientation of the oscillations (green) for the electric wave components of the propagating light in the moving plane perpendicular to the propagation direction.  $\vec{J}_P$  describes the state of polarization following the Jones calculus.

The shape of the ellipse is a secondary representation of the polarization state, visualizing the primary and fundamental representation as defined by equations (1.4) and (1.5). When one of the semi-axes of the ellipse is zero the light is linearly polarized and when they are equal it is circular. Any state of polarization in between these two extremes is called elliptical. The inclination angle of the ellipse  $\Psi$  is determined by the amplitude of the horizontal and vertical components of the oscillations, i.e.  $E_x$  and  $E_y$ . The ellipticity depends on the relative phase of the oscillation components. Linearly polarized light can only occur when the  $x$  and  $y$  component of the electric field travel with the same phase component, i.e.  $\varphi_x = \varphi_y$ . In any other polarization state there is a phase difference, which is  $\pm\pi/2$  for circularly polarized light.

When a representation of the polarization state describes the entire intensity of the propagating light wave, the light is called fully polarized. Naturally, this does not have to be the case, since light can be either randomly polarized or partially polarized as well. This is the basis for the division of Jones and Stokes calculus.

The Jones representation of fully polarized light originates directly from the fundamental representation, focusing on the magnitude and relative phase of the individual vector components., indicated by Jones vector  $\vec{J}_P$ .<sup>33</sup>

$$\vec{J}_P = \begin{pmatrix} E_x \exp(i\varphi_x) \\ E_y \exp(i\varphi_y) \end{pmatrix} \quad (1.6)$$

<sup>33</sup>R. C. JONES *J. Opt. Soc. Am.* 1941 **31**: 488

The Stokes representation is not related directly to the magnitude and relative phase, but to the combination of polarization states in terms of linearly and circularly polarized light.<sup>34</sup> Any elliptical state of polarization can be described as a combination of linearly polarized light along the  $x$  and  $y$ -axis  $P_{0/90}$ , combined with linearly polarized light along the diagonal axis  $P_{45/135}$  and circularly polarized light  $P_{l/r}$ . These quantities range from -1 to 1 due to normalization. The interpretation of the sign determines the axis of polarization, e.g. for  $P_{0/90}$  positive values indicate polarization along the  $x$ -axis, while negative values are used for polarization along the  $y$ -axis. As a result the Stokes vector  $\vec{S}_P$  consists of four elements and it can represent any state and degree of polarization. The degree of polarization is given by  $\rho_P$ , see equation (1.7).

$$\vec{S}_P = \begin{pmatrix} S_0 \\ S_1 \\ S_2 \\ S_3 \end{pmatrix} = \begin{pmatrix} \rho_P \\ P_{0/90} \\ P_{45/135} \\ P_{l/r} \end{pmatrix} \quad \text{with} \quad \rho_P = \sqrt{P_{0/90}^2 + P_{45/135}^2 + P_{l/r}^2} \quad (1.7)$$

The Jones vector  $\vec{J}_P$  can be transformed into a Stokes vector  $\vec{S}_P$  but when the degree of polarization is not unity not the other way around.

## 1.2.2 Polarization Interaction with Materials

A change of polarization state can occur when light interacts with a material. This can either change the type of polarization or the degree of polarization. The mathematical description of one Jones or Stokes vector into another Jones or Stokes vector implies the usage of matrices to account for the change induced by the material.<sup>35</sup> These contain the optical characterization of the material. In general, the change in polarization state and degree of polarization after interaction with a material can be described in terms of three fundamental polarimetric properties, namely dichroism, birefringence and depolarization.<sup>36</sup> The first two describe a change in *type* of polarization, e.g. a transition from linearly to circularly polarized light. The latter describes a change in *degree* of polarization.

Dichroism is the material property describing the dependence of the transmittance with the type of polarization. Dichroism is closely related to diattenuation, but they differ slightly in definition.<sup>37</sup> This means that for materials with dichroism properties some states of polarized light are able to propagate through the material while others are blocked. This property can be related to the internal

<sup>34</sup>G. G. STOKES *Trans. Cambridge Philos. Soc.* 1851 **9**: 399

<sup>35</sup>E. HECHT 2002 ISBN: 9780805385663

<sup>36</sup>E. GARCIA-CAUREL et al. 2013 ISBN: 978-3-642-33956-1

<sup>37</sup>O. ARTEAGA and A. CANILLAS *J. Opt. Soc. Am. A* 2009 **26**: 783

molecular structure inside the material. The occurrence of linear dichroism is generally detected in solid materials, related to the buildup structure and orientation of the molecules.<sup>38</sup> Circular dichroism occurs less often in solid materials, but rather in liquids, caused by the chirality of the aqueous species.<sup>39</sup> Materials with dichroism are usually referred to as polarizers, since they are often used to go from unpolarized light to a known polarized light state.

Birefringence occurs in absorbing and transparent materials and expresses the difference in refractive index experienced by light polarized in a specific way depending on the material orientation. In general, when the refractive index of a material is non-uniform some components of the light will travel faster than others, creating a phase difference when exiting the material. This means that e.g. linearly polarized light can be turned into a circular polarization state by using a quarter wave plate. This phase retardance is coupled directly to the birefringence and consequently to a change in the (experienced) refractive index. It occurs often in materials that lack certain symmetries (e.g. the mineral Calcite), i.e. most non-cubic structures.<sup>40</sup> Also, birefringence can be induced externally by applying stress to the materials.

Depolarization is a global property of materials that relates to a loss in degree of polarization during the interaction. This can be induced by e.g. internal scattering or surface roughness. Contrary to the diattenuation and birefringent properties, the depolarization can only be described using Stokes calculus and not with Jones calculus. This is because Jones calculus only describes fully polarized light.

The way these optical properties are included in the description of the materials initiates with the definition of the Jones and Stokes vectors, see respectively equations (1.6) and (1.7). Consequently, the Jones matrices are of size  $2 \times 2$ , while the “Stokes” matrices are  $4 \times 4$ . Since the Jones vectors have an imaginary part, consisting of their relative phase, the matrix can also be imaginary. For Stokes calculus this is not the case since the relative phase is included by describing the light as a combination of  $P_{0/90}$ ,  $P_{45/135}$  and  $P_{l/r}$ . These  $4 \times 4$  matrices are always called the Mueller matrices (instead of Stokes matrices).

To illustrate the meaning of the mathematical matrices two examples are used. Firstly, as stated, materials with birefringent properties can induce a change of linearly polarized light to circularly polarized light. Light polarized linearly along the  $+45^\circ$  axis only becomes circularly polarized when it interacts with a material that causes the horizontal component to travel faster / slower than the vertical component. Hence a quarter wave plate can be used when it is oriented with its fast axis at  $0^\circ$  (horizontal), but not when it is oriented at  $45^\circ$  (diagonally). This is described mathematically by a change of an initial Jones vector  $J_1$  into a

---

<sup>38</sup>Y. MATSUOKA and B. NORDEN *J. Phys. Chem.* 1982 **86**: 1378–1386

<sup>39</sup>T. B. FREEDMAN et al. *Chirality* 2003 **15**: 743–758

<sup>40</sup>C. MALGRANGE et al. 2014 ISBN: 978-94-017-8992-9

secondary Jones vector  $J_2$ , when Jones calculus is followed, or respectively  $S_1$  and  $S_2$  when Stokes calculus is used. Since the initial and outgoing vectors are fixed, as defined by equations (1.6) and (1.7), specific mathematical matrices  $M_J$  and  $M_S$  are necessary to describe this change in polarization, as shown in table 1.1 for case 1.

A second case is shown where right handed circularly polarized light encounters a linear polarizer with its axis vertical. Consequently, the resulting outgoing state of polarization is vertically linear as well, since the horizontal component of the circular polarization is not transmitted. The intensity of the light has thereby decreased. Again the Jones and Mueller matrices are mathematically fixed as a result to describe this change in polarization. The two cases shown in table 1.1 illustrate that the mathematical matrix of a material directly relates to the optical properties it possesses (e.g. birefringence or dichroism). By examining the mathematical matrix, the material is optically characterized.

Table 1.1: Two examples of the application of Jones and Stokes calculus to describe the interaction of linearly polarized light with a quarter wave plate (case 1, relating to birefringence) and of circularly polarized light with a linear polarizer (case 2, relating dichroism). The resulting Jones and Stokes vectors, i.e.  $J_2$  and  $S_2$ , show the outgoing state of polarization after interaction with the material.

Jones	$\vec{J}_1$	$M_J$	$\vec{J}_2$
case 1	$\frac{1}{\sqrt{2}} \begin{pmatrix} 1 \\ 1 \end{pmatrix}$	$\exp(-i\pi/4) \begin{pmatrix} 1 & 0 \\ 0 & i \end{pmatrix}$	$\frac{\exp(-i\pi/4)}{\sqrt{2}} \begin{pmatrix} 1 \\ i \end{pmatrix}$
case 2	$\frac{1}{\sqrt{2}} \begin{pmatrix} 1 \\ -i \end{pmatrix}$	$\begin{pmatrix} 0 & 0 \\ 0 & 1 \end{pmatrix}$	$\begin{pmatrix} 0 \\ \frac{-i}{\sqrt{2}} \end{pmatrix}$
Stokes	$\vec{S}_1$	$M_S$	$\vec{S}_2$
case 1	$\begin{pmatrix} 1 \\ 0 \\ 1 \\ 0 \end{pmatrix}$	$\begin{pmatrix} 1 & 0 & 0 & 0 \\ 0 & 1 & 0 & 0 \\ 0 & 0 & 0 & 1 \\ 0 & 0 & -1 & 0 \end{pmatrix}$	$\begin{pmatrix} 1 \\ 0 \\ 0 \\ -1 \end{pmatrix}$
case 2	$\begin{pmatrix} 1 \\ 0 \\ 0 \\ 1 \end{pmatrix}$	$\frac{1}{2} \begin{pmatrix} 1 & -1 & 0 & 0 \\ -1 & 1 & 0 & 0 \\ 0 & 0 & 0 & 0 \\ 0 & 0 & 0 & 0 \end{pmatrix}$	$\frac{1}{2} \begin{pmatrix} 1 \\ -1 \\ 0 \\ 0 \end{pmatrix}$

### 1.2.3 Polarization Diagnostics

Since the polarization of light can change when interacting with a material, it can be used as a diagnostic tool. This can either focus specifically on one of the optical properties or on the entire optical matrix of the material that is investigated.

The latter is done using either *ellipsometry* or *Mueller polarimetry*, depending on whether Jones or Stokes calculus is followed respectively.

Generally, when the interest of the material lies with a specific optical property instead of the total optical matrix, a simpler setup can be used. For instance the Sénarmont setup can be used to detect only linear retardance of a material along a chosen axis. The downside of this approach is that no information is obtained about any other optical property and assumptions have to be made for the observed effect, i.e. that other optical properties play no role. All the effects are taken into account when the total optical matrix is examined. This, however, complicates both the experimental setup and the data treatment.

Ellipsometry and Mueller polarimetry follow the same principle of measurement. A known state of polarized light is sent to the material, which changes it. The new state is examined by using a known analyzer and collecting the light behind it. The intensity of the light is analyzed and modeled since both the initial state of polarization and the optical properties of the analyzer are known. This allows for the acquisition of the optical properties of the material.<sup>36</sup>

With ellipsometry, by following the Jones representation, the material properties are examined as a change of polarization  $\rho$  in terms of a change in amplitude  $\Psi$  and phase retardance  $\Delta$ , see equation (1.8). The main restriction of this technique is that, since it is based on Jones formalism, it required light to be fully polarized.

$$\rho = \tan(\Psi) \exp(i\Delta) \tag{1.8}$$

Ellipsometry has been applied mostly in reflection allowing for the investigation of thin films, in terms of e.g. refractive index, dielectric properties, surface roughness and sample homogeneity. It has been used for the investigation of plasma surface interactions with these thin films.<sup>41–43</sup> The examined surface has to be ideally flat, homogeneous and thin, since depolarization has to be prevented.

Mueller polarimetry investigates materials following the Stokes formalism. In this case the measurement of the polarization state and eventually the polarization degree is represented in terms of a Mueller matrix. The Mueller matrix has to be analyzed to retrieve the optical properties of the material. The experimental setup, called the *polarimeter* which is an instrument used to measure Mueller matrices, will be introduced and explained more thoroughly in the next chapter.

The Mueller matrix that is obtained contains, due to the followed formalism, the diattenuation, birefringence and depolarization properties. The main advantage of Mueller polarimetry over ellipsometry is the addition of depolarization. This means that the examined sample does not have to be homogeneous, thin and

---

<sup>41</sup>H. G. TOMPKINS and E. A. IRENE 2005 ISBN: 978-3-540-22293-4

<sup>42</sup>H. FUJIWARA 2007 ISBN: 9780470060193

<sup>43</sup>M. LOSURDO and K. HINGERL 2013 ISBN: 978-3-642-33955-4

ideally flat. Additionally, the optical properties are further represented inside the Mueller matrix to circular contributions and the two linear ones, along the 0/90 axis and along the 45/135 axis, as introduced above. This representation of the optical properties in different coordinate systems is beneficial to describe materials in a more detailed way. For instance, birefringent properties of electro-optic materials induced by external electric field can be explicitly contributed to a specific linear coordinate system of polarization, as will be often used throughout this thesis.

Since the measured Mueller matrices that are obtained include all these optical properties, they offer an ideal tool to characterize a whole variety of samples, e.g. ranging from the cuticles of different beetles,<sup>44,45</sup> to human tissue for dermatology<sup>46</sup> or even cancer detection.<sup>47</sup> The most difficult part of Mueller polarimetry is that physical meaning has to be given to a mathematical  $4 \times 4$  matrix. This is because all the optical information is entangled within the matrix. The optical properties can be separated through modeling or by applying a decomposition.<sup>36</sup> Both methods will be introduced in the next chapter.

Next chapter will also include the design of the experimental setup, as well as the measurement procedure of acquisition and the data treatment that has to be done to obtain the changes induced by the plasma-target interaction. However first, the plasma which is used throughout this work is introduced.

## 1.3 Non-Thermal Atmospheric Pressure Plasmas

In section 1.1 an introduction is given for plasma surface interactions and the various applications that exist in which a plasma interacts with a targeted material. This section will provide more background in the types of plasmas that are used during these non-thermal exposures and how they are generated.

Generally a plasma, also referred to as *ionized gas* or simply a (gas) discharge, describes a gaseous mixture in which electrons, ions, radicals and other excited species are present. A plasma can be generated from a neutral gas by externally adding energy to the system. How the energy gets distributed into the ionized gas depends on the pressure and greatly influences the type of plasma which is induced. The type of plasma can be categorized based upon various parameters, e.g. degree of ionization, densities of species or energy of the species (i.e. temperature).

The most common way to generate a plasma is by applying high electric fields in between two electrodes. Initial seed electrons in the vicinity of the electrode get

---

<sup>44</sup>I. HODGKINSON et al. *Appl. Opt.* 2010 **49**: 4558

<sup>45</sup>H. ARWIN et al. *Opt. Express* 2013 **21**: 22645

<sup>46</sup>M. H. SMITH et al. 2000 ISBN: 0277-786X

<sup>47</sup>A. PIERANGELO et al. *Opt. Express* 2011 **19**: 1582

accelerated to higher energies and if they gain enough energy their impact with neutrals can induce new electrons and consequently also ions. The new electrons get accelerated on their turn which could initiate an electron avalanche. This electron avalanche is crucial for the generation of a plasma.

For a plasma that is generated at low / reduced pressures, the mean free path of the particles is relatively large. This means the seed electrons are “easily” accelerated to the point in which an avalanche occurs and the plasma ignites. This is described by the *Townsend* mechanism.<sup>48</sup> At atmospheric pressure the mean free path of the particles is relatively small, compared to low pressure systems. As a result, the *streamer* mechanism often describes the generation of the plasma.<sup>49</sup> This is because the collision frequency of electrons with the background gas is much higher, meaning the effective time to accelerate the electrons is reduced. Consequently high electric fields are needed for ignition.

High applied electric fields lead to a high localized charge density. The electric field created by the localized charge density assists in inducing new electron avalanches in that direct vicinity. This initiates a propagation of the location of enhanced ionization,<sup>50</sup> called the *ionization front*. The total discharge corresponding to the propagating ionization front is called an *ionization wave*.

A difference can be made between ionization waves that have a *random / arbitrary* direction and those that are *repetitive* and follow the same path. Intrinsically, ionization waves create their path arbitrarily due to branching.<sup>51,52</sup> These discharges are called *streamers*. A reproducible motion of these discharge can result from different causes. Firstly, pre-ionization (e.g. induced by a laser or by previous discharges) can assist the avalanche dynamics of the discharge. This can guide the streamer along a preferred path. Secondly a non-homogeneous gas mixing can have the same effect, as will be introduced later for gas mixing which is crucial for plasma jets. When the ionization waves travel along the same path, they are referred to as *guided ionization waves* (previously also named plasma bullets or guided streamers).

At atmospheric pressure, due to the high collision frequency, there is an increased energy transfer from the electrons to the heavy species. This means that the temperature of the heavy species is increased. When it becomes equal to the temperature (i.e. energy) of the electrons, the discharge is categorized as *thermal*. This can be prevented in two ways, necessary for applications regarding the treatment of temperature sensitive targets. The first is to reduce the interaction time of the discharge by applying pulsed voltages. The second way is to limit the current transfer, which is done by applying dielectric barriers in between the

---

<sup>48</sup>Y. P. RAIZER 1991 ISBN: 978-3-642-64760-4

<sup>49</sup>J. M. MEEK *Phys. Rev.* 1940 **57**: 722–728

<sup>50</sup>A. LUQUE et al. *J. Phys. D. Appl. Phys.* 2008 **41**: 234005

<sup>51</sup>M. ARRAYÁS et al. *Phys. Rev. Lett.* 2002 **88**: 174502

<sup>52</sup>E. M. VAN VELDHIJZEN and W. R. RUTGERS *J. Phys. D. Appl. Phys.* 2002 **35**: 313

electrodes. Dielectric barrier discharges (DBD) with different configurations and operating parameters can be used to generate a non-thermal atmospheric pressure plasma.<sup>53,54</sup>

These types of plasmas are beneficial for the treatment of temperature sensitive targets. This is because reactive species are produced, charges are deposited, electric fields are generated and heat is limited. The control of the plasma allows for a controlled treatment of the surface. However, this 'control' is often complex and consequently limited. The conditions of the generation of a plasma can be optimized as well as the configuration of the electrodes.

Often plasmas used for surface treatment are generated between two parallel plates and as a result (e.g. with etching applications) the exposed sample can act as one of the electrodes. Atmospheric pressure plasma jets have been developed to remove this restriction.<sup>55,56</sup> Due to the design of the electrode configuration, as will be explained below, the plasma is partially generated outside of the electrodes, creating a plasma plume. Still a dielectric barrier is in between the electrodes and the timescales of the applied voltage ensure these plasmas remain *non-thermal*. Hence, plasma jets are still a particular case of a DBD. Hence, the gas temperature is low, while the electrons have high energies. This allows spatial treatment / modification of temperature sensitive targets.

Both for (surface) DBDs and plasma jets the applications have been numerous for the treatment at atmospheric pressure and of temperature sensitive materials.<sup>7</sup> Besides modification of polymers<sup>5,6</sup> and treatment for biomedical applications,<sup>10-12</sup> non-thermal atmospheric pressure discharges have been used for the investigation relating plasma catalysis,<sup>9</sup> flow actuators<sup>57,58</sup> and nitrification of liquids and the treatment in agriculture.<sup>59</sup>

Challenges to investigate these plasmas come from the transient behavior of the individual ionization events (below  $\mu\text{s}$  timescales), the small dimensions in which the characteristic events take place (100  $\mu\text{m}$  upto a few mm), the strong spatial gradients of species densities and electric fields that are induced and the complex surfaces that are used as targets.

The plasma jet is the chosen discharge used throughout this work, to show the way Mueller polarimetry can be applied as a plasma diagnostic for surface interactions, for two main reasons. Firstly, the guided ionization waves generated by the plasma jet are very repetitive with a very low jitter (ns range). Secondly, the plasma jet can be positioned at a 45 degree impact angle towards the targeted surface in order to leave space to examine the surface by Mueller polarimetry, as

<sup>53</sup>H.-E. WAGNER et al. *Vacuum* 2003 **71**: 417–436

<sup>54</sup>R. BRANDENBURG *Plasma Sources Sci. Technol.* 2017 **26**: 053001

<sup>55</sup>A. SCHUTZE et al. *IEEE Trans. Plasma Sci.* 1998 **26**: 1685–1694

<sup>56</sup>X. LU et al. *Plasma Sources Sci. Technol.* 2012 **21**: 034005

<sup>57</sup>D. M. ORLOV et al. *AIAA J.* 2008 **46**: 3142–3148

<sup>58</sup>T. UNFER and J. P. BOEUF *J. Phys. D: Appl. Phys.* 2009 **42**: 194017

<sup>59</sup>A. LINDSAY et al. *Plasma Chem. Plasma Process.* 2014 **34**: 1271–1290

will be shown later in the experimental setup. Mueller polarimetry will be able to address the identified challenges because it will be designed as an imaging system capable of examining time-resolved the changes of a target during the repetitive interaction with the discharges.

### 1.3.1 Plasma Jet Design and Basic Operation

The plasma examined in this work is generated using a kHz-driven plasma jet operated at atmospheric pressure. A coaxial dielectric barrier configuration is used to maintain the plasma at non-thermal conditions. As a result, only the electrons are able to reach elevated temperatures / energies, while the heavy particles remain at low temperature. This section will elaborate on the design of the jet and the operating conditions.

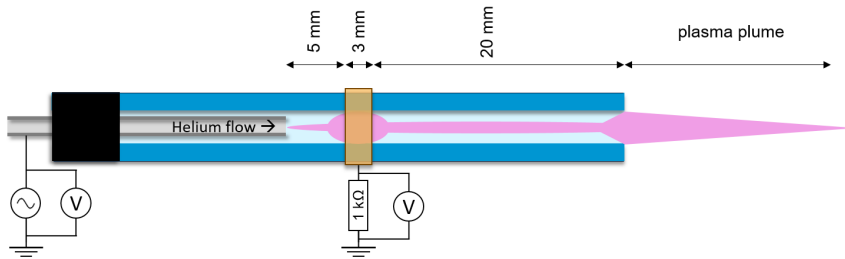


Figure 1.3: The configuration of the plasma jet, consisting of a stainless steel powered electrode (inner diameter 0.8 mm and outer 1.6 mm) through which helium flows into a dielectric Pyrex capillary (inner 2.5 mm and outer 4.0 mm). A grounded ring shaped electrode is placed 5 mm downstream from the powered electrode, leaving 20 mm remaining to the end of the capillary tube. A high voltage probe is used to measure the applied voltage, while the voltage measured over a 1 k $\Omega$  resistor is used to capture the displacement current at the grounded electrode.

The design of the plasma jet is shown in figure 1.3. Helium flows through a stainless steel tube (inner diameter 0.8 mm and outer 1.6 mm) into a Pyrex capillary (inner 2.5 mm and outer 4.0 mm) before mixing with the air environment. The stainless steel tube acts as powered electrode and a grounded ring (width of 3 mm) is placed around the Pyrex capillary at 5 mm downstream from the end of the electrode. The remaining distance from the ground towards the end of the capillary is maintained at 20 mm.

Two different voltage types are applied throughout this work to generate the plasma, either 30 kHz AC sine waves or 5 kHz square-wave pulses of 1  $\mu$ s length (50 ns risetime). Because of the differences in frequency and profile shape of the applied voltage, the plasma is generated at different voltage amplitudes. The AC

case usually operates around 2 kV, while when applying the 5 kHz pulses of 1  $\mu$ s a higher voltage is required, i.e. between 3 and 6 kV.

The *guided ionization waves* can be generated with this jet design using both the voltage types. The coaxial configuration used in this work differs from other jet designs where e.g. two outer rings are used or there is no ring at all.<sup>56</sup> In general, it is possible to operate plasma jets using short nanosecond pulses or radiofrequency signals, in addition to the  $\mu$ s / kHz generation used in this work. Also, different operating carrier gasses can be used instead of pure Helium and the dimensions of a jet differs often between different designs / configurations. These differences in jet design and operating parameters make it non-trivial to compare results obtained for different jets. The overall description of the guided ionization waves however does show similar behaviors.

The ionization wave initiates from the inner powered electrode propagating towards the outer grounded electrode. When the dielectric facing the ground is charged enough to shield the applied field, the ionization wave starts propagating further than the grounded electrode inside the capillary tube. Then after exiting the capillary, the ionization wave propagates in the area referred to as the plasma plume. A sample or material can be placed in this region for treatment applications. A preferential / repetitive path for the ionization waves is created due to left-over charges from previous cycles and the in-homogeneous (helium-in-air) gas mixing which is induced. The latter is important because each species has a different required electron impact energy to ionize. Additionally with the presence of molecular species (e.g. nitrogen or oxygen) the plasma dynamics become more complex due to vibrational and rotational excitation together with dissociative reactions. Lastly, when oxygen is present there will be regions, due to the jet induced gas mixing, where electron attachment is more important than in other regions.

All these effects depend on the local gas mixing, which as a result could create a preferential path for the ionization wave to take. Left-over charge distributions and / or metastable states of noble gases remaining from the previous discharge (often referred to as “memory effect”) enforce this. Consequently the arbitrary nature of the discharge disappears, which is why they are referred to as *guided ionization waves*.

### 1.3.2 Investigation of Guided Ionization Waves

Initial research of the discharges generated with a plasma jet at atmospheric pressure was done through imaging of the plasma plume, i.e. the region outside the capillary where the ionization waves propagate, and characterization of the voltage-current wave forms.

It was observed that the ionization wave initially propagates in a toroidal

(“donut”) shape,<sup>60</sup> after exiting the capillary. Then along the axis of propagation the discharge shape reduces in size until the donut shape has disappeared. The total distance which the ionization wave is able to propagate, i.e. the length of the plasma plume, depends on the operating parameters and jet design. Generally, a larger plasma plume is observed when the plasma jet is operated with higher voltages or (helium) gas flows. The effect of many other operating parameters like pulse duration, inner electrode configuration or thickness of capillary have been reported and discussed in reviews.<sup>56,61</sup> Additionally a lot of investigation has been carried out on the type of reactive species produced by the plume of these discharges (e.g. O atoms<sup>62</sup> or OH densities<sup>19</sup>). Less amount of research is done towards the electric field and electron properties of these ionization waves<sup>63–65</sup> but some of them have been obtained with the jet source in use for this work.<sup>17,66</sup>

An extensive optical and electrical characteristics of the plasma jet used in this work has been published in the past as well when operating the jet with the 30 kHz AC sine waves.<sup>67</sup> The location and formation of the guided ionization wave is coupled to the measured current over a 1 k $\Omega$  resistor added at the grounded ring, see figure 1.4. One ionization wave is generated each cycle during the positive half period of the sine wave indicated by a significant current peak measured when the dielectric Pyrex capillary is charging underneath the grounded ring. A characteristic *dip* in the current profile is observed when the ionization wave leaves the capillary. The power dissipated when applying a 2 kV voltage amplitude is estimated at 0.2 W.<sup>67</sup> Also the capacitive nature of the plasma jet is examined and a change of capacitance of the system of 1.5 pF is observed when the plasma is created.

### 1.3.3 Interaction with Dielectric Materials

The interest in these types of non-thermal plasma jets generated at atmospheric pressure has always been strongly driven by application. There is no risk with placing the guided ionization waves in direct contact with temperature sensitive samples,<sup>12</sup> like polymers or biological tissues, since heavy species remain at low temperatures and the current remains low due to the dielectric barrier.

For biomedical purposes a positive effect of the plasma has been reported in terms of sterilization, wound healing, blood coagulation and even (assisted) cancer treatment.<sup>10,11</sup> The positive influence of the plasma has been attributed to the

---

<sup>60</sup>M. TESCHKE et al. *IEEE Trans. Plasma Sci.* 2005 **33**: 310–311

<sup>61</sup>X. LU et al. *Phys. Rep.* 2014 **540**: 123–166

<sup>62</sup>N. KNAKE et al. *Appl. Phys. Lett.* 2008 **93**: 131503

<sup>63</sup>P. OLSZEWSKI et al. *Plasma Sources Sci. Technol.* 2014 **23**: 015010

<sup>64</sup>E. ROBERT et al. *Phys. Plasmas* 2015 **22**: 122007

<sup>65</sup>R. WILD et al. *J. Phys. D: Appl. Phys.* 2014 **47**: 042001

<sup>66</sup>A. SOBOTA et al. *Plasma Sources Sci. Technol.* 2016 **25**: 065026

<sup>67</sup>A. SOBOTA et al. *Plasma Sources Sci. Technol.* 2014 **23**: 025016

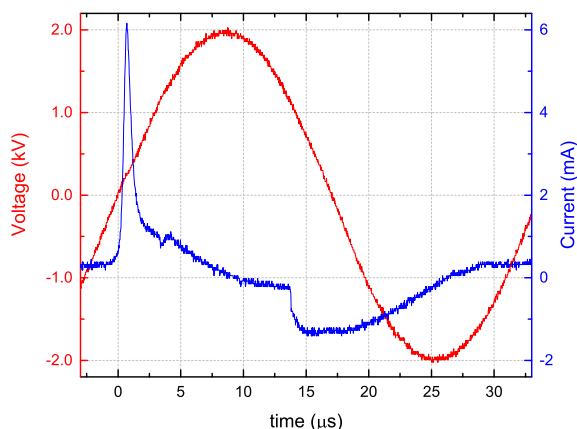


Figure 1.4: The current (blue) measured at the grounded ring electrode when applying the voltage (2 kV sine waves with 30 kHz frequency) to generate the plasma jet. A significant increase of current is observed, indicating the ignition around the electrodes, followed by a small *dip* (at 3  $\mu\text{s}$ ) indicating the moment when the ionization waves propagates in the *plasma plume* area.

reactive oxygen and nitrogen species that are generated,<sup>68–70</sup> the charges and electric fields to which the target gets exposed to,<sup>71,72</sup> (UV)-radiation and heat delivered by the discharge.<sup>12</sup> Application of these discharges for the treatment of polymers has focused on e.g. etching rates<sup>20</sup> and the modification of the surface energy / wettability<sup>21</sup> caused by the same influences. As with all applications the plasma surface interaction is crucial for the understanding of the occurring plasma induced effect to the material.

The primary aspect of the plasma surface interactions is the propagation and generation dynamics of the plasma and alteration in vicinity of a dielectric target. This is important for all the aforementioned applications. The effects occurring in the materials are caused by the plasma, but naturally the material has influenced the plasma as well. For instance charge deposition on the surface will induced fields that change the propagation along the surface. Additionally, the potential lines are influenced by the presence of the dielectric material, although not as much as when metallic targets are used.

The examination of the target influence on filamentary discharges initiated with the investigation of streamers on dielectrics. Experimental observations and numerical work showed that streamers prefer to propagate along a dielectric sur-

<sup>68</sup>D. B. GRAVES *J. Phys. D. Appl. Phys.* 2012 **45**: 263001

<sup>69</sup>W. TIAN and M. J. KUSHNER *J. Phys. D. Appl. Phys.* 2014 **47**: 165201

<sup>70</sup>A. LINDSAY et al. *J. Phys. D. Appl. Phys.* 2015 **48**: 424007

<sup>71</sup>L. STOLLENWERK et al. *Phys. Rev. Lett.* 2007 **98**: 255001

<sup>72</sup>A. SOBOTA et al. *J. Phys. D. Appl. Phys.* 2013 **46**: 372001

face placed tangential to the propagation direction, rather than through the gas directly.<sup>73–75</sup>

The dynamics are different when a dielectric target is present perpendicular to the propagation of the discharge, since then axial motion is forced to turn radially. The advantage of modelling to monitor the electric field has been exploited to investigate the influence of the dielectric properties of the material for the propagation of both streamers and guided ionization waves.<sup>76–79</sup>

It is more difficult to know experimentally the electric field everywhere and investigate the plasma surface interaction in this way. Instead, changes induced by the presence of a dielectric target are more easily observed through Schlieren visualization of the altered gas mixing.<sup>80,81</sup> In addition, the orientation of the impact of the discharge relative to the dielectric material changes the observed dynamics through observations of the light emission at the surface.<sup>82</sup>

A series of capacitively coupled probes to segmented electrodes have allowed for the investigation of electric fields and surface charge for surface DBDs.<sup>23,24,83</sup> This approach cannot be used to examine the electric fields to which complex samples are exposed to when treated by a plasma jet. The electric field of a plasma jet can be measured in the gas phase, however the field created by surface charges deposited during the interaction is not the same as generated by the volume charges inside the ionization wave.

The only way (known today) to investigate to which fields targets are exposed to is by using electro-optic crystals, by exploiting the Pockels effect. Materials that have been used for this respond to electric fields generated only by surface charges and are consequently an ideal tool to monitor the spatial and time-resolved surface dynamics of the plasma impact. This has been applied for the investigation of streamers on targets,<sup>84,85</sup> but also for plasma jets<sup>65,72,86,87</sup> and DBDs<sup>71,88,89</sup> interacting with materials.

In this work Mueller polarimetry will be used for the first time to investigate

---

<sup>73</sup>N. ALLEN and P. MIKROPOULOS *IEEE Trans. Dielectr. Electr. Insul.* 1999 **6**: 357–362

<sup>74</sup>A SOBOTA et al. *J. Phys. D. Appl. Phys.* 2009 **42**: 015211

<sup>75</sup>A. DUBINOVA et al. *Plasma Sources Sci. Technol.* 2016 **25**: 055021

<sup>76</sup>Y. SAKIYAMA et al. *J. Phys. D. Appl. Phys.* 2008 **41**: 095204

<sup>77</sup>F. PECHEREAU et al. *Plasma Sources Sci. Technol.* 2012 **21**: 055011

<sup>78</sup>D. BREDEN and L. L. RAJA *Plasma Sources Sci. Technol.* 2014 **23**: 065020

<sup>79</sup>S. A. NORBERG et al. *J. Appl. Phys.* 2015 **118**: 013301

<sup>80</sup>J.-S. OH et al. *J. Phys. D. Appl. Phys.* 2011 **44**: 155206

<sup>81</sup>M. BOSELLI et al. *Plasma Chem. Plasma Process.* 2014 **34**: 853–869

<sup>82</sup>O GUAITELLA and A SOBOTA *J. Phys. D. Appl. Phys.* 2015 **48**: 255202

<sup>83</sup>S. B. LEONOV et al. *J. Phys. D. Appl. Phys.* 2014 **47**: 465201

<sup>84</sup>T. KAWASAKI et al. *Jpn. J. Appl. Phys.* 1991 **30**: 1262–1265

<sup>85</sup>Y. ZHU et al. *J. Phys. D. Appl. Phys.* 1995 **28**: 1468–1477

<sup>86</sup>E. SLIKBOER et al. *Plasma Sources Sci. Technol.* 2016 **25**: 03LT04

<sup>87</sup>E. SLIKBOER et al. *Plasma Sources Sci. Technol.* 2017 **26**: 035002

<sup>88</sup>M BOGACZYK et al. *J. Phys. D. Appl. Phys.* 2012 **45**: 465202

<sup>89</sup>R. TSCHERSCH et al. *J. Phys. D. Appl. Phys.* 2014 **47**: 365204

electro-optic targets under plasma exposure, not only for the “conventional” electric field examination, but to also broaden this and show how the technique opens a whole new area of possibilities to examine the interaction occurring between non-thermal atmospheric pressure plasmas and dielectric targets.

## 1.4 Outline of this PhD Thesis

The thesis manuscript is divided as follows:

- This **first chapter** has given the introduction to the topics of this thesis, namely plasma surface interactions and the diagnostic technique of Mueller polarimetry. The approach to study the interactions is introduced, together with the type of plasma that is used throughout this work, i.e. guided ionization waves generated by a non-thermal atmospheric pressure plasma jet.
- The experimental setup, called the Mueller polarimeter, is shown and explained in detail in **Chapter 2**. In addition, the measurement procedure and calibration is elaborated on and the necessary analyses (decomposition) of the obtained Mueller matrix is introduced to retrieve the optical properties in terms of diattenuation, birefringence and depolarization. The Mueller polarimeter that is used throughout this work is specifically built for the acquisition of *time-resolved* Mueller matrices to do *in-situ* investigations of plasma surface interactions.
- **Chapter 3** introduces the electro-optic  $\text{Bi}_{12}\text{SiO}_{20}$  materials (BSO) that are used as a diagnostic tool for the examination of externally induced electric fields in targets. The relation between the measured birefringence and the electric field that has caused it is derived, after which stationary fields are generated to verify the obtained relation and to show how the decomposition is used.
- Plasma-induced anisotropies in the electro-optic targets are examined in **Chapter 4**, for various cases to examine both the axial and radial electric field components inside the targets under plasma exposure. This is done by examining BSO and  $\text{Fe}:\text{LiNbO}_3$  (Felinbo) at normal incidence with the polarimeter, while the plasma jet impacts at a 45 degree angle. The influence of a controlled environment is examined for the AC driven plasma jet and the applied voltage amplitude is varied for the pulsed plasma jet.
- The electric field induced by the pulsed plasma jet is further examined in **Chapter 5** where the ionization waves are impacting the target perpendicularly, rather than at an inclined angle. This changes the measurement procedure and allows to detect simultaneously all the individual electric field components inside a target. Again the influence of voltage amplitude is examined but the surface dynamics are different due to the perpendicular orientation of the jet. This also provides symmetry, which enables a phenomenological comparison with a numerical 2D-fluid model.
- In **Chapter 6** the dependence is investigated of the measured birefringence (of the electro-optic target) on the internal temperature gradients caused by

the plasma interaction. An analytically derived relation is used to construct a fitting procedure to retrieve the inhomogeneous temperature distribution from a birefringent pattern. After calibration, the fitting procedure allows a unique simultaneous investigation of the electric field pattern and the temperature pattern that are induced by the plasma jet in the targeted sample. This is applied in **Chapter 7** where the effect of operating frequency of the plasma jet is examined. Additionally, the temperature in the plasma plume is measured to identify the origin of the heating. Lastly, the fitting procedure is applied to the background images obtained during the electric field measurements of chapter 4.

- **Chapter 8** focuses on the examination of depolarization to do a more complete investigation with Mueller polarimetry of plasma surface interactions occurring when treating a sample for a certain application. A thin organic layer is investigated under plasma exposure in combination with the electro-optic crystals. This enables a unique investigation where surface modifications are captured, through depolarization, simultaneously with the electric field which the sample experiences (through birefringence). This allows to relate *in-situ* any material changes to the plasma that has induced them.

## References

- [1] R. G. POULSEN. *J. Vac. Sci. Technol.* **14**: 266–274, 1977. DOI: [10.1116/1.569137](https://doi.org/10.1116/1.569137) (see p. 3)
- [2] J. W. COBURN and H. F. WINTERS. *J. Vac. Sci. Technol.* **16**: 391–403, 1979. DOI: [10.1116/1.569958](https://doi.org/10.1116/1.569958) (see p. 3)
- [3] H. B. PROFIJT, S. E. POTTS, M. C. M. VAN DE SANDEN, and W. M. M. KESSELS. *J. Vac. Sci. Technol. A Vacuum, Surfaces, Film.* **29**: 050801, 2011. DOI: [10.1116/1.3609974](https://doi.org/10.1116/1.3609974) (see p. 3)
- [4] M. A. LIEBERMAN and A. J. LICHTENBERG. *Principles of Plasma Discharges and Materials Processing*. Hoboken, NJ, USA: John Wiley & Sons, Inc., 2005. ISBN: 9780471724254 DOI: [10.1002/0471724254](https://doi.org/10.1002/0471724254) (see p. 3)
- [5] E. LISTON, L. MARTINU, and M. WERTHEIMER. *J. Adhes. Sci. Technol.* **7**: 1091–1127, 1993. DOI: [10.1163/156856193X00600](https://doi.org/10.1163/156856193X00600) arXiv: [arXiv:1011.1669v3](https://arxiv.org/abs/1011.1669v3) (see pp. 3, 17)
- [6] D. L. FLAMM and O. AUCIELLO. *Plasma deposition, treatment, and etching of polymers: the treatment and etching of polymers*. 1st Elsevier, 1990. ISBN: 978-0-12-200430-8 (see pp. 3, 17)
- [7] F. FANELLI and F. FRACASSI. *Surf. Coatings Technol.* **322**: 174–201, 2017. DOI: [10.1016/j.surfcoat.2017.05.027](https://doi.org/10.1016/j.surfcoat.2017.05.027) (see pp. 3, 17)
- [8] M. LAROUSI and F. LEIPOLD. *Int. J. Mass Spectrom.* **233**: 81–86, 2004. DOI: [10.1016/j.ijms.2003.11.016](https://doi.org/10.1016/j.ijms.2003.11.016) (see p. 3)
- [9] E. C. NEYTS. *Plasma Chem. Plasma Process.* **36**: 185–212, 2016. DOI: [10.1007/s11090-015-9662-5](https://doi.org/10.1007/s11090-015-9662-5) (see pp. 3, 4, 17)
- [10] G. FRIDMAN, G. FRIEDMAN, A. GUTSOL, A. B. SHEKHTER, V. N. VASILETS, and A. FRIDMAN. *Plasma Process. Polym.* **5**: 503–533, 2008. DOI: [10.1002/ppap.200700154](https://doi.org/10.1002/ppap.200700154) (see pp. 3, 17, 20)
- [11] M. G. KONG, G KROESEN, G MORFILL, T NOSENKO, T SHIMIZU, J VAN DIJK, and J. L. ZIMMERMANN. *New J. Phys.* **11**: 115012, 2009. DOI: [10.1088/1367-2630/11/11/115012](https://doi.org/10.1088/1367-2630/11/11/115012) (see pp. 3, 17, 20)
- [12] K.-D. WELTMANN, E KINDEL, R BRANDENBURG, C MEYER, R BUSSIAHN, C WILKE, and T VON WOEDTKE. *Contrib. to Plasma Phys.* **49**: 631–640, 2009. DOI: [10.1002/ctpp.200910067](https://doi.org/10.1002/ctpp.200910067) (see pp. 3, 17, 20, 21, 161, 179)
- [13] E STOFFELS, A. J. FLIKWEERT, W. W. STOFFELS, and G. M. W. KROESEN. *Plasma Sources Sci. Technol.* **11**: 383–388, 2002. DOI: [10.1088/0963-0252/11/4/304](https://doi.org/10.1088/0963-0252/11/4/304) (see p. 3)
- [14] Y. S. SEO, A.-A. H. MOHAMED, K. C. WOO, H. W. LEE, J. K. LEE, and K. T. KIM. *IEEE Trans. Plasma Sci.* **38**: 2954–2962, 2010. DOI: [10.1109/TPS.2010.2058870](https://doi.org/10.1109/TPS.2010.2058870) (see p. 3)

- [15] J. EHLBECK, U. SCHNABEL, M. POLAK, J. WINTER, T. VON WOEDTKE, R. BRANDENBURG, T VON DEM HAGEN, and K.-D. WELTMANN. *J. Phys. D. Appl. Phys.* **44**: 013002, 2011. DOI: [10.1088/0022-3727/44/1/013002](https://doi.org/10.1088/0022-3727/44/1/013002) (see p. 3)
- [16] O. GUAITELLA, F. THEVENET, C. GUILLARD, and A. ROUSSEAU. *J. Phys. D. Appl. Phys.* **39**: 2964–2972, 2006. DOI: [10.1088/0022-3727/39/14/015](https://doi.org/10.1088/0022-3727/39/14/015) (see p. 4)
- [17] G. B. SRETENOVIĆ, I. B. KRSTIĆ, V. V. KOVAČEVIĆ, B. M. OBRADOVIĆ, and M. M. KURAICA. *Appl. Phys. Lett.* **99**: 161502, 2011. DOI: [10.1063/1.3653474](https://doi.org/10.1063/1.3653474) (see pp. 4, 20)
- [18] T DARNY, J.-M. POUVESLE, V PUECH, C DOUAT, S DOZIAS, and E. ROBERT. *Plasma Sources Sci. Technol.* **26**: 045008, 2017. DOI: [10.1088/1361-6595/aa5b15](https://doi.org/10.1088/1361-6595/aa5b15) (see pp. 4, 146, 181)
- [19] S. YONEMORI, Y. NAKAGAWA, R. ONO, and T. ODA. *J. Phys. D. Appl. Phys.* **45**: 225202, 2012. DOI: [10.1088/0022-3727/45/22/225202](https://doi.org/10.1088/0022-3727/45/22/225202) (see pp. 4, 20)
- [20] K. FRICKE, H. STEFFEN, T. VON WOEDTKE, K. SCHRÖDER, and K.-D. WELTMANN. *Plasma Process. Polym.* **8**: 51–58, 2011. DOI: [10.1002/ppap.201000093](https://doi.org/10.1002/ppap.201000093) (see pp. 5, 21)
- [21] R. FOEST, E. KINDEL, A. OHL, M. STIEBER, and K.-D. WELTMANN. *Plasma Phys. Control. Fusion* **47**: B525–B536, 2005. DOI: [10.1088/0741-3335/47/12B/S38](https://doi.org/10.1088/0741-3335/47/12B/S38) (see pp. 5, 21)
- [22] E STOFFELS, I. E. KIEFT, R. E. J. SLADEK, L. J. M. VAN DEN BEDEM, E. P. VAN DER LAAN, and M STEINBUCH. *Plasma Sources Sci. Technol.* **15**: S169–S180, 2006. DOI: [10.1088/0963-0252/15/4/S03](https://doi.org/10.1088/0963-0252/15/4/S03) (see p. 5)
- [23] C. L. ENLOE, G. I. FONT, T. E. MCLAUGHLIN, and D. M. ORLOV. *AIAA J.* **46**: 2730–2740, 2008. DOI: [10.2514/1.33973](https://doi.org/10.2514/1.33973) (see pp. 5, 22)
- [24] V. R. SOLOVIEV, I. V. SELIVONIN, and I. A. MORALEV. *Phys. Plasmas* **24**: 103528, 2017. DOI: [10.1063/1.5001136](https://doi.org/10.1063/1.5001136) (see pp. 5, 22)
- [25] J. GIL and R. OSSIKOVSKI. *Polarized Light and the Mueller Matrix Approach*. 1st CRC Press, 2016. ISBN: 9781482251555 (see p. 5)
- [26] M.-J. J. WU. In: *Optical Properties of Materials*. 45–69. Boston, MA: Springer US, 1995. DOI: [10.1007/978-1-4615-2273-7\\_2](https://doi.org/10.1007/978-1-4615-2273-7_2) (see p. 6)
- [27] E NEUMANN, M SCHAEFER-RIDDER, Y WANG, and P. H. HOFSCHEIDER. *EMBO J.* **1**: 841–5, 1982. DOI: [10.1002/j.1460-2075.1982.tb01257.x](https://doi.org/10.1002/j.1460-2075.1982.tb01257.x) (see p. 6)
- [28] J. C. WEAVER. *J. Cell. Biochem.* **51**: 426–435, 1993. DOI: [10.1002/jcb.2400510407](https://doi.org/10.1002/jcb.2400510407) (see p. 6)

- [29] R. PETHIG, Y. HUANG, X.-B. WANG, and J. P. H. BURT. *J. Phys. D. Appl. Phys.* **25**: 881–888, 1992. DOI: [10.1088/0022-3727/25/5/022](https://doi.org/10.1088/0022-3727/25/5/022) (see p. 6)
- [30] P. R. C. GASCOYNE and J. VYKOUKAL. *Electrophoresis* **23**: 1973–83, 2002. DOI: [10.1002/1522-2683\(200207\)23:13<1973::AID-ELPS1973>3.0.CO;2-1](https://doi.org/10.1002/1522-2683(200207)23:13<1973::AID-ELPS1973>3.0.CO;2-1) (see p. 6)
- [31] J. KERR. *London, Edinburgh, Dublin Philos. Mag. J. Sci.* **50**: 337–348, 1875. DOI: [10.1080/14786447508641302](https://doi.org/10.1080/14786447508641302) (see p. 6)
- [32] F. POCKELS. *Ueber den Einfluss des elektrostatischen Feldes auf das optische Verhalten Piezoelektrischer Krystalle*. vol. 39 *Abhandlungen der Königlichen Gesellschaft der Wissenschaften in Göttingen*, 1894. (see p. 6)
- [33] R. C. JONES. *J. Opt. Soc. Am.* **31**: 488, 1941. DOI: [10.1364/JOSA.31.000488](https://doi.org/10.1364/JOSA.31.000488) (see p. 10)
- [34] G. G. STOKES. *Trans. Cambridge Philos. Soc.* **9**: 399, 1851. (see p. 11)
- [35] E. HECHT. *Optics 4th (International) edition*. Addison Wesley Publishing Company Boston, MA, USA, 2002. ISBN: 9780805385663 (see p. 11)
- [36] E. GARCIA-CAUREL, R. OSSIKOVSKI, M. FOLDYNA, A. PIERANGELO, B. DRÉVILLON, and A. DE MARTINO. In: *Advanced Mueller Ellipsometry Instrumentation and Data Analysis*. M. LOSURDO and K. HINGERL, eds. 31–143. Berlin, Heidelberg: Springer Berlin Heidelberg, 2013. DOI: [10.1007/978-3-642-33956-1\\_2](https://doi.org/10.1007/978-3-642-33956-1_2) (see pp. 11, 14, 15, 34, 42–44)
- [37] O. ARTEAGA and A. CANILLAS. *J. Opt. Soc. Am. A* **26**: 783, 2009. DOI: [10.1364/JOSAA.26.000783](https://doi.org/10.1364/JOSAA.26.000783) (see p. 11)
- [38] Y. MATSUOKA and B. NORDEN. *J. Phys. Chem.* **86**: 1378–1386, 1982. DOI: [10.1021/j100397a033](https://doi.org/10.1021/j100397a033) (see p. 12)
- [39] T. B. FREEDMAN, X. CAO, R. K. DUKOR, and L. A. NAFIE. *Chirality* **15**: 743–758, 2003. DOI: [10.1002/chir.10287](https://doi.org/10.1002/chir.10287) (see p. 12)
- [40] C. MALGRANGE, C. RICOLLEAU, and M. SCHLENKER. *Symmetry and Physical Properties of Crystals*. Dordrecht: Springer Netherlands, 2014. ISBN: 978-94-017-8992-9 DOI: [10.1007/978-94-017-8993-6](https://doi.org/10.1007/978-94-017-8993-6) (see pp. 12, 55, 57, 88, 162, 163)
- [41] H. G. TOMPKINS and E. A. IRENE. *Handbook of Ellipsometry*. Springer Berlin Heidelberg, 2005. ISBN: 978-3-540-22293-4 DOI: [10.1007/3-540-27488-X](https://doi.org/10.1007/3-540-27488-X) (see p. 14)
- [42] H. FUJIWARA. *Spectroscopic Ellipsometry*. Chichester, UK: John Wiley & Sons, Ltd, 2007. ISBN: 9780470060193 DOI: [10.1002/9780470060193](https://doi.org/10.1002/9780470060193) (see p. 14)

- [43] M. LOSURDO and K. HINGERL. *Ellipsometry at the Nanoscale*. Berlin, Heidelberg: Springer Berlin Heidelberg, 2013. ISBN: 978-3-642-33955-4 DOI: [10.1007/978-3-642-33955-4](https://doi.org/10.1007/978-3-642-33955-4) (see p. 14)
- [44] I. HODGKINSON, S. LOWREY, L. BOURKE, A. PARKER, and M. W. MCCALL. *Appl. Opt.* **49**: 4558, 2010. DOI: [10.1364/AO.49.004558](https://doi.org/10.1364/AO.49.004558) (see p. 15)
- [45] H. ARWIN, T. BERLIND, B. JOHS, and K. JÄRREND AHL. *Opt. Express* **21**: 22645, 2013. DOI: [10.1364/OE.21.022645](https://doi.org/10.1364/OE.21.022645) (see p. 15)
- [46] M. H. SMITH, P. D. BURKE, A. LOMPADO, E. A. TANNER, and L. W. HILLMAN. “Mueller matrix imaging polarimetry in dermatology” in: *Proc. SPIE*. ed. by T. VO-DINH, W. S. GRUNDFEST, and D. A. BENARON vol. 3911 May 2000. 210–216 DOI: [10.1117/12.384904](https://doi.org/10.1117/12.384904) (see p. 15)
- [47] A. PIERANGELO, A. BENALI, M.-R. ANTONELLI, T. NOVIKOVA, P. VALIDIRE, B. GAYET, and A. DE MARTINO. *Opt. Express* **19**: 1582, 2011. DOI: [10.1364/OE.19.001582](https://doi.org/10.1364/OE.19.001582) (see p. 15)
- [48] Y. P. RAIZER. *Gas Discharge Physics*. Springer, 1991. ISBN: 978-3-642-64760-4 (see p. 16)
- [49] J. M. MEEK. *Phys. Rev.* **57**: 722–728, 1940. DOI: [10.1103/PhysRev.57.722](https://doi.org/10.1103/PhysRev.57.722) (see p. 16)
- [50] A. LUQUE, V. RATUSHNAYA, and U. EBERT. *J. Phys. D. Appl. Phys.* **41**: 234005, 2008. DOI: [10.1088/0022-3727/41/23/234005](https://doi.org/10.1088/0022-3727/41/23/234005) (see p. 16)
- [51] M. ARRAYÁS, U. EBERT, and W. HUNSDORFER. *Phys. Rev. Lett.* **88**: 174502, 2002. DOI: [10.1103/PhysRevLett.88.174502](https://doi.org/10.1103/PhysRevLett.88.174502) (see p. 16)
- [52] E. M. VAN VELDHUIZEN and W. R. RUTGERS. *J. Phys. D. Appl. Phys.* **35**: 313, 2002. DOI: [10.1088/0022-3727/35/17/313](https://doi.org/10.1088/0022-3727/35/17/313) (see p. 16)
- [53] H.-E. WAGNER, R. BRANDENBURG, K. KOZLOV, A. SONNENFELD, P. MICHEL, and J. BEHNKE. *Vacuum* **71**: 417–436, 2003. DOI: [10.1016/S0042-207X\(02\)00765-0](https://doi.org/10.1016/S0042-207X(02)00765-0) (see p. 17)
- [54] R. BRANDENBURG. *Plasma Sources Sci. Technol.* **26**: 053001, 2017. DOI: [10.1088/1361-6595/aa6426](https://doi.org/10.1088/1361-6595/aa6426) (see p. 17)
- [55] A SCHUTZE, J. JEONG, S. BABAYAN, JAEYOUNG PARK, G. SELWYN, and R. HICKS. *IEEE Trans. Plasma Sci.* **26**: 1685–1694, 1998. DOI: [10.1109/27.747887](https://doi.org/10.1109/27.747887) (see p. 17)
- [56] X LU, M LAROSSI, and V PUECH. *Plasma Sources Sci. Technol.* **21**: 034005, 2012. DOI: [10.1088/0963-0252/21/3/034005](https://doi.org/10.1088/0963-0252/21/3/034005) (see pp. 17, 19, 20, 113)
- [57] D. M. ORLOV, G. I. FONT, and D. EDELSTEIN. *AIAA J.* **46**: 3142–3148, 2008. DOI: [10.2514/1.37514](https://doi.org/10.2514/1.37514) (see pp. 17, 98, 135)
- [58] T. UNFER and J. P. BOEUF. *J. Phys. D. Appl. Phys.* **42**: 194017, 2009. DOI: [10.1088/0022-3727/42/19/194017](https://doi.org/10.1088/0022-3727/42/19/194017) (see pp. 17, 98)

- [59] A. LINDSAY, B. BYRNS, W. KING, A. ANDHVARAPOU, J. FIELDS, D. KNAPPE, W. FONTENO, and S. SHANNON. *Plasma Chem. Plasma Process.* **34**: 1271–1290, 2014. DOI: [10.1007/s11090-014-9573-x](https://doi.org/10.1007/s11090-014-9573-x) (see p. 17)
- [60] M. TESCHKE, J. KEDZIERSKI, E. FINANTU-DINU, D. KORZEC, and J. ENGMANN. *IEEE Trans. Plasma Sci.* **33**: 310–311, 2005. DOI: [10.1109/TPS.2005.845377](https://doi.org/10.1109/TPS.2005.845377) (see pp. 20, 125)
- [61] X. LU, G. NAIDIS, M. LAROUSSE, and K. OSTRIKOV. *Phys. Rep.* **540**: 123–166, 2014. DOI: [10.1016/j.physrep.2014.02.006](https://doi.org/10.1016/j.physrep.2014.02.006) (see pp. 20, 113)
- [62] N. KNAKE, K. NIEMI, S. REUTER, V. SCHULZ-VON DER GATHEN, and J. WINTER. *Appl. Phys. Lett.* **93**: 131503, 2008. DOI: [10.1063/1.2995983](https://doi.org/10.1063/1.2995983) (see p. 20)
- [63] P OLSZEWSKI, E WAGENAARS, K MCKAY, J. W. BRADLEY, and J. L. WALSH. *Plasma Sources Sci. Technol.* **23**: 015010, 2014. DOI: [10.1088/0963-0252/23/1/015010](https://doi.org/10.1088/0963-0252/23/1/015010) (see p. 20)
- [64] E ROBERT, T DARNY, S DOZIAS, S ISENI, and J. M. POUVESLE. *Phys. Plasmas* **22**: 122007, 2015. DOI: [10.1063/1.4934655](https://doi.org/10.1063/1.4934655) (see p. 20)
- [65] R WILD, T GERLING, R BUSSIAHN, K.-D. WELTMANN, and L STOLLENWERK. *J. Phys. D. Appl. Phys.* **47**: 042001, 2014. DOI: [10.1088/0022-3727/47/4/042001](https://doi.org/10.1088/0022-3727/47/4/042001) (see pp. 20, 22, 53, 80, 96)
- [66] A. SOBOTA, O GUAITELLA, G. B. SRETENOVIĆ, I. B. KRSTIĆ, V. V. KOVAČEVIĆ, A OBRUSNÍK, Y. N. NGUYEN, L ZAJÍČKOVÁ, B. M. OBRADOVIĆ, and M. M. KURAICA. *Plasma Sources Sci. Technol.* **25**: 065026, 2016. DOI: [10.1088/0963-0252/25/6/065026](https://doi.org/10.1088/0963-0252/25/6/065026) (see pp. 20, 102, 146, 179, 183)
- [67] A SOBOTA, O GUAITELLA, and A ROUSSEAU. *Plasma Sources Sci. Technol.* **23**: 025016, 2014. DOI: [10.1088/0963-0252/23/2/025016](https://doi.org/10.1088/0963-0252/23/2/025016) (see pp. 20, 182)
- [68] D. B. GRAVES. *J. Phys. D. Appl. Phys.* **45**: 263001, 2012. DOI: [10.1088/0022-3727/45/26/263001](https://doi.org/10.1088/0022-3727/45/26/263001) (see pp. 21, 178)
- [69] W. TIAN and M. J. KUSHNER. *J. Phys. D. Appl. Phys.* **47**: 165201, 2014. DOI: [10.1088/0022-3727/47/16/165201](https://doi.org/10.1088/0022-3727/47/16/165201) (see p. 21)
- [70] A. LINDSAY, C. ANDERSON, E. SLIKBOER, S. SHANNON, and D. GRAVES. *J. Phys. D. Appl. Phys.* **48**: 424007, 2015. DOI: [10.1088/0022-3727/48/42/424007](https://doi.org/10.1088/0022-3727/48/42/424007) (see pp. 21, 178, 204)
- [71] L. STOLLENWERK, J. G. LAVEN, and H.-G. PURWINS. *Phys. Rev. Lett.* **98**: 255001, 2007. DOI: [10.1103/PhysRevLett.98.255001](https://doi.org/10.1103/PhysRevLett.98.255001) (see pp. 21, 22, 53, 80, 96)

- [72] A SOBOTA, O GUAITELLA, and E GARCIA-CAUREL. *J. Phys. D. Appl. Phys.* **46**: 372001, 2013. DOI: [10.1088/0022-3727/46/37/372001](https://doi.org/10.1088/0022-3727/46/37/372001) (see pp. 21, 22, 80, 96)
- [73] N. ALLEN and P. MIKROPOULOS. *IEEE Trans. Dielectr. Electr. Insul.* **6**: 357–362, 1999. DOI: [10.1109/94.775623](https://doi.org/10.1109/94.775623) (see p. 22)
- [74] A SOBOTA, A LEBOUVIER, N. J. KRAMER, E. M. VAN VELDHUIZEN, W. W. STOFFELS, F MANDERS, and M HAVERLAG. *J. Phys. D. Appl. Phys.* **42**: 015211, 2009. DOI: [10.1088/0022-3727/42/1/015211](https://doi.org/10.1088/0022-3727/42/1/015211) (see pp. 22, 181)
- [75] A. DUBINOVA, D. TRIENEKENS, U. EBERT, S. NIJDAM, and T. CHRISTEN. *Plasma Sources Sci. Technol.* **25**: 055021, 2016. DOI: [10.1088/0963-0252/25/5/055021](https://doi.org/10.1088/0963-0252/25/5/055021) (see p. 22)
- [76] Y. SAKIYAMA, D. B. GRAVES, and E. STOFFELS. *J. Phys. D. Appl. Phys.* **41**: 095204, 2008. DOI: [10.1088/0022-3727/41/9/095204](https://doi.org/10.1088/0022-3727/41/9/095204) (see pp. 22, 143)
- [77] F. PECHEREAU, J. JÁNSKÝ, and A. BOURDON. *Plasma Sources Sci. Technol.* **21**: 055011, 2012. DOI: [10.1088/0963-0252/21/5/055011](https://doi.org/10.1088/0963-0252/21/5/055011) (see pp. 22, 143)
- [78] D. BREDEN and L. L. RAJA. *Plasma Sources Sci. Technol.* **23**: 065020, 2014. DOI: [10.1088/0963-0252/23/6/065020](https://doi.org/10.1088/0963-0252/23/6/065020) (see pp. 22, 143)
- [79] S. A. NORBERG, E. JOHNSEN, and M. J. KUSHNER. *J. Appl. Phys.* **118**: 013301, 2015. DOI: [10.1063/1.4923345](https://doi.org/10.1063/1.4923345) (see pp. 22, 89, 143)
- [80] J.-S. OH, O. T. OLABANJI, C. HALE, R. MARIANI, K. KONTIS, and J. W. BRADLEY. *J. Phys. D. Appl. Phys.* **44**: 155206, 2011. DOI: [10.1088/0022-3727/44/15/155206](https://doi.org/10.1088/0022-3727/44/15/155206) (see p. 22)
- [81] M. BOSELLI, V. COLOMBO, E. GHEDINI, M. GHERARDI, R. LAURITA, A. LIGUORI, P. SANIBONDI, and A. STANCAMPIANO. *Plasma Chem. Plasma Process.* **34**: 853–869, 2014. DOI: [10.1007/s11090-014-9537-1](https://doi.org/10.1007/s11090-014-9537-1) (see p. 22)
- [82] O GUAITELLA and A SOBOTA. *J. Phys. D. Appl. Phys.* **48**: 255202, 2015. DOI: [10.1088/0022-3727/48/25/255202](https://doi.org/10.1088/0022-3727/48/25/255202) (see pp. 22, 83, 95)
- [83] S. B. LEONOV, V. PETRISHCHEV, and I. V. ADAMOVICH. *J. Phys. D. Appl. Phys.* **47**: 465201, 2014. DOI: [10.1088/0022-3727/47/46/465201](https://doi.org/10.1088/0022-3727/47/46/465201) (see p. 22)
- [84] T. KAWASAKI, Y. ARAI, and T. TAKADA. *Jpn. J. Appl. Phys.* **30**: 1262–1265, 1991. DOI: [10.1143/JJAP.30.1262](https://doi.org/10.1143/JJAP.30.1262) (see pp. 22, 53, 80, 96)
- [85] Y. ZHU, T. TAKADA, and D. TU. *J. Phys. D. Appl. Phys.* **28**: 1468–1477, 1995. DOI: [10.1088/0022-3727/28/7/028](https://doi.org/10.1088/0022-3727/28/7/028) (see pp. 22, 53)
- [86] E. SLIKBOER, O. GUAITELLA, and A. SOBOTA. *Plasma Sources Sci. Technol.* **25**: 03LT04, 2016. DOI: [10.1088/0963-0252/25/3/03LT04](https://doi.org/10.1088/0963-0252/25/3/03LT04) (see pp. 22, 53, 79, 80, 83, 95, 96, 160, 181)

- [87] E. SLIKBOER, E. GARCIA-CAUREL, O. GUAITELLA, and A. SOBOTA. *Plasma Sources Sci. Technol.* **26**: 035002, 2017. DOI: [10.1088/1361-6595/aa53fe](https://doi.org/10.1088/1361-6595/aa53fe) (see pp. 22, 53, 80, 83, 96, 101, 102, 160)
- [88] M BOGACZYK, R WILD, L STOLLENWERK, and H.-E. WAGNER. *J. Phys. D. Appl. Phys.* **45**: 465202, 2012. DOI: [10.1088/0022-3727/45/46/465202](https://doi.org/10.1088/0022-3727/45/46/465202) (see pp. 22, 53, 80, 96)
- [89] R. TSCHIRSCH, M. BOGACZYK, and H.-E. WAGNER. *J. Phys. D. Appl. Phys.* **47**: 365204, 2014. DOI: [10.1088/0022-3727/47/36/365204](https://doi.org/10.1088/0022-3727/47/36/365204) (see pp. 22, 53, 80, 96)

# Chapter 2

## Experimental Setup and Measurement Procedure

### Contents

---

<b>2.1 The Mueller Polarimeter</b> . . . . .	<b>34</b>
2.1.1 Setup Design . . . . .	34
2.1.2 Choice of the Orientations of the Liquid Crystals . . . . .	37
<b>2.2 Measurement Procedure and Calibration</b> . . . . .	<b>41</b>
2.2.1 Calibration Procedure . . . . .	41
<b>2.3 Analyses of the Mueller Matrix</b> . . . . .	<b>43</b>
2.3.1 Optically Active Targets . . . . .	44
2.3.2 Logarithmic (Differential) Decomposition . . . . .	45
2.3.3 Homogeneous Elliptical Retarder Model . . . . .	47
<b>References</b> . . . . .	<b>49</b>

---

This chapter focuses on the experimental setup, called the *Mueller polarimeter*. The first part discusses the design of the polarimeter and how to build it. Then, the measurement procedure is described including the calibration that has to be done. Lastly, the analysis (decomposition) of the Mueller matrix, which is necessary in order to retrieve the optical properties, is discussed.

## 2.1 The Mueller Polarimeter

The goal to build a Mueller polarimeter is to examine optically active targets under plasma exposure to identify various effects occurring during a plasma surface interaction. For this purpose, the Mueller matrix of those samples should be identified and analyzed. The main objective is to build a setup which can be used *in-situ* to investigate plasma surface interactions. Therefore the Mueller matrices have to be obtained time-resolved to follow changes during the transient interaction. This means that the user of the polarimeter should be able to have control of the states of the polarizing optics and the acquisition with the detector. This is normally not the case since Mueller polarimetry is usually only applied to static samples.

### 2.1.1 Setup Design

Figure 2.1 shows the experimental setup designed for the study of plasma surface interactions and used throughout this work, called the Mueller polarimeter. The sample which is to be investigated is located in between the *Polarizer State Generator* (PSG) and *Polarizer State Analyzer* (PSA). Both PSG and PSA consist of a linear polarizer and two ferroelectric liquid crystals.<sup>90</sup> The ferroelectric liquid crystals make it possible to control the polarization state of the light beam which is going through the system. The setup consists of one part related to the control of the liquid crystals and a second part related to the configuration of the total optical system.

The PSG is used to create a (known) polarization state of the light which is sent to the sample. As it interacts with the sample the polarization state changes. The transformed state is examined by sending the polarized light through the PSA and collecting it with the iCCD camera. The obtained intensity  $I$  forms the first element of the  $4 \times 4$  intensity matrix  $B$ . This matrix is needed to retrieve the Mueller matrix  $M$  of the sample.<sup>36</sup> To obtain the other elements and thus the full  $4 \times 4$  intensity matrix, different polarization states are generated that propagate through the sample and are analyzed and collected afterwards. In total 16 intensity images  $I$  are obtained to build the intensity matrix  $B$ , according to equation (2.1). Specifically chosen polarization states are generated by using the ferroelectric liquid crystals. Their orientations can be switched between two states by applying an external voltage. This changes the total polarization state of the polarized light beam.<sup>91</sup> Two possible orientations can be chosen for each liquid crystal ( $\alpha_{pos}$  and  $\alpha_{neg}$ ). By sequentially switching in a fixed order the states of each liquid crystal between a negative and a positive state, different polarization states are generated and analyzed. This means that different intensity images  $I$  are obtained at the de-

<sup>90</sup>A. DE MARTINO et al. *Opt. Lett.* 2003 **28**: 616–618

<sup>36</sup>E. GARCIA-CAUREL et al. 2013 ISBN: 978-3-642-33956-1

<sup>91</sup>A. DE MARTINO et al. *Thin Solid Films* 2004 **455-456**: 112–119

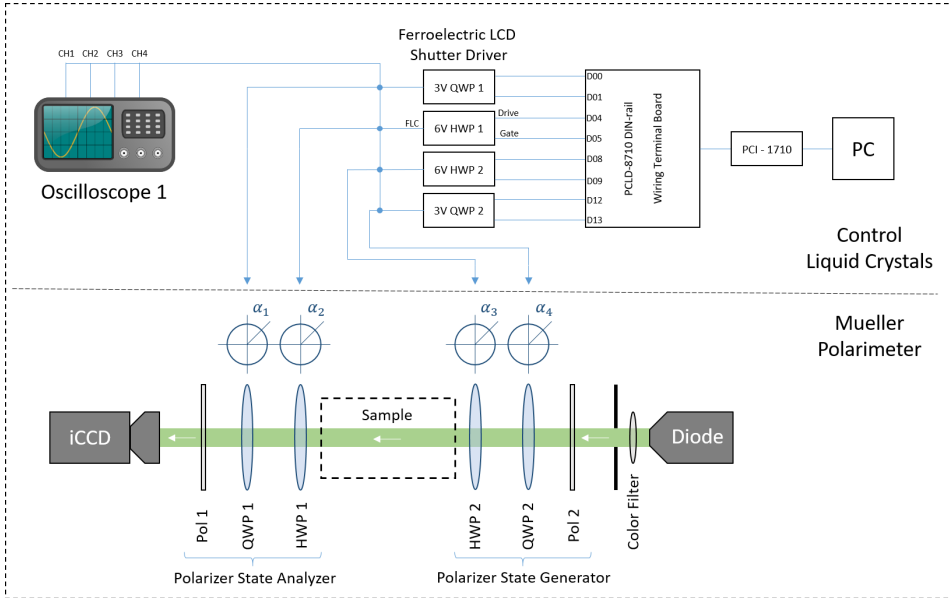


Figure 2.1: The Mueller Polarimeter: the experimental setup used throughout this work. The sample which is under investigation is placed in between the *Polarizer State Generator* (PSG) and *Polarizer State Analyzer* (PSA). By sequentially switching the liquid crystals (QWP1, HWP1, HWP2 and QWP2) between their two orientation states, 16 intensity images  $I$  are obtained with the iCCD camera that form the  $4 \times 4$  intensity matrix  $B$ . The control of the liquid crystals is done using four ferroelectric LCD shutter drivers.

tor. For each liquid crystal the difference in orientation between the two states is fixed by the crystal itself meaning that the initial orientation (negative state) has to be chosen carefully. The different intensity images are used to construct the intensity matrix  $B$ .

$$B = \begin{pmatrix} I(1) & I(2) & I(3) & I(4) \\ I(5) & I(6) & I(7) & I(8) \\ I(9) & I(10) & I(11) & I(12) \\ I(13) & I(14) & I(15) & I(16) \end{pmatrix} \quad (2.1)$$

The chosen order of sequentially switching the liquid crystals is shown in figure 2.2, with two representations. The order itself is chosen arbitrarily, but it is important that always the same order is used during calibration and measurement of a sample. At the first acquisition step all the liquid crystals are in the negative orientation state. Sequentially, they are switched to the positive state until step 16 when all of them are positive.

The liquid crystals indicated as *HWP* are driven with a  $\pm 5$  volt signal, while

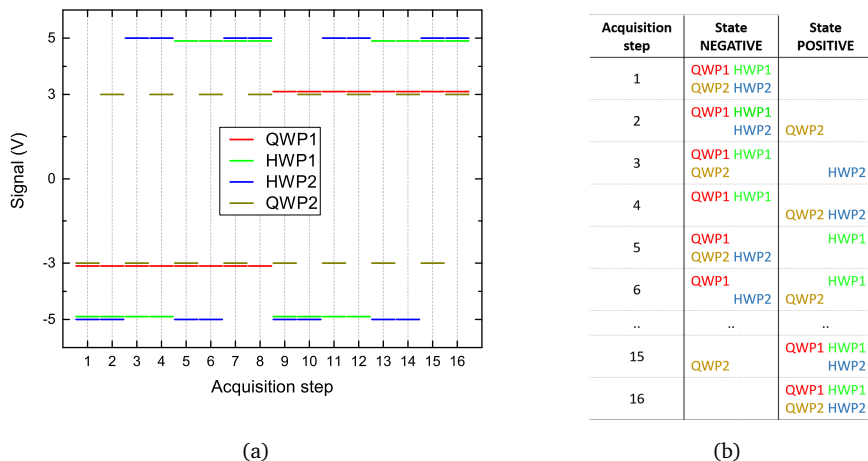


Figure 2.2: The sequence order of switching the liquid crystals from negative to positive state. In the first acquisition step all the liquid crystals are in the negative state, while at the last step (16) they are all positive. A different voltage is applied to the liquid crystals labeled as QWP than to the ones labeled HWP.

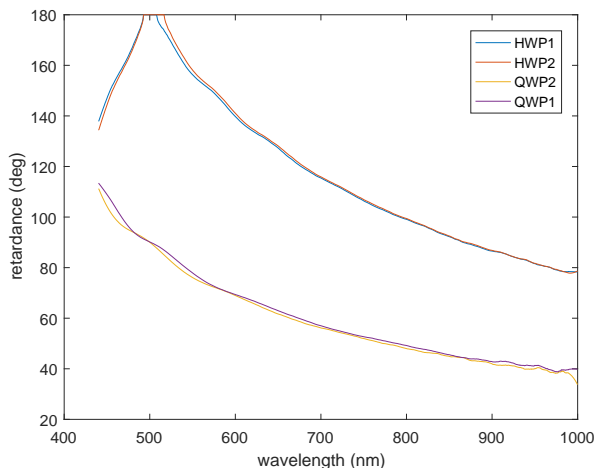


Figure 2.3: The retardance of the liquid crystals obtained spectroscopically using the commercially available *MM16 Spectroscopic Ellipsometer* from *Horiba Jobin Yvon*.

the two liquid crystals indicated with *QWP* operate at a  $\pm 3$  volt signal. The respective indications *HWP* and *QWP* are given because of their retardance at 500 nm matching a *half-wave* and *quarter-wave* plate, see figure 2.3. The spectroscopic retardance of the liquid crystals is obtained using the *MM16 Spectroscopic Ellipsometer* from *Horiba Jobin Yvon*. The orientation states of the liquid crystals are irrelevant for the maximum retardance they can induce. The actual retardance which is induced does depend on the orientation relative to the (vertical) orientation of the linear polarizers and the other optical elements.

The positive or negative voltage applied to each liquid crystal is generated by a *Ferroelectric LCD Shutter Driver*. These are operated using a drive and gate signal, which are controlled through a *Writing Terminal Board*. With *MATLAB* the acquisition of the 16 intensity images with the iCCD camera (*Princeton Pi-Max4 "PM4-1024f-RB-PS-18-P43-FM"*) is automated with the sequencing of the orientations of the liquid crystals. The polarimeter shown in figure 2.1 operates with a green color filter, transmitting light with wavelength  $530 \pm 10$  nm. A collimated LED light source is used emitting white light with a total beam power of 440 mW (Thorlabs item number MCWHL5-C1). Since the control of the liquid crystals is done through *MATLAB* it can easily be coupled to external (trigger) events to do time-resolved examinations of the optical properties of a sample.

### 2.1.2 Choice of the Orientations of the Liquid Crystals

Ferroelectric liquid crystals are used for the Mueller polarimeter because they allow controlling the polarization state of the light beam used to examine samples optically. The retardance of the liquid crystals is fixed, shown in figure 2.3, but the orientation can be varied, by applying a small DC voltage. The switching sequence changes the orientations of the liquid crystals from a  $\alpha_{i,neg}$  to a  $\alpha_{i,pos}$ , with  $i = 1, 2, 3$  or  $4$  for respectively *QWP1*, *HWP1*, *HWP2* and *QWP2*. The orientation depends on the polarity of the applied voltage to the liquid crystals. The change in orientation is named  $\Delta\alpha_i$ . The choice of the initial orientations  $\alpha_{i,neg}$  of the liquid crystals is the most important part of the design of the polarimeter since  $\Delta\alpha_i$  is determined by the liquid crystals itself.

The combination of the orientations of the liquid crystals determines which polarized states are generated by the PSG and analyzed with the PSA. The four Stokes vectors that represent the states that are generated by the PSG form a  $4 \times 4$  matrix, defined as  $W$ . This name is traditionally given. The vectors are used as columns of this matrix. Similarly, the four Stokes vectors that represent the states of the PSA form matrix  $A$  (more logically named after the *Analyzer*), using the transposed vectors as rows. These Mueller matrices  $A$  and  $W$  are essential to transform the intensity matrix  $B$  into the Mueller matrix of the sample  $M$ , following equation (2.3).

$$B = A \cdot M \cdot W \quad (2.2)$$

$$\Leftrightarrow M = A^{-1} \cdot B \cdot W^{-1} \quad (2.3)$$

The four states of both the PSG and PSA have to create a corresponding matrix  $W$  and  $A$  that are well-conditioned to be able to measure all the optical properties of a sample.<sup>92,93</sup> This is because the condition number of a matrix determines the propagation of error when it is used in calculation. To minimize this, the condition numbers of the matrices  $A$  and  $W$  have to be optimized. Through prediction of the condition number using calculation of the generated polarization states, the best initial orientations  $\alpha_{i,neg}$  of the liquid crystals can be found. However, this requires knowledge of the orientations of the liquid crystals within their mount  $\Lambda_i$ , i.e. the angle of the fast or slow axis when the rotation holder is placed at  $0^\circ$ .

$$\alpha_{i,pos} = \alpha_{i,neg} + \Delta\alpha_i + \Lambda_i \quad \text{with } i=1, 2, 3, 4 \quad (2.4)$$

The information of  $\Delta\alpha_i$  and  $\Lambda_i$  is retrieved by measuring the 16 elements of intensity matrix  $B$  for various angles of  $\alpha_{1,neg}$ , while the other liquid crystals mounts are at zero degree position, i.e.  $\alpha_{i,neg} = 0$  with  $i = 2, 3$  or  $4$ . No sample is placed in between the *PSG* and *PSA*. The intensity images of matrix  $B$  are normalized using the maximum intensity and averaged to obtain the mean normalized intensity value of each  $B$  element as a function of  $\alpha_{1,neg}$ , as shown in figure 2.4 in blue. Numerically  $\Delta\alpha_i$  and  $\Lambda_i$  are found for all elements by calculating the intensity reaching the detector, with the fitted result shown in the same figure in red. The obtained results for  $\Delta\alpha_i$  and  $\Lambda_i$  are shown in table 2.1.

Table 2.1: The numerically obtained fitted value for  $\Delta\alpha_i$  and  $\Lambda_i$  to match the measured mean normalized intensity value of each element of  $B$  as a function of the rotation  $\alpha_{1,neg}$ .

		$\Lambda_i$	$\Delta\alpha_i$
$i = 1$	QWP1	$32.6^\circ$	$-23.6^\circ$
$i = 2$	HWP1	$44.9^\circ$	$-35.8^\circ$
$i = 3$	HWP2	$54.0^\circ$	$-40.4^\circ$
$i = 4$	QWP2	$5.0^\circ$	$+40.6^\circ$

A basic iterative fitting procedure has been followed. Initially,  $\Delta\alpha_i$  and  $\Lambda_i$  are chosen randomly for all liquid crystals and the resulting intensity for each combination of the liquid crystal states (i.e. element of  $B$ ) is calculated for all  $\alpha_{1,neg}$  rotations and compared with the measurement. The average deviation of

<sup>92</sup>M. H. SMITH *Appl. Opt.* 2002 **41**: 2488–2493

<sup>93</sup>J. S. TYO *Appl. Opt.* 2002 **41**: 619–630

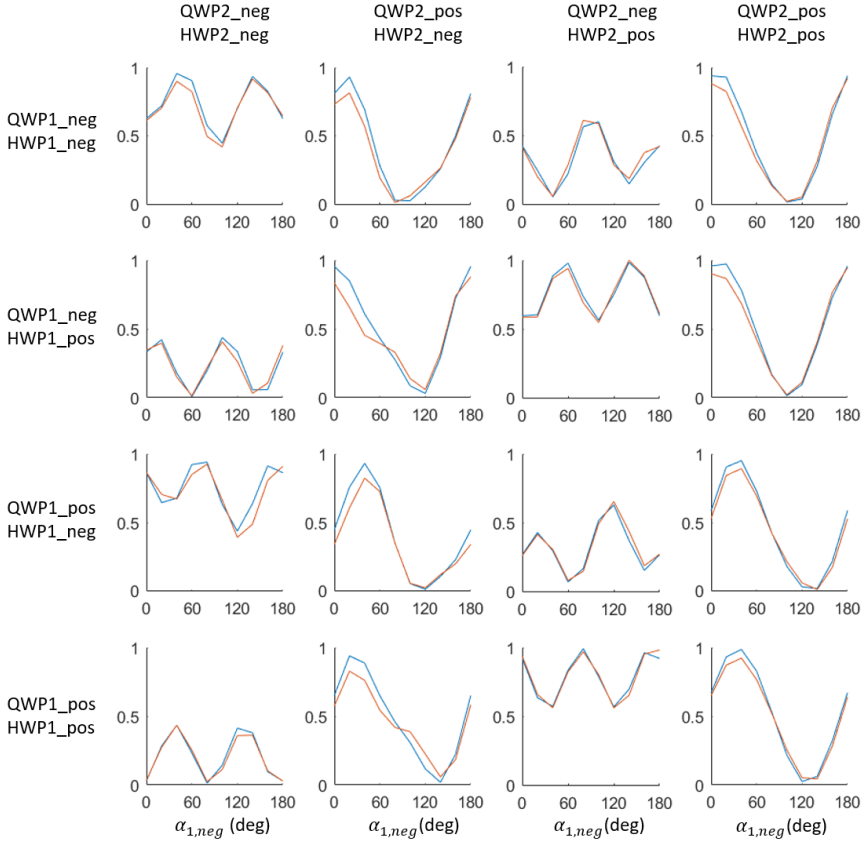


Figure 2.4: The mean normalized intensity value of each  $B$  element as a function of the rotation  $\alpha_{1, neg}$  with the others  $\alpha_{i, neg} = 0$ . Each resulting graph represents an element value of intensity matrix  $B$  as defined by equation (2.1) and the sequence shown in figure 2.2. The measured values are shown in blue, while the numerical fitted result is given in red. Table 2.1 gives the final fitted values of  $\Delta\alpha_i$  and  $\Lambda_i$  that are used to obtain the fitted results.

the numerical values from the measurements is used as optimization factor. New values of  $\Delta\alpha_i$  and  $\Lambda_i$  are searched to minimize this deviation. The obtained final results are shown in table 2.1 and account for an average 7% deviation between the numerical calculation and measurement, see figure 2.4.

With the knowledge of  $\Delta\alpha_i$  and  $\Lambda_i$  for all liquid crystals, the initial orientation of all liquid crystal mounts can be found which optimizes the resulting condition number of the PSA and PSG. Instead of optimizing the Mueller matrices  $A$  and  $W$  also the resulting intensity matrix  $B$  can be optimized (with no sample present) through its condition number since it is the product of the condition number of  $A$

and  $W$ .

This is done by applying a *singular value decomposition* on the intensity matrix of  $B$  and taking the square root of the ratio between the smallest and the largest (singular) value. The resulting value, i.e. the reciprocal condition number, has a maximum value of  $3^{-1/2} \approx 0.577$ .<sup>93</sup> Through modeling (trial and error) the best combinations of  $\alpha_{i,neg}$  can be found for which the condition number is closest to this value. This minimizes the propagation of error in matrix multiplications. For this calculation, the input is used from figure 2.3 to calculate the optimized angles at different color filter wavelengths.

The resulting optimized angles are found in table 2.2, for the different color filters cyan ( $490 \pm 5$  nm), green ( $530 \pm 10$  nm), orange ( $605 \pm 10$  nm) and red ( $650 \pm 10$  nm). The (reciprocal) condition numbers are closest to the maximum value for cyan and green. It is lower for orange and red because the retardance of the liquid crystals decreases for higher wavelengths, as measured and shown in figure 2.3. The possibility to be able to measure at a different wavelength is interesting since it could offer some (limited) spectroscopic information in the visible spectrum.

Table 2.2: The numerically found optimized angles of  $\alpha_{i,neg}$  for all four liquid crystals for different color filter wavelength and the resulting (reciprocal) condition number. Two combinations of orientations are shown per color filter that result in the highest condition number.

Wavelength (nm)	Condition number	$\alpha_{1,neg}$ (deg)	$\alpha_{2,neg}$ (deg)	$\alpha_{3,neg}$ (deg)	$\alpha_{4,neg}$ (deg)
$490 \pm 5$ (cyan)	0.513	159	8	67	108
$490 \pm 5$ (cyan)	0.511	77	141	157	4
$530 \pm 10$ (green)	0.494	76	145	159	10
$530 \pm 10$ (green)	0.493	76	141	154	14
$605 \pm 10$ (orange)	0.405	71	14	20	10
$605 \pm 10$ (orange)	0.402	72	121	92	10
$650 \pm 10$ (red)	0.382	73	128	140	30
$650 \pm 10$ (red)	0.377	163	38	51	122

Most of the work in this thesis is done using the green color filter transmitting light at  $530 \pm 10$  nm. This is chosen because the reciprocal condition number is higher than the orange and red filter and there is more light reaching the detector than with the cyan filter. When it is desired that the samples are investigated at a different wavelength, simply the color filter has to be changed and the initial angles  $\alpha_{i,neg}$  have to be modified according to table 2.2.

## 2.2 Measurement Procedure and Calibration

To measure the Mueller matrix of a sample the following general procedure has to be done. First, the wavelength is chosen and the initial angles of the liquid crystals are set. Then, the iCCD camera is properly focused on the target and the acquisition settings are determined. The acquisition is coupled automatically to the control of the liquid crystals to obtain all the 16 intensity elements of matrix  $B$ . The *region of interest* can be selected and the gain of the camera has to be set, together with the exposure time, the delay time and averaging settings. The latter relates to the number of acquisitions on the iCCD chip and the number of repetitions. All the acquisitions and repetitions are done per sequenced acquisition step, as shown by figure 2.2, before changing the state of a liquid crystal to proceed to the next step. In order to do time-resolved measurements, the control of the liquid crystals and acquisition of the intensity images have to be synchronized to an external trigger event. This will be used for the first time in chapter 4, where it will be elaborated further. Before the intensity matrix of a sample is measured a calibration of the entire system has to be done to retrieve  $A$  and  $W$ .

### 2.2.1 Calibration Procedure

Theoretically, the Mueller matrices  $W$  and  $A$ , representing the polarization states generated by the PSG and analyzed with the PSA, can be modeled since both the retardances and the orientations of the liquid crystals are now known. These matrices are necessary to retrieve the Mueller matrix of the sample from the intensity matrix  $B$ , according to equation (2.3). Instead of modeling  $A$  and  $W$  it is more accurate to perform a calibration of the polarimeter in which the Mueller matrices  $A$  and  $W$  are retrieved experimentally. While doing the calibration the sample is removed, since 4 calibration samples have to be measured. This calibration procedure follows the *Eigenvalue Calibration Method* (ECM)<sup>94,95</sup> in which the intensity matrices are analyzed of air ( $B_0$ ), a horizontal polarizer ( $B_1$ ), vertical polarizer ( $B_2$ ) and a wave retarder at inclined orientation ( $B_3$ ). This calibration procedure has become the standard in Mueller polarimetry over other methods that have been used in the past.<sup>96-99</sup>

With these four intensity matrices ( $B_j$  with  $j = 0, 1, 2, 3$ ) the  $A$  and  $W$  matrices are obtained by taking the following steps. Firstly, the intensity matrices are multiplied with the inverse of  $B_0$ , defining 4 matrices  $C_j$ . The eigenvalues of

<sup>94</sup>E. COMPAIN et al. *Appl. Opt.* 1999 **38**: 3490-3502

<sup>95</sup>C. MACÍAS-ROMERO and P. TÖRÖK *J. Eur. Opt. Soc. Rapid Publ.* 2012 **7**: 12004

<sup>96</sup>R. M. A. AZZAM et al. *Rev. Sci. Instrum.* 1988 **59**: 84-88

<sup>97</sup>R. M. A. AZZAM and A. G. LOPEZ *J. Opt. Soc. Am. A* 1989 **6**: 1513-1521

<sup>98</sup>K. BRUDZEWSKI *Journal of Modern Optics* 1991 **38**: 889-896

<sup>99</sup>D. S. SABATKE et al. *Conf. Proc. SPIE* 2000 **75**-81

these matrices are the same as the corresponding calibration samples, i.e. respectively air, twice a polarizer and a retarder. Thus, the eigenvalue matrices of  $C_j$  are taken ( $\equiv D_j$ ) and used to build the numerical Mueller matrices of the calibration samples.

$$C_j = B_0^{-1} \cdot B_j \quad (2.5)$$

$$D_j = \text{eig}(C_j) \quad (2.6)$$

$$\text{with } D_j = \begin{cases} \text{diag}(D_0) \hat{=} \{1, 1, 1, 1\} \\ \text{diag}(D_1) \hat{=} \{\tau, 0, 0, 0\} \\ \text{diag}(D_2) \hat{=} \{\tau, 0, 0, 0\} \\ \text{diag}(D_3) \hat{=} \{R_1, R_2, C_-, C_+\} \end{cases} \quad (2.7)$$

The diagonal values of the eigenvalue matrices  $D_j$  should resemble equation (2.7), with  $\tau$  the transmission of the respective polarizers and for the retarder two real ( $R_1$  and  $R_2$ ) and two imaginary eigenvalues ( $C_-$  and  $C_+$ ). In general, the four eigenvalues of each  $D_j$  matrix, called  $D_j(1)$  to  $D_j(4)$ , are used to build the numerical Mueller matrix  $N_j$  of the calibration samples according to equation (2.8) for  $j = 0, 1, 2, 3$ . This comes from the general model of a Mueller matrix represented by the ellipsometric angles  $\Psi$  and  $\Delta$ .<sup>36</sup>

$$\left. \begin{aligned} t_{j,1} &= \frac{1}{2} (D_j(1) + D_j(2)) \\ t_{j,2} &= \frac{D_j(1) - D_j(2)}{D_j(1) + D_j(2)} \\ t_{j,3} &= \frac{D_j(3) + D_j(4)}{D_j(1) + D_j(2)} \\ t_{j,4} &= -1i \cdot \frac{D_j(3) - D_j(4)}{D_j(1) + D_j(2)} \end{aligned} \right\} \Rightarrow N_j = t_{j,1} \begin{pmatrix} 1 & -t_{j,2} & 0 & 0 \\ -t_{j,2} & 1 & 0 & 0 \\ 0 & 0 & t_{j,3} & t_{j,4} \\ 0 & 0 & -t_{j,4} & t_{j,3} \end{pmatrix} \quad (2.8)$$

Though the  $N_j$  matrices resemble the calibration samples that are used, the orientations of the samples are not included yet. These are obtained using the *Null Space Method* as part of the ECM through vectorization. This is done by calculating matrices  $H_j$  according to equation (2.9), with  $I$  the  $4 \times 4$  identity matrix,  $\otimes$  the Kronecker product and  $R(\varphi)$  the  $4 \times 4$  rotation matrix depending on a rotation  $\varphi_j$ . The rotation angle of air and the first polarizer are set to zero, meaning only  $\varphi_2$  and  $\varphi_3$  have to be found. The  $16 \times 16$   $H_j$  matrices are summed to  $K_{tot}$ , see equation (2.10). The eigenvalues of  $K_{tot}$  are calculated for various  $\varphi_2$  and  $\varphi_3$  to find which orientations give the maximized ratio between the smallest and the second-smallest eigenvalue of  $K_{tot}$ .

$$H_j = I \otimes (R(-\varphi_j) \cdot N_j \cdot R(+\varphi_j)) - C_j^T \otimes I \quad (2.9)$$

$$K_{tot}(\varphi_2, \varphi_3) = \sum_{j=1}^4 H_j^T H_j \quad (2.10)$$

The  $K_{tot}$  matrix associated to the obtained orientations  $\varphi_2$  and  $\varphi_3$  is used to retrieve the PSA and PSG Mueller matrix  $A$  and  $W$ . The  $16 \times 1$  eigenvector belonging to the lowest eigenvalue of  $K_{tot}$  is reshaped to a  $4 \times 4$  matrix. This is the Mueller matrix  $W$ . From  $B_0$  then easily  $A$  is obtained as well. If desired the Mueller matrices of the calibration samples can be calculated. With the calibration procedure completed the sample that is to be examined is placed back and the intensity matrix  $B$  is obtained and transformed to the Mueller matrix of the sample using equation (2.3).

## 2.3 Analyses of the Mueller Matrix

The Mueller matrix that is obtained from a sample using the measured intensity matrix contains all the optical properties, in terms of diattenuation, birefringence and depolarization, as introduced in chapter 1. Unfortunately, when a sample exhibits multiple optical properties, they get entangled within the matrix. This means a model or a decomposition is necessary to extract the information. Various models and decompositions exist and the proper one has to be chosen based on the experimental setup and the sample which is investigated.<sup>36,100</sup> Nowadays, there exist three types of decomposition, namely the product, the sum and the differential decomposition. Each of them is applicable to a particular physical scenario.

The product decomposition is used when a non-homogeneous or layered sample is measured. In this scenario, the obtained Mueller matrix is related to the optical properties of a specific layer or a small part of the sample, instead of the entire optical path. The product decomposition models the Mueller matrix of the sample as the combined product of an individual retarder multiplied with a diattenuator and a depolarizer. The product decomposition that is traditionally used in this way is called the *Lu and Chipman* decomposition, which models the Mueller matrix as the product of first the diattenuator, then the retarder and lastly the depolarizer.<sup>101</sup> However, different product orders can be used creating a different

<sup>100</sup>R. OSSIKOVSKI et al. *Phys. status solidi* 2008 **205**: 720–727

<sup>101</sup>S.-Y. LU and R. A. CHIPMAN *J. Opt. Soc. Am. A* 1996 **13**: 1106–1113

product decomposition.<sup>102–104</sup>

The sum decomposition is applicable in cases when a combination of multiple beams arise after passing through the material, propagating each in a particular polarization state that combine incoherently as they reach the detector. This is the typical case of scattering, where scattered light can combine with non-scattered light.<sup>105</sup>

Lastly, the differential decomposition (also referred to as the logarithmic decomposition) should be used when homogeneous samples are examined and consequently the optical changes induced for the propagating polarized light beam are a cumulative effect along the path of propagation.<sup>106–108</sup> This is modeled as a series of infinitesimal changes along the entire interaction as the light propagates through the material. Hence, this decomposition requires measurements in transmission, as is used in the setup throughout this work. This type of decomposition is well suited for the investigation of optically active targets under plasma exposure since the plasma induced changes of the material will create a change in polarization along the entire medium.

### 2.3.1 Optically Active Targets

In chapter 1 the use of optically active targets is proposed to investigate plasma surface interactions by focusing on specific optical effects some materials possess. The electro-optic effect can be exploited to e.g. examine electric fields generated inside materials by the plasma. Mueller polarimetry can be used for this since the electric field induces changes in the refractive index (anisotropies), making them birefringent. This optical property has to be retrieved from the measured Mueller matrix.

The relation between the change in index of refraction and electric field depends on the material that is used and the way it is diagnosed using the polarimeter. The relation will be derived for each case that is used in this work individually in the respective chapters where they are presented. The way how the birefringence is retrieved from the Mueller matrix is independent from the choice of materials by using the logarithmic decomposition, which will be discussed here.

When materials are examined for which no depolarization and dichroism properties are present, the Mueller matrix of the sample can also be modeled directly following the *homogeneous elliptical retarder*-model.<sup>36</sup> This model allows the extraction of the birefringent properties directly by comparison of several of the

---

<sup>102</sup>J. MORIO and F. GOUDAIL *Opt. Lett.* 2004 **29**: 2234–2236

<sup>103</sup>R. OSSIKOVSKI et al. *Opt. Lett.* 2007 **32**: 689–691

<sup>104</sup>R. OSSIKOVSKI *J. Opt. Soc. Am. A* 2009 **26**: 1109–1118

<sup>105</sup>S. CLOUDE and E. POTTIER *IEEE Trans. Geosci. Remote Sens.* 1996 **34**: 498–518

<sup>106</sup>R. M. A. AZZAM *J. Opt. Soc. Am.* 1978 **68**: 1756–1767

<sup>107</sup>R. OSSIKOVSKI *Opt. Lett.* 2011 **36**: 2330–2332

<sup>108</sup>O. ARTEAGA *J. Opt. Soc. Am. A* 2017 **34**: 410–414

Mueller matrix elements, as will be introduced later. This model will be used in addition to the logarithmic decomposition to check the validity of the results. Throughout this thesis, different examples have to be analyzed following the measurements using different approaches to investigate optically active targets using Mueller polarimetry. In some cases this means dichroism is observed and depolarization is added, meaning that the homogeneous elliptical retarder-model is not valid anymore. The logarithmic decomposition, however, stays applicable and is therefore used in all cases throughout this thesis.

### 2.3.2 Logarithmic (Differential) Decomposition

The materials that will be used are homogeneous meaning that the total phase retardance that the light experiences due to the birefringent properties is an accumulation along the entire path through the sample. This makes the *logarithmic decomposition* the best choice for examining the Mueller matrices since the obtained Mueller matrix  $M$  is modeled as an infinite series of differential matrices  $m$ . This prompts the following differential equation, with  $z$  the optical axis of light propagation<sup>106–108</sup>:

$$\frac{dM(z)}{dz} = m \cdot M(z) \quad (2.11)$$

When the differential matrix  $m$  is considered as constant within the integration domain, this leads to the following and simple definition of the matrix  $L$ , according to (2.12).

$$M = \exp(md) \equiv \exp(L) \quad (2.12)$$

By taking the logarithm of the measured Mueller matrix  $M$ , information is obtained about the differential matrix  $m$  multiplied with thickness  $d$ . The differential matrix of an ideal sample, without absorption and depolarization, is defined as shown in equation (2.13) with  $\psi$  the diattenuation properties and  $\gamma$  the birefringence. Indications are given for the contributions to linear polarization in  $0/90^\circ$  coordinate system, linear  $45/135^\circ$  and circular  $l/r$  (left and right handed), similar as introduced with the Stokes formalism in chapter 1. When the exponential of the differential matrix  $m$  is taken according to equation (2.12), it is easily observed that all the optical properties are represented within the Mueller matrix  $M$  but in an entangled manner.

$$m = \begin{pmatrix} 0 & \psi_{0/90} & \psi_{45/135} & \psi_{l/r} \\ \psi_{0/90} & 0 & \gamma_{l/r} & -\gamma_{45/135} \\ \psi_{45/135} & -\gamma_{l/r} & 0 & \gamma_{0/90} \\ \psi_{l/r} & \gamma_{45/135} & -\gamma_{0/90} & 0 \end{pmatrix} \quad (2.13)$$

A measurement is never ideal, having depolarization and / or absorption present. Additionally, experimental errors cannot be fully prevented, which propagate through the analyses via matrix multiplication. Consequently, the obtained  $L$  matrix does not always show the symmetry as is expected from the definition of  $m$  in equation (2.13). This can be dealt with by modeling the differential matrix as the sum of an ideal matrix  $m_m$ , like equation (2.13), and a depolarizing one  $m_u$ . Equivalently the matrix logarithm  $L$  can be defined as the sum  $L_m + L_u$ . The separation of the two from  $L$  is done using the Minkowski metric  $G$ , with  $G = \text{diag}(1, -1, -1, -1)$ , according to equations (2.14) and (2.15).<sup>107</sup>

$$L_m = \frac{1}{2}(L - G \cdot L^T G) \quad (2.14)$$

$$L_u = \frac{1}{2}(L + G \cdot L^T G) \quad (2.15)$$

This means that the elements of  $L$ , represented by  $L_{ij}$ , are compared to create  $L_m$  and  $L_u$  in the following way:

$$L_m = \frac{1}{2} \begin{pmatrix} 0 & L_{12} + L_{21} & L_{13} + L_{31} & L_{14} + L_{41} \\ L_{12} + L_{21} & 0 & L_{23} - L_{32} & L_{24} - L_{42} \\ L_{13} + L_{31} & L_{23} - L_{32} & 0 & L_{34} - L_{43} \\ L_{14} + L_{41} & L_{24} - L_{42} & L_{34} - L_{43} & 0 \end{pmatrix} \quad (2.16)$$

$$L_u = \frac{1}{2} \begin{pmatrix} 2L_{11} & L_{12} - L_{21} & L_{13} - L_{31} & L_{14} - L_{41} \\ L_{12} - L_{21} & 2L_{22} & L_{23} + L_{32} & L_{24} + L_{42} \\ L_{13} - L_{31} & L_{23} + L_{32} & 2L_{33} & L_{34} + L_{43} \\ L_{14} - L_{41} & L_{24} + L_{42} & L_{34} + L_{43} & 2L_{44} \end{pmatrix} \quad (2.17)$$

As a result,  $L_m$  is always symmetrical, while  $L_u$  contains the *mismatching* between the elements of  $L$  that should have been (anti) symmetrical. This means the off-diagonal elements of  $L_u$  give an estimate of the uncertainty of the mean optical properties given by the corresponding elements within the  $L_m$  matrix. They relate to systematic deviations. More importantly, within the obtained matrix  $L_m$  the optical properties are separated and are no longer entangled, as they are within the Mueller matrix  $M$ . This is shown in equation (2.18) with  $\Psi$  and  $\Gamma$  the line integrated diattenuation and birefringence along the three polarization states. The  $L_u$  matrix contains the depolarization properties and (uncertainty) correlations between all the optical properties. The off-diagonal elements have been linked to the correlation function between two optical properties.<sup>109</sup>

<sup>109</sup>R. OSSIKOVSKI and O. ARTEAGA *Opt. Lett.* 2014 **39**: 4470–4473

$$L_m = \begin{pmatrix} 0 & \Psi_{0/90} & \Psi_{45/135} & \Psi_{l/r} \\ \Psi_{0/90} & 0 & \Gamma_{l/r} & -\Gamma_{45/135} \\ \Psi_{45/135} & -\Gamma_{l/r} & 0 & \Gamma_{0/90} \\ \Psi_{l/r} & \Gamma_{45/135} & -\Gamma_{0/90} & 0 \end{pmatrix} \quad (2.18)$$

### 2.3.3 Homogeneous Elliptical Retarder Model

When the samples that are investigated lack dichroism and depolarization properties, a second option can be used to retrieve the birefringent properties by applying the *homogeneous elliptical retarder model* (HER). Then the Mueller matrix is directly modeled as a function of the total circular birefringence  $CB$  experienced through the material, together with  $LB$  and  $LB'$ , respectively the linear birefringence in the 0/90 deg optical system and 45/135 deg system. No diattenuation or depolarization is added, see equation (2.19) with the total birefringence given by  $\Delta$ .

$$M_{HER} = \frac{1}{\Delta^2} \cdot \begin{pmatrix} \Delta^2 & 0 & 0 & 0 \\ 0 & LB^2 + (CB^2 + LB'^2) \cos \Delta & LB \cdot LB' \cdot R1 + CB \cdot R2 & CB \cdot LB \cdot R1 - LB' \cdot R2 \\ 0 & LB \cdot LB' \cdot R1 - CB \cdot R2 & LB'^2 + (CB^2 + LB^2) \cos \Delta & CB \cdot LB' \cdot R1 + LB \cdot R2 \\ 0 & CB \cdot LB \cdot R1 + LB' \cdot R2 & CB \cdot LB' \cdot R1 - LB \cdot R2 & CB^2 + (LB^2 + LB'^2) \cos \Delta \end{pmatrix} \quad (2.19)$$

$$\begin{aligned} \text{with} \quad \Delta &= \sqrt{LB^2 + LB'^2 + CB^2} \\ R1 &= 1 - \cos \Delta \\ R2 &= \Delta \sin \Delta \end{aligned} \quad (2.20)$$

With this model, the birefringences can be immediately obtained from the Mueller matrix through simple subtraction and addition of some of the elements. This is shown in equation (2.22) with the brackets  $\{ , \}$  indicating which element of the Mueller matrix  $M$  has to be taken.

$$\Delta = \arccos \left( \frac{M\{2, 2\} + M\{3, 3\} + M\{4, 4\} - 1}{2} \right) \quad (2.21)$$

$$\Rightarrow \begin{cases} LB &= (M\{3, 4\} - M\{4, 3\}) \frac{\Delta}{2 \sin \Delta} \\ LB' &= (M\{4, 2\} - M\{2, 4\}) \frac{\Delta}{2 \sin \Delta} \\ CB &= (M\{2, 3\} - M\{3, 2\}) \frac{\Delta}{2 \sin \Delta} \end{cases} \quad (2.22)$$

With this definition of  $M_{HER}$  a comparison between the two techniques for

analysis can be made by taking the logarithm of  $M_{HER}$ . The result shown by equation (2.23) indicates that the logarithmic decomposed matrix  $L$  does not have to be separated in  $L_m$  and  $L_u$  when no depolarization is present and a measurement is perfect. In that case, the  $\Gamma$  and birefringent properties obtained from  $M_{HER}$  are identical.

$$\log(M_{HER}) = \begin{pmatrix} 0 & 0 & 0 & 0 \\ 0 & 0 & CB & -LB' \\ 0 & CB & 0 & LB \\ 0 & LB' & LB & 0 \end{pmatrix} \quad (2.23)$$

## References

- [36] E. GARCIA-CAUREL, R. OSSIKOVSKI, M. FOLDYNA, A. PIERANGELO, B. DRÉVILLON, and A. DE MARTINO. In: *Advanced Mueller Ellipsometry Instrumentation and Data Analysis*. M. LOSURDO and K. HINGERL, eds. 31–143. Berlin, Heidelberg: Springer Berlin Heidelberg, 2013. DOI: [10.1007/978-3-642-33956-1\\_2](https://doi.org/10.1007/978-3-642-33956-1_2) (see pp. 11, 14, 15, 34, 42–44)
- [90] A. DE MARTINO, Y.-K. KIM, E. GARCIA-CAUREL, B. LAUDE, and B. DRÉVILLON. *Opt. Lett.* **28**: 616–618, 2003. DOI: [10.1364/OL.28.000616](https://doi.org/10.1364/OL.28.000616) (see p. 34)
- [91] A. DE MARTINO, E. GARCIA-CAUREL, B. LAUDE, and B. DRÉVILLON. *Thin Solid Films* **455-456**: 112–119, 2004. DOI: [10.1016/j.tsf.2003.12.052](https://doi.org/10.1016/j.tsf.2003.12.052) (see p. 34)
- [92] M. H. SMITH. *Appl. Opt.* **41**: 2488–2493, 2002. DOI: [10.1364/AO.41.002488](https://doi.org/10.1364/AO.41.002488) (see p. 38)
- [93] J. S. TYO. *Appl. Opt.* **41**: 619–630, 2002. DOI: [10.1364/AO.41.000619](https://doi.org/10.1364/AO.41.000619) (see pp. 38, 40)
- [94] E. COMPAIN, S. POIRIER, and B. DREVILLON. *Appl. Opt.* **38**: 3490–3502, 1999. DOI: [10.1364/AO.38.003490](https://doi.org/10.1364/AO.38.003490) (see p. 41)
- [95] C. MACÍAS-ROMERO and P. TÖRÖK. *J. Eur. Opt. Soc. Rapid Publ.* **7**: 12004, 2012. DOI: [10.2971/jeos.2012.12004](https://doi.org/10.2971/jeos.2012.12004) (see p. 41)
- [96] R. M. A. AZZAM, E. MASETTI, I. M. ELMINYAWI, and F. G. GROSZ. *Rev. Sci. Instrum.* **59**: 84–88, 1988. DOI: [10.1063/1.1139971](https://doi.org/10.1063/1.1139971) (see p. 41)
- [97] R. M. A. AZZAM and A. G. LOPEZ. *J. Opt. Soc. Am. A* **6**: 1513–1521, 1989. DOI: [10.1364/JOSAA.6.001513](https://doi.org/10.1364/JOSAA.6.001513) (see p. 41)
- [98] K. BRUDZEWSKI. *Journal of Modern Optics* **38**: 889–896, 1991. DOI: [10.1080/09500349114550871](https://doi.org/10.1080/09500349114550871) (see p. 41)
- [99] D. S. SABATKE, A. M. LOCKE, M. R. DESCOUR, W. C. SWEATT, J. P. GARCIA, E. L. DERENIAK, S. A. KEMME, and G. S. PHIPPS. *Conf. Proc. SPIE*, 75–81, 2000. DOI: [10.1117/12.406613](https://doi.org/10.1117/12.406613) (see p. 41)
- [100] R. OSSIKOVSKI, M. ANASTASIADOU, S. BEN HATTI, E. GARCIA-CAUREL, and A. DE MARTINO. *Phys. status solidi* **205**: 720–727, 2008. DOI: [10.1002/pssa.200777793](https://doi.org/10.1002/pssa.200777793) (see p. 43)
- [101] S.-Y. LU and R. A. CHIPMAN. *J. Opt. Soc. Am. A* **13**: 1106–1113, 1996. DOI: [10.1364/JOSAA.13.001106](https://doi.org/10.1364/JOSAA.13.001106) (see p. 43)
- [102] J. MORIO and F. GOUDAIL. *Opt. Lett.* **29**: 2234–2236, 2004. DOI: [10.1364/OL.29.002234](https://doi.org/10.1364/OL.29.002234) (see p. 44)
- [103] R. OSSIKOVSKI, A. DE MARTINO, and S. GUYOT. *Opt. Lett.* **32**: 689–691, 2007. DOI: [10.1364/OL.32.000689](https://doi.org/10.1364/OL.32.000689) (see p. 44)

- [104] R. OSSIKOVSKI. *J. Opt. Soc. Am. A* **26**: 1109–1118, 2009. DOI: [10.1364/JOSAA.26.001109](https://doi.org/10.1364/JOSAA.26.001109) (see p. 44)
- [105] S. CLOUDE and E. POTTIER. *IEEE Trans. Geosci. Remote Sens.* **34**: 498–518, 1996. DOI: [10.1109/36.485127](https://doi.org/10.1109/36.485127) (see p. 44)
- [106] R. M. A. AZZAM. *J. Opt. Soc. Am.* **68**: 1756–1767, 1978. DOI: [10.1364/JOSA.68.001756](https://doi.org/10.1364/JOSA.68.001756) (see pp. 44, 45)
- [107] R. OSSIKOVSKI. *Opt. Lett.* **36**: 2330–2332, 2011. DOI: [10.1364/OL.36.002330](https://doi.org/10.1364/OL.36.002330) (see pp. 44–46)
- [108] O. ARTEAGA. *J. Opt. Soc. Am. A* **34**: 410–414, 2017. DOI: [10.1364/JOSAA.34.000410](https://doi.org/10.1364/JOSAA.34.000410) (see pp. 44, 45)
- [109] R. OSSIKOVSKI and O. ARTEAGA. *Opt. Lett.* **39**: 4470–4473, 2014. DOI: [10.1364/OL.39.004470](https://doi.org/10.1364/OL.39.004470) (see pp. 46, 68)

# Chapter 3

## Electro-Optic Properties of $\text{Bi}_{12}\text{SiO}_{20}$

### Contents

---

<b>3.1 Introduction of BSO</b>	<b>52</b>
<b>3.2 Relation between Birefringence and Electric Field</b>	<b>53</b>
3.2.1 Index Ellipsoid	55
3.2.2 Light Propagation	56
<b>3.3 DC Electric Fields Applied to BSO</b>	<b>60</b>
3.3.1 Logarithmic Decomposition	61
3.3.2 Homogeneous Elliptical Retarder Model	71
<b>3.4 Summary and Perspectives</b>	<b>74</b>
<b>References</b>	<b>75</b>

---

This chapter introduces the electro-optic  $\text{Bi}_{12}\text{SiO}_{20}$  (BSO) materials used for the investigation of plasma surface interactions. The materials are used since their refractive index depends on the externally induced electric field. The relation between the resulting anisotropies and the electric field is derived analytically using the index ellipsoid. DC-induced electric fields inside the BSO material are applied to verify the theory and calibrate the material's constants. The main method of analysis, the logarithmic decomposition, is applied and also the homogeneous elliptical retarder model for comparison and verification.

### 3.1 Introduction of BSO

The Mueller polarimeter, as designed and built according to the description given in the previous chapter, will be used to investigate plasma surface interactions by exploiting optical effects in certain materials exposed to a plasma jet. The primary focus lies with the electro-optic effect for reasons stated in Chapter 1. One of the most generally used electro-optic materials is  $\text{Bi}_{12}\text{SiO}_{20}$  (BSO).

$\text{Bi}_{12}\text{SiO}_{20}$  (BSO) is a body-centered cubic crystal with a rotational tetrahedral symmetry point group. It was first discovered in Mexico by Swedish chemist Lars Gunnar Sillén in the 1940s to whom the mineral is named “Sillénite”.<sup>110</sup> Synthesized in the laboratory the material was first investigated in the 60s and 70s focusing on growth mechanisms<sup>111,112</sup> and the optical properties it possesses.<sup>113,114</sup> Because BSO lacks inversion symmetry it has noticeable electro-optic properties, i.e. it develops a linear birefringence proportional to the intensity of an externally applied electric field. This effect, known as the Pockels effect, comes in addition to a second-order effect (scaling quadratically to the electric field) known as the Kerr effect which occurs in all materials. Since the first order Pockels effect is present, the second order effect can be neglected. Besides its electro-optic behavior, the material also exhibits photo-refractive, elasto-optic, magneto-optic, and thermo-optic effects.

BSO crystals have been used mostly because of their electro-optical properties. By applying a homogeneous electric field a *Pockels cell* can be used as variable optical (polarized) switchable modulator, called PROM (Pockels Readout Optical Modulator).<sup>115,116</sup> Other applications include phase conjugation, beam amplification, and holographic storage.<sup>117,118</sup>

Instead of exploiting the electro-optic behavior to control and manipulate the (polarized) light which passes through the material, it can also be applied as a sensor. By investigating the change in polarization state, a measure is obtained that can be related to the intensity of an unknown electric field to which the material is exposed. This sensor capability makes it ideal for the investigation of plasma surface interactions. It was first applied in this way by the research group lead by Prof. Takada,<sup>119</sup> focusing on surface charge distributions induced

---

<sup>110</sup>R. A. BIDEAUX et al. 1995 ISBN: 0962209716

<sup>111</sup>J. BRICE et al. *J. Cryst. Growth* 1974 **24-25**: 429–431

<sup>112</sup>A. TANGUAY et al. *J. Cryst. Growth* 1977 **42**: 431–434

<sup>113</sup>E. L. VENTURINI et al. *J. Appl. Phys.* 1969 **40**: 1622–1624

<sup>114</sup>R. E. ALDRICH et al. *J. Appl. Phys.* 1971 **42**: 493–494

<sup>115</sup>S. L. HOU and D. S. OLIVER *Appl. Phys. Lett.* 1971 **18**: 325–328

<sup>116</sup>P. NISENSEN and S. IWASA *Appl. Opt.* 1972 **11**: 2760–2767

<sup>117</sup>J. P. HUIGNARD and F. MICHÉRON *Appl. Phys. Lett.* 1976 **29**: 591–593

<sup>118</sup>J. HUIGNARD and A. MARRAKCHI *Opt. Commun.* 1981 **38**: 249–254

<sup>119</sup>T. TAKADA 1999 *Annu. Rep. Conf. Electr. Insul. Dielectr. Phenom.* 1999 **6**: 1–14

by streamer patterns.<sup>84,85</sup> Since then, the technique has also been used for plasma jets<sup>65,86,87,120</sup> and DBDs.<sup>71,88,89</sup>

All reports published to date use a Sénarmont type setup to investigate either electric field or surface charge, by coupling a change in total transmission of the optical system to the (average) electric field inside the material. This experimental setup uses an optical compensator to determine the linear retardance in an optical system, from which the electric field is retrieved following the Pockels effect. The electric field is reported by some<sup>86,87,120</sup>, while the other publications focus on the surface charge distribution. This is obtained by applying a homogeneous field approximation to the electric field inside the material. This approximation is only valid when the discharge size is relatively large compared to the thickness of the material, creating a homogeneous electric field pattern. When this is not the case, a compensation procedure or algorithm is needed to gain information about surface charge using the average electric field throughout the material.<sup>87,121</sup>

Throughout this work, the (average) electric field patterns induced by the plasma inside the materials will be used for the investigation of plasma surface interactions. The average electric field, throughout the 0.5 mm thick material, gives the information about the fields to which materials are exposed to. Mueller polarimetry is applied, rather than a simplified Sénarmont setup, to extend the investigation of the materials towards all the optical properties and have the capability to not only measure a single retardance but to focus on both  $\Gamma_{0/90}$  and  $\Gamma_{45/135}$ . This will turn out to be a significant advantage that Mueller polarimetry has over other techniques.

The relation between the different retardances and the external electric field is derived in the next section for two cases. The first examines the BSO crystal at normal incidence, while the second uses an inclined angle of  $45^\circ$ . In the last section, homogeneous constant electric fields are applied to investigate the measurement technique that is used and the data analyses which has to be performed.

## 3.2 Relation between Birefringence and Electric Field

The birefringence that is experienced by the polarized light traveling through the material depends on the difference in refractive index that is present between

<sup>84</sup>T. KAWASAKI et al. *Jpn. J. Appl. Phys.* 1991 **30**: 1262–1265

<sup>85</sup>Y. ZHU et al. *J. Phys. D. Appl. Phys.* 1995 **28**: 1468–1477

<sup>65</sup>R WILD et al. *J. Phys. D. Appl. Phys.* 2014 **47**: 042001

<sup>86</sup>E. SLIKBOER et al. *Plasma Sources Sci. Technol.* 2016 **25**: 03LT04

<sup>87</sup>E. SLIKBOER et al. *Plasma Sources Sci. Technol.* 2017 **26**: 035002

<sup>120</sup>A. SOBOTA et al. *J. Phys. D. Appl. Phys.* 2013 **46**: 372001

<sup>71</sup>L. STOLLENWERK et al. *Phys. Rev. Lett.* 2007 **98**: 255001

<sup>88</sup>M BOGACZYK et al. *J. Phys. D. Appl. Phys.* 2012 **45**: 465202

<sup>89</sup>R. TSCHERSCH et al. *J. Phys. D. Appl. Phys.* 2014 **47**: 365204

<sup>121</sup>H. MU and G. ZHANG *Plasma Sci. Technol.* 2011 **13**: 645–650

the electro-magnetic wave components since this causes a different phase velocity with which they travel. This is shown in equation (3.1), with  $\Gamma$  the retardance in a certain optical system,  $\Delta n$  the difference in refractive index in this system (caused by the anisotropy),  $\lambda$  the wavelength of the light in vacuum and  $d$  the length of the optical path.<sup>122</sup> The relation between  $\Delta n$  and the external source of the birefringence depends on the symmetry point group of the material, the direction that the light is propagating in and the axes in which the components of the light are oscillating (its polarization state).<sup>123</sup>

$$\Gamma = \frac{2\pi d}{\lambda} \Delta n \quad (3.1)$$

Since the linear retardance  $\Gamma$  depends on the oscillation direction of the light, two different linear retardances are used within Mueller polarimetry to account for this, namely  $\Gamma_{0/90}$  and  $\Gamma_{45/135}$ . The first indicates that a phase retardance can be induced when horizontal and vertical oscillation components travel with different velocities through the material, see figure 3.1. The second occurs because the diagonal components (along the  $45^\circ$  deg and  $135^\circ$  deg axes) travel at different velocities. This occurs only when there is a difference between the refractive index of those specific axes along which the light is oscillating, i.e.  $\Delta n_{0/90}$  for  $\Gamma_{0/90}$  and  $\Delta n_{45/135}$  for  $\Gamma_{45/135}$ .

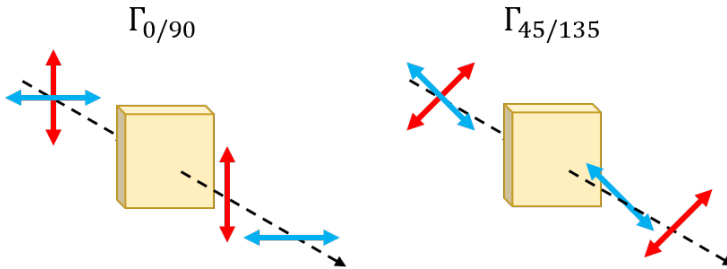


Figure 3.1: The linear retardance which is induced when light propagates through a birefringent material depends on the axes of oscillation of the light components (i.e. the polarization state). A difference between refractive index for horizontal and vertical components cause retardance  $\Gamma_{0/90}$ , while differences in the diagonal system correspond to  $\Gamma_{45/135}$ .

The location of  $\Gamma_{0/90}$  and  $\Gamma_{45/135}$  within the Mueller matrix relates with the  $L_m$  matrix shown by equation (2.18). This is because e.g.  $\Gamma_{0/90}$  can only induce a phase retardance when *diagonally* linearly polarized light is passing through the material, since then the horizontal and vertical components are present.  $\Gamma_{0/90}$

<sup>122</sup>M. BORN and E. WOLF 1999 ISBN: 9781139644181

<sup>123</sup>R. C. POWELL 2010 ISBN: 978-1-4419-7597-3

cannot change vertically or horizontally polarized light into diagonally polarized light since there is only one component present. For this,  $\Gamma_{45/135}$  is needed. Consequently, these two linear retardances are not the same, since they depend on relatively  $\Delta n_{0/90}$  and  $\Delta n_{45/135}$ , see figure 3.1. These specific changes in the (experienced) index of refraction can be influenced externally, e.g. during a plasma-surface interaction on electro-optic targets.

### 3.2.1 Index Ellipsoid

Changes induced by external electric field to the index of refraction are caused by anisotropies. This can be described by deformations within the index ellipsoid. The index ellipsoid is a visualization of the refractive index of the material in all directions, given by equation (3.2) with  $n$  the refractive index along the optical axes  $x$ ,  $y$  and  $z$ . Important for this analytical derivation is the orientation of the optical axes  $x$ ,  $y$  and  $z$ . This is chosen according to the growth of the crystal and the way it is *cut*. The materials used in this work have been cut along the (001) axis, meaning that the  $z$ -axis is defined perpendicular to the surface (normal incident). The  $x$  and  $y$  axis are defined to relate respectively to the horizontal  $0^\circ$  deg and vertical  $90^\circ$  deg axis. Consequently, the diagonal system is defined by the  $45^\circ$  deg axis ( $x + y$ ) and the  $135^\circ$  deg axis ( $y - x$ ). Hypothetically, there is no limitation for the crystal to be rotated causing that the optical  $x$  and  $y$  axis corresponds to e.g. the diagonal axes instead of the horizontal / vertical axes. This reverses the definition of  $\Gamma_{0/90}$  and  $\Gamma_{45/135}$ .

For cubic isotropic crystals the refractive indices along the optical axes are the same  $n_o$ , but externally they can be influenced due to anisotropies. This changes the impermeability tensor  $A_\epsilon$ , described by the addition of six  $\Delta\eta_i$  terms, shown in equation (3.3).<sup>40</sup>

$$\frac{x^2}{n_x^2} + \frac{y^2}{n_y^2} + \frac{z^2}{n_z^2} = 1 \quad (3.2)$$

$$\Rightarrow (x \quad y \quad z) \cdot A_\epsilon \cdot \begin{pmatrix} x \\ y \\ z \end{pmatrix} = 1 \quad (3.3)$$

$$\text{with } A_\epsilon = \begin{pmatrix} \frac{1}{n_x^2} + \Delta\eta_1 & \Delta\eta_6 & \Delta\eta_5 \\ \Delta\eta_6 & \frac{1}{n_y^2} + \Delta\eta_2 & \Delta\eta_4 \\ \Delta\eta_5 & \Delta\eta_4 & \frac{1}{n_z^2} + \Delta\eta_3 \end{pmatrix}$$

<sup>40</sup>C. MALGRANGE et al. 2014 ISBN: 978-94-017-8992-9

### 3.2.2 Light Propagation

The addition of the  $\Delta\eta_i$  terms describes how the entire index ellipsoid is deformed by an external cause. The birefringence that the polarized light experiences as it passes through the material depends on the way the light goes through the material relative to the orientation of the material. The plane wave perpendicular to the propagation direction, indicated by wave vector  $\vec{k}$ , is used for this, see equation (3.4) with  $x$ ,  $y$  and  $z$  corresponding to the optical axes of the material. It describes the plane in which the electro-magnetic components are oscillating. It is necessary to know in which direction the oscillation is occurring, since then the refractive index that is experienced can be examined, which determines the retardance of  $\Gamma_{0/90}$  or  $\Gamma_{45/135}$ .

$$x \cdot k_x + y \cdot k_y + z \cdot k_z = 0 \quad (3.4)$$

A phase retardance is only induced when the polarization components of the light travel with different velocities through the material. The plane wave is simply intersected with the index ellipsoid to find the refractive index determining the phase velocity that the different electro-magnetic wave components experience. This forms an ellipse and depending on the orientation of the polarization within the plane wave the refractive indices can be obtained within this intersecting ellipse determining the retardance.<sup>124</sup> This will be illustrated for two cases, where the light propagates through the material in different directions.

#### Case 1: Normal incidence

When light travels at normal incidence to the material the plane wave equation is simplified to  $z = 0$ , since  $z$  is the principal axis. This simplifies the three-dimensional index ellipsoid to a two-dimensional ellipse in the  $XY$ -plane, see equation (3.5). Only anisotropies  $\Delta\eta_1$ ,  $\Delta\eta_2$  and  $\Delta\eta_6$  are causing any alteration in this plane.

$$x^2 \left( \frac{1}{n_o^2} + \Delta\eta_1 \right) + y^2 \left( \frac{1}{n_o^2} + \Delta\eta_2 \right) + 2xy\Delta\eta_6 = 1. \quad (3.5)$$

Two linear retardances (birefringence) are examined using Mueller polarimetry, i.e. in the 0/90 deg coordinate system and the diagonal 45/135 deg system. The experienced refractive indices are simply found by finding the radii of the ellipse at those axes. For the retardance experienced in the 0/90 deg system, this is shown by equations (3.6) and (3.7). Since the anisotropies are assumed to be small, a Taylor expansion is allowed of the form  $(1 + \alpha)^{-0.5} \approx 1 - \alpha/2$ .

<sup>124</sup>L. DUVILLARET et al. *J. Opt. Soc. Am. B* 2002 **19**: 2704-2715

$$\begin{aligned}
 y \rightarrow 0 &\Rightarrow x^2 \left( \frac{1}{n_o^2} + \Delta\eta_1 \right) = 1 \\
 &\Leftrightarrow x \cong \pm n_o \left( 1 - \frac{1}{2} \Delta\eta_1 n_o^2 \right)
 \end{aligned} \tag{3.6}$$

$$\begin{aligned}
 x \rightarrow 0 &\Rightarrow y^2 \left( \frac{1}{n_o^2} + \Delta\eta_2 \right) = 1 \\
 &\Leftrightarrow y \cong \pm n_o \left( 1 - \frac{1}{2} \Delta\eta_2 n_o^2 \right)
 \end{aligned} \tag{3.7}$$

The difference is taken to obtain  $\Delta n_{0/90}$ , i.e. the difference in the experienced refractive index in the 0/90 deg system. This is shown in equation (3.8) and can be used to calculate  $\Gamma_{0/90}$ . The same derivation is followed to obtain  $\Delta n_{45/135}$ , as is shown in equation (3.9), used to calculate  $\Gamma_{45/135}$ .

$$\Delta n_{0/90} = n_0 - n_{90} = \pm \frac{1}{2} n_o^3 (\Delta\eta_1 - \Delta\eta_2) \tag{3.8}$$

$$\Delta n_{45/135} = n_{45} - n_{135} = \pm n_o^3 \Delta\eta_6 \tag{3.9}$$

Interestingly, since the material is investigated at normal incidence, the retardances that are obtained with Mueller polarimetry depend on different external anisotropies. The retardance in the 0/90 deg system depends on  $\Delta\eta_1$  and  $\Delta\eta_2$ , while polarization in the diagonal 45/135 deg system changes with anisotropy  $\Delta\eta_6$ . All the induced anisotropies  $\Delta\eta_i$  are coupled to the external cause through tensors. When an electric field is the source the relation is described using the electro-optic tensor of the material that is used. Other tensors have to be used to describe other materials or other optically active effects, such as the thermo-optic or elasto-optic effect. Almost all the elements of the  $6 \times 3$  (reduced) electro-optic tensor  $\bar{T}$  are zero for cubic crystals, except  $r_{41} = r_{52} = r_{63}$ , see equation (3.10) with  $r_{ij}$  the electro-optic constants in m/V.<sup>40</sup>

$$\bar{T} = \begin{pmatrix} 0 & 0 & 0 \\ 0 & 0 & 0 \\ 0 & 0 & 0 \\ r_{41} & 0 & 0 \\ 0 & r_{41} & 0 \\ 0 & 0 & r_{41} \end{pmatrix} \tag{3.10}$$

Consequently, when the electro-optic tensor is multiplied with the electric field vector  $\vec{E} = (E_x, E_y, E_z)$  to obtain the anisotropy terms,  $\Delta\eta_1$  and  $\Delta\eta_2$  are zero. Using equation (3.11) the final relation between the experienced retardance  $\Gamma$  and the electric field is obtained in both linear polarization systems, see equation

(3.12). The only electric field contribution in this configuration is due to  $E_z$ , i.e. the axial field perpendicular to the surface of the material. The relation includes a  $\pm$  sign since analytically, following the derivation as shown above, it is arbitrary whether a positive or negative phase retardance is induced depending on the orientation of the axes of the material. This means that when the crystal is rotated the sign changes and the linear retardances can be reversed.

$$\begin{pmatrix} \Delta\eta_1 \\ \Delta\eta_2 \\ \Delta\eta_3 \\ \Delta\eta_4 \\ \Delta\eta_5 \\ \Delta\eta_6 \end{pmatrix} = \overline{\mathbf{T}} \cdot \vec{E} = \begin{pmatrix} 0 & 0 & 0 \\ 0 & 0 & 0 \\ 0 & 0 & 0 \\ r_{41} & 0 & 0 \\ 0 & r_{41} & 0 \\ 0 & 0 & r_{41} \end{pmatrix} \cdot \begin{pmatrix} E_x \\ E_y \\ E_z \end{pmatrix} = \begin{pmatrix} 0 \\ 0 \\ 0 \\ r_{41}E_x \\ r_{41}E_y \\ r_{41}E_z \end{pmatrix} \quad (3.11)$$

$$\begin{cases} \Gamma_{0/90} &= \frac{2\pi d}{\lambda} \Delta n_{0/90} = 0 \\ \Gamma_{45/135} &= \frac{2\pi d}{\lambda} \Delta n_{45/135} = \pm \frac{2\pi d}{\lambda} n_o^3 r_{41} E_z \end{cases} \quad (3.12)$$

### Case 2: Examination at oblique incidence (45° angle)

The dependence of the retardance with the electric field changes when the target is examined at an oblique angle. The following case will be presented where light travels through the material at a 45° angle. As a result, first a coordinate transformation is performed according to equation (3.13), after which the three-dimensional ellipsoid is simplified using  $z' = 0$ .

$$\begin{pmatrix} x \\ y \\ z \end{pmatrix} \rightarrow \begin{pmatrix} \frac{x+z'}{\sqrt{2}} \\ y' \\ \frac{-x'+z'}{\sqrt{2}} \end{pmatrix} \quad (3.13)$$

Consequently, the intersecting two-dimensional ellipse that is formed is shown by equation (3.14). The anisotropy terms  $\Delta\eta_i$  are already substituted using equation (3.11).

$$x'^2 \left( \frac{1}{n_o^2} - r_{41} E_y \right) + \frac{y'^2}{n_o^2} + \sqrt{2} r_{41} x' y' (E_z - E_x) = 1 \quad (3.14)$$

Similar as for the normal incidence case, the difference in experienced refractive index is found by examining the radii of this ellipse at the right coordinate systems. For the refractive index in the 0/90 deg system, this is shown in equations (3.15) and (3.16).

$$\begin{aligned}
 y' \rightarrow 0 &\Rightarrow x'^2 \left( \frac{1}{n_o^2} - E_y r_{41} \right) = 1 \\
 &\Leftrightarrow x' \cong \pm n_o \left( 1 + \frac{1}{2} E_y r_{41} n_o^2 \right)
 \end{aligned} \tag{3.15}$$

$$\begin{aligned}
 x' \rightarrow 0 &\Rightarrow \frac{y'^2}{n_o^2} = 1 \\
 &\Leftrightarrow y' = \pm n_o
 \end{aligned} \tag{3.16}$$

The resulting difference in index of refraction is shown in equation (3.17). A birefringence is induced in this optical system depending on only the axial (vertical)  $E_y$  component along the path of propagation  $d^* = \sqrt{2}d$ , when electric field is applied externally.

$$\begin{aligned}
 \pm \Delta n_{0/90} &= n_o \left( 1 + \frac{1}{2} E_y r_{41} n_o^2 \right) - n_o \\
 &= \frac{1}{2} E_y r_{41} n_o^3
 \end{aligned} \tag{3.17}$$

$$\begin{aligned}
 \Gamma_{0/90} &= \frac{2\pi d^*}{\lambda} \Delta n_{0/90} \\
 &= \pm \frac{2\pi d^*}{\lambda} \frac{1}{2} E_y r_{41} n_o^3
 \end{aligned} \tag{3.18}$$

For the diagonal 45/135 deg optical system a similar approach is taken to retrieve the dependence of the retardance with the applied electric field. In this coordinate system the diagonal axes of the ellipse, given by equation (3.14), are examined. This can simply be done using a coordinate transformation with  $x' = (u + v)/\sqrt{2}$  and  $y' = (u - v)/\sqrt{2}$  and calculating the radii respectively when  $u \rightarrow 0$  and  $v \rightarrow 0$ , see equations (3.19) and (3.20).

$$\begin{aligned}
 u \rightarrow 0 &\Rightarrow \frac{v^2}{2} \left( \frac{1}{n_o^2} - r_{41} E_y \right) + \frac{v^2}{2n_o^2} - \sqrt{2} \cdot r_{41} \frac{v^2}{2} (E_z - E_x) = 1 \\
 &\Leftrightarrow v = \pm \frac{n_o}{\sqrt{1 - \frac{r_{41} E_y}{2} n_o^2 - \frac{r_{41} (E_z - E_x)}{\sqrt{2}} n_o^2}} \\
 &\cong \pm n_o \left( 1 + \frac{r_{41} E_y}{4} n_o^2 + \frac{r_{41} (E_z - E_x)}{2\sqrt{2}} n_o^2 \right)
 \end{aligned} \tag{3.19}$$

$$\begin{aligned}
 v \rightarrow 0 &\Rightarrow \frac{u^2}{2} \left( \frac{1}{n_o^2} - r_{41} E_y \right) + \frac{u^2}{2n_o^2} + \sqrt{2} \cdot r_{41} \frac{u^2}{2} (E_z - E_x) = 1 \\
 &\Leftrightarrow u = \pm \frac{n_o}{\sqrt{1 - \frac{r_{41} E_y}{2} n_o^2 + \frac{r_{41} (E_z - E_x)}{\sqrt{2}} n_o^2}} \\
 &\cong \pm n_o \left( 1 + \frac{r_{41} E_y}{4} n_o^2 - \frac{r_{41} (E_z - E_x)}{2\sqrt{2}} n_o^2 \right) \quad (3.20)
 \end{aligned}$$

The resulting difference in refractive index, given by equation (3.21), depends on a combination of the axial  $E_z$  component with the radial (horizontal)  $E_x$  component of the applied electric field. The obtained linear retardance in this optical system is given by equation (3.22).

$$\begin{aligned}
 \Delta n_{45/135} &= \pm n_o^3 \left( \frac{r_{41} E_y}{4} + \frac{r_{41} (E_z - E_x)}{2\sqrt{2}} - \frac{r_{41} E_y}{4} + \frac{r_{41} (E_z - E_x)}{2\sqrt{2}} \right) \\
 &= \pm \frac{1}{\sqrt{2}} n_o^3 r_{41} (E_z - E_x) \quad (3.21)
 \end{aligned}$$

$$\begin{aligned}
 \Gamma_{45/135} &= \frac{2\pi d^*}{\lambda} \Delta n_{45/135} = \\
 &= \pm \frac{2\pi d^*}{\lambda} \frac{1}{\sqrt{2}} n_o^3 r_{41} (E_z - E_x) \quad (3.22)
 \end{aligned}$$

### 3.3 DC Electric Fields Applied to BSO

A test case is examined, before the technique is applied to investigate plasma-surface interactions, to verify the analytically obtained relations between the phase retardance  $\Gamma$  and the externally applied electric field. Homogeneous constant electric fields are applied to a 0.5 mm thick BSO crystal coated with a thin conductive ITO layer on both sides. A mask is used during the coating procedure in order to have a circularly shaped coating pattern with a diameter of approximately 15 mm. Through variation of the applied voltage  $V$ , different birefringence is induced which is measured with the Mueller polarimeter setup. This allows for the investigation of the electro-optic constant of  $r_{41}$  and the main method of analyses which is used, i.e. the logarithmic decomposition. Additionally, the homogeneous elliptical retarder model is applied for comparison and verification.

The measurements are performed at normal incidence and therefore the induced birefringence relates to the applied potential difference  $V$  according to equation (3.12), with  $\vec{E} = (0, 0, V/d)$ . A calibration of the Mueller polarimeter is done prior to any measurement as discussed before in 2.2.1. This calibration provides the A and W matrices that allow to transform the measured intensity matrix to the Mueller matrix.

Figure 3.2 shows the obtained Mueller matrix of BSO with the circular ITO

coating, without an applied voltage. Figure 3.3 shows the Mueller matrix when a constant potential difference of 1 kV is applied between the ITO coatings on both sides. This clearly visualizes the location of the ITO-coated regions. Semi-spherically shaped golden electrodes on a small spring are used to connect the power supply to the material. These partially block the light, which is visible in all the Mueller matrix elements. The matrices are normalized through division using the  $\{1,1\}$  element. Throughout this work brackets  $\{, \}$  are used to indicate an element within a matrix. Two different color scales are used, ranging from either -0.2 to 0.2 or from -1.1 to 1.1. The border of each element (solid or dashed) indicates which color scale is used. Element values are only shown where light emission reaching the iCCD camera was high, meaning that the edge of the region of interest is left out of the images that are shown. The average and standard deviation of each element are taken in the center of the images and shown by equations (3.23) and (3.24).

When the definition of the Mueller matrix is followed, as presented by equations (2.12) and (2.13), it is clear that the individual elements of a Mueller matrix  $M$  can contain entangled information of the optical properties since the matrix exponential is used. Elements  $\{1,2-4\}$  and  $\{2-4,1\}$  (respectively the top row and left column) of both matrices are small, with absolute maximum values smaller than 0.04 rad except for  $\{1,4\}$  of  $M_2$  which is approximately 0.08 rad. The diagonal elements are non-zero for both  $M_1$  and  $M_2$ , together with the off-diagonal elements  $\{2,3\}$  and  $\{3,2\}$ . The biggest changes due to the application of the potential difference of 1 kV are observed in elements  $\{3-4,4\}$  and  $\{4,3-4\}$ , which are close to zero before applying the potential difference. The diagonal elements also change slightly due to the application of the voltage difference to the ITO coatings. All these changes are caused by the birefringences that are externally induced.

The Mueller matrices have to be analyzed to retrieve the optical characteristics of the induced birefringence. This can be done using the logarithmic decomposition or by applying the homogeneous elliptical retarder model, as explained in the previous chapter in 2.3.

### 3.3.1 Logarithmic Decomposition

The logarithmic (differential) decomposition consists of taking the logarithm of the measured Mueller matrix to obtain matrix  $L$ . This matrix is separated using the Minkowski metric  $G$  into the ideal, non-depolarizing matrix  $L_m$  and the depolarizing matrix  $L_u$  (a broader introduction is given in 2.3.2). Figures 3.4 to 3.7 show the logarithmically decomposed and separated matrices  $L_m$  and  $L_u$  for both Mueller matrices  $M_1$  and  $M_2$ . The average and standard deviation are taken within the region where the ITO coating is present, shown below each figure by equations (3.25) to (3.28).

Notably, both the  $L_m$  and  $L_u$  matrices have symmetrical properties for the off-

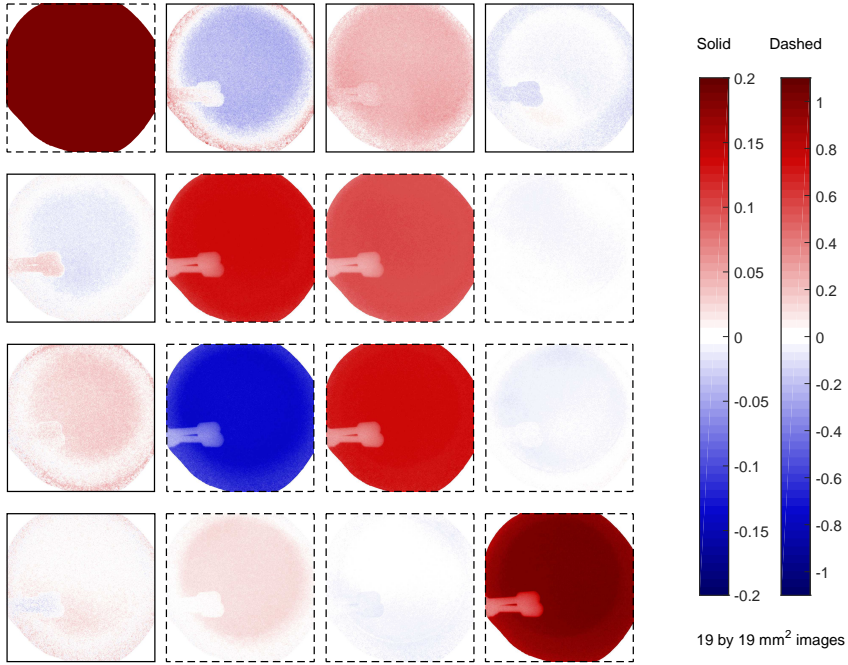


Figure 3.2: The measured Mueller matrix  $M_1$  of a BSO crystal with circularly shaped ITO coatings on both sides. A potential difference can be applied using two small semi-spherical gold electrodes on a spring, which partially block the light in all the elements.  $M_1$  is obtained with no applied voltage present, rendering it difficult to observe the ITO region. The border of each element (solid or dashed) indicates which color scale is applied and show a  $19 \times 19 \text{ mm}^2$  area. The central average values and standard deviations of each elements are shown by equation (3.23).

$$M_1 = \begin{pmatrix} 1 & -0.0385 & 0.040 & -0.008 \\ -0.013 & 0.742 & 0.550 & -0.039 \\ 0.024 & -0.74 & 0.736 & -0.046 \\ 0.003 & 0.11 & -0.0002 & 1.029 \end{pmatrix} \pm \begin{pmatrix} 0 & 0.006 & 0.004 & 0.004 \\ 0.004 & 0.008 & 0.007 & 0.006 \\ 0.006 & 0.01 & 0.009 & 0.009 \\ 0.006 & 0.01 & 0.009 & 0.009 \end{pmatrix} \quad (3.23)$$

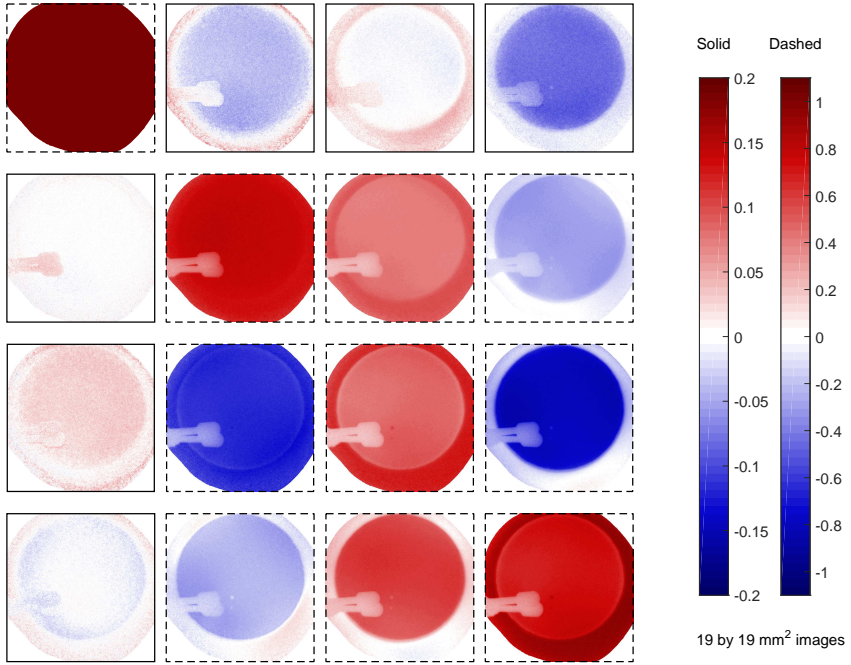


Figure 3.3: The second obtained Mueller matrix  $M_2$ , measured with an applied potential difference (over the 0.5 mm thick BSO) of 1000 volt between the ITO coated circular regions. This makes them distinctively different and observable from the uncoated BSO regions. Same remarks as given in figure 3.2 are valid.

$$M_2 = \begin{pmatrix} 1 & -0.036 & -0.007 & -0.080 \\ -0.001 & 0.79 & 0.388 & -0.306 \\ 0.026 & -0.64 & 0.44 & -0.81 \\ -0.003 & -0.23 & 0.61 & 0.70 \end{pmatrix} \pm \begin{pmatrix} 0 & 0.007 & 0.004 & 0.005 \\ 0.004 & 0.01 & 0.007 & 0.008 \\ 0.007 & 0.01 & 0.01 & 0.01 \\ 0.006 & 0.01 & 0.01 & 0.01 \end{pmatrix} \quad (3.24)$$

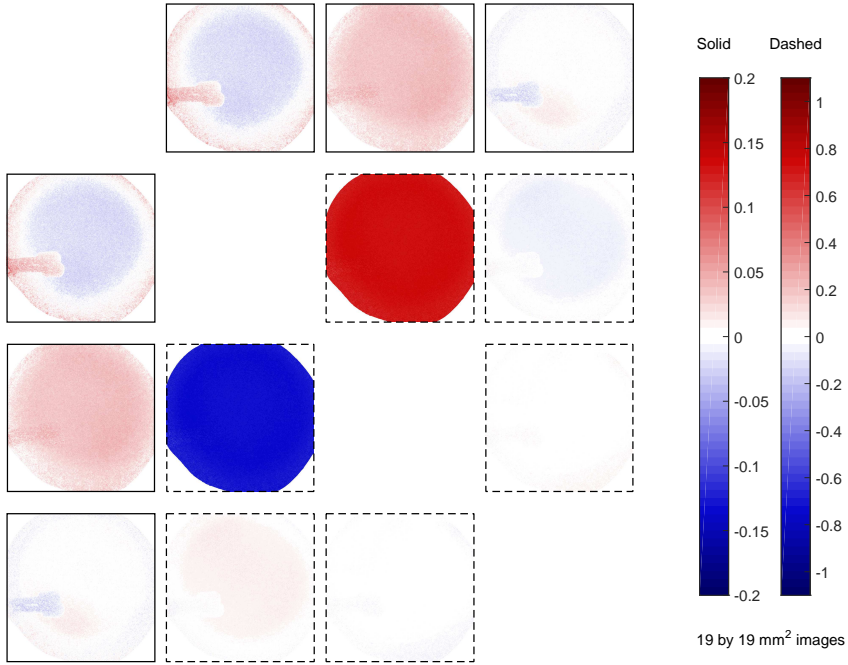


Figure 3.4: The non-depolarizing part  $L_{m,1}$  of the logarithmically decomposed matrix  $L$ , using Mueller matrix  $M_1$ . Hence, no voltage difference is applied. The diagonal elements are removed since they do not contain any information due to the separation. The optical properties, diattenuation and birefringence, are included as defined by equation (2.18). Similar remarks hold as discussed in figure 3.2.

$$L_{m,1} = \begin{pmatrix} & -0.020 & 0.034 & -0.001 \\ -0.020 & & 0.716 & -0.064 \\ 0.034 & -0.716 & & -0.013 \\ -0.001 & 0.064 & 0.013 & \end{pmatrix} \pm \begin{pmatrix} & 0.005 & 0.004 & 0.003 \\ 0.005 & & 0.007 & 0.008 \\ 0.004 & 0.007 & & 0.006 \\ 0.003 & 0.008 & 0.006 & \end{pmatrix} \quad (3.25)$$

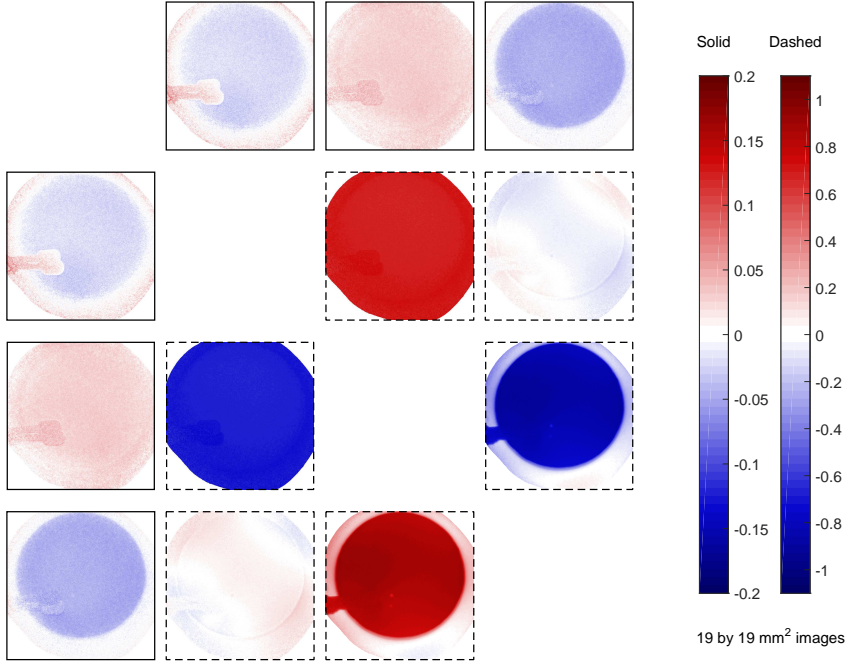


Figure 3.5: The obtained  $L_{m,2}$  matrix using Mueller matrix  $M_2$ , hence including the effect of the applied 1 kV potential difference between the ITO coated regions. Similar remarks hold as discussed in previous figures.

$$L_{m,2} = \begin{pmatrix} & -0.020 & 0.028 & -0.045 \\ -0.020 & & 0.660 & -0.061 \\ 0.028 & -0.660 & & -0.884 \\ -0.045 & 0.061 & 0.884 & \end{pmatrix} \pm \begin{pmatrix} & 0.005 & 0.004 & 0.004 \\ 0.005 & & 0.007 & 0.010 \\ 0.004 & 0.007 & & 0.009 \\ 0.004 & 0.01 & 0.009 & \end{pmatrix} \quad (3.26)$$

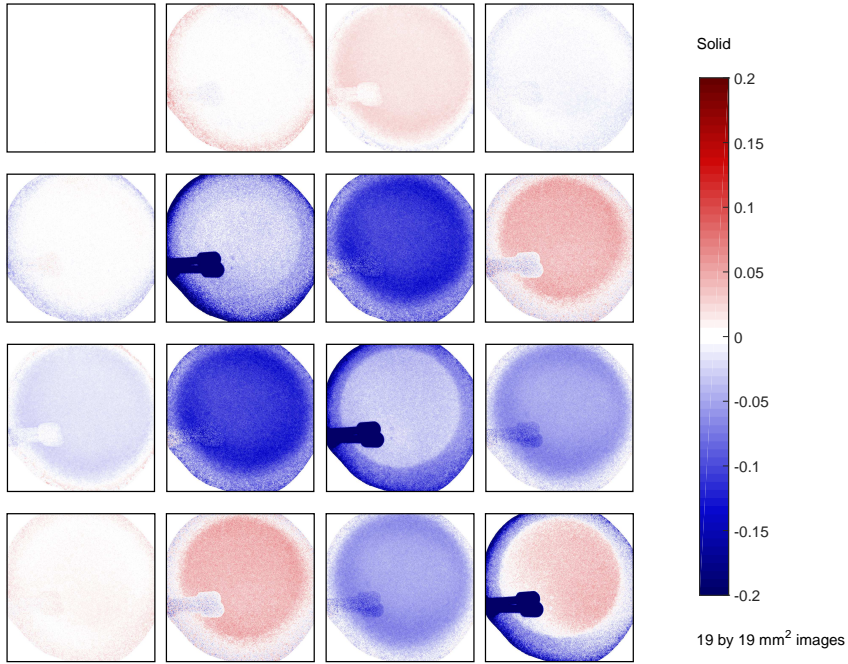


Figure 3.6: The separated depolarization part  $L_{u,1}$  of the logarithmically decomposed matrix  $L$ , using measured Mueller matrix  $M_1$ . No voltage difference is applied and similar remarks hold as with the previous figures. Depolarization properties are shown by the diagonal elements, while the off-diagonal elements relate to the uncertainty of the diattenuation and birefringent properties.

$$L_{u,1} = \begin{pmatrix} -0.0007 & -0.000 & 0.016 & -0.005 \\ 0.000 & -0.022 & -0.101 & 0.040 \\ -0.016 & -0.101 & -0.031 & -0.047 \\ 0.005 & 0.040 & -0.047 & 0.029 \end{pmatrix} \pm \begin{pmatrix} 0.0002 & 0.004 & 0.003 & 0.003 \\ 0.004 & 0.013 & 0.008 & 0.008 \\ 0.003 & 0.008 & 0.007 & 0.005 \\ 0.003 & 0.008 & 0.005 & 0.009 \end{pmatrix} \quad (3.27)$$

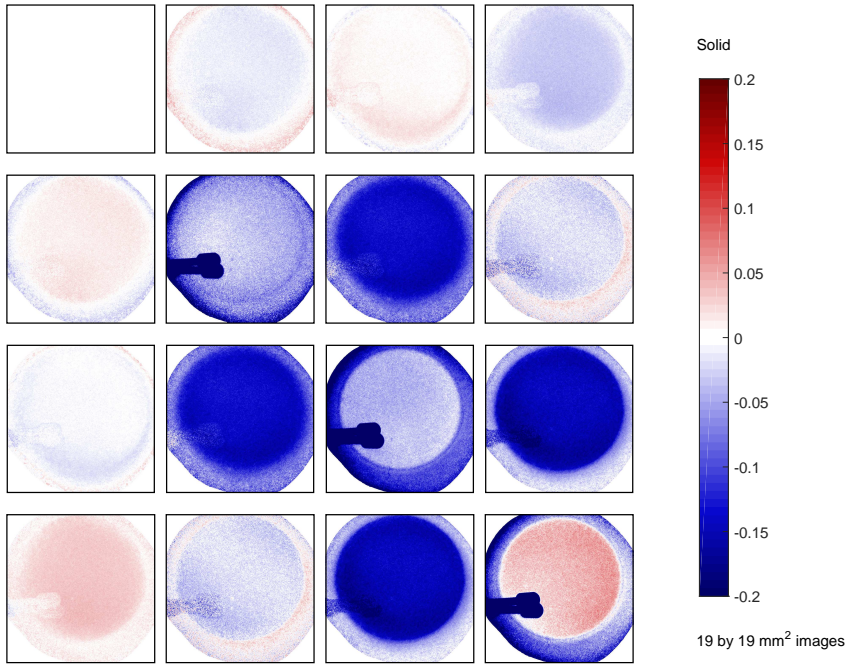


Figure 3.7: The depolarizing  $L_{u,2}$  matrix, obtained using  $M_2$  when applying a 1 kV potential difference, with similar remarks as indicated before.

$$L_{u,2} = \begin{pmatrix} -0.0007 & -0.012 & 0.006 & -0.032 \\ 0.012 & -0.03 & -0.132 & -0.02 \\ -0.006 & -0.132 & -0.04 & -0.142 \\ 0.032 & -0.02 & -0.142 & 0.04 \end{pmatrix} \pm \begin{pmatrix} 0.0003 & 0.004 & 0.003 & 0.004 \\ 0.004 & 0.01 & 0.008 & 0.01 \\ 0.003 & 0.008 & 0.01 & 0.009 \\ 0.004 & 0.01 & 0.009 & 0.01 \end{pmatrix} \quad (3.28)$$

diagonal elements, due to their defined separation from  $L$ . The top row and left column are identical, while the off-diagonal elements in the remaining sub  $3 \times 3$  matrix are anti-symmetric. These properties are always valid for the separated logarithmically decomposed matrices, but not necessarily true for the Mueller matrices.

As explained in section 2.3.2 for the introduction of the logarithmic decomposition, each element of  $L_m$  represents a specific optical property, relating to either diattenuation  $\Psi$  or birefringence  $\Gamma$ , within a polarization direction (linear 0/90 deg, linear 45/135 deg and circular) see equation (2.18).

The first non-depolarizing  $L_{m,1}$  matrix, shown in figure 3.4, indicates the presence of only one optical property, namely circular birefringence  $\Gamma_{l/r}$ . This is shown by element  $\{2,3\}$  and  $\{3,2\}$ , with an absolute value of  $0.72 \pm 0.01$  rad. The other elements are close to zero, with elements  $\{2,4\}$  and  $\{4,2\}$  the second biggest element with value  $0.06 \pm 0.01$  rad. The diattenuation properties are below  $0.05 \pm 0.005$  rad in all the coordinate systems (elements  $\{1,2-4\}$ ), independent of the potential difference which is applied. This is because the transmission of the BSO material (with the partial ITO coating) does not depend on the polarization state and it is investigated at normal incidence.

Changes are observed in  $L_{m,2}$  when a potential difference is applied of 1 kV between the ITO coatings. Still, diattenuation properties are close to zero, but a linear birefringence is induced. The absolute average value of  $\Gamma_{0/90}$  (element  $\{3,4\}$ ) increases from  $0.013 \pm 0.006$  rad to  $0.884 \pm 0.009$  rad. In the other optical coordinate system the absolute average value of  $\Gamma_{45/135}$  (element  $\{2,4\}$ ) remains  $0.06 \pm 0.01$  rad. There is however an observed pattern present within  $\Gamma_{45/135}$  induced by the application of the potential difference. Additionally, a small difference has been induced for the circular birefringence,  $\Delta\Gamma_{l/r} = -0.06 \pm 0.01$  rad.

The  $L_u$  matrices shown in figures 3.6 and 3.7 contain the information of depolarization and covariances between the optical properties.<sup>109</sup> Since BSO is non-depolarizing, because it is transparent and has a polished smooth surface, most elements are close to zero, as shown by the averaged values and the standard deviation in equations (3.27) and (3.28). A small difference is observed in the region where the ITO coating is present. This could be due to the interface between the coating and the crystal. Theoretically, all diagonal elements of  $L_u$  should be negative, which is not the case. This means that there is some non-physical behavior included. This can be removed by analyzing the eigenvalues of the related coherency matrix, but since the (positive) values are small, i.e. smaller than 0.05 and close to the noise level, we consider that this is not a major problem.

The induced change in the linear retardance is due to the application of the potential difference and the resulting homogeneous electric field between the

---

<sup>109</sup>R. OSSIKOVSKI and O. ARTEAGA *Opt. Lett.* 2014 **39**: 4470–4473

ITO coatings in the material. This dependency follows equation (3.12), however changes in  $\Gamma$  are observed in the 0/90 degree system rather than in the diagonal system as was derived and shown by the equation. This is simply due to a rotation variance resulting from the material. The derivation is done by finding the radii of the intersecting ellipse of the plane wave and the index ellipsoid. A rotation of the material changes the relative angle of the polarization axis to the principle axis of the material. Thus, when the material is rotated this can shift the induced retardance from  $\Gamma_{0/90}$  to  $\Gamma_{45/135}$ .

The difference of induced birefringences  $\Delta\Gamma$  in the individual optical systems is taken to only include effects induced by the application of the potential difference, shown in figure 3.8(a). Clearly visible is the induced spatial pattern for  $\Delta\Gamma_{45/135}$ . A similar pattern is present with  $\Delta\Gamma_{0/90}$ , but hardly visible due to the high offset of the linear retardance, of approximately -0.88 rad.

The electric field which is applied can be retrieved by looking at the *total* linear retardance  $\Gamma_{tot}$  of the system, regardless whether the changes of the linear birefringence are induced in the 0/90 deg system or the diagonal system. This is simply obtained by quadratically adding  $\Delta\Gamma_{0/90}$  and  $\Delta\Gamma_{45/135}$  and taking the square root. Equation (3.29) is then applied to obtain the electric field, with thickness  $d = 0.5$  mm, wavelength  $\lambda = 530$  nm, (unperturbed) refractive index  $n_o = 2.54$  and electro-optic constant  $r_{41} = 4.8$  pm/V. The resulting electric field is shown twice in figure 3.8(b) with different color scales.

$$|E_z| = \frac{\Gamma_{tot}}{\frac{2\pi d}{\lambda} n_o^3 r_{41}} \quad (3.29)$$

The two different color scales are used to visualize that the obtained pattern is not homogeneous, which is a surprise since conductive ITO coatings are used. The average electric field value is 18.7 kV/cm with a standard deviation of 0.2 kV/cm. This value is lower than the expected 20 kV/cm, assuming a homogeneous field resulting from a 1 kV potential difference over a 0.5 mm distance.

The fact that a lower field is measured could indicate that the used (electro-optic) constant value of  $r_{41} = 4.8$  pV/m is inaccurate, but the material properties  $n_o$  and  $r_{41}$  are calibrated and reported by the supplier and other users in literature. Another cause that can explain the difference between the expected and the measured values of the electric field, is that the potential difference of a 1000 volt is actually not reached, because of the way the voltage is applied. The semi-spherical golden electrodes on a spring are gently pushed to the ITO coated surface to create a contact. When this contact is not perfect, due to the shape of the electrodes, an equivalent series resistance is added to the system. In that case the resistor lowers the potential difference applied to the surface and the resulting measured electric field is lower. In addition, this could provide a possible explanation for the inhomogeneous pattern that is observed. The resistor created by the non-ideal

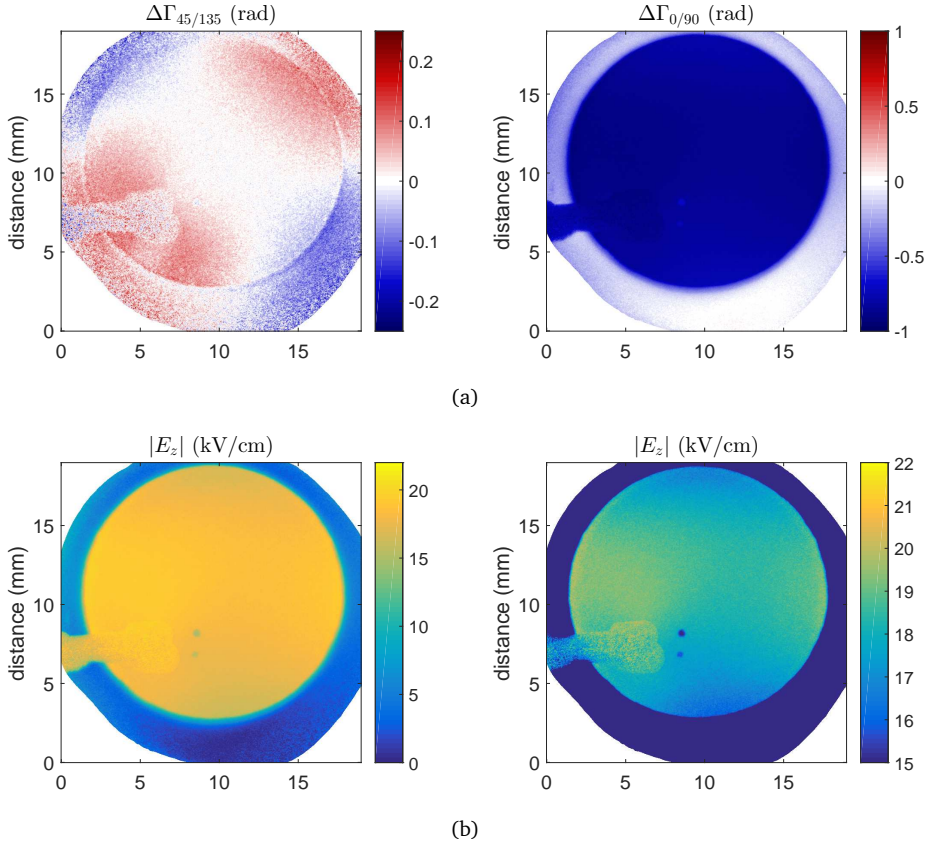


Figure 3.8: The difference in linear retardance due to the application of the voltage potential for both coordinate systems,  $\Delta\Gamma_{0/90}$  and  $\Delta\Gamma_{45/135}$  shown in 3.8(a). These are used to calculate the electric field, using equation (3.29), shown twice with difference color scales in 3.8(b).

contact is causing a local temperature increase, originating from the point of contact. BSO materials are not only sensitive to external electric field according to the Pockels effect, but they are also sensitive for other external effects of anisotropy, e.g. thermal or pressure effects. This is the topic of chapters 6 and 7.

The inhomogeneous pattern is only observed within the birefringent properties. Since it is not present in the other elements, the pattern is surely due to an induced birefringence (although the origin is not certain). It would not have been possible to make this conclusion when a simpler setup, like the Sénarmont setup, would have been used to examine the birefringence, since no information would have been obtained about diattenuation and / or depolarization. This is a significant advantage that Mueller polarimetry offers over other techniques.

The hypothesis that the non-ideal contact lowers the applied potential is sup-

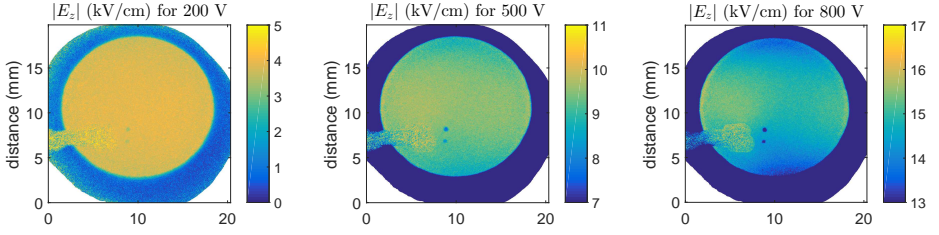


Figure 3.9: The obtained electric field for different applied voltages (sample thickness = 0.5 mm). The color scale is adapted to visualize the possible appearance of the inhomogeneous pattern, which becomes more significant with higher applied voltages.

ported when the electric field is examined for different applied voltages, see figure 3.9. With low voltages the measured electric field matches the expected value ( $E = \Delta V/d$ ) indicating that the correct value of  $r_{41}$  is used. Only with higher applied voltages the electric field deviates slightly. This decrease is accompanied with the appearance of the inhomogeneous pattern. If this pattern is indeed caused by local heating, it is understandable why it emerges with higher applied voltages.

The appearance of the inhomogeneous pattern means that the electric field shown is possibly not the electric field to which the crystal is exposed to. A combination of the electric field is observed with another (small) anisotropy, now falsely interpreted as electric field. Because a constant electric field is applied, the different causes of the anisotropies cannot be separated from each other. This would be possible if a time varying electric field is applied while the other source of anisotropy, e.g temperature or pressure, are constant. In any case, the value of the observed electric field is close enough to the expected value to trust the electro-optic constant given by the supplier.

### 3.3.2 Homogeneous Elliptical Retarder Model

The second way to analyze the measured Mueller matrices  $M_1$  and  $M_2$  is by applying the homogeneous elliptical retarder model (HER model). Within this model only retardance is included along the different polarization directions, called  $CB$ ,  $LB$  and  $LB'$ . Different names are used compared to the logarithmic decomposition, i.e.  $\Gamma_{1/r}$ ,  $\Gamma_{0/90}$  and  $\Gamma_{45/135}$ , to indicate the use of a different method and show the resulting differences that arise.

In the previous chapter in section 2.3.3 the model is explained, showing the relation between  $M$  and  $CB$ ,  $LB$  and  $LB'$ . Since no diattenuation or depolarization properties are included in the model, the analysis is straightforward following equations (2.22). The birefringent properties can simply be obtained through subtraction and addition of some of the Mueller matrix elements.

Resultingly, the obtained birefringent properties are shown in figure 3.10. The difference is taken to see the changes, i.e.  $\Delta CB$ ,  $\Delta LB$  and  $\Delta LB'$ , induced by the applied potential difference. The circular birefringence has decreased with  $0.07 \pm 0.01$  rad, while  $LB$  changed with  $-0.849 \pm 0.009$  rad and  $LB'$  with  $-0.03 \pm 0.01$  rad. These values correspond well with the values observed when applying the logarithmic decomposition. The correspondence is only present since the measured samples do not posses diattenuation or depolarization, as is shown by the low value elements of  $L_u$ .

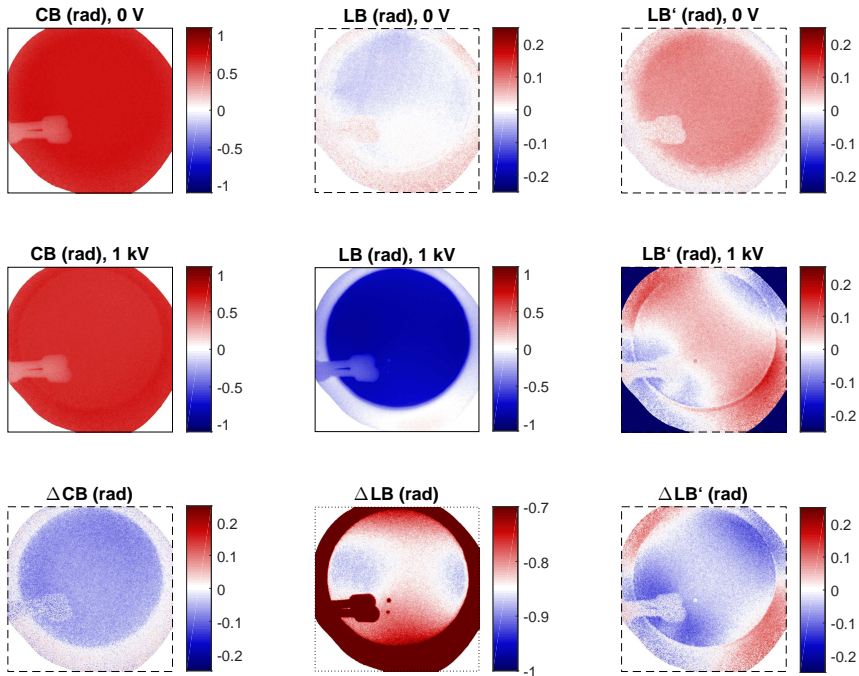


Figure 3.10: The linear and circular retardances ( $LB$ ,  $LB'$  and  $CB$ ) obtained by applying the homogeneous elliptical retarder model to the measured Mueller matrices,  $M_1$  and  $M_2$ .

A similar non-homogeneous pattern is observed in the linear birefringences. If only the *HER*-model would have been applied, without the logarithmic decomposition, it would have been impossible to say whether this pattern is a *real* birefringent property or if it is actually either diattenuation or depolarization which was not included in the model. This is an important advantage of the logarithmic decomposition where all the optical parameters are part of the examination.

The difference in linear retardance can be used similarly as with the logarithmically decomposed obtained quantities to retrieve the electric field pattern, as shown in figure 3.11. The average value,  $18.2 \pm 0.2$  kV/cm, corresponds with the earlier found value.

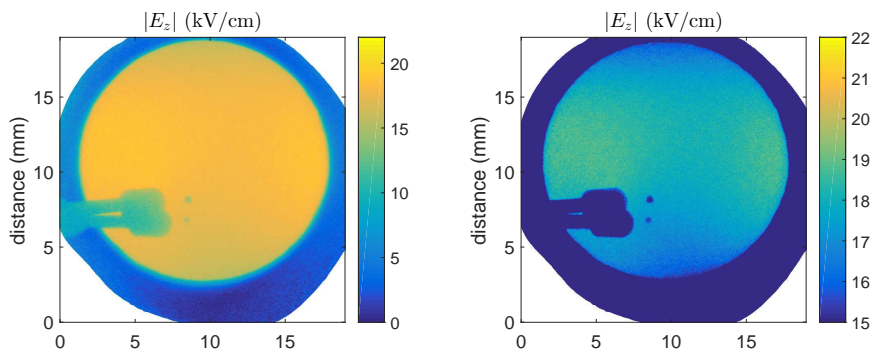


Figure 3.11: The electric field calculated using the linear retardances obtained from the applied homogeneous elliptical retarder model, shown twice with different color scales, which matches the results shown in figure 3.8(b).

### 3.4 Summary and Perspectives

- The relation between the induced retardance / birefringence in BSO with the externally applied electric field is derived using the index ellipsoid. This relation depends on the orientation of the material, the propagation direction of the light and the polarization axis.
- Electric fields induced using a constant potential difference applied to circularly, ITO coated patterns on both sides of the BSO crystals are examined with the Mueller polarimeter. The measured Mueller matrices are analyzed using the logarithmic decomposition and the homogeneous elliptical retarder (HER) model. Both analyses show similar results in terms of changes in (circular and linear) birefringence and electric field, induced by the applied potential difference. This means that the derived relation and the electro-optic constant of BSO are verified.
- A lower electric field than expected is measured for relatively high voltages, most probably due to a loss in applied potential by the addition of a resistor because a non-ideal contact has been used. This also resulted in an additional non-homogeneous birefringent pattern, due to heat delivered through the resistor / contact point. This is inseparable from the birefringence related to the induced (constant) electric fields.
- The unexpected (and for this case undesirable) non-homogeneous pattern is identified as a real birefringence since diattenuation and depolarization properties are also examined with Mueller polarimetry. This is not possible for simpler techniques where not all the optical properties are monitored, making the interpretation of such a pattern difficult. This creates an advantage for Mueller polarimetry over these other techniques. When an unexpected pattern is attributed to a real birefringence, it relates to a change in index of refraction. Therefore it can be analyzed to examine the external cause that has induced it. This can provide new information of the interaction that has taken place (e.g. for a plasma surface interaction) as will be shown in chapter 6 and 7.
- When time-dependent electric fields are applied instead of constant fields, the background patterns can be separated, since birefringence induced by temperature or pressure will still be constant or averaged over time. This is perfect for the use of these materials for the investigation of plasma surface interactions since the electric fields that are generated are almost always transient. The Mueller polarimeter will allow for the time-resolved acquisition of the Mueller matrix of the samples as will be shown in next chapters.

## References

- [40] C. MALGRANGE, C. RICOLLEAU, and M. SCHLENKER. *Symmetry and Physical Properties of Crystals*. Dordrecht: Springer Netherlands, 2014. ISBN: 978-94-017-8992-9 DOI: [10.1007/978-94-017-8993-6](https://doi.org/10.1007/978-94-017-8993-6) (see pp. 12, 55, 57, 88, 162, 163)
- [65] R WILD, T GERLING, R BUSSIAHN, K.-D. WELTMANN, and L STOLLENWERK. *J. Phys. D. Appl. Phys.* **47**: 042001, 2014. DOI: [10.1088/0022-3727/47/4/042001](https://doi.org/10.1088/0022-3727/47/4/042001) (see pp. 20, 22, 53, 80, 96)
- [71] L. STOLLENWERK, J. G. LAVEN, and H.-G. PURWINS. *Phys. Rev. Lett.* **98**: 255001, 2007. DOI: [10.1103/PhysRevLett.98.255001](https://doi.org/10.1103/PhysRevLett.98.255001) (see pp. 21, 22, 53, 80, 96)
- [84] T. KAWASAKI, Y. ARAI, and T. TAKADA. *Jpn. J. Appl. Phys.* **30**: 1262–1265, 1991. DOI: [10.1143/JJAP.30.1262](https://doi.org/10.1143/JJAP.30.1262) (see pp. 22, 53, 80, 96)
- [85] Y. ZHU, T. TAKADA, and D. TU. *J. Phys. D. Appl. Phys.* **28**: 1468–1477, 1995. DOI: [10.1088/0022-3727/28/7/028](https://doi.org/10.1088/0022-3727/28/7/028) (see pp. 22, 53)
- [86] E. SLIKBOER, O. GUAITELLA, and A. SOBOTA. *Plasma Sources Sci. Technol.* **25**: 03LT04, 2016. DOI: [10.1088/0963-0252/25/3/03LT04](https://doi.org/10.1088/0963-0252/25/3/03LT04) (see pp. 22, 53, 79, 80, 83, 95, 96, 160, 181)
- [87] E. SLIKBOER, E. GARCIA-CAUREL, O. GUAITELLA, and A. SOBOTA. *Plasma Sources Sci. Technol.* **26**: 035002, 2017. DOI: [10.1088/1361-6595/aa53fe](https://doi.org/10.1088/1361-6595/aa53fe) (see pp. 22, 53, 80, 83, 96, 101, 102, 160)
- [88] M BOGACZYK, R WILD, L STOLLENWERK, and H.-E. WAGNER. *J. Phys. D. Appl. Phys.* **45**: 465202, 2012. DOI: [10.1088/0022-3727/45/46/465202](https://doi.org/10.1088/0022-3727/45/46/465202) (see pp. 22, 53, 80, 96)
- [89] R. TSCHIRSCH, M. BOGACZYK, and H.-E. WAGNER. *J. Phys. D. Appl. Phys.* **47**: 365204, 2014. DOI: [10.1088/0022-3727/47/36/365204](https://doi.org/10.1088/0022-3727/47/36/365204) (see pp. 22, 53, 80, 96)
- [109] R. OSSIKOVSKI and O. ARTEAGA. *Opt. Lett.* **39**: 4470–4473, 2014. DOI: [10.1364/OL.39.004470](https://doi.org/10.1364/OL.39.004470) (see pp. 46, 68)
- [110] R. A. BIDEAUX, K. W. BLADH, M. C. NICHOLS, and J. W. ANTHONY. *Handbook of Mineralogy. Vol2: Silica, Silicates*. Mineral Data Publishing Tuscon, 1995. ISBN: 0962209716 (see p. 52)
- [111] J. BRICE, T. BRUTON, O. HILL, and P. WHIFFIN. *J. Cryst. Growth* **24-25**: 429–431, 1974. DOI: [10.1016/0022-0248\(74\)90351-0](https://doi.org/10.1016/0022-0248(74)90351-0) (see p. 52)
- [112] A. TANGUAY, S. MROCZKOWSKI, and R. BARKER. *J. Cryst. Growth* **42**: 431–434, 1977. DOI: [10.1016/0022-0248\(77\)90227-5](https://doi.org/10.1016/0022-0248(77)90227-5) (see p. 52)

- [113] E. L. VENTURINI, E. G. SPENCER, and A. A. BALLMAN. *J. Appl. Phys.* **40**: 1622–1624, 1969. DOI: [10.1063/1.1657822](https://doi.org/10.1063/1.1657822) (see p. 52)
- [114] R. E. ALDRICH, S. L. HOU, and M. L. HARVILL. *J. Appl. Phys.* **42**: 493–494, 1971. DOI: [10.1063/1.1659638](https://doi.org/10.1063/1.1659638) (see p. 52)
- [115] S. L. HOU and D. S. OLIVER. *Appl. Phys. Lett.* **18**: 325–328, 1971. DOI: [10.1063/1.1653681](https://doi.org/10.1063/1.1653681) (see p. 52)
- [116] P. NISENSEN and S. IWASA. *Appl. Opt.* **11**: 2760–2767, 1972. DOI: [10.1364/AO.11.002760](https://doi.org/10.1364/AO.11.002760) (see p. 52)
- [117] J. P. HUIGNARD and F. MICHERON. *Appl. Phys. Lett.* **29**: 591–593, 1976. DOI: [10.1063/1.89153](https://doi.org/10.1063/1.89153) (see p. 52)
- [118] J. HUIGNARD and A. MARRAKCHI. *Opt. Commun.* **38**: 249–254, 1981. DOI: [10.1016/0030-4018\(81\)90392-8](https://doi.org/10.1016/0030-4018(81)90392-8) (see p. 52)
- [119] T. TAKADA. *1999 Annu. Rep. Conf. Electr. Insul. Dielectr. Phenom.* **6**: 1–14, 1999. DOI: [10.1109/CEIDP.1999.804581](https://doi.org/10.1109/CEIDP.1999.804581) (see p. 52)
- [120] A. SOBOTA, O. GUAITELLA, and E. GARCIA-CAUREL. *J. Phys. D. Appl. Phys.* **46**: 372001, 2013. DOI: [10.1088/0022-3727/46/37/372001](https://doi.org/10.1088/0022-3727/46/37/372001) (see p. 53)
- [121] H. MU and G. ZHANG. *Plasma Sci. Technol.* **13**: 645–650, 2011. DOI: [10.1088/1009-0630/13/6/02](https://doi.org/10.1088/1009-0630/13/6/02) (see pp. 53, 97)
- [122] M. BORN and E. WOLF. *Principles of Optics*. Cambridge University Press, 1999. ISBN: 9781139644181 DOI: [10.1017/CB09781139644181](https://doi.org/10.1017/CB09781139644181) (see p. 54)
- [123] R. C. POWELL. *Symmetry, Group Theory, and the Physical Properties of Crystals*. vol. 824 Lecture Notes in Physics New York, NY: Springer New York, 2010. ISBN: 978-1-4419-7597-3 DOI: [10.1007/978-1-4419-7598-0](https://doi.org/10.1007/978-1-4419-7598-0) (see pp. 54, 162)
- [124] L. DUVILLARET, S. RIALLAND, and J.-L. COUTAZ. *J. Opt. Soc. Am. B* **19**: 2704–2715, 2002. DOI: [10.1364/JOSAB.19.002704](https://doi.org/10.1364/JOSAB.19.002704) (see p. 56)

# Chapter 4

## Electric Field Patterns Induced by Plasma at 45° Incidence

### Contents

---

<b>4.1 Investigating Electric Fields Induced by Plasma . . . . .</b>	<b>78</b>
<b>4.2 Measuring Axial Electric Fields . . . . .</b>	<b>79</b>
4.2.1 BSO examined at Normal Incidence . . . . .	79
4.2.2 Measurement Example with the AC Jet at 45° . . . . .	80
<b>4.3 Measuring Radial Electric Fields . . . . .</b>	<b>87</b>
4.3.1 Electro-Optic Fe:LiNbO <sub>3</sub> . . . . .	87
4.3.2 Measurement Example using Felinbo . . . . .	89
<b>4.4 Electric Field Patterns . . . . .</b>	<b>90</b>
4.4.1 AC Plasma Jet . . . . .	90
4.4.2 Influence of a Controlled Environment . . . . .	98
4.4.3 Time-Resolved Investigation of a Pulsed Plasma Jet in Air	106
<b>4.5 Summary and Perspectives . . . . .</b>	<b>117</b>
<b>References . . . . .</b>	<b>119</b>

---

This chapter shows various ways to investigate the transient electric fields induced in electro-optic targets during a repetitive plasma surface interaction. Electro-optic BSO is examined under normal incidence with the polarimeter to investigate the axial  $E_z$  component. Complementary, Fe:LiNbO<sub>3</sub> is used as a targeted surface to measure the radial field components ( $E_x$  and  $E_y$ ) inside the material under exposure of a plasma jet which is oriented at 45°. The electric field patterns are used to examine the plasma surface interaction. First, the influence of the surrounding gas with the AC-driven plasma jet in a controlled environment is examined this way. Then, the dependence on voltage amplitude is investigated for ionization waves generated with 1  $\mu$ s mono-polar positive voltage pulses.

## 4.1 Investigating Electric Fields Induced by Plasma

The investigation of the electric field induced in targets under plasma exposure is important for controlling the treatment of the targeted material and for the understanding of the applied plasma surface interaction. Electro-optic targets allow for the investigation of electric fields induced inside the material due to surface charges deposited during the interaction, by exploiting the Pockels effect. The purpose of this chapter is to show how Mueller polarimetry is able to measure the electric field using different approaches, leading to the determination of both the radial (parallel) and axial (normal) components of the induced field.

For the investigation of electric fields generated during a plasma impact, time-dependent fields are expected. The Mueller polarimeter can be used to investigate time-resolved an electro-optic target under plasma exposure to capture the transient electric field patterns induced during the interaction. This offers a unique way to investigate the conditions to which targets are exposed to when they are treated for a certain application in a plasma environment. Additionally, it allows for the examination of the deposition of surface charge, which influences the surface propagation of the discharges.

These aspects of plasma surface interactions are generally difficult to investigate, due to the transient behavior of these non-thermal plasmas, as well as their apparent size and simply due to an absence of diagnostic tools. Available methods to determine in the gas phase the electric field (and estimation of volume charge), like Stark shift spectroscopy or four-wave mixing, are suitable for the investigation of the dynamics occurring *inside* the plasma volume, e.g. the plume of a plasma jet, however extrapolation of these values towards a targeted surface is difficult and not straightforward. Electro-optic crystals do allow for this, as has been shown in the previous chapter for constant DC fields.

Surface charges deposited during the plasma interaction induce electric fields that change the refractive index of the crystals according to the Pockels effect, which can be detected optically. When a BSO crystal is investigated at normal incidence, as was done in the previous chapter, only the electric field component perpendicular to the surface is obtained, i.e. the axial  $E_z$  component. In literature, this component has been used to estimate the surface density of the deposited charges by applying a homogeneous field approximation.

However, inhomogeneous electric field patterns are usually present due to the relatively small discharge size. Average fields are always obtained throughout the thickness of the targeted material (0.5 mm). A better way to still investigate the charging of the material while not applying incorrectly a homogeneous field approximation is by obtaining a complete overview of the induced electric field components by also acquiring the radial patterns. In this chapter, it will be shown that by applying Mueller polarimetry to a different electro-optic crystal the radial components of the field (parallel to the target surface) are obtained for the first

time.

These techniques are applied to investigate the influence of the environmental surrounding gas for the guided ionization waves produced by a plasma jet to illustrate the benefits these techniques have for the examination of a plasma surface interaction. Additionally, the field is investigated when a pulsed plasma jet is used instead of the AC driven jet and the dependence with the voltage amplitude of the 1  $\mu$ s constant voltage pulses is studied.

## 4.2 Measuring Axial Electric Fields

### 4.2.1 BSO examined at Normal Incidence

The easiest way to investigate the electro-optic BSO material with the Mueller polarimeter is by examining it at normal incidence. This means the polarized light coming from the *Polarizer State Generator* (PSG) passes perpendicularly through the material before going to the *Polarizer State Analyzer* (PSA). Since the examination is done at normal incidence refraction and internal reflection of the light is prevented.

The acquisition of the intensity matrix, needed to calculate the Mueller matrix of the sample, is done similarly as described in chapter 2. However, as stated, time-resolved measurements have to be done in order to see optical changes caused by charge deposition during the transient plasma interaction occurring at nanosecond to microsecond timescale. The input voltage used to generate the plasma is also used to initiate a trigger signal. A time delay relative to this trigger and exposure time is chosen together with the number of frames that are captured for each element of the intensity matrix. The time delay can be varied to measure the Mueller matrix of the sample at different time instances within the repetitive voltage period. This allows to investigate the changes induced during the plasma impact. This is only possible since repetitive behavior is expected. Every frame at every liquid crystal state combination is obtained during a different voltage period.

Figure 1.4 shown in chapter 1 visualizes a typical voltage-current waveform obtained when operating the plasma jet with 30 kHz AC sine waves. One ionization wave is generated per cycle, during the positive half period. This is indicated by the characteristic current *dip* after the observed current peak. The Mueller matrix can be measured before and after this dip to investigate the charging of the surface by the plasma interaction. Time-resolved measurements done in previous works with a simpler setup<sup>86</sup> show that constant electric fields are obtained after impact of the ionization wave at the surface for almost 10  $\mu$ s, until the negative half period of the voltage cycle initiates a weak discharge at the surface and resultingly the removal of the surface charges.

---

<sup>86</sup>E. SLIKBOER et al. *Plasma Sources Sci. Technol.* 2016 **25**: 03LT04

The time-resolved Mueller matrix is calculated from the measured intensity matrix by using the  $A$  and  $W$  matrices of the PSG and PSA that are obtained through the *eigenvalue calibration method*. The logarithmic decomposition is applied to retrieve the optical properties of the examined electro-optic target for the chosen time delays. The obtained linear birefringent patterns in the two examined coordinate systems (0/90 and 45/135 deg) relate to the externally applied electric field according to equation (3.12), as derived in chapter 3. By comparing the time-resolved birefringent patterns before and after the impact of the ionization waves any *background* is removed and only the influence of electric field induced by temporally deposited surface charge is examined.

$$\begin{cases} \Gamma_{0/90} &= \frac{2\pi d}{\lambda} \Delta n_{0/90} = 0 \\ \Gamma_{45/135} &= \frac{2\pi d}{\lambda} \Delta n_{45/135} = \frac{2\pi d}{\lambda} n_o^3 r_{41} E_z \end{cases} \quad (3.12 \text{ revisited})$$

Since an optical response is expected in only one of the coordinate systems, a Sénarmont setup could be used as well.<sup>125</sup> This intensity based measurement setup is much simpler in operation than the Mueller polarimeter and has been used to investigate electric fields<sup>72,86,87</sup> and surface charge<sup>65,71,84,88,89</sup> during a plasma-target interaction. However, assumptions have to be made about the presumed absence of other optical properties when using an optical compensator for the determination of the linear birefringence, which is not the case with Mueller polarimetry. Additionally, the ability to detect linear birefringence simultaneously in both coordinate systems using Mueller polarimetry will become important when investigating the electric fields using different approaches (shown later in this chapter for measuring radial fields and in chapters 5-7) as well as examining partially depolarizing samples (chapter 8).

## 4.2.2 Measurement Example with the AC Jet at 45°

The plasma jet, as introduced in section 1.3.1, is used to investigate plasma surface interactions for two clear reasons. Firstly, this jet is similar to a wide range of jets that are used directly for applications ranging from surface functionalization and modification to biomedical treatment. Secondly, the jet is a very reproducible plasma source which is well characterized and has already been used for previous studies.

---

<sup>125</sup>H. G. JERRARD *J. Opt. Soc. Am.* 1948 **38**: 35–39

<sup>72</sup>A SOBOTA et al. *J. Phys. D. Appl. Phys.* 2013 **46**: 372001

<sup>87</sup>E. SLIKBOER et al. *Plasma Sources Sci. Technol.* 2017 **26**: 035002

<sup>65</sup>R WILD et al. *J. Phys. D. Appl. Phys.* 2014 **47**: 042001

<sup>71</sup>L. STOLLENWERK et al. *Phys. Rev. Lett.* 2007 **98**: 255001

<sup>84</sup>T. KAWASAKI et al. *Jpn. J. Appl. Phys.* 1991 **30**: 1262–1265

<sup>88</sup>M BOGACZYK et al. *J. Phys. D. Appl. Phys.* 2012 **45**: 465202

<sup>89</sup>R. TSCHERSCH et al. *J. Phys. D. Appl. Phys.* 2014 **47**: 365204

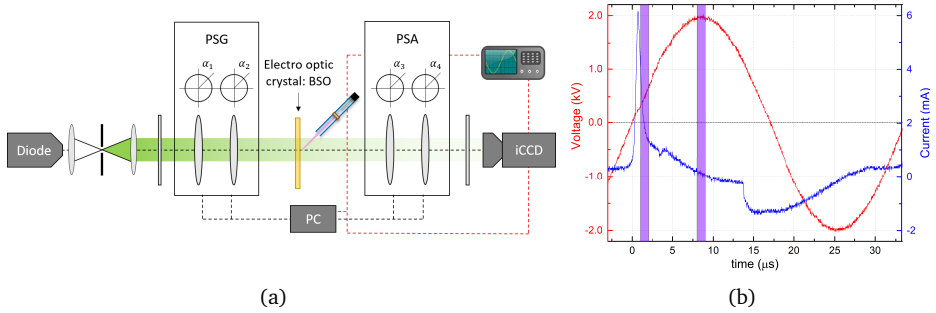


Figure 4.1: The polarimeter used to examine the electro-optic BSO material at normal incidence while the plasma jet impacts at a 45 degree angle, shown in (a). The time-resolved acquisition of the Mueller matrix can be done at a time delay  $t_d$  relative to an external trigger related to the rise of the voltage potential, shown in (b) for two examples in purple ( $1 \mu\text{s}$  exposure time) where the Mueller matrix is measured before impact (at  $t_d = 1 \mu\text{s}$ ) and after at  $t_d = 8 \mu\text{s}$ . The impact is characterized by the current dip at approximately  $3.5 \mu\text{s}$ .

The jet is mounted horizontally at a 45 degree impact angle (see figure 4.1(a)) to minimize blockage of the polarized light beam from the polarimeter by the capillary tube of the jet, which is at 7 mm away from the target. The plasma jet is operated using a 1 slm helium flow and a 2.0 kV amplitude sine wave with a frequency of 30 kHz. As shown with the characteristic voltage-current waveform in figure 4.1(b), in these conditions there is one ionization event occurring during each voltage period, during the positive half cycle after approximately  $3.5 \mu\text{s}$ . Mueller Polarimetry will be applied to examine the optical state of the electro-optic BSO material before and after the impact event, occurring every voltage cycle indicated in purple in figure 4.1(b). The acquisition of the Mueller matrices follows the same procedure as introduced in Chapter 2 and shown for DC applied fields in Chapter 3, with the addition of the trigger signal as explained above.

Figure 4.2 shows the two imaging Mueller matrices that are obtained when either a time delay is set of  $1 \mu\text{s}$  (top image) or  $8 \mu\text{s}$ , relative to the start of the positive half period of the high voltage sine wave. The exposure time of every acquired frame is set to  $1 \mu\text{s}$  and each element of the intensity matrix is obtained through averaging of 200 frames. The time delays are chosen specifically to examine the optical properties of the electro-optic crystal before and after the impact of the ionization wave. Consequently, the first Mueller matrix represents the state of the electro-optic crystal without the external influence due to temporally deposited surface charges and induced electric field, while the second one does incorporate these.

The respective time delays are chosen around the appearance of the character-

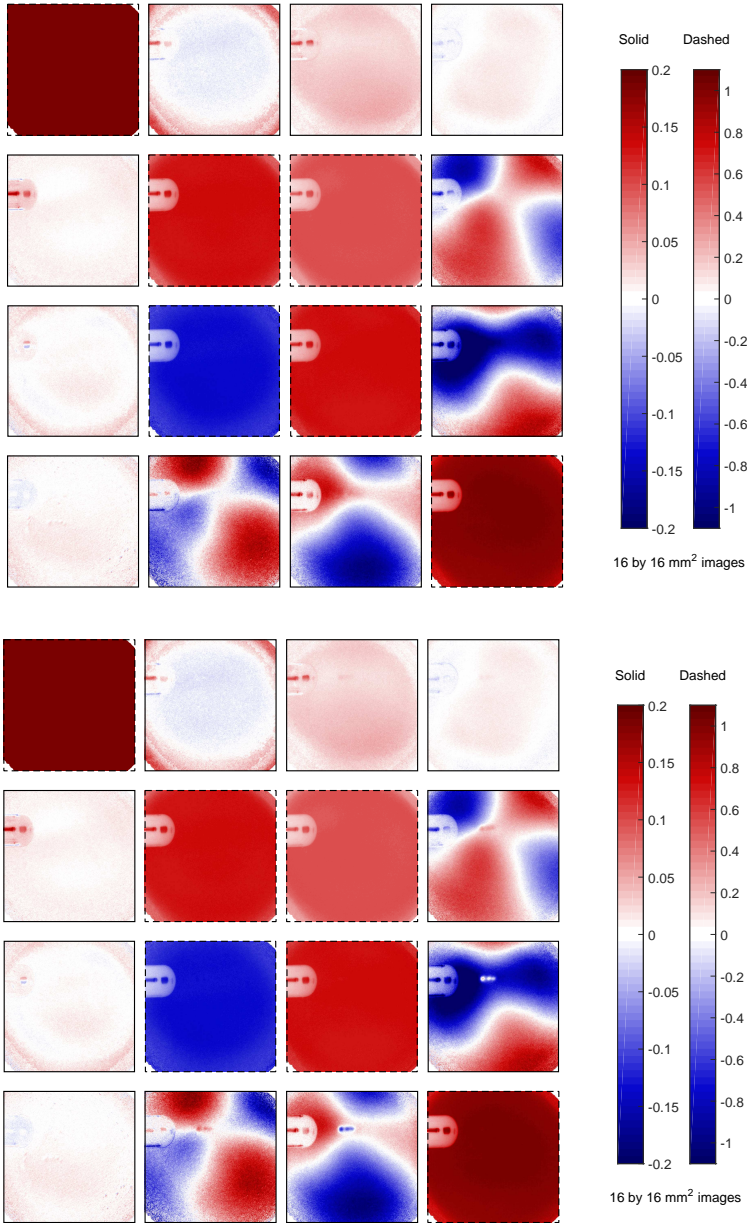


Figure 4.2: The obtained Mueller matrices of the electro-optic BSO examined at normal incidence under exposure of guided ionization waves produced with a plasma jet driven by a 30 kHz AC sine wave with 2.0 kV amplitude at 1 slm helium, shown before impact  $t_d = 1 \mu s$  (top matrix) and after  $t_d = 8.0 \mu s$  (bottom). The border (solid or dashed) of each  $16 \times 16 \text{ mm}^2$  element indicates which colorscale is used. The end of the 4 mm wide capillary tube is clearly visible in all elements blocking partially the polarized light on the left side of the images.

istic current *dip* in the current waveform as shown in purple in figure 4.1(b). Due to the impact event, indicated by the current dip, charge has been deposited by the ionization wave on the surface of the targeted material. It has been shown that these charges remain stable until the start of the negative voltage half period (reversal of the applied potential), approximately  $10 \mu\text{s}$  after the dip.<sup>86</sup> That is why a time delay of  $8 \mu\text{s}$  relative to the start of the positive half period represents well the optical state of the material with the surface charges included and  $1 \mu\text{s}$  exposure times can be taken without problems in order to capture more light and improve the measurement quality (signal to noise ratio). A weak afterglow is initiated when the polarity of the sine wave changes, which is related to a back discharge causing removal / recombination of the charged species at the targeted surface. This has been observed through imaging<sup>82</sup> as well as electric field measurements in an electro-optic target.<sup>86</sup> The latter was done using a simpler Sénarmont setup instead of the Mueller polarimeter as is used in this work.

The measured matrices shown in figure 4.2 will be discussed per element of the  $4 \times 4$  imaging matrix, similar as was done in the previous chapter. Throughout this work brackets “{, }” are used to indicate an element (pattern) within an obtained matrix. The only elements that are close to zero are the top row and first column without the primary image, i.e. elements  $\{1, 2-4\}$  and  $\{2-4, 1\}$  respectively. This is because the electro-optic crystals do not contain any diattenuation properties and they are examined at normal incidence, as stated in chapter 3.

After the ionization waves have impacted (Mueller matrix at  $t_d = 8\mu\text{s}$ ), only a small change is observable for elements  $\{4, 2-3\}$  and  $\{2-3, 4\}$ , additional to a constant *background* pattern which is also observable before impact. This non-uniform background pattern is constant in time and only present when the plasma jet is turned on. It shows resemblance with the non-uniform birefringent patterns observed when applying (relatively high potential) constant DC fields, shown in the previous chapter in figure 3.8. But as was shown in figure 3.8, without an external influence (e.g. a DC voltage of plasma jet exposure) elements  $\{2-3, 4\}$  are zero.

A similar stationary *background* structure has been reported in previous works<sup>86,87</sup> but no valid explanation has been given. This will be the subject of chapter 6 and 7, where the influence of temperature gradients is examined. As stated, the background pattern does not seem to change due to the plasma-target interaction, nor do the non-zero diagonal elements and the off-diagonal elements  $\{2, 3\}$  and  $\{3, 2\}$ . The only change is induced by the deposition of charge and the resulting electric field, which creates a small additional pattern in the center of the images.

The elements of the Mueller matrices containing a stationary background pattern are not anti-symmetrical, see e.g.  $\{2, 4\} \neq -\{4, 2\}$ . This is an indication that the underlying optical properties are entangled within the Mueller matrix. This

<sup>82</sup>O GUAITELLA and A SOBOTA *J. Phys. D. Appl. Phys.* 2015 **48**: 255202

means that a decomposition of the original Mueller matrix has to be performed in order to retrieve them, as was shown in the previous chapter. The logarithmic decomposition is applied to separate the individual optical properties since they are a result from the accumulative path of the polarized light through the electro-optic material.

Figure 4.3 shows the logarithmically decomposed  $L_m$  matrices before and after impact using the Mueller matrices that were measured at  $t_d = 1 \mu\text{s}$  (top matrix) and  $t_d = 8 \mu\text{s}$  relative to the start of the positive half period of the applied sine wave. Only the diattenuation and birefringent properties are shown, leaving empty diagonal elements (see the introduction given in section 2.3.2). The depolarization properties are separated and shown in the  $L_u$  matrices in figure 4.4, which also contains the uncertainty images of the diattenuation and birefringent properties.

Naturally, the  $L_m$  matrices before and after impact share great similarities with the measured Mueller matrices, but also some differences are observed. The stationary background patterns are still present, but elements  $\{2, 4\}$  and  $\{4, 2\}$  are now anti-symmetric and relate to the linear birefringence in the diagonal coordinate system, i.e.  $\Gamma_{45/135}$ . Also the elements  $\{3, 4\}$  and  $\{4, 3\}$  are anti-symmetric and represent  $\Gamma_{0/90}$ . After impact, the induced internal anisotropy due to electric fields generated externally by surface charges change the  $\Gamma_{0/90}$  pattern.

The diattenuation properties, shown in the first column and top row, remain close to zero during the plasma interaction, i.e smaller than  $0.02 \pm 0.01$  rad. The circular retardance / birefringence  $\Gamma_{l/r}$  is non-zero but not influenced by the surface charges, as indicated by the anti-symmetrical constant patterns shown by elements  $\{2, 3\}$  and  $\{3, 2\}$  with an average value of  $0.72 \pm 0.11$  rad. The uncertainty of each optical property is obtained from the corresponding element in the  $L_u$  matrices.

The  $L_u$  matrix contains the depolarization properties, shown in the diagonal elements, and the uncertainty of the diattenuation and birefringent properties, shown in the off-diagonal elements. The three depolarization (diagonal) elements are smaller than  $-0.05$  rad. The uncertainties for the other optical properties remain small as well. The largest uncertainty is observed for  $\Gamma_{l/r}$  in element  $\{2, 3\}$  and  $\{3, 2\}$ .

The electric field induced by surface charges deposited during the plasma-target interaction can easily be examined using the linear birefringent patterns since time-resolved imaging is performed before and after impact. Simple subtraction of the birefringent patterns obtained before and after impact removes the stationary *background* patterns and allows examination of the electric field, according to equation (3.29). For this purpose, first  $\Gamma_{tot}$  is calculated by quadratically adding  $\Gamma_{0/90}$  and  $\Gamma_{45/135}$  and taking the square root.

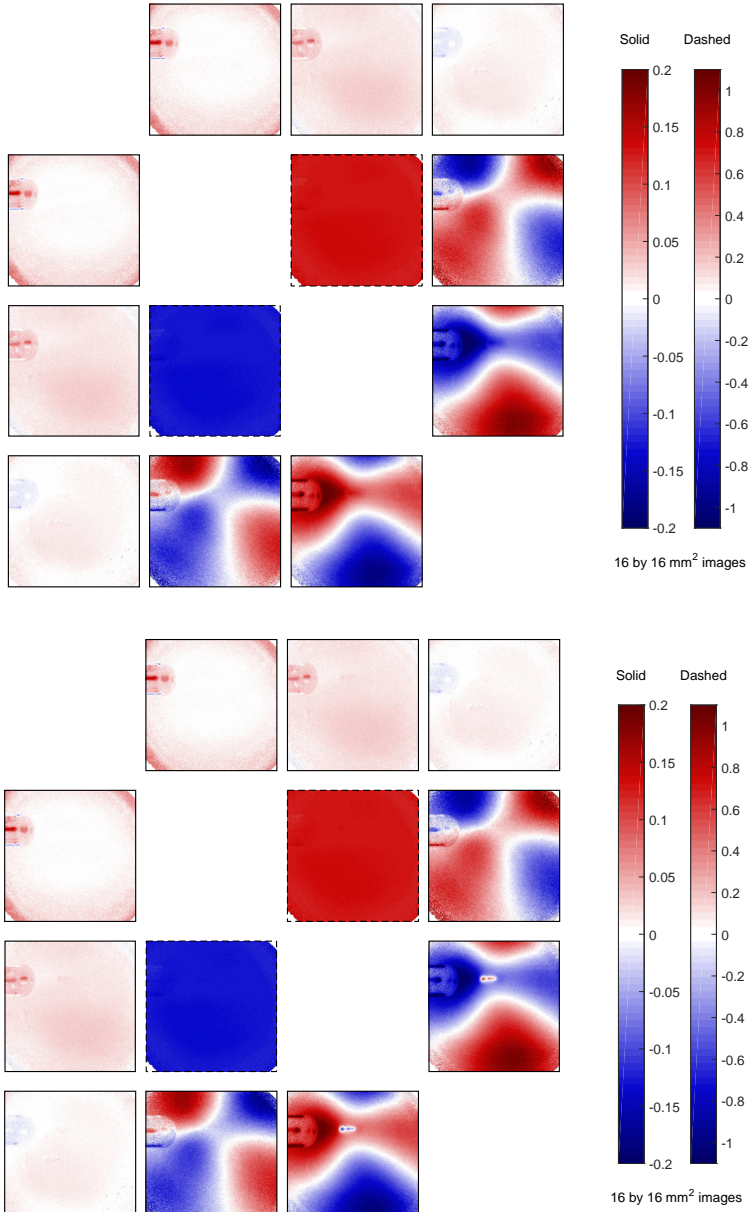


Figure 4.3: Logarithmically decomposed matrices  $L_m$  for the electro-optic BSO under exposure of the AC-driven plasma jet, shown before charge deposition has occurred ( $t_d = 1 \mu\text{s}$ ) in the top matrix and after impact ( $t_d = 8.0 \mu\text{s}$ ) in the bottom matrix. The individual elements represent diattenuation, which are close to zero value in these measurements, and birefringent properties (non-zero) as introduced in section 2.3.2. Similar as for the shown Mueller matrices the border of the  $16 \times 16 \text{ mm}^2$  images indicates which colorscale is applied.

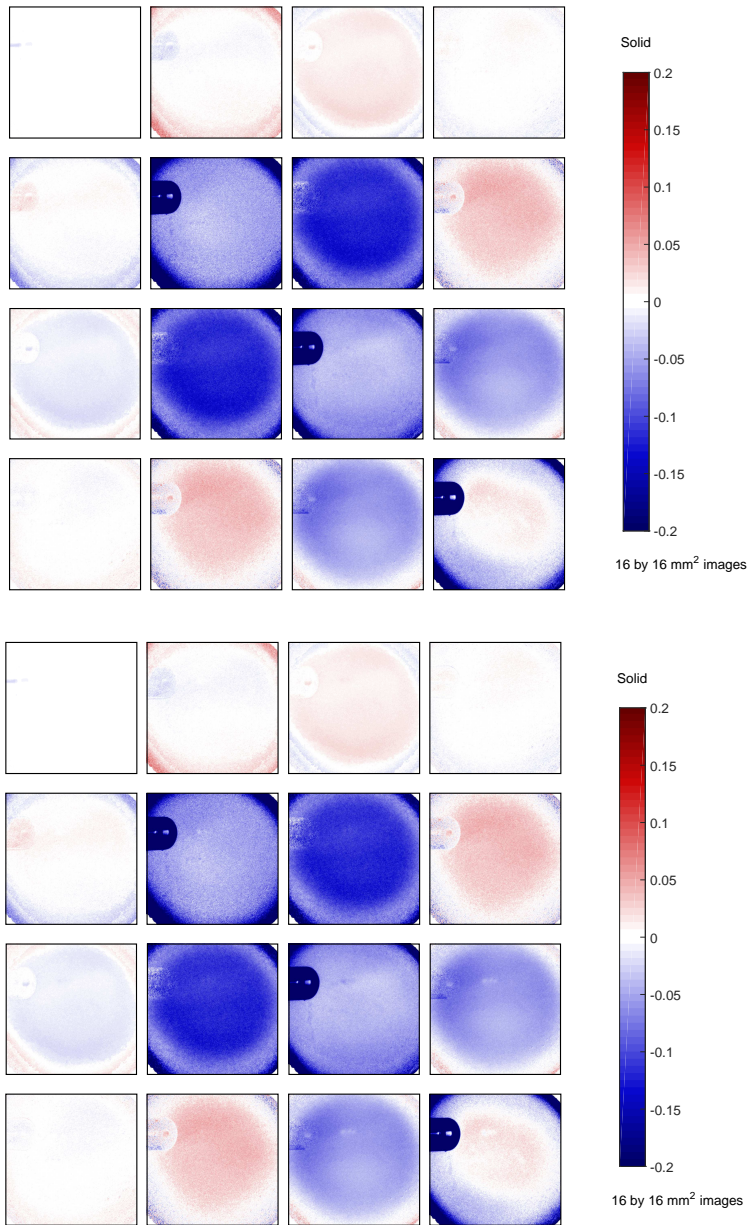


Figure 4.4: Logarithmically decomposed matrices  $L_u$  for the electro-optic BSO under exposure of the AC-driven plasma jet, shown before and after impact of the ionization waves, respectively in the top and bottom matrix. The diagonal elements represent the depolarization properties, while the off-diagonal elements are related to the uncertainties of the optical property elements of the  $L_m$  matrix.

$$|E_z| = \frac{\Gamma_{tot}}{\frac{2\pi d}{\lambda} n_o^3 r_{41}} \quad (3.29 \text{ revisited})$$

The obtained electric field pattern will be shown later in section 4.4. This approach to examine the electro-optic BSO material under normal incidence allows for the imaging of the axial electric field patterns. The axial field pattern relates to the location of the charge deposition and therefore is key to understand the surface dynamics. However, a complete view is only obtained when all electric field components are examined including the radial components. This requires a different approach which is shown in the next section.

### 4.3 Measuring Radial Electric Fields

The main reason why BSO can only be used to study the axial electric field components when it is examined under normal incidence is because of its symmetry point group. The relation as it is derived in the previous chapter follows the intersection of the plane wave and the index ellipsoid. The index ellipsoid is perturbed under external influence by the addition of induced anisotropies  $\Delta\eta_i$ . The relation between the anisotropies and the external influence, i.e. electric field, is determined by the electro-optic tensor. This is dependent only on the symmetry point group of the sample which, at normal incidence, restricts BSO from being able to show any relation to the radial electric field components.

Two things can be done to be able to detect the radial electric field components. The first option is to change the intersecting ellipse to change the relation between the birefringence and the induced anisotropies. This can be done by examining the sample at an oblique angle of incidence with respect to its surface. The second option is to use a different material with another symmetry point group to still allow the examination of the sample to be done at normal incidence. This second option will be exploited first, while measurements at an inclined angle are investigated in the next chapter.

#### 4.3.1 Electro-Optic Fe:LiNbO<sub>3</sub>

As stated, the final relation between the experienced birefringence and the externally induced electric field is greatly dependent upon the symmetry point group of the material. To be able to measure the radial electric field component a different material point group than the cubic 23 of BSO has to be used. For this purpose Fe:LiNbO<sub>3</sub> (“iron-doped lithium niobate”, but named *Felinbo* throughout this work) is chosen, which is a material with trigonal 3m symmetry.

In the past Felinbo has been used mostly for holographic storage of informa-

tion<sup>126–128</sup> due to the photorefractive properties it possesses.<sup>129</sup> The properties have been investigated for different crystal compositions and dopant levels to lithium niobate.<sup>130,131</sup>

The Felinbo material will be examined in a similar way as was done with the BSO, meaning the polarized light passes through at normal incidence. As a result, the normal incidence ellipse that determines the birefringent properties remains the same as was derived in chapter 3, see equation (3.5).

$$x^2 \left( \frac{1}{n_o^2} + \Delta\eta_1 \right) + y^2 \left( \frac{1}{n_o^2} + \Delta\eta_2 \right) + 2xy\Delta\eta_6 = 1. \quad (3.5 \text{ revisited})$$

The quantities that change since a different material is chosen are the externally induced anisotropies  $\Delta\eta_i$ . They are coupled to the electric field using the electro-optic tensor, shown for Felinbo in equation (4.1).<sup>40</sup>

$$\begin{pmatrix} \Delta\eta_1 \\ \Delta\eta_2 \\ \Delta\eta_3 \\ \Delta\eta_4 \\ \Delta\eta_5 \\ \Delta\eta_6 \end{pmatrix} = \bar{T} \cdot \begin{pmatrix} E_x \\ E_y \\ E_z \end{pmatrix} = \begin{pmatrix} r_{11} & 0 & r_{13} \\ -r_{11} & 0 & r_{13} \\ 0 & 0 & r_{33} \\ 0 & r_{42} & 0 \\ r_{42} & 0 & 0 \\ 0 & -r_{11} & 0 \end{pmatrix} \cdot \begin{pmatrix} E_x \\ E_y \\ E_z \end{pmatrix} = \begin{pmatrix} r_{11}E_x + r_{13}E_z \\ -r_{11}E_x + r_{13}E_z \\ r_{33}E_z \\ r_{42}E_y \\ r_{42}E_x \\ -r_{11}E_y \end{pmatrix} \quad (4.1)$$

The added  $\Delta\eta_i$  terms are changed since the electro-optic tensor  $\bar{T}$  is different compared to the one of BSO. The final relations between the birefringent properties in the different coordinate systems ( $\Gamma_{0/90}$  and  $\Gamma_{45/135}$ ) and the electric field components are derived by examining the respective axes of the normal incidence ellipse. After substitution of equation (4.1), the following relations are obtained:

$$\begin{cases} \Gamma_{0/90} = \frac{2\pi d}{\lambda} n_o^3 r_{11} E_x \\ \Gamma_{45/135} = \frac{2\pi d}{\lambda} n_o^3 r_{11} E_y \end{cases} \quad (4.2)$$

The retardance obtained in the diagonal system scales with the vertical axial  $E_y$  component, while the horizontal axial  $E_x$  component determines the retardance obtained in the 0/90 deg optical system. The only relevant electro-optic constant

<sup>126</sup>F. H. MOK *Opt. Lett.* 1993 **18**: 915–917

<sup>127</sup>G. W. BURR and D. PSALTIS *Opt. Lett.* 1996 **21**: 893–895

<sup>128</sup>X. AN et al. *Appl. Opt.* 1999 **38**: 386–393

<sup>129</sup>Y FURUKAWA et al. *Opt. Lett.* 1997 **22**: 501–503

<sup>130</sup>C. YANG et al. *Opt. Commun.* 2000 **175**: 247–252

<sup>131</sup>Z. XU et al. *J. Cryst. Growth* 2005 **280**: 227–233

<sup>40</sup>C. MALGRANGE et al. 2014 ISBN: 978-94-017-8992-9

in these relations is  $r_{11}$  which is  $6.8 \cdot 10^{-12}$  m/V. This is provided by the same manufacturer as the examined BSO materials (© MolTech GmbH Berlin). It has been shown that the electro-optic properties of Felinbo depend on the composition,<sup>132</sup> therefore it is best to rely on the manufacturer of the crystals for the value of the electro-optic constants since they have controlled the dopant levels. A calibration of the  $25 \times 25 \times 0.5$  mm<sup>3</sup> crystals is difficult since constant homogeneous radial electric field should be applied. The *ordinary* index of refraction  $n_o$  of Felinbo is equal to 2.29. Felinbo is a biaxial crystal, meaning an *extraordinary* axis is present with index of refraction  $n_z \neq n_x = n_y$  equal to 2.20. It is important to notice that the derivation is done assuming that a *z-cut* crystal is used. This means the extraordinary axis is parallel to the axis of propagation of the light. Consequently, the oscillations of the light only depend on the *x* and *y*-axis, which are the same without external influence. Equation (4.2) changes when a *x* or *y*-cut crystal is used.

### 4.3.2 Measurement Example using Felinbo

Felinbo is examined using imaging Mueller Polarimetry under continuous exposure of guided ionization waves generated by the plasma jet in a similar way as was done for BSO in section 4.2.2. The material is examined under normal incidence while the plasma jet is oriented horizontally at a 45 degree impact angle with a 7 mm gap between the end of the capillary and the target. A 1 slm helium flow is used while the plasma jet operates using the 2.0 kV sine waves with a frequency of 30 kHz.

Even though the plasma jet is operated in the same way as in section 4.2.2, the examined interaction could be altered since a different target is used. The importance of the target's dielectric constant (relative permittivity) has been stressed in numerical work<sup>79</sup> and both BSO and Felinbo have a relatively high constant, respectively 56 for BSO and 85 ( $\epsilon_{11}$ ) and 30 ( $\epsilon_{33}$ ) for Felinbo. Imaging of the ionization wave propagation and the characteristics of the voltage-current waveforms show similar plasma propagation for both the different targets, closely related to when a glass target is used. Additionally, the targets are always polished to have no surface roughness effects. The potential merits of using Felinbo, to obtain the unknown radial electric field patterns that have never been measured before, outweigh the possible alteration of the interaction. Both materials are therefore used and the final field patterns will be compared *a posteriori* in section 4.4.

The obtained Mueller matrices for Felinbo under exposure of the AC plasma jet are shown in figure 4.5, while the logarithmically decomposed matrices  $L_m$  and  $L_u$  are shown in figures 4.6 and 4.7. Again two matrices are shown in each figure representing the optical state before and after the impact of the ionization wave,

<sup>132</sup>K CHAH et al. *Opt. Commun.* 2000 **176**: 261–265

<sup>79</sup>S. A. NORBERG et al. *J. Appl. Phys.* 2015 **118**: 013301

by setting the time delay  $t_d$  relative to the start of the positive half period of the sine wave. The first (top)  $4 \times 4$  imaging matrix shows the state of the material before impact, hence without the influence of electric field, measured at  $t_d = 1 \mu\text{s}$ . The second (bottom) imaging matrix shows the material after the impact of discharge which has caused deposition of surface charge, hence includes the effect of electric field, measured at  $t_d = 8 \mu\text{s}$ .

Diattenuation properties are again not present since the material is still examined at normal incidence. This is observed in all matrices by images with values close to zero for the top row  $\{2 - 4, 1\}$  and first column  $\{1, 2 - 4\}$ . Felinbo does not have any circular retardance, unlike BSO, since there is no optical activity (optical rotatory power). Hence elements  $\{2, 3\}$  and  $\{3, 2\}$  are close to zero as well. The only optical properties that are included are the linear retardances in both optical systems. Since these are the only observed optical properties, there is not much information entangled. This means that the Mueller matrices are already (anti) symmetric and very similar to the logarithmically decomposed  $L_m$  matrices. Consequently, the elements of the imaging  $L_u$  matrices are all close to zero.

The linear birefringent patterns, shown by elements  $\{2 - 3, 4\}$  and  $\{4, 2 - 3\}$ , change slightly due to the impact of the ionization waves. A stationary background pattern is observed before and after impact but an additional pattern is present due to the deposition of surface charge and the generated electric field.

The background patterns show similarities with the stationary images observed within the optical properties of BSO, but they are not identical. Inhomogeneity of the iron doping in the material could play a role in this.<sup>133</sup> The background patterns can be simply disregarded from the investigation by subtraction since they are the same before and after impact, to focus solely on the change in birefringent patterns induced by the electric field.

The relations given by equation (4.2) can be used to transform the changes in the birefringent patterns to the electric fields that have caused them. This gives a complementary view of the total electric field patterns induced by the impact of the guided ionization waves, since  $E_z$  can be obtained using BSO and the examination of Felinbo allows for the imaging of  $E_x$  and  $E_y$ , as is shown in the next section.

## 4.4 Electric Field Patterns

### 4.4.1 AC Plasma Jet

The electric field patterns obtained from the change in the birefringent patterns of BSO and Felinbo during a plasma surface interaction are shown in figure 4.8. All the individual components of the electric field are obtained separately, using the examination of both BSO and Felinbo that are subjected to a plasma exposure in

<sup>133</sup>F. JERMANN et al. *J. Opt. Soc. Am. B* 1995 **12**: 2066–2070

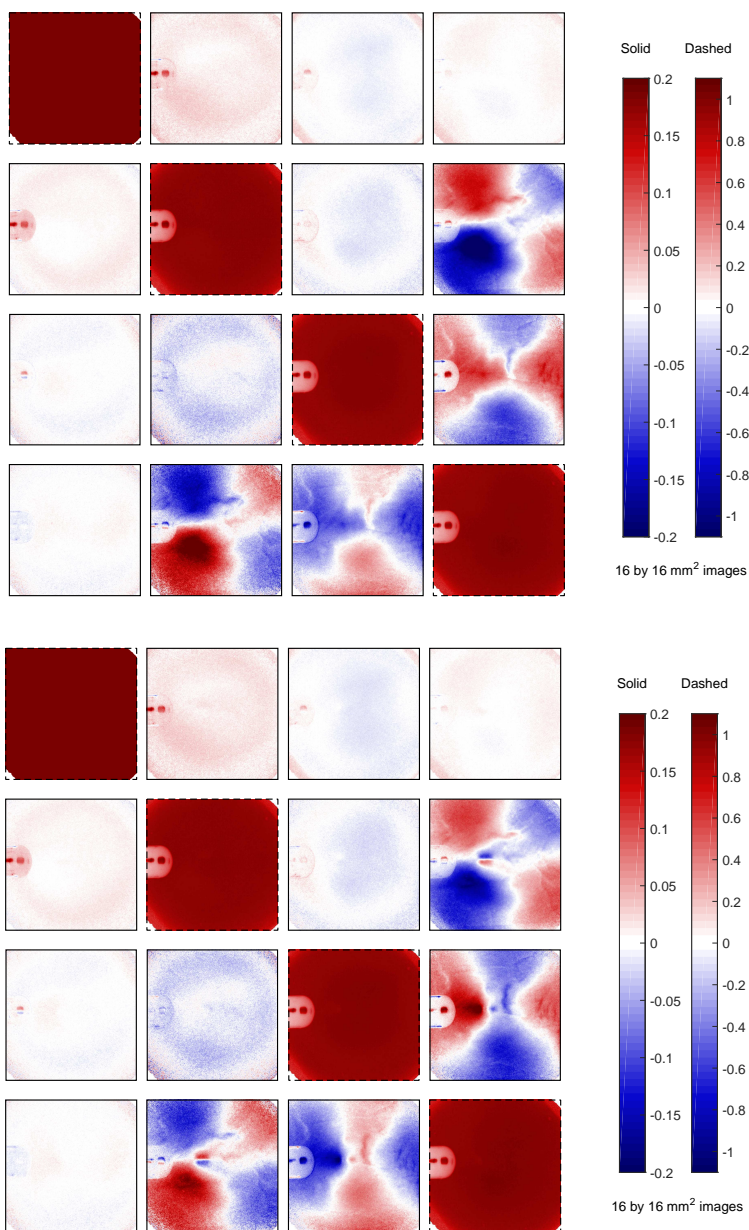


Figure 4.5: The obtained Mueller matrices ( $16 \times 16 \text{ mm}^2$  images) of the electro-optic Felinbo examined under normal incidence under exposure of guided ionization waves produced using a plasma jet driven by 30 kHz AC sine waves with 2.0 kV amplitude at 1 slm helium, shown before (top matrix,  $t_d = 1 \mu s$ ) and after (bottom matrix,  $t_d = 8.0 \mu s$ ) impact of the ionization waves. The colorscale is indicated by the border of the images.

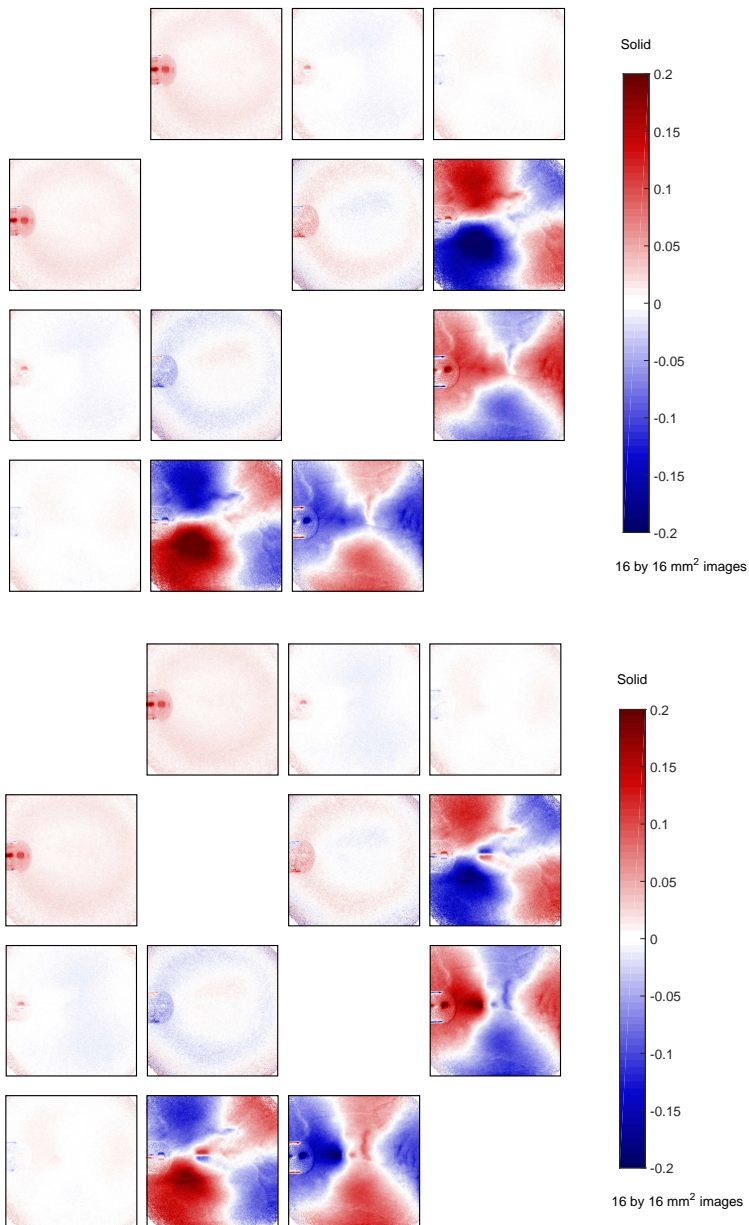


Figure 4.6: Logarithmically decomposed matrices  $L_m$  of the electro-optic Felinbo under exposure of the AC-driven plasma jet, shown before (top) and after (bottom) impact of the ionization waves. Same remarks hold as with the previous figures of  $L_m$ , which only includes the diattenuation and birefringent properties.

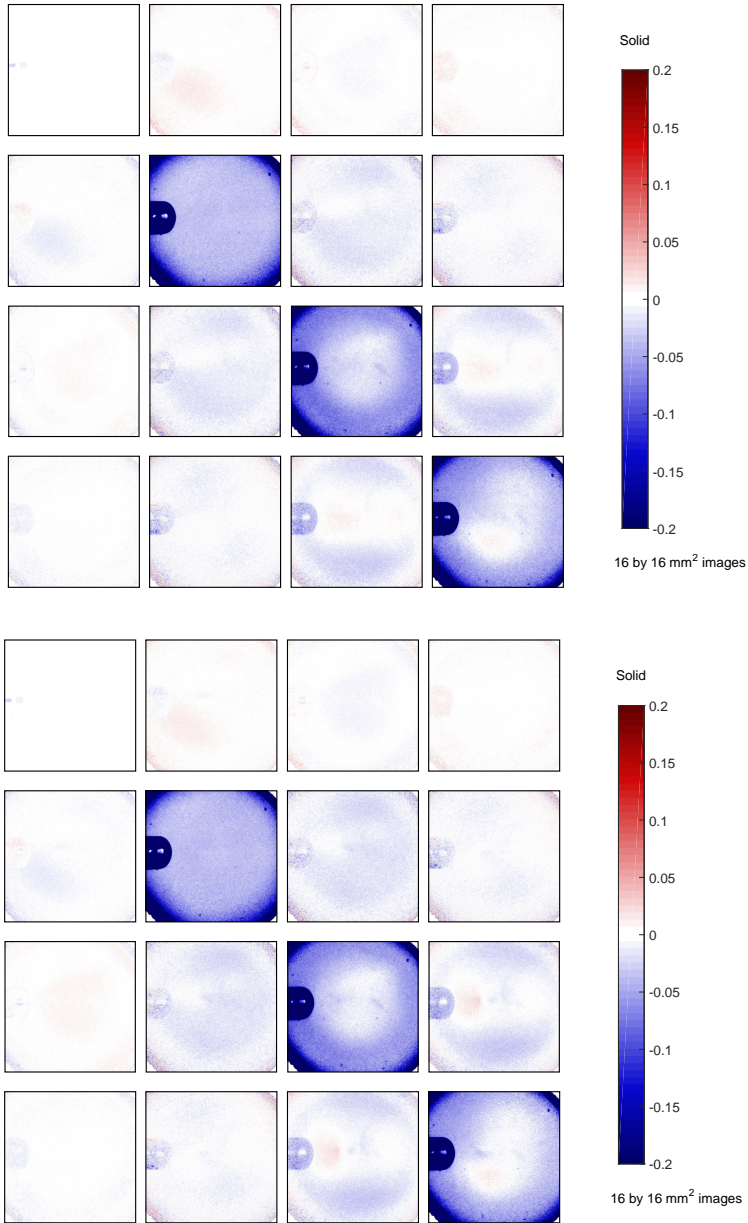


Figure 4.7: Logarithmically decomposed matrices  $L_u$  of the electro-optic Felinbo under exposure of the AC-driven plasma jet, shown before (top) and after impact (bottom). The diagonal elements represent the depolarization properties, while the off-diagonal elements relate to the uncertainty of the diattenuation and birefringent properties.

similar conditions, as described in previous sections. Equations (3.29) and (4.2) are used to calculate the electric field patterns from the measured birefringent patterns. The (total) radial electric field pattern  $E_r$  is obtained from  $E_x$  and  $E_y$ .

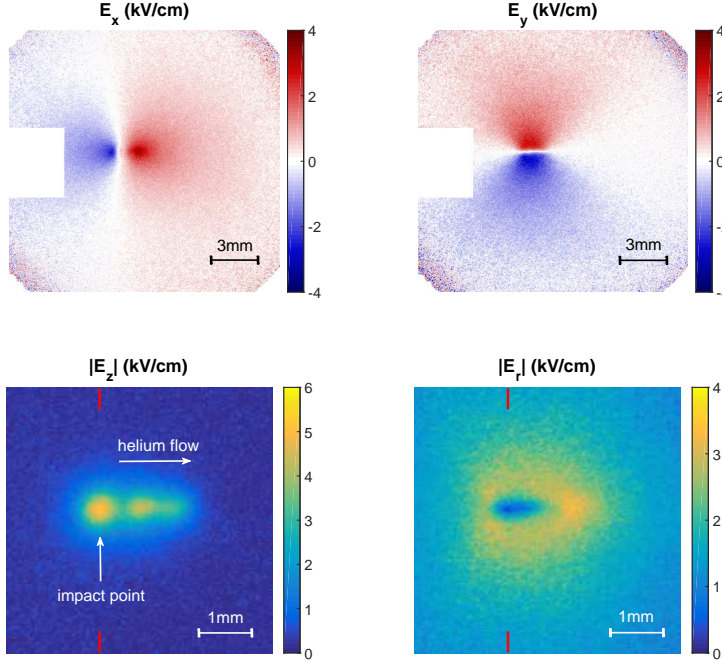


Figure 4.8: The axial  $E_x$  and  $E_y$  electric field components (top images, with the end of the capillary in white), obtained using the change in the birefringent patterns in the two coordinate systems induced by charge deposition during the plasma surface interaction with Felinbo. The resulting absolute radial electric field  $|E_r|$  is shown as well, together with the axial  $|E_z|$  field obtained from the examination of BSO under plasma exposure in similar conditions, namely a 1 slm helium flow and 30 kHz sine waves with 2.0 kV voltage amplitude. The capillary is located on the left hand side at a 45 degree impact angle 7 mm away from the surface. The electric field patterns are an average throughout the 0.5 mm thickness of the targeted samples. Red lines indicate the location of the vertical cross-sections that are taken and shown in figure 4.9.

The difference between the axial  $E_z$  and radial  $E_r$  profile of the induced electric field is clearly visible. The axial field is highest at the center of the charge deposition, while the radial field has the maximum at the edges of the impact region. A *tail* structure is present behind the impact point in the direction of the helium flow towards the right side. This means a surface discharge has propagated on the material after the ionization wave has impacted. An estimation of the uncertainty

is obtained by examining the maximum level of noise around the axial pattern where the electric field is zero, resulting in an uncertainty of approximately  $\pm 0.23$  kV/cm.

The (axial) electric field decreases along the path of the surface discharge indicating that the charge deposition is diminishing along the discharge propagation on the dielectric. The pattern and values of the axial electric field matches with previous measurements done using the simpler S enarmont setup.<sup>86</sup>

The axial electric field indicates the location of the charge deposition, which matches with the light emission from the impacting ionization waves at the target. Positive charges are deposited that are removed when the polarity of the applied potential changes. The polarity of the deposited charge is obtained from the sign of the induced changes for the measured retardance. The light emission pattern of the discharge at the surface changes when the plasma jet is interacting with the surface in a different manner, for instance when changing the impact angle.<sup>82</sup>

The radial fields induced *inside* a targeted material under exposure of impacting guided ionization waves have never been measured before. The maximum values indicate the contour of the area where the surface charge has been deposited, which by eye fits reasonably well with the pattern shown for the axial electric field. This is highlighted in figure 4.9, where the vertical cross section lines are shown going through the impact point (indicated in figure 4.8 with red lines). The decrease in the radial field (red curve) matches almost perfectly with the rise of the axial field (blue curve). This indicates that although slightly different targets are used in terms of dielectric constants, the surface deposition that are causing the fields should be fairly similar in both cases.

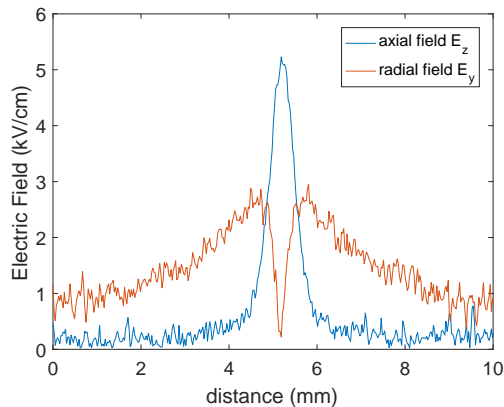


Figure 4.9: The electric field (axial  $E_z$  and radial  $E_y$ ) along a vertical cross-section going through the impact point of the patterns shown in figure 4.8, indicated by the area where  $E_z$  is maximal.

Furthermore, what figure 4.9 shows is that the maximum axial field values are higher in amplitude, i.e. 5.2 kV/cm, while the radial field patterns spread over a further distance. Axial electric fields are only generated in the vicinity of the surface charges and hence are related to the local surface charge density. The radial fields are a consequence of all the contributions of the deposited charges, hence scale more with the total charge deposition.

The field patterns are an accumulated result due to the propagation of the polarized light through the material. Hence, electric field patterns and values obtained through the exploitation of the Pockels effect are always an average throughout the thickness of the sample (0.5 mm). Both the axial and radial electric field patterns indicate that a surface charging has taken place by the impact of the ionization waves around an area of approximately  $2 \times 0.5 \text{ mm}^2$ . The electric field values are expected to be non-homogeneous throughout the thickness since the thickness of the crystals is 0.5 mm. This complicates the analysis to examine the amount and distribution of the surface charge  $\sigma$  that has been deposited during the interaction.

As indicated in the introduction, the exploitation of the Pockels effect (of BSO) has been used for a limited amount of plasma surface interactions in the past, which reported on either the electric field values<sup>72,86,87</sup> or the surface charge distributions.<sup>65,71,84,88,89</sup> The latter was done by applying a homogeneous field approximation in which the (average) electric field obtained via exploitation of the Pockels effect was linearly coupled to the local surface charge value. Resultingly, images of the electric field (which are unreported in those works) are transformed linearly to spatial images of  $\sigma$ . Although spatial information of  $\sigma$  deposited during the plasma interaction has great relevance for both the understanding of the plasma propagation and treatment of surfaces, it has been decided in this work not to follow this approach due to two main reasons.

Firstly, the plasma-target interaction at atmospheric pressure will almost always take place at relatively small spatial scales ( $\sim$ mm). As a result, the electric field generated inside the dielectric material will not be constant in the axial direction meaning that the average electric field will be lower than at the surface. When this field is (falsely) considered as homogeneous and used to calculate  $\sigma$ , these values will be underestimated. Additionally, the profile of the  $\sigma$  distribution will not be retrieved accurately due to the averaging of the electric field throughout the thickness which *smooths out* the surface charge distribution to an unknown degree.

This has already been discussed and shown in a previous work<sup>87</sup> where a procedure has been proposed to compensate for the underestimation of the amount of deposited charge. The smoothed shape of  $\sigma$  is more difficult to compensate for, so it was proposed to focus on the total deposited charge  $Q$  rather than the charge

density  $\sigma$ . A different approach is given by<sup>121,134</sup>. The compensation procedure is based upon a lookup table in which the amount of compensation for the average electric field or total charge is listed as a function of discharge size relative to the thickness of the crystals. This table has been made by calculating the (inhomogeneous) electric field inside a dielectric with a homogeneous elliptical surface charge distribution on one side. This calculation is only based on charge proximity and does not include alteration / redistribution of the potential lines (determining the electric field) since an interface is present between air (low permittivity) and BSO (high permittivity).

This relates to the second reason why in this work the reported electric fields are not used to show values or distributions of  $\sigma$ . Even in cases where the homogeneous field approximation would be applicable, i.e. large areas of plasma interactions or relatively thin targeted materials, the relation between  $\sigma$  and the obtained electric field is not straightforward. This is because intrinsically the electric fields are determined by the redistribution of the potential lines, due to  $\sigma$  but also the location of the zero potential points (grounding of the system) and the interface between air (low permittivity) and BSO (high permittivity). In most experimental examinations the targeted material is at floating potential, but it can be grounded at the backside as well (not throughout this thesis). The locations of the local grounds of the experimental setup have to be considered carefully and ideally investigated analytically or numerically using the Poisson equation.

This has not been done in this work since the focus was primarily with the design of the new diagnostic method and exploration of the possibilities it gives for the investigation of plasma surface interactions (electric field, temperature and depolarization from complex targets). Follow-up research where this new diagnostic technique is applied in practice for a more detailed study on the amount and distribution of the deposited surface charge should investigate first how the convolution should be done from the (average) electric field patterns to  $\sigma$ . The ideal way to do this is to calibrate the electric field measurements for a known amount of deposited  $\sigma$  with an a priori known distribution. This cannot be achieved in a plasma environment, but an approach can be followed where a spatial charge distribution is deposited in a controlled way through a (high voltage) needle.<sup>135</sup>

It is the first time, to the best of our knowledge, that radial electric field patterns induced inside a target under plasma exposure have been examined, complementary to the axial field components. Even though two different materials are used (BSO and Felinbo) the vertical cross section shown in figure 4.9 shows remarkable similarities. The decrease in radial field in the center of the cross-section matches almost perfectly with the axial electric field profile. The maximum radial field occurs where both field profiles intersect, which indicates the edge of the area

<sup>121</sup>H. MU and G. ZHANG *Plasma Sci. Technol.* 2011 **13**: 645–650

<sup>134</sup>D. FAIRCLOTH and N. ALLEN *IEEE Trans. Dielectr. Electr. Insul.* 2003 **10**: 285–290

<sup>135</sup>C. W. J. BERENDSEN et al. *Soft Matter* 2013 **9**: 4900–4910

where charge deposition has occurred. It is important to have a total image of all the electric field components induced inside the target for the study of plasma surface interactions, for e.g. the examination of the conditions for surface propagation and reignition of the discharge.<sup>136</sup> Accurate values of the induced electric field in targeted materials are obtained, which is not only useful for applications like e.g. plasma actuators for flow control<sup>57,58</sup> and plasma catalysis,<sup>137</sup> but also plays a role for surface chemistry, e.g. transport in cells through electroporation<sup>138</sup> and growth of carbon nanotubes,<sup>139</sup> where for instance it is shown that the plasma-assisted growth of carbon nanotubes depends on the electric field present and even low range fields (0.1 - 10 kV/cm) change the dynamics that are involved.

Although the surface charging cannot be studied yet directly from the electric field patterns, analyses of the shape and values of the patterns and the differences between the axial and radial profiles allow already for an indirect examination of the charging. For this purpose, it is crucial to have all the individual components, both axial and radial, caused by the deposited surface charge during the plasma interaction. This will be shown in the next subsection where the environmental gas is examined. This is a parameter that influences the propagation of the ionization waves from the capillary towards the target. As a result, the interaction with the target is influenced as well as the charge deposition. By applying Mueller Polarimetry to visualize both the axial and radial electric field patterns due to the charge deposition, this can be investigated in a way which was not possible before.

#### 4.4.2 Influence of a Controlled Environment

Mueller polarimetry is applied to optically investigate BSO and Felinbo under exposure of the AC driven plasma jet in a controlled environment. There are no constraints a priori to apply Mueller polarimetry in any type of gas mixture. Only high temperatures and some damaging of the crystal induced by the plasma for some peculiar conditions (as will be discussed later) can limit its use. The resulting axial and radial electric field patterns can be used to examine the changes induced for the occurring interaction of the plasma with the surface when the surrounding gas of the environment is changed. The propagation of the ionization waves generated by the plasma jet depends on this due to the helium gas mixing with the environment.

Both the plasma jet and the targeted electro-optic materials are placed in a closed glass cell, for which the environment is controlled by applying a constant

---

<sup>136</sup>F. PECHEREAU and A. BOURDON *J. Phys. D. Appl. Phys.* 2014 **47**: 445206

<sup>57</sup>D. M. ORLOV et al. *AIAA J.* 2008 **46**: 3142–3148

<sup>58</sup>T. UNFER and J. P. BOEUF *J. Phys. D. Appl. Phys.* 2009 **42**: 194017

<sup>137</sup>E. C. NEYTS and K. M. BAL *Plasma Process. Polym.* 2017 **14**: 1–6

<sup>138</sup>M. YUSUPOV et al. *Biochim. Biophys. Acta - Gen. Subj.* 2017 **1861**: 839–847

<sup>139</sup>E. C. NEYTS et al. *J. Am. Chem. Soc.* 2012 **134**: 1256–1260

secondary (surrounding) gas flow of 1 slm of O<sub>2</sub>, N<sub>2</sub>, (dry) air or CO<sub>2</sub> with a 2.5% admixture of O<sub>2</sub>. By keeping the surrounding atmospheric flow constant, no significant differences are expected between the helium-in-environment gas flow mixing since density differences between helium and the varied surrounding gasses are similar. The helium flow of the plasma jet and the AC voltage amplitude are varied for each environment which is examined. A different capillary tube of the plasma jet is used, with an inner diameter of 2.0 mm instead of 2.5 mm (outer diameter remains 4.0 mm). The distance between the end of the capillary and the target remains 7 mm and the impact angle is again 45 degrees.

The electric field patterns are obtained in a similar way as was done for the results shown in figure 4.8. The Mueller matrix is measured before and after impact by setting the acquisition delay relative to the trigger signal relating to the start of the positive half period. The Mueller matrices are analyzed with the logarithmic decomposition and the differences in the obtained linear retardances are used to calculate the electric field patterns according to equation 3.29 for the axial field (BSO) and equation 4.2 for the radial field (Felinbo).

First, measurements are performed in a dry air environment. Figure 4.10 shows the axial (top) and radial (bottom) electric field patterns obtained while the voltage amplitude and the helium flow of the plasma jet are varied. The obtained patterns show great similarities with figure 4.8, even though a thicker capillary is used and the environment is controlled dry air rather than open “room” air. This suggests that the humidity of the open air and the gas flow dynamics of the environment in the controlled glass cell are not very influential for the plasma surface interaction in terms of the electric field patterns that are induced.

The axial field patterns show a clear division between the impact point and the so-called *tail* (surface discharge behind the impact point), but this is not the case for the radial patterns. For all the varied voltages and flows, the radial field patterns are elliptically shaped around the region of charge deposition. In the center of the charge deposition, the radial field is expected to be zero, due to symmetry, while the maximum lies at the edge of the charge deposited area. This is because the radial patterns depend on the charge contributions of the entire distribution, while the axial field depends more strongly on the local surface charge value.

The plasma surface interaction that occurs changes as a function of voltage amplitude and helium gas flow. This is examined by analyzing the shape and values of both the axial and radial electric field patterns that have been measured. First, the dependence with helium gas flow is discussed.

When the helium flow is increased, it is clearly visible from the shape of the electric field patterns that the surface discharge becomes longer. This means that the ionization wave was able to propagate further along the surface. The patterns increase in length from approximately 1.5 mm to 3.0 mm as the helium flow is varied from 700 to 1500 sccm.

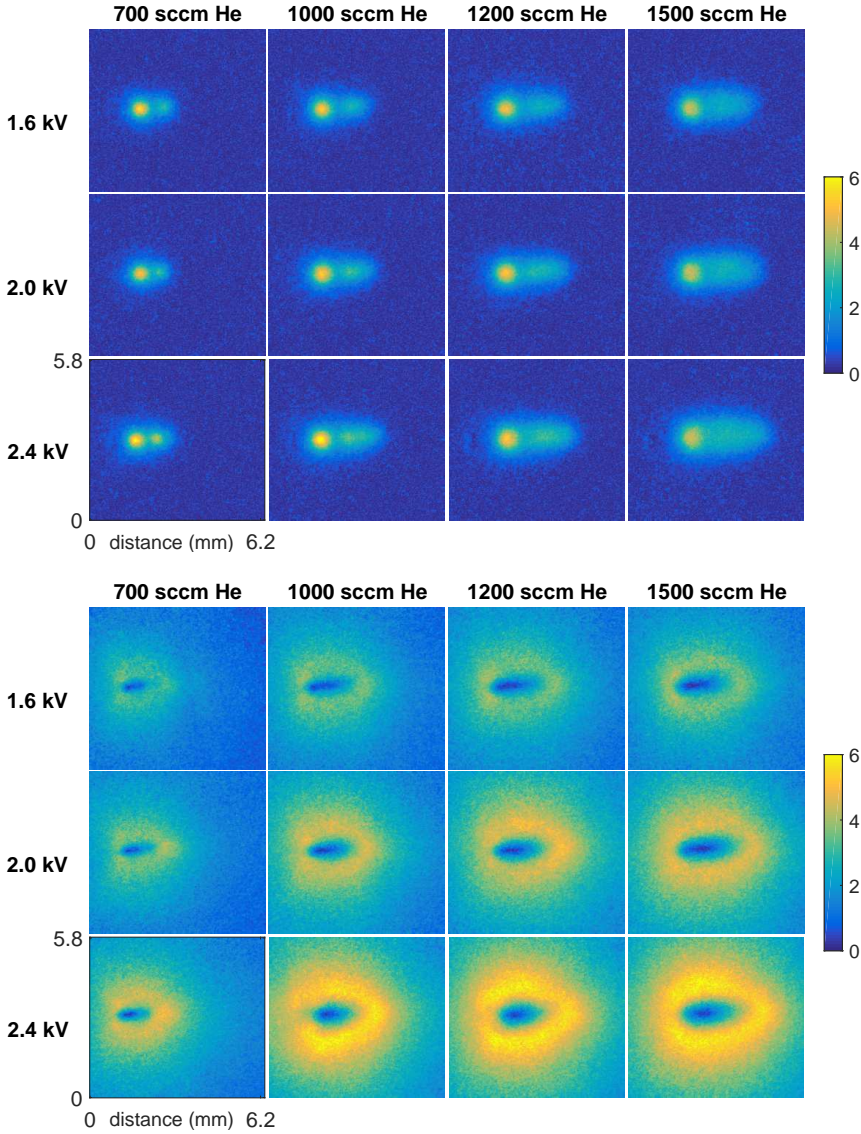


Figure 4.10: The axial (top) and radial (bottom) electric field patterns (kV/cm) induced inside electro-optic targets (BSO and Felinbo) under exposure of the AC driven plasma jet in a controlled dry air environment by the temporal deposition of surface charge. The plasma jet is located on the left-hand side at a 45 degree impact angle at 7 mm distance from the targeted surface. The voltage amplitude of the applied 30 kHz sine waves is varied, together with the amount of helium flowing through the capillary of the jet into the (controlled dry air) environment.

The ionization waves are able to travel further on the surface for higher helium flows due to the changed helium-in-air mixing, which results in higher helium densities and lower oxygen and nitrogen densities at the surface. This makes it easier for the ionization wave to propagate since charge losses due to e.g. electron attachment and vibrational / rotation excitation of (nitrogen and oxygen) molecules have decreased. This has been shown as well in a previous work without a controlled environment<sup>87</sup> where the simpler Sénarmont setup has been used to examine only BSO under plasma exposure (axial fields).

Since the ionization wave is able to travel further for higher helium gas flows the area where the plasma is interacting with the surface also increases. This explains why the radial electric field patterns increase in value (additionally to the increase in length / shape) since the total area has grown where the charge has been deposited. The local charge density, however, has decreased. This is suggested since it is observed that the maximum axial electric field values (in the impact point) decrease to approximately  $4.5 \pm 0.3$  kV/cm for higher helium flows.

Changes in the maximum induced values of the axial and radial fields are better observed when the vertical cross-sections through the impact point are taken, as shown in figure 4.11.

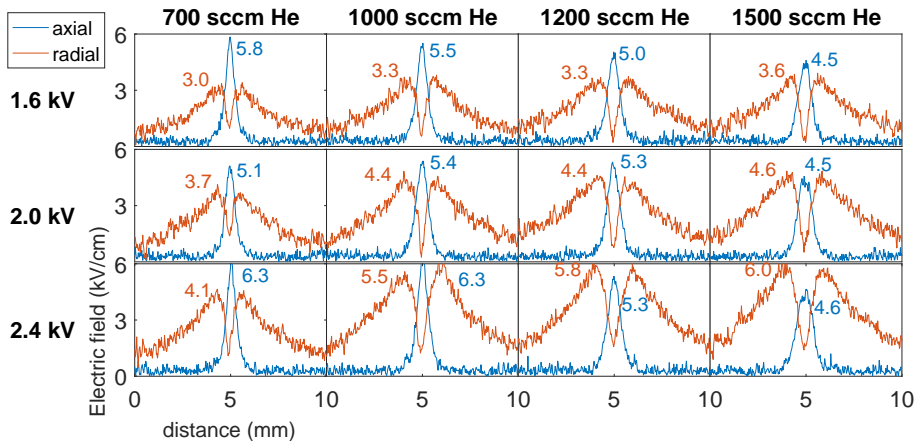


Figure 4.11: The vertical cross-section lines of the axial (blue) and radial (red) electric field going through the impact point for the electric field patterns obtained in dry air shown in figure 4.10. The maximum values of the radial and axial fields are denoted, with an estimated uncertainty of 0.3 kV/cm.

Two hypothesis can be formulated explaining the decrease of local surface charge density for higher helium gas flows.

Firstly, it can be argued that the ionization waves propagate in an energy efficient way. This suggests that with higher helium densities (and fewer energetic losses due to air entrainment) the ionization waves propagate with a lower vol-

ume charge density and lower electric field in the head of the ionization wave. This is supported in literature where it is shown that the ionization wave in the gas phase becomes wider with higher helium flows, which lowers the peak electric field measured with Stark spectroscopy.<sup>66</sup> As a result, the flux of charged species to the surface during the interaction with the target is lower since the charge density in the gas phase is lower. This means that the local surface charge density decreases as well.

However, it can also be argued that when there are fewer energetic losses due to the changed gas mixing that the ionization wave will travel faster, meaning the local interaction time with the surface decreases and there is less surface deposition because the ionization wave simply traveled further away more quickly.

To examine these hypotheses more investigation has to be done, either on the ionization wave itself (by imaging or volume charge characterization) or higher time-resolved tracking on the charging of the targeted surface. Similar measurements as shown in this work can be done, with a higher time resolution (rather than solely before and after impact) to potentially learn about changes in surface fluxes towards the dielectric target.

Figure 4.10 also indicates that the plasma surface interaction depends on the applied voltage amplitude of the plasma jet.

The influence of voltage amplitude (varied from 1.6 kV to 2.4 kV) was part of the previously published result in an open environment as well<sup>87</sup> for the axial field pattern. It was demonstrated before that the influence of voltage amplitude is less significant than the influence of the helium gas flow and that is again shown here for a controlled dry air environment in figure 4.10 for the axial fields, where the voltage amplitude does not seem to change the axial patterns drastically, both in shape as in value.

On one hand, this can be related to the use of 30 kHz AC sine waves to power the plasma jet. Due to the relatively slow change of applied potential, the guided ionization waves are already initiated at a breakdown voltage, meaning that an increase of voltage after initiation could be less influential. This is most likely different when constant high voltage pulses are used with a fast rise time (50 ns) since then the ionization waves can be generated at an *over-voltage*. This will be examined in the next subsection.

However, on the other hand, the radial field patterns do show an influence on the applied voltage amplitude. The maximum radial field value increases with higher voltage amplitudes for given helium flows. It is possible that the surface interaction depends on the AC voltage amplitude even though the ionization wave has already been generated before the applied potential has reached these higher values since a conductive channel is present between the high voltage electrode and the ionization front. However since the axial induced electric fields are rather

---

<sup>66</sup>A. SOBOTA et al. *Plasma Sources Sci. Technol.* 2016 **25**: 065026

undisturbed, it is remarkable at first, how both can be true at the same time, assuming that a similar plasma surface interaction on both surfaces has taken place.

The radial field patterns depend more strongly on the total charge deposition, rather than the local surface charge density. This explains why the radial field values increase with higher applied voltages, although the axial fields indicate that the local surface charge does not change significantly. This means that the interaction area where charge deposition has occurred has increased since in total there is more charge deposition. Taking the case of a 1000 sccm helium flow, the length of the surface discharge increases from 2.0 to 2.7 mm when the voltage is increased from 1.6 to 2.4 kV, while the width increases from 0.9 to 1.1 mm. This means that the area has increased by a factor of 1.65 which corresponds well with the increase of radial amplitude from 3.3 to 5.5 kV/cm.

The change in length and width of the surface discharge is not very distinct within the axial electric field measurements, because the axial values at the edge of the discharge are rather small and the maximum values in the impact point do not depend on this. This is why it was suggested at first that the plasma surface interaction was unchanged by the voltage amplitude. It is only because the axial fields were determined that it was shown that the surface interactions did depend on the voltage amplitude since the interaction area was increased for higher applied voltages. This can be explained by an increase of input power, which either energizes the discharge through the conductive channel, making it possible to spread slightly further, or it causes heating of the gas which changes the helium density and consequently the helium-in-air mixing. Again, more investigation is needed to examine how the plasma surface interaction has changed due to the applied voltage, but with Mueller polarimetry it has been shown that the dependence exists with consequences for the targeted surface in terms of charge deposition and induced (radial) electric fields.

The behavior observed when varying the helium gas flow rate and the voltage amplitude as shown in figure 4.10 for dry air is comparable when those operating parameters are varied with different (environmental) gas surroundings, i.e. pure O<sub>2</sub>, N<sub>2</sub> or CO<sub>2</sub> with an admixture of 2.5 % O<sub>2</sub>. This is shown in figure 4.12 where the axial and radial patterns are shown for different controlled environments for either a 1.6 kV voltage AC amplitude with a 0.7 slm helium flow or a 2.4 kV amplitude when using a 1.5 slm helium flow. For all environments the electric field patterns become elongated when a higher helium flow is used and the radial field amplitudes increase with higher voltage amplitudes, pointing to more charge on the surface.

Even though the general changes induced by the varying helium flow and voltage amplitude are similar for different environments, the plasma surface interaction that has occurred is different. This is clearly visible when especially the axial

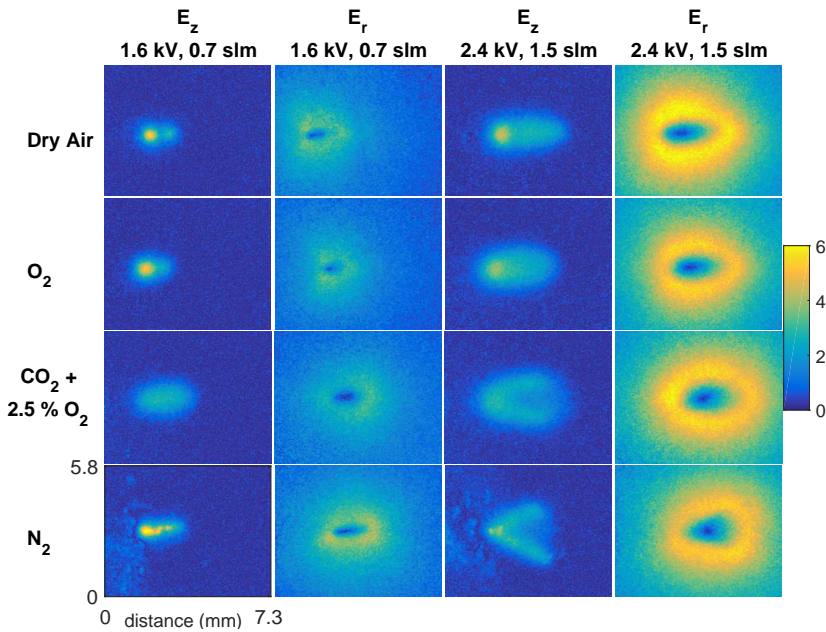


Figure 4.12: The axial and radial electric field patterns (kV/cm) induced inside the electro-optic targets, shown for different operating parameters (columns) of the plasma jet and environmental gas surroundings (rows) in which the ionization waves are travelling towards the targeted material.

field patterns are compared. The dry air and oxygen environments induce similar axial field patterns where a maximum field value is observed in the impact point and a clear distinct profile is seen for the *tail* behind the impact point in the direction of the helium flow. For the predominant  $\text{CO}_2$  and pure  $\text{N}_2$  environment there is no clear distinction present between the impact point and the surface discharge following behind it, but both show great differences as well.

The predominant  $\text{CO}_2$  environment causes a homogeneous axial electric field in the area where charge is deposited, with values lower than observed in dry air or  $\text{O}_2$ . The  $\text{N}_2$  environment shows patterns that indicate that a type of surface interaction has occurred which is more filamentary in nature, with higher local electric field values (axial) but smaller interaction areas. The measurements are acquired over several periods, meaning the observed branching structures are stable.

Comparing  $\text{O}_2$  and  $\text{N}_2$  can change many things but in particular the presence of negative ions or not. Negative ions can have relatively long lifetimes (comparable with tens of kHz periods) especially if adsorbed.<sup>140</sup> Additionally, they can provide

<sup>140</sup>J.-S. OH et al. *J. Phys. D: Appl. Phys.* 2011 **44**: 365202

seed electrons through photo-deattachment along the main helium stream. This changes the generation, and thus the propagation, of the ionization wave.<sup>141</sup> With N<sub>2</sub> Penning ionization could play a role more on the edge of the helium/nitrogen mixing regions in the gas phase.<sup>142</sup> CO<sub>2</sub> has vibrational losses similar as N<sub>2</sub>, but can also produce negative ions.

For the N<sub>2</sub> environment the crystal was additionally optically blackened quite quickly during the measurements. This has occurred in air as well, but only when the material was exposed to the plasma jet on the same spot for long time scales (> 30 minutes), while in the N<sub>2</sub> environment this happens within the measurement time. This blackening causes errors in the measurement of the electric field, which is visible on the left side of the axial field patterns. The structures observed there (only present for pure N<sub>2</sub>) are caused by a blackening of the crystal and not due to surface charge induced electric fields.

The blackening happens as well for a pure CO<sub>2</sub> environment but with an admixture of 2.5% O<sub>2</sub> this is prevented. The same admixture has been tried for the nitrogen environment, which limited the blackening, but it also immediately reduced the characteristic filamentary surface behavior of the discharges (due to the addition of negative ions / electron detachment). The transition from filamentary to diffuse mode due to the addition of oxygen admixtures has been described in literature before.<sup>143</sup>

The radial field patterns show less differences between the distinct environments. This is again because they depend more on the total charge deposition rather than the local distribution of charge density. Elliptical shapes are seen for dry air, oxygen and CO<sub>2</sub>, while a more triangular shape is visible for the radial field in the nitrogen environment. This is caused by the appearance of two *branches* that are visible in the axial field pattern using 1.5 slm helium.

Even though the axial and radial field patterns cannot be used yet to construct the actual surface charge distribution, this subsection shows that already a lot of information can be gained about the trends in local charge densities or total charge deposition by analyzing the shape and relative amplitude of the obtained electric field patterns. The electric field patterns are not only useful for trends on surface charging but remain crucial for the surface processes that occur, as has been emphasized before. That is why it is important that the field values are accurately determined with a low uncertainty (< 0.5 kV/cm based on analysis of noise levels).

All of the patterns shown so far are induced by the impact of guided ionization waves generated by the AC driven plasma jet using 30 kHz sine waves with a certain voltage amplitude. With the AC driven voltage profile, the ionization waves are always generated at the breakdown point since a relatively slow change of

<sup>141</sup>N. L. ALLEN and A. A. R. HASHEM *J. Phys. D. Appl. Phys.* 2002 **35**: 2551–2557

<sup>142</sup>S. RAZAVIZADEH et al. *Plasma Sources Sci. Technol.* 2018 **27**: 075016

<sup>143</sup>K. V. KOZLOV et al. *J. Phys. D. Appl. Phys.* 2005 **38**: 518–529

potential is applied, minimizing the influence of the voltage amplitude. As stated, this probably changes when constant high voltage pulses are used with a fast rise time (50ns). This will be introduced in the next subsection (impacting at 45 degree) and further examined in the next chapter (impacting perpendicularly to the surface).

### 4.4.3 Time-Resolved Investigation of a Pulsed Plasma Jet in Air

The plasma jet can generate repetitive ionization waves with different applied voltage profiles, i.e. with AC sine waves and mono-polar pulsed voltages. For both operating modes a helium flow is necessary to create a gas mixing preferential for the generation of guided ionization waves.

The main differences induced by the operating voltage profile is the rise time of the applied potential. When the relative change of the high voltage potential is relatively slow (like with the 30 kHz AC sine waves) compared to the propagation dynamics of the ionization waves, they are generated at the minimum breakdown voltage. It has been shown in the previous section that the influence of the applied voltages changes the radial field amplitude more than the axial field patterns. When the relative change in high voltage potential is fast, like when applying constant high voltage pulses with a rise time of 50 ns, the ionization waves can be initiated with an over-voltage, compared to the minimum breakdown voltage.

Then, after the initiation, the potential at the high voltage electrode remains constant during the propagation of the ionization wave along the capillary tube and all the way to the targeted surface when using the constant pulses. The potential influences the plasma even when the ionization wave is moving away from it because of the conductive channel between the front of the ionization wave and the electrode. With the AC sine wave the potential at the high voltage electrode and the conductive channel varies in time. Therefore, the behavior of the ionization waves generated with the AC sine waves or with constant pulses could be significantly different, even though the same geometry of the plasma source and gas mixing is used.

The electric field patterns shown in the previous sections are obtained for the AC driven jet, but in this section the plasma jet will be powered by the mono-polar high voltage pulses of 1  $\mu$ s with a repetition frequency of 5 kHz. The pulse amplitude is varied from 3 to 6 kV. A similar helium gas flow is used as before of 1 slm and the plasma jet is oriented at a 45 degree impact angle at 10 mm from the targeted material in open air. The distance towards the target is increased since the plasma plume is longer than for the AC driven plasma jet. The examination of the electro-optic material is only done for BSO at normal incidence to focus on the axial  $E_z$  field component as well as the location of the charge deposition.

The time-resolved acquisition of the Mueller matrices is done similarly as before, but 100 ns exposure times are taken. Instead of investigating the optical

state of the sample during the continuous plasma exposure only before and after impact, now it is done time-resolved by varying the time delay  $t_d$  relative to the rise of the constant high voltage pulse.

Before the electric field is measured, first the light emission from the ionization waves impacting the BSO at 45 degree is captured with the same acquisition settings to examine the propagation dynamics. Similar settings are used since then the light emission images can be used as *dark*-image for the time-resolved Mueller polarimetry examinations. These dark images are subtracted from the intensity images needed to construct the Mueller matrices and obtain the optical properties of the electro-optic target. The subtraction is necessary since these time-resolved measurements are performed *during* the propagation of the ionization waves, meaning additional (unpolarized) light is reaching the detector which originates from the plasma.

The imaging is done time-resolved using the trigger signal from the rise of the high voltage pulse. The entire high voltage pulse is desired to be examined, meaning the trigger signal is used to examine the next high voltage pulse, to be able to observe the rise of the voltage pulse as well. As a result the time delay will be varied from  $t_d = 199.6 \mu\text{s}$  to  $t_d = 202.0 \mu\text{s}$ , since the pulse frequency is 5 kHz meaning 200  $\mu\text{s}$  are in between the 1  $\mu\text{s}$  high voltage pulses. In the discussion of the results the 200  $\mu\text{s}$  is omitted for simplicity, so  $t_d$  is shown while a pulse is applied between 0 and 1.0  $\mu\text{s}$ .

For the acquisition of the light emission at the surface impact, the experimental setup of the Mueller polarimeter is used, but the liquid crystals are not controlled to a certain state. This means that they remain at neutral orientation. Consequently, there is no information about the polarization of the light reaching the detector, which in any case is out of the scope for the present study. For each time-delay, 1000 images are accumulated with an exposure time of 100 ns when a voltage amplitude is applied of 3, 4 or 5 kV. For voltage pulses of 6 kV, only 200 frames are captured to limit the total acquisition time. This is done as a precaution to protect the targeted crystal from long-term exposure (blackening) as was briefly discussed in the previous section and observed for a nitrogen environment.

The light emission from the impacting ionization waves is captured as front view seen from the targeted material, with the plasma jet oriented on the left-hand side at a 45 degree impact angle. As stated, the distance between the capillary and the target is 10 mm and a 1 slm helium flow is applied. Figure 4.13 shows in the left column the time-resolved light emission from the impact of the ionization waves when a voltage amplitude is used of 3 kV. With this voltage amplitude the ionization wave takes approximately 0.7  $\mu\text{s}$  after the rise of the voltage pulse (shown at rel.  $t_d = 0.7 \mu\text{s}$ ) to reach the sample. Then, light emission remains visible at the impact point until the end of the voltage pulse ( $t_d = 1.0 \mu\text{s}$ ), after which it decays fast. A small surface propagation is visible next to the original

impact spot which extends slightly to the right of the impact region. Light emission in the impact region is always much weaker than the light emission in the plasma plume. At  $t_d = 1.0 \mu\text{s}$ , i.e. the moment the pulse ends, the light emission slightly increases compared to  $t_d = 0.9 \mu\text{s}$ , indicating a response of the discharge to the drop of the applied potential at the inner electrode of the plasma jet.

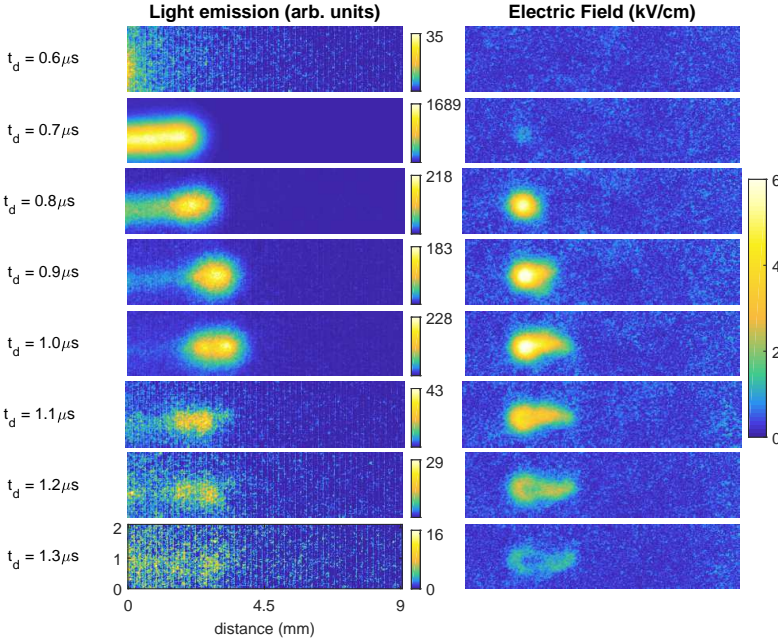


Figure 4.13: The time-resolved light emission (arb. units) and electric field captured from the ionization waves generated with a high voltage pulse of 3 kV applied between  $t_d = 0.0$  and  $t_d = 1.0 \mu\text{s}$ . A front view of the targeted material is shown, so only when the ionization wave impacts the target (at  $t_d = 0.7 \mu\text{s}$ ) the plasma becomes visible, together with the last part of the plasma plume. Exposure times of 100 ns are applied, while 20 acquisitions are accumulated each frame which are repeated for averaging 50 times (meaning 1000 impact events are examined) at each time delay  $t_d$  relative to the rise of the voltage pulse (5 kHz repetition frequency). The colormap is slightly adapted for better visualization.

During the interaction of the ionization waves with the target, as indicated with the light emission, charge is deposited and electric fields are generated. The obtained Mueller matrices are not shown, neither the log-decomposed  $L_m$  and  $L_u$  matrices, since they share great similarities to the obtained matrices shown earlier this chapter when operating the plasma jet with the AC sine wave. The electric field is retrieved from the change in linear retardance obtained by analyzing the logarithmically decomposed  $L_m$  matrices by using equation (3.29), with the resulting axial patterns shown in the right column of figure 4.13.

The electric field is induced  $0.8 \mu\text{s}$  after the rise of the  $1 \mu\text{s}$  constant high voltage pulse. This means that the electric field is observed one time step (of 100 ns) after the ionization wave has reached the target, which was shown through light emission. More detailed time-resolved measurements are needed, e.g. of 10 ns, to see how the initial impact and charge deposition follows in time. For now the focus lies with the entire pulse development at the surface.

In the impact point the axial electric field pattern remains stable until the voltage pulse ends at  $t_d = 1.0 \mu\text{s}$ , after which it decreases to zero which takes approximately  $0.4 \mu\text{s}$ . The pattern slightly stretches in the direction of the propagation of the surface ionization wave during the pulse. This matches the light emission evolution in time. The maximum value of the electric field is  $6.0 \pm 0.3 \text{ kV/cm}$ . The time-resolved electric field patterns clearly show that charges are deposited where light emission is present at the surface. The deposited charge remains at the surface until the applied voltage potential is returned to zero at  $t_d = 1.0 \mu\text{s}$ .

The axial electric field patterns share similarities with the axial electric field pattern obtained when operating the plasma jet with AC sine waves, shown in figure 4.8 both in value and shape / length indicating that a similar plasma surface interaction has taken place. The noise to signal ratio indicates an uncertainty for the electric field measurements of approximately  $0.3 \text{ kV/cm}$ .

The same combined examination of time-resolved imaging of light emission and electric field is done for different applied voltage amplitudes of the pulsed plasma jet. This is shown in figure 4.14 for 4 kV constant high voltage pulses and figure 4.15 for 5 kV pulses. These are obtained with the same acquisition settings as used for the 3 kV examination. When the voltage amplitude is increased to 6 kV the number of ionization events averaged during the acquisition is decreased from 1000 to 200, to reduce the total acquisition time and hence to limit surface damage (blackening) that occurs at the targeted electro-optic BSO material. The resulting time-resolved imaging of light emission and electric field patterns are shown in figure 4.16.

The ionization waves that are generated by the jet change when the voltage pulse amplitude is varied. This is observed both through imaging of the light emission and through the measured electric field patterns. First, the imaging of the light emission is discussed. The time-resolved tracking of the light emission as the ionization waves impact the targeted materials are shown in the left columns of figures 4.14, 4.15 and 4.16 for respectively 4, 5 and 6 kV amplitudes. For these voltage amplitudes two events are observed that change the light emission, one generated by the positive slope of the high voltage pulse and a second one during the negative slope when the pulse drops back to zero (at  $t_d = 1.0 \mu\text{s}$ ). The light emission from the second event during the negative slope is generally much weaker and concentrates only around the impact region. The intensity in the plasma plume during the decay of the potential increases strongly with applied

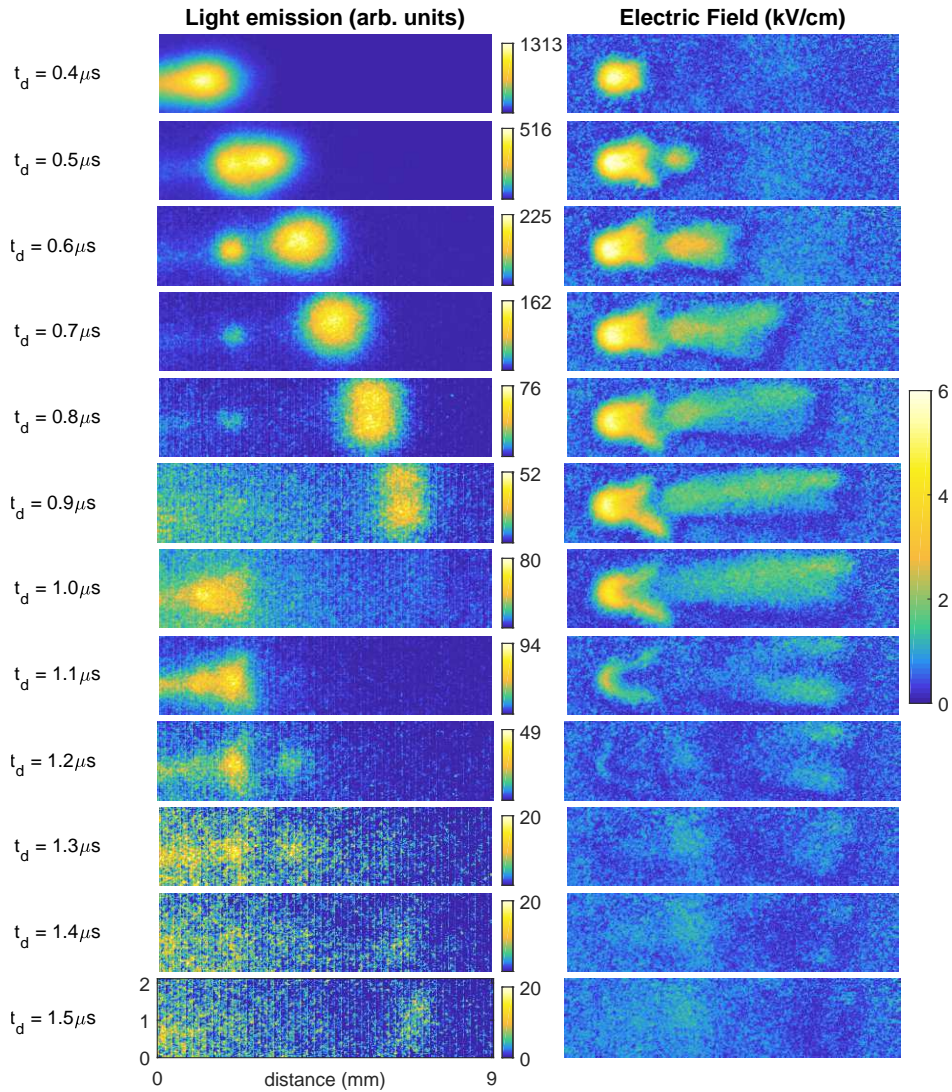


Figure 4.14: The light emission (arb. units) and electric field (kV/cm) from the impacting ionization waves on BSO generated when operating the plasma jet with 4 kV pulses, obtained time-resolved by varying the time delay  $t_d$  relative to the rise of the voltage pulse. A secondary (weaker) ionization wave is visible impacting the surface after the potential drops back to zero ( $t_d > 1.0 \mu\text{s}$ ).

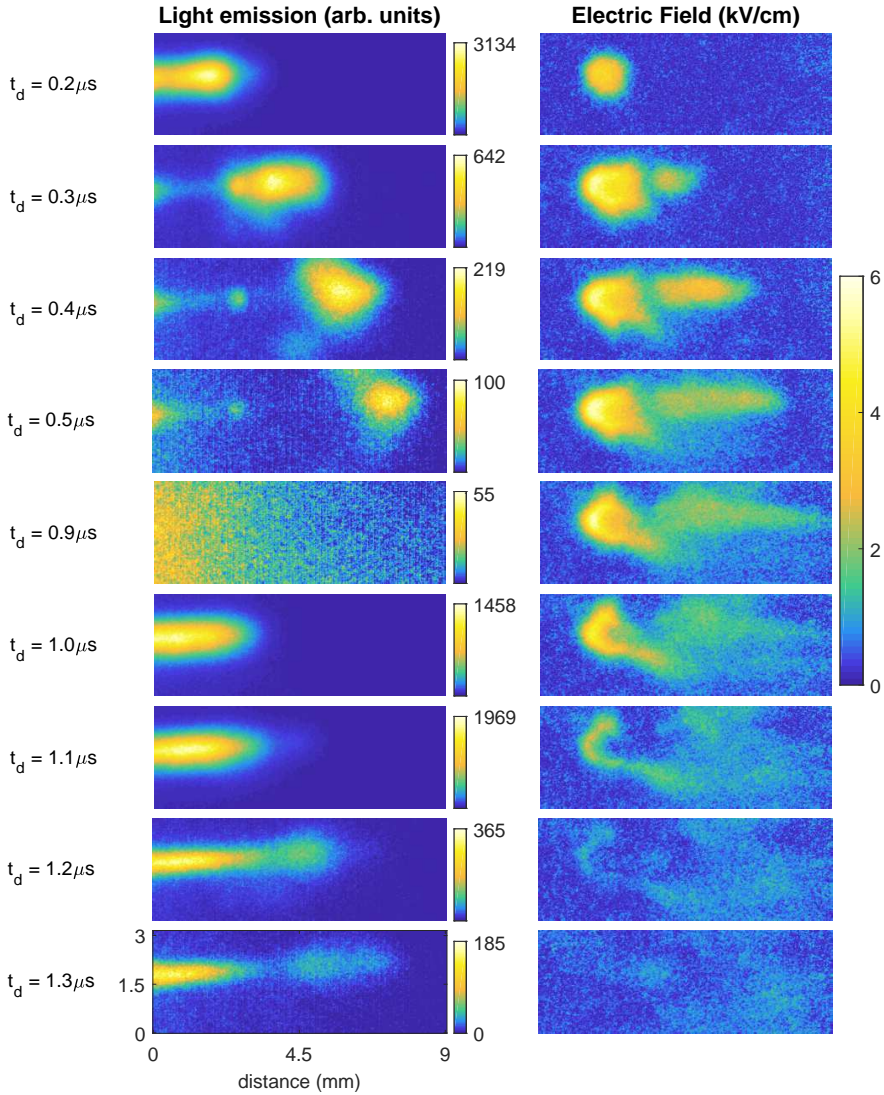


Figure 4.15: Similarly as figures 4.13 and 4.14 the light emission (arb. units) and electric field (kV/cm) are measured time-resolved during and after the impact of the ionization waves. Here, voltage pulses are applied of 5 kV amplitude. Again, the colormap is slightly adapted for better visualization.

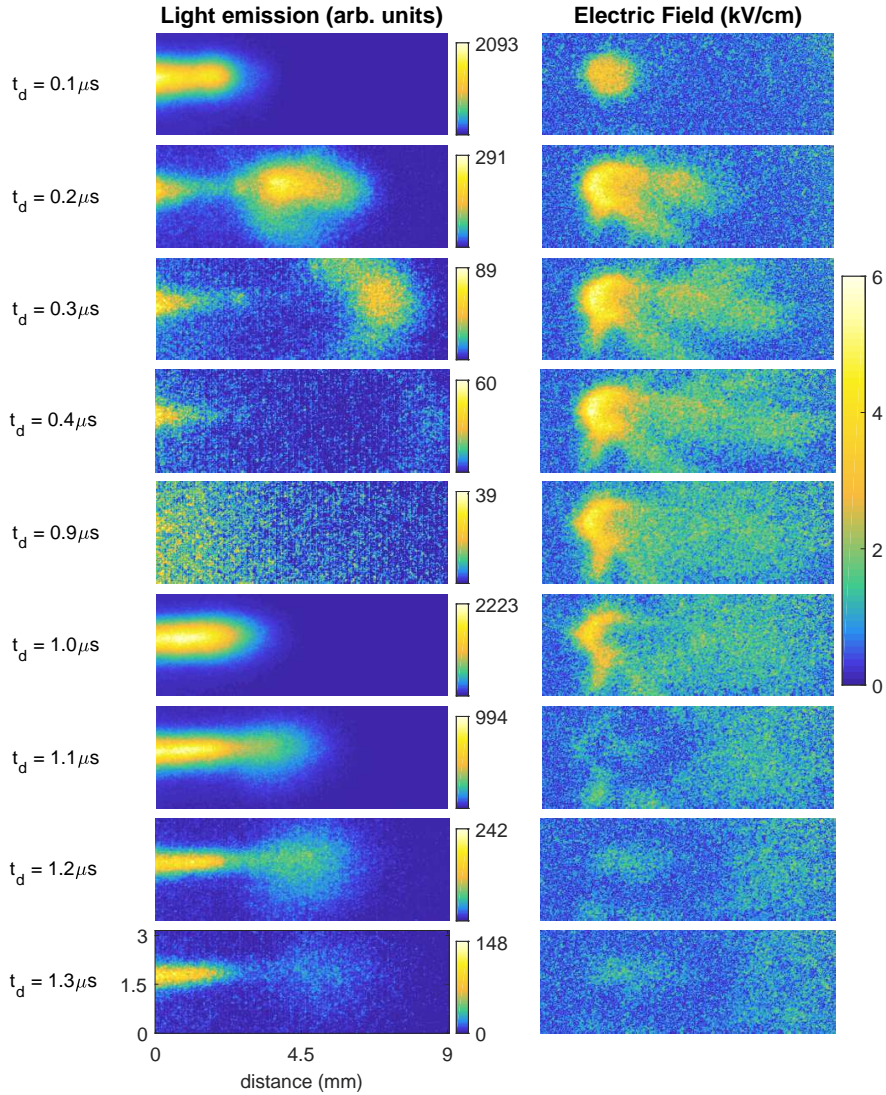


Figure 4.16: The light emission (arb. units) reaching the iCCD detector and electric field (kV/cm) from the guided ionization waves (8 events accumulated per frame which is averaged 25 times) impacting the targeted electro-optic BSO material, generated with the plasma jet using 6 kV pulses. Exposure times of 100 ns are used, while the time-delay  $t_d$  is varied relative to the rise of the previous voltage pulse.

voltage amplitude. The first ionization event during the high voltage pulse starts at the impact point and then travels to the right-hand side along the surface of the targeted material.

The moment of impact varies for the applied voltage amplitude, indicating faster velocities of the ionization wave propagating in the plasma plume. For the 4 kV voltage pulses it takes  $0.4 \mu\text{s}$  for the impact to occur, while for the 5 and 6 kV pulses this is after respectively 0.2 and  $0.1 \mu\text{s}$ . Faster propagation of the guided ionization waves with higher applied voltage amplitudes is a common phenomenon that has been observed in many other plasma jet systems,<sup>56,61</sup> which is directly related to the generation of the ionization waves at an *over-voltage* relative to the breakdown voltage since higher initial electric fields are generated.

Not only the dynamics of the ionization waves in the plasma plume is changing (faster propagation) with the voltage amplitude, but also the surface dynamics after / during the impact. For the 4 kV voltage pulses, first a single surface ionization front is observed, but after  $t_d = 0.7 \mu\text{s}$  this splits in two. Since 1000 images are taken it cannot be concluded whether there are in fact two ionization waves each period or if they are two trajectories that are taken at random. For 5 and 6 kV pulses, a wider surface pattern is observed with indications of surface branching occurring. The surface branching patterns that are observed from the light emission still follow the direction of the helium in air mixing (towards the right of the impact point), but it is likely that an average branching pattern is observed since many discharge events are accumulated per frame, meaning aperiodic (surface) behavior. In the plasma plume branching does not occur for these higher applied voltages, meaning these discharges are still categorized as guided ionization waves.

Besides the time-resolved imaging of the ionization wave propagation at the surface also the electric field induced inside the targeted BSO material is examined using Mueller Polarimetry. The corresponding temporal (axial) electric field patterns are shown in the right columns of figures 4.14, 4.15 and 4.16 for the applied voltage amplitudes of 4, 5 and 6 kV.

Similar as shown in figure 4.13 for 3 kV voltage amplitudes, the electric field is induced after impact by charges deposited in the location where the light emission is high at the surface of the targeted materials. The resulting electric fields remain constant until the end of the voltage pulse at  $t_d = 1.0 \mu\text{s}$ . Since the ionization waves travel faster, while the pulse remains  $1 \mu\text{s}$ , the time for which electric fields are induced each period increases for higher voltage pulses. The electric field patterns around the impact point do not change after the surface ionization wave travels along the dielectric material further away from it.

The shape of the electric field pattern in the impact point changes for different

---

<sup>56</sup>X LU et al. *Plasma Sources Sci. Technol.* 2012 **21**: 034005

<sup>61</sup>X. LU et al. *Phys. Rep.* 2014 **540**: 123–166

voltage amplitudes as well as the subsequent surface *tail* behind it. The branching of the ionization wave at the surface is observed within the electric field patterns for 5 kV and 6 kV constant pulses. Field values in the tail are always lower than in the impact point and decay slowly during the pulse from 3 to  $1.8 \pm 0.3$  kV/cm. Lower fields in the *tail* are possibly observed because a large number of exposure events are taken while unstable branches are observed. When the branches take different paths, the average pattern that is observed will have a lower field than the individual branches.

When the potential of the high voltage pulse is decreasing back to zero, the constant field patterns start to decrease. This matches the light emission, which indicates that recombination is triggered by a negative pulse / ionization wave. In the center of the surface charged area and not the impact point, the electric field pattern goes to zero immediately followed by a short temporal increase of electric field. All the electric field patterns that are shown are obtained using equation (3.29), meaning absolute values are examined. Through the examination of the changes in the birefringence however, it is observed that the charge deposited after the pulse ended is of opposite sign compared to the charge deposition during the pulse. With this knowledge, it can be said that the second event, occurring when the potential goes back to zero, functions as a recombination wave of the surface charges that have been deposited before.

This is highlighted with more detail in figure 4.17, where the electric field values are shown (with a presumed sign based upon observations from the retardance) in time for two spatial locations, i.e. the impact point and in the *tail* next to the center of the impacted area. It is shown that the electric field in the impact point is highest when voltages are applied with an amplitude of 3 or 4 kV. When higher applied voltages are used the electric field maximum is reduced slightly in the impact point.

In the figure a 5th case is added showing the electric field values in those two points for 6 kV pulses but with a helium flow of 1500 sccm instead of 1000 sccm. These electric field results have not been shown spatially, but what can be seen directly in figure 4.17 is that the electric field reduces since the helium density increases at the surface while oxygen and nitrogen density decrease. This is similar as shown before for the AC powered jet.

This decrease of axial electric field values for higher voltage amplitudes is more strongly observable in the beginning of the surface *tail* structure, right next to the impact point. For 3 kV the spatial location where the second light emission point is observed (next to the impact point) is taken since there is no elongated tail structure. When the applied voltage is increased in amplitude, the maximum electric field values in this tail area decrease. This means that the local surface charge density has decreased. While studying the AC-case in section 4.4.2, two hypotheses were postulated that could explain a decrease in local surface charge

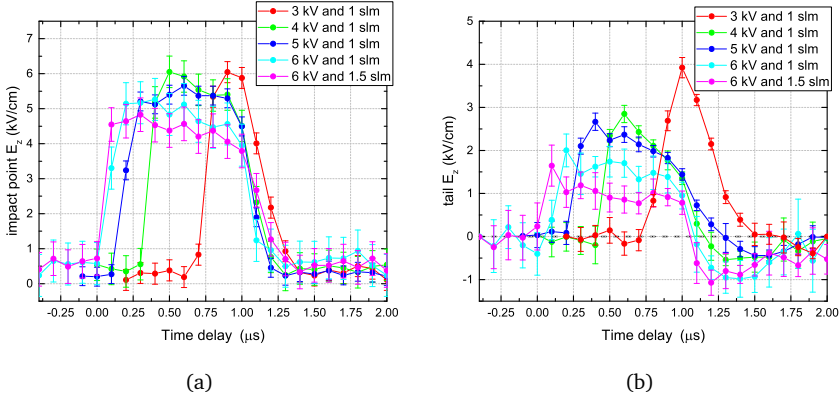


Figure 4.17: Maximum electric field values (kV/cm) observed in the impact point shown in (a) and the field observed in the beginning of the surface *tail* structure right next to the impact point shown in (b) for different applied voltage amplitudes. A 5th case is added for 6 kV pulses where the helium flow is increased from 1 slm to 1.5 slm.

density. Here, it can be argued that the local surface charge density has decreased since the ionization waves propagate faster over the surface. From light emission it is observed that for 4 kV pulses it takes the ionization waves approximately 0.5  $\mu\text{s}$  to finish its surface path, while for 5 and 6 kV pulses this is respectively 0.3 and 0.2  $\mu\text{s}$ . Because the ionization wave propagates faster over the surface, there is less time for charge deposition to occur. This can explain why the surface charge density is lower and consequently the electric field experienced due to these charges is lower as well. The ionization waves travel faster since they are generated at higher voltages by higher external electric fields.

While the applied voltage potential is high, the experienced field values in the surface tail decrease in time. For the fields observed the impact point (figure 4.17(a)) this is less significant, since they remain relatively constant until the high voltage pulse ends. In the surface tail structure negative electric field values are measured after the pulse has ended. This is related to the drop of the high voltage potential which initiates a second discharge event. This back discharge causes deposition of negative charge which recombines with the already deposited positive charges. An overshoot of negative charges eventually induces negative fields with relatively low amplitude for short time scales.

More negative charge is deposited at higher applied voltages, which coincides with the increase of light emission that is observed when the voltage pulse ends. An important aspect of this could be related to the total charge that has been deposited during the high voltage pulse. For higher voltage amplitudes, more total charge has been deposited even though the local surface charge density is

lower indicated by the axial field values. This is because the total area where the interaction has taken place has increased. Since there is more charge present (in total) when the voltage pulse returns to zero, the back discharge that is generated due to the drop of the applied potential is stronger, which generates more light and deposits more negative charge.

A relatively long surface propagation is observed because of the inclined angle of 45 deg. When the plasma jet would impact perpendicularly, as is often the case for applications, the surface dynamics will be different. This will be investigated in the next chapter since this requires a slightly different examination. Additionally, it provides symmetry that allows to compare with a numerical model as will be done in the next chapter.

## 4.5 Summary and Perspectives

- Electric field patterns induced repetitively on a  $\mu\text{s}$ -timescale during a plasma surface interaction have been investigated by examining time-resolved the targeted electro-optic materials with Mueller polarimetry.
- From the measured Mueller matrices before and after the impact of the ionization waves, the birefringence is obtained by using the logarithmic decomposition. The linear birefringence scales with the axial electric field component  $E_z$ , induced by temporarily deposited surface charges, when BSO is examined under normal incidence by the Mueller polarimeter. When a different electro-optic crystal is used, i.e. Fe:LiNbO<sub>3</sub> (Felinbo), the linear birefringence depends on the radial ( $E_x$  and  $E_y$ ) electric field patterns that are induced.
- As a result, both the axial and radial electric field patterns induced inside a target are obtained while under exposure of ionization waves generated by an AC driven plasma jet impacting at a 45 degree angle. The electric field patterns suggest that the temporal, repetitive charge deposition that occurs each kHz-period is similar on both targets (BSO and Felinbo).
- This allows a more detailed investigation on the surface charging since the axial field relates to the local surface charge density while the radial field is influenced by the total charge that is deposited on the entire surface. The use of time-resolved Mueller polarimetry to investigate different electro-optic targets to obtain all the individual electric field components has not been shown in literature before but has great potential for the investigation of plasma surface interactions relating e.g. plasma catalysis, surface functionalization, plasma medicine and plasma actuators for flow control.
- The plasma surface interaction is examined, through images of the induced electric fields components, for the ionization waves impacting at 45° as a function of the operating parameters of the AC plasma jet (voltage amplitude and helium gas flow) in a controlled environment for different surrounding gas.
- With an increase of helium flow the surface patterns get elongated and the axial field values indicate that the local surface charge density has decreased. For an increase of AC amplitude the axial electric field patterns change minimally (around 5 kV/cm), while the radial amplitude of the electric field increases from 3.1 to 6.0 kV/cm. This indicates that the total charge deposited has increased, due to the increase of surface area where the interaction has taken place.

- When the environmental gas is changed from dry air to  $O_2$ ,  $N_2$  or  $CO_2 + 2.5\%$   $O_2$ , the observed electric field patterns change in shape. Because of the role of negative ions, either a more filamentary surface pattern is observed ( $N_2$ ) or more diffuse ( $CO_2$ ), compared to dry air and  $O_2$ . Also Penning ionization and vibrational losses play a role in the surface dynamics.
- The minimal influence of AC amplitude is related to the relatively slow temporal evolution compared to the discharge dynamics. For the pulsed plasma jet (using  $1\ \mu s$  mono-polar positive pulses) the voltage amplitude influences the (surface) discharge dynamics significantly. With a higher voltage amplitude, the velocity of the ionization wave increases and longer surface discharges are observed. The induced axial electric field values decrease, which suggests that locally less charge is deposited. This could be because there is less interaction time with the targeted sample due to the increased propagation velocity. In total there is more charge deposited since the area has increased, which influences the back discharge that is generated when the high voltage potential returns to zero at the end of the pulse. Although the interaction time is shorter, the electric fields are induced for longer times because there is more time between the impact and the end of the pulse (which initiates the removal of surface charge).

## References

- [40] C. MALGRANGE, C. RICOLLEAU, and M. SCHLENKER. *Symmetry and Physical Properties of Crystals*. Dordrecht: Springer Netherlands, 2014. ISBN: 978-94-017-8992-9 DOI: [10.1007/978-94-017-8993-6](https://doi.org/10.1007/978-94-017-8993-6) (see pp. 12, 55, 57, 88, 162, 163)
- [56] X LU, M LAROUSI, and V PUECH. *Plasma Sources Sci. Technol.* **21**: 034005, 2012. DOI: [10.1088/0963-0252/21/3/034005](https://doi.org/10.1088/0963-0252/21/3/034005) (see pp. 17, 19, 20, 113)
- [57] D. M. ORLOV, G. I. FONT, and D. EDELSTEIN. *AIAA J.* **46**: 3142–3148, 2008. DOI: [10.2514/1.37514](https://doi.org/10.2514/1.37514) (see pp. 17, 98, 135)
- [58] T. UNFER and J. P. BOEUF. *J. Phys. D. Appl. Phys.* **42**: 194017, 2009. DOI: [10.1088/0022-3727/42/19/194017](https://doi.org/10.1088/0022-3727/42/19/194017) (see pp. 17, 98)
- [61] X. LU, G. NAIDIS, M. LAROUSI, and K. OSTRIKOV. *Phys. Rep.* **540**: 123–166, 2014. DOI: [10.1016/j.physrep.2014.02.006](https://doi.org/10.1016/j.physrep.2014.02.006) (see pp. 20, 113)
- [65] R WILD, T GERLING, R BUSSIAHN, K.-D. WELTMANN, and L STOLLENWERK. *J. Phys. D. Appl. Phys.* **47**: 042001, 2014. DOI: [10.1088/0022-3727/47/4/042001](https://doi.org/10.1088/0022-3727/47/4/042001) (see pp. 20, 22, 53, 80, 96)
- [66] A. SOBOTA, O GUAITELLA, G. B. SRETENOVIĆ, I. B. KRSTIĆ, V. V. KOVAČEVIĆ, A OBRUSNÍK, Y. N. NGUYEN, L ZAJÍČKOVÁ, B. M. OBRADOVIĆ, and M. M. KURAICA. *Plasma Sources Sci. Technol.* **25**: 065026, 2016. DOI: [10.1088/0963-0252/25/6/065026](https://doi.org/10.1088/0963-0252/25/6/065026) (see pp. 20, 102, 146, 179, 183)
- [71] L. STOLLENWERK, J. G. LAVEN, and H.-G. PURWINS. *Phys. Rev. Lett.* **98**: 255001, 2007. DOI: [10.1103/PhysRevLett.98.255001](https://doi.org/10.1103/PhysRevLett.98.255001) (see pp. 21, 22, 53, 80, 96)
- [72] A SOBOTA, O GUAITELLA, and E GARCIA-CAUREL. *J. Phys. D. Appl. Phys.* **46**: 372001, 2013. DOI: [10.1088/0022-3727/46/37/372001](https://doi.org/10.1088/0022-3727/46/37/372001) (see pp. 21, 22, 80, 96)
- [79] S. A. NORBERG, E. JOHNSEN, and M. J. KUSHNER. *J. Appl. Phys.* **118**: 013301, 2015. DOI: [10.1063/1.4923345](https://doi.org/10.1063/1.4923345) (see pp. 22, 89, 143)
- [82] O GUAITELLA and A SOBOTA. *J. Phys. D. Appl. Phys.* **48**: 255202, 2015. DOI: [10.1088/0022-3727/48/25/255202](https://doi.org/10.1088/0022-3727/48/25/255202) (see pp. 22, 83, 95)
- [84] T. KAWASAKI, Y. ARAI, and T. TAKADA. *Jpn. J. Appl. Phys.* **30**: 1262–1265, 1991. DOI: [10.1143/JJAP.30.1262](https://doi.org/10.1143/JJAP.30.1262) (see pp. 22, 53, 80, 96)
- [86] E. SLIKBOER, O. GUAITELLA, and A. SOBOTA. *Plasma Sources Sci. Technol.* **25**: 03LT04, 2016. DOI: [10.1088/0963-0252/25/3/03LT04](https://doi.org/10.1088/0963-0252/25/3/03LT04) (see pp. 22, 53, 79, 80, 83, 95, 96, 160, 181)
- [87] E. SLIKBOER, E. GARCIA-CAUREL, O. GUAITELLA, and A. SOBOTA. *Plasma Sources Sci. Technol.* **26**: 035002, 2017. DOI: [10.1088/1361-6595/aa53fe](https://doi.org/10.1088/1361-6595/aa53fe) (see pp. 22, 53, 80, 83, 96, 101, 102, 160)

- [88] M BOGACZYK, R WILD, L STOLLENWERK, and H.-E. WAGNER. *J. Phys. D. Appl. Phys.* **45**: 465202, 2012. DOI: [10.1088/0022-3727/45/46/465202](https://doi.org/10.1088/0022-3727/45/46/465202) (see pp. 22, 53, 80, 96)
- [89] R. TSCHERSCH, M. BOGACZYK, and H.-E. WAGNER. *J. Phys. D. Appl. Phys.* **47**: 365204, 2014. DOI: [10.1088/0022-3727/47/36/365204](https://doi.org/10.1088/0022-3727/47/36/365204) (see pp. 22, 53, 80, 96)
- [121] H. MU and G. ZHANG. *Plasma Sci. Technol.* **13**: 645–650, 2011. DOI: [10.1088/1009-0630/13/6/02](https://doi.org/10.1088/1009-0630/13/6/02) (see pp. 53, 97)
- [125] H. G. JERRARD. *J. Opt. Soc. Am.* **38**: 35–39, 1948. DOI: [10.1364/JOSA.38.000035](https://doi.org/10.1364/JOSA.38.000035) (see p. 80)
- [126] F. H. MOK. *Opt. Lett.* **18**: 915–917, 1993. DOI: [10.1364/OL.18.000915](https://doi.org/10.1364/OL.18.000915) (see p. 88)
- [127] G. W. BURR and D. PSALTIS. *Opt. Lett.* **21**: 893–895, 1996. DOI: [10.1364/OL.21.000893](https://doi.org/10.1364/OL.21.000893) (see p. 88)
- [128] X. AN, D. PSALTIS, and G. W. BURR. *Appl. Opt.* **38**: 386–393, 1999. DOI: [10.1364/AO.38.000386](https://doi.org/10.1364/AO.38.000386) (see p. 88)
- [129] Y FURUKAWA, K KITAMURA, Y JI, G MONTEMEZZANI, M ZGONIK, C MEDRANO, and P GÜNTER. *Opt. Lett.* **22**: 501–503, 1997. DOI: [10.1364/OL.22.000501](https://doi.org/10.1364/OL.22.000501) (see p. 88)
- [130] C. YANG, Y. ZHAO, R. WANG, and M. LI. *Opt. Commun.* **175**: 247–252, 2000. DOI: [10.1016/S0030-4018\(99\)00753-1](https://doi.org/10.1016/S0030-4018(99)00753-1) (see p. 88)
- [131] Z. XU, S. XU, J. ZHANG, X. LIU, and Y. XU. *J. Cryst. Growth* **280**: 227–233, 2005. DOI: [10.1016/j.jcrysgro.2005.03.058](https://doi.org/10.1016/j.jcrysgro.2005.03.058) (see p. 88)
- [132] K CHAH, M AILLERIE, M. FONTANA, and G MALOVICHKO. *Opt. Commun.* **176**: 261–265, 2000. DOI: [10.1016/S0030-4018\(00\)00506-X](https://doi.org/10.1016/S0030-4018(00)00506-X) (see p. 89)
- [133] F. JERMANN, M. SIMON, and E. KRÄTZIG. *J. Opt. Soc. Am. B* **12**: 2066–2070, 1995. DOI: [10.1364/JOSAB.12.002066](https://doi.org/10.1364/JOSAB.12.002066) (see p. 90)
- [134] D. FAIRCLOTH and N. ALLEN. *IEEE Trans. Dielectr. Electr. Insul.* **10**: 285–290, 2003. DOI: [10.1109/TDEI.2003.1194112](https://doi.org/10.1109/TDEI.2003.1194112) (see p. 97)
- [135] C. W. J. BERENDSEN, C. J. KUIJPERS, J. C. H. ZEEGERS, and A. A. DARHUBER. *Soft Matter* **9**: 4900–4910, 2013. DOI: [10.1039/c3sm27944h](https://doi.org/10.1039/c3sm27944h) (see pp. 97, 204)
- [136] F. PECHEREAU and A. BOURDON. *J. Phys. D. Appl. Phys.* **47**: 445206, 2014. DOI: [10.1088/0022-3727/47/44/445206](https://doi.org/10.1088/0022-3727/47/44/445206) (see p. 98)
- [137] E. C. NEYTS and K. M. BAL. *Plasma Process. Polym.* **14**: 1–6, 2017. DOI: [10.1002/ppap.201600158](https://doi.org/10.1002/ppap.201600158) (see p. 98)

- 
- [138] M. YUSUPOV, J. VAN DER PAAL, E. NEYTS, and A. BOGAERTS. *Biochim. Biophys. Acta - Gen. Subj.* **1861**: 839–847, 2017. DOI: [10.1016/j.bbagen.2017.01.030](https://doi.org/10.1016/j.bbagen.2017.01.030) (see p. 98)
- [139] E. C. NEYTS, A. C. T. VAN DUIN, and A. BOGAERTS. *J. Am. Chem. Soc.* **134**: 1256–1260, 2012. DOI: [10.1021/ja2096317](https://doi.org/10.1021/ja2096317) (see p. 98)
- [140] J.-S. OH, Y. ARANDA-GONZALVO, and J. W. BRADLEY. *J. Phys. D. Appl. Phys.* **44**: 365202, 2011. DOI: [10.1088/0022-3727/44/36/365202](https://doi.org/10.1088/0022-3727/44/36/365202) (see p. 104)
- [141] N. L. ALLEN and A. A. R. HASHEM. *J. Phys. D. Appl. Phys.* **35**: 2551–2557, 2002. DOI: [10.1088/0022-3727/35/20/314](https://doi.org/10.1088/0022-3727/35/20/314) (see p. 105)
- [142] S. RAZAVIZADEH, H. GHOMI, and A. SOBOTA. *Plasma Sources Sci. Technol.* **27**: 075016, 2018. DOI: [10.1088/1361-6595/aacd73](https://doi.org/10.1088/1361-6595/aacd73) (see p. 105)
- [143] K. V. KOZLOV, R. BRANDENBURG, H.-E. WAGNER, A. M. MOROZOV, and P. MICHEL. *J. Phys. D. Appl. Phys.* **38**: 518–529, 2005. DOI: [10.1088/0022-3727/38/4/003](https://doi.org/10.1088/0022-3727/38/4/003) (see p. 105)



# Chapter 5

## Study of a Plasma Target Interaction at Normal Incidence

### Contents

---

<b>5.1 Measuring the Plasma Jet Dynamics Impacting on a Target .</b>	<b>124</b>
5.1.1 Imaging of Ionization Wave Propagation . . . . .	124
5.1.2 Adapting the Measurement Procedure for Electric Field Investigation . . . . .	129
5.1.3 Time-Resolved Plasma Impact on BSO . . . . .	131
<b>5.2 Time-Resolved Electric Field Patterns . . . . .</b>	<b>135</b>
5.2.1 Electric Field Patterns during Interaction . . . . .	140
5.2.2 Comparison with a Numerical Fluid Model . . . . .	142
5.2.3 Variation of Voltage Amplitude . . . . .	148
<b>5.3 Summary and Perspectives . . . . .</b>	<b>154</b>
<b>References . . . . .</b>	<b>156</b>

---

In this chapter, Mueller polarimetry is applied to study the perpendicular impact of ionization waves generated with the pulsed plasma jet. Therefore, the targeted sample is examined with the Mueller polarimeter at a  $45^\circ$  angle which changes the measurement procedure and enables detection of all the induced electric field components separately. This is used to examine the influence of the applied voltage amplitude, similarly as done in section 4.4.3. Because of the changed impact angle of the ionization waves, the plasma surface interaction is significantly altered. Additionally, symmetry is provided which allows a comparison with a numerical fluid model to examine the charge dynamics and plasma propagation at the targeted surface.

## 5.1 Measuring the Plasma Jet Dynamics Impacting on a Target

In the previous chapter various approaches have been shown to examine the electric field patterns induced inside an electro-optic material under exposure of a plasma jet. The targeted materials were examined optically with the Mueller polarimeter at normal incidence, meaning that the plasma jet was oriented at a 45 degree angle. Different electro-optic targets have been used (i.e. BSO and Felinbo) to examine both axial and radial components. Relatively long surface discharges formed behind the impact point were observed, through imaging and electric field, especially when operating the plasma jet with constant high voltage pulses. The appearance of these directed surface discharges is related to the impact angle of the ionization waves.

In this chapter the impact will be examined where the plasma jet is at normal incidence to the targeted material, instead of 45 degrees. This changes the system which allows a more detailed investigation of the plasma target interaction for two reasons. Firstly, symmetry is provided by the orientation and propagation of the ionization waves, meaning that a phenomenological comparison with a numerical fluid model is possible. This is provided with a collaborate work done with Pedro Viegas and Anne Bourdon (*LPP, Ecole Polytechnique*) to examine the relative importance of surface charges compared to the volume charges and the electric field contributions they have to the propagation dynamics of the ionization waves in the vicinity of the dielectric target.

Secondly, since the plasma jet is oriented at normal incidence, the Mueller polarimeter is used to examine the electro-optic target at a 45 degree angle. As briefly suggested in the previous chapter, this changes the relation between the induced birefringence and the external electric field components. All the electric field components (axial  $E_z$  and radial  $E_x$  and  $E_y$ ) can be determined simultaneously following this new approach without using different materials.

This is applied to further study the interaction by ionization waves generated with the plasma jet operated by the mono-polar high voltage pulses. This operating regime allows for the comparison with the numerical fluid model. Different voltage amplitudes will be examined experimentally, comparable to the last section of the previous chapter, by imaging of light emission and electric field.

### 5.1.1 Imaging of Ionization Wave Propagation

The easiest way to investigate the plasma surface interaction is by monitoring the plasma propagation in vicinity of the material. The light emission which is captured from the plasma with the detector (iCCD camera) includes the entire visible range and results from a combination of gas phase species and local electron den-

sity / energy levels. As a consequence, the brightest emission from the plasma is most of the time located where the electric field is the highest in the streamer head. Relatively long lived species can create luminescence at more long-term timescales. Fast imaging in the vicinity of the targeted sample is a good tracer of the characteristic time of the dynamics of interaction of the ionization front with the surface.

The light emission from the ionization waves generated with the pulsed plasma jet is captured time-resolved with 25 ns exposure times, while varying the trigger delay relative to the rise of the 1  $\mu$ s constant high voltage pulse. The resulting plasma propagation for varying voltage amplitudes is shown in figure 5.1 for different time instances.

The pulsed plasma jet is operated horizontally at 10 mm away from a 0.5 mm thick glass target. The voltage amplitude is varied from 3 to 6 kV while a helium flow of 1 slm is used. The light emission is shown with a logarithmic colorscale for different time instances per measurement series. Each image represents an average over 1250 images taken at that time delay with an exposure time of 25 ns.

The ionization wave is generated at the inner powered electrode, located on the left border of the images. Then, it propagates towards the outer grounded ring, which blocks the light in that region. In between the electrodes the light emission is high. The ionization wave will propagate further downstream towards the end of the capillary when enough charge has accumulated beneath the grounded ring. The discharge moves initially along the walls of the dielectric barrier tube before it turns towards a more centered discharge. For higher voltage amplitudes the discharge is less centered and propagates faster.

Outside of the capillary tube, in the region referred to as plasma plume, the light emission from the ionization wave increases as it accelerates towards the 0.5 mm thick glass target, which is at floating potential. At the target, the axial movement is turned to a radial spread along the surface of the glass. The light emission for the radial spread is stronger with higher applied voltages and appears slightly above the surface (located on the right side at 38 mm distance from the inner powered electrode).

When a voltage amplitude is applied of 4 kV, it takes the ionization wave approximately  $100 \pm 25$  ns to cross the 10 mm gap between the end of the capillary tube and the target, shown between 0.300 and 0.400  $\mu$ s. The estimated velocity of  $10^5$  m/s of the ionization wave within the plasma plume corresponds well with values reported in literature<sup>144-146</sup>, while ionization fronts travelling at lower velocities have been reported as well.<sup>60</sup> The velocity is further discussed below.

---

<sup>144</sup>X. LU and M. LAROSSI *J. Appl. Phys.* 2006 **100**: 063302

<sup>145</sup>Z. XIONG et al. *J. Appl. Phys.* 2010 **108**: 103303

<sup>146</sup>G. V. NAIDIS *J. Phys. D. Appl. Phys.* 2011 **44**: 215203

<sup>60</sup>M. TESCHKE et al. *IEEE Trans. Plasma Sci.* 2005 **33**: 310-311

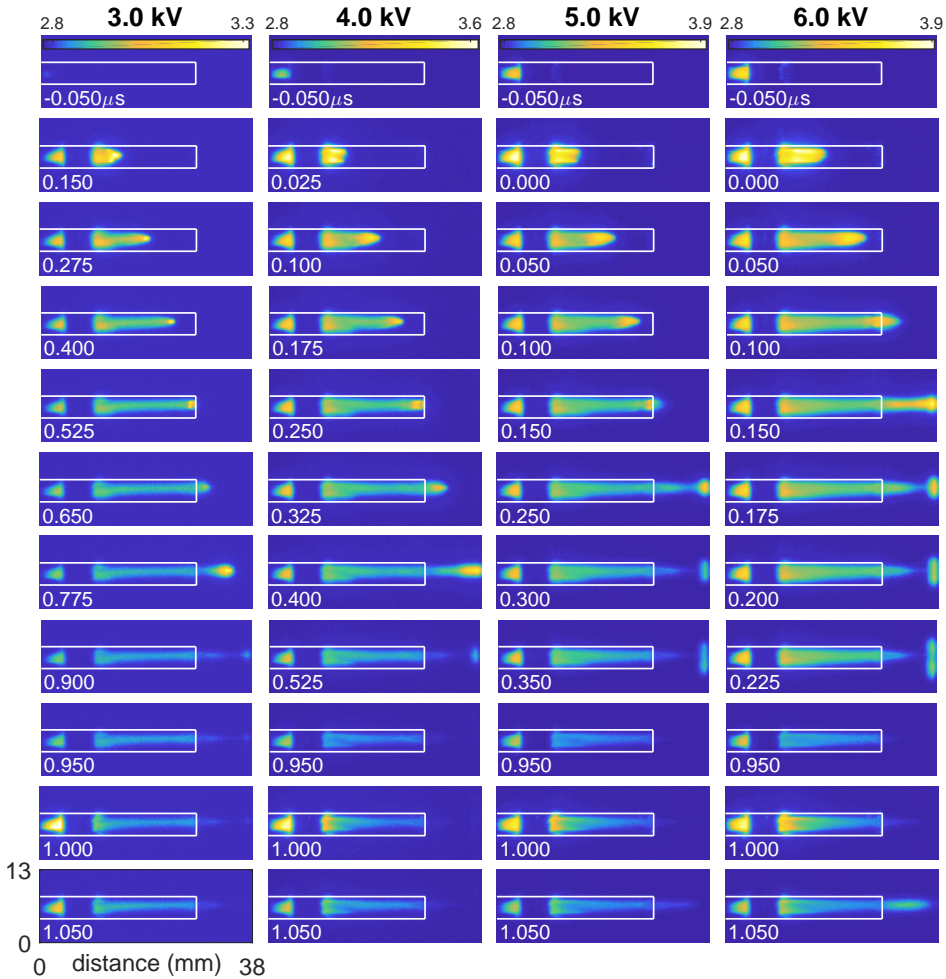


Figure 5.1: Light emission (log-colorscale, arb. units) from the propagating ionization waves generated from the inner powered electrode on the left side (capillary shown by white border, 4 mm width), towards the glass target (right side) observed from the side. Exposure times of 25 ns are used and 1250 frames are accumulated at every time delay (shown by white numbers in  $\mu\text{s}$ ) relative to the onset of the voltage pulse. The 0.5 mm glass target is located at 10 mm downstream of the 28 mm shown capillary tube. A helium flow of 1 slm is applied and constant voltage pulses (rise time of 50 ns) with different amplitudes of 1  $\mu\text{s}$  (repetition frequency of 5 kHz) are used to generate the plasma.

The light emission observed in the capillary tube remains visible during the entire pulse, however, it decreases slightly until the pulse ends after 1  $\mu\text{s}$ . Then an increase is observed for all applied voltage amplitudes, indicating a response to the drop of the applied high potential at the inner electrode through the con-

ductive channel that has formed. The response is also visible in the plume area and consequently affects the target as well. This has been observed in the previous chapter also with the jet impacting at 45 degree, where the second wave of light emission coincides with the onset of removal of charge at the surface of the dielectric material. Hence the name recombination wave was suggested for this back discharge which depends on the amount of charge that has been deposited during the pulse.

The velocity of the discharges generated at different voltages is examined by monitoring the spatial change of the maximum light emission in the front part of the ionization wave compared to the previous time step. The resulting velocity-distance graph is shown in figure 5.2(a).

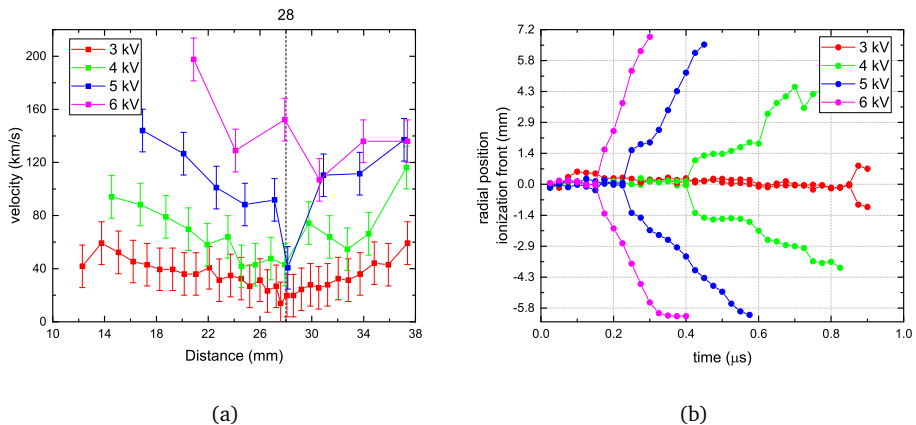


Figure 5.2: The velocity (km/s) of the ionization waves along the distance of (axial) propagation is shown in (a) for the applied voltage amplitudes. The distance is given relative to the end of the inner powered electrode, meaning the region between the grounded ring and the edge of the capillary is given between 10 and 28 mm, while the target is located at 38 mm. Figure (b) shows the radial spread (mm) along the dielectric glass surface as a function of time. Both results are obtained by analyzing the 25 ns time-resolved light emission images as shown (partially) in figure 5.1.

For all applied voltage amplitudes the velocity of the ionization wave decreases as it travels inside the capillary tube (edge of the capillary located at 28 mm). This can be explained due to charge losses with the dielectric walls and an increasing distance between the ionization front and the inner electrode. The velocity increases when the ionization waves propagate outside of the capillary tube. This is most likely caused by contraction of the ionization front due to the helium-in-air

mixing.<sup>147</sup> The typical velocity increases from approximately 50 km/s to 150 km/s when the voltage amplitude is increased from 3 to 6 kV. The uncertainties shown in the graph take into account a spatial and temporal uncertainty of 0.4 mm (= 10 px) and 10 ns.

The spreading of the ionization wave at the surface can be followed by monitoring the radial position along the surface where light emission occurs. This is shown as a function of time in figure 5.2(b) for the different applied voltages. For higher applied voltage amplitudes the radial spread of the ionization wave at the surface of the targeted material occurs earlier in time, since there is faster propagation in the gas phase. The surface interaction starts after 850 ns for the 3 kV pulses and respectively after 400, 225 and 150 ns for the 4, 5 and 6 kV pulses.

The spread at the surface shows two sequential stages. The first involves an isotropic spread at the surface, observed until a radial spread of approximately 2 mm is reached. Then a second stage initiates surface streamers, characterized by a faster spread along the dielectric surface. The intensity of the light decreases in both stages while spreading radially for all voltages. For 3 kV a minimum spread is observed, while for 6 kV the spread is the fastest and furthest.

For 4 kV the radial spread occurs at an estimated average velocity of approximately 6.7 km/s, which is much slower than the propagation of the ionization wave inside the capillary or in the plume. For 5 kV the average spreading velocity is 15 km/s and for 6 kV pulses it is 32 km/s.

To investigate further the dynamics that occur during the plasma-target interaction in terms of charge deposition and the electric fields that are generated, the glass target is substituted for the electro-optic BSO material. Mueller polarimetry is applied to examine time-resolved the linear birefringence, as part of the measured Mueller matrices, to investigate the electric fields to which targets are exposed to. The plasma jet will still be oriented at normal incidence to the target. This means that the polarized beam used for Mueller polarimetry has to propagate through the examined target at an inclined angle.

The next section will elaborate how the measurements are done at a 45 degree measurement angle between the electro-optic BSO material and the probing polarized light beam of the polarimeter, after which new imaging is again performed in the new measurement conditions. This means that the impact is seen on BSO at a 45 degree angle, which reveals the ionization propagation at the surface with the surface streamers that have been mentioned already on glass (but hardly visible because it was seen from the side). Since BSO and glass differ in dielectric character it is good to have both imaging available to compare how the interaction has changed.

---

<sup>147</sup>J. JARRIGE et al. *Plasma Sources Sci. Technol.* 2010 **19**: 065005

### 5.1.2 Adapting the Measurement Procedure for Electric Field Investigation

The investigation of the plasma-target interaction will be performed while the plasma jet impacts perpendicularly. As a consequence, the BSO material has to be examined at a 45 degree angle with respect to the probing light propagation direction. In chapter 3 the relation between the induced birefringence and the external electric field has been derived for two cases. The first involved the investigation of the electro-optic BSO crystal at normal incidence, which allows for the detection of the axial  $E_z$  field component. The second case involved the examination of the BSO crystals at a 45 degree inclination. Then the birefringences in both coordinate systems respond to all electric field components, according to equations (3.18) and (3.22). The coordinate system is defined by the orientation of the electro-optic crystal. This means that the  $z$ -direction is perpendicular to the surface. This direction is referred to as the axial direction since it aligns with the axis / orientation of the plasma jet.

$$\Gamma_{0/90} = \pm \frac{2\pi d^*}{\lambda} \frac{1}{2} E_y r_{41} n_o^3 \quad (3.18 \text{ revisited})$$

$$\Gamma_{45/135} = \pm \frac{2\pi d^*}{\lambda} \frac{1}{\sqrt{2}} n_o^3 r_{41} (E_z - E_x) \quad (3.22 \text{ revisited})$$

The ionization waves first travel axially until the surface interaction starts and the axial propagation is turned into a radial spread, along the surface of the targeted material, as has been showed in figure 5.1. The radial spread is in the  $XY$ -plane, where the  $y$ -direction is the vertical component and the  $x$ -direction the horizontal component.

The derived relationships between  $\vec{E}$  and  $\Gamma$  depend on the refractive index  $n_o$ , wavelength of light  $\lambda$  and the electro-optic constant  $r_{41}$ . For the case of normal incidence the path of propagation is equal to thickness  $d$  of the sample, while for the second case  $d^* = \sqrt{2}d$  due to the inclined angle of examination.

The linear birefringent patterns that are obtained from the measured Mueller matrices scale according to  $E_y$  on one hand and  $E_z - E_x$  on the other hand. To separate all the three electric field components from the measured birefringences a solution has to be found. This can be done by measuring the BSO target in two different configurations, with respectively the plasma jet impacting either on the front or the backside of the material, see figure 5.3.

The induced electric field changes sign in the axial direction when the measurement is repeated with the plasma jet impacting on the other side of the electro-optic material. As a result, the linear birefringent patterns can be compared and used to separate the individual effect of  $E_z$  and  $E_x$  from the measured  $\Gamma$ s, according to equations (5.1) to (5.3) with  $\Delta\Gamma_A$  and  $\Delta\Gamma_B$  respectively the change in the

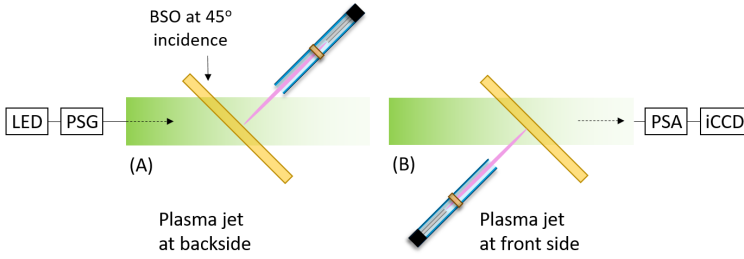


Figure 5.3: Top view image of the plasma-target configuration with regard to the axis of propagation of the polarized light beam within the Mueller polarimeter. Polarized light set using the *Polarizer State Generator* travels through the electro-optic material at 45 degrees, after which it passes through the *Polarizer State Analyzer* and reaches the iCCD camera. Two configurations are used (called configuration A on the left and B on the right) where the plasma jet is either impacting on the front or backside of the electro-optic BSO crystals.

birefringent pattern (in a certain coordinate system) measured during impact with the plasma jet on either the back side or front side.

$$E_y = \frac{\Delta\Gamma_{0/90,A} + \Delta\Gamma_{0/90,B}}{2} \cdot \left( \frac{2\pi d^*}{\lambda} \cdot \frac{r_{41} n_o^3}{2} \right)^{-1} \quad (5.1)$$

$$E_x = \frac{\Delta\Gamma_{45/135,A} + \Delta\Gamma_{45/135,B}}{2} \cdot \left( \frac{2\pi d^*}{\lambda} \cdot r_{41} n_o^3 \cdot \frac{1}{\sqrt{2}} \right)^{-1} \quad (5.2)$$

$$E_z = \frac{\Delta\Gamma_{45/135,A} - \Delta\Gamma_{45/135,B}}{2} \cdot \left( \frac{2\pi d^*}{\lambda} \cdot r_{41} n_o^3 \cdot \frac{1}{\sqrt{2}} \right)^{-1} \quad (5.3)$$

The examination done in this chapter focuses on the surface dynamics of the ionization waves impacting perpendicularly for different applied voltage amplitudes of the pulsed plasma jet. The plasma jet is first positioned according to configuration A, where the ionization waves impact the side of the electro-optic material facing the PSA and iCCD camera. Time-resolved measurements of the Mueller matrix are performed, similarly as discussed in the previous chapter. A trigger signal is used to measure the optical properties time-resolved for the different applied voltages. Then the plasma jet is moved to the other side (configuration B) facing the light source and PSG, where the measurements are repeated. Afterwards, the resulting birefringent images are compared to retrieve images of all the electric field components individually.

Before the electric field measurements are performed, first imaging of the light emission during the impact of the ionization waves is captured. This is necessary for two reasons. Firstly, since a time-resolved examination is done during the

interaction, there is light emission from the plasma that reaches the detector. This has to be subtracted from the intensity elements that are used for the measurement of the Mueller matrices (i.e. the *dark* images). Secondly, the ionization waves impact the electro-optic BSO material, rather than glass as was used for figure 5.1. Imaging of light emission allows a comparison of the dynamics that occur for the different targets. The imaging is performed at the same settings as will be used for the electric field measurements using the Mueller polarimeter and will be shown first in the next section.

### 5.1.3 Time-Resolved Plasma Impact on BSO

Imaging of the light emission is done to capture the impact dynamics of the ionization waves generated with the  $1\ \mu\text{s}$  pulsed plasma jet for various voltage amplitudes. A trigger signal is used relating to the rise of the high voltage pulse (50 ns rise time and 5 kHz repetition frequency). The trigger is set similarly as in the previous chapter, meaning the delay is varied from 199.6 to 202.0  $\mu\text{s}$  to capture the entire pulse dynamics. There are 200  $\mu\text{s}$  in between the pulses so the high voltage potential is applied between 200.0 and 201.0  $\mu\text{s}$ . The exposure time at each time instance is set to 100 ns, instead of 25 ns as shown in the beginning of this chapter. This is done since the same settings will be used for the electric field measurements and the acquisitions with the Mueller polarimeter takes longer. The chosen exposure times of 100 ns reduces the total acquisition time, hence limits possible surface damage, but yet is still accurate enough to capture the characteristic surface dynamics as will be shown.

The light emission is captured with the BSO tilted at 45 degrees and the plasma jet oriented perpendicularly to the surface. As a result the impact is seen from an angle. The lateral dimensions are compensated to represent the *XY*-plane, i.e. the radial plane in which the ionization waves spread after impacting on the surface perpendicularly. The time-resolved light emission imaging is shown in two parts, the first part during the pulse is shown in figure 5.4, while the light emission after the pulse is shown in figure 5.5. The time delay is shown relative to the pulse cycle, applied from 0.0 to 1.0  $\mu\text{s}$ , meaning in these figures the additional 200  $\mu\text{s}$  is left out.

The number of images taken per time step is not the same for the different applied voltages. This is important to notice when comparing light intensities in for instance in the plume. When applying the 3 kV constant high voltage pulses 10 images were accumulated in each frame, which was repeated and averaged 50 times. The same was done for the 6 kV pulses with a 1.5 slm helium flow. This examination case was added to examine the changes that occur when the 1.0 slm helium flow is increased. The measurements with 4 and 5 kV pulses accumulated 20 images per frame and were averaged 50 times, meaning the intensity shown in figures 5.4 and 5.5 are automatically 2 times higher. The same is true for the

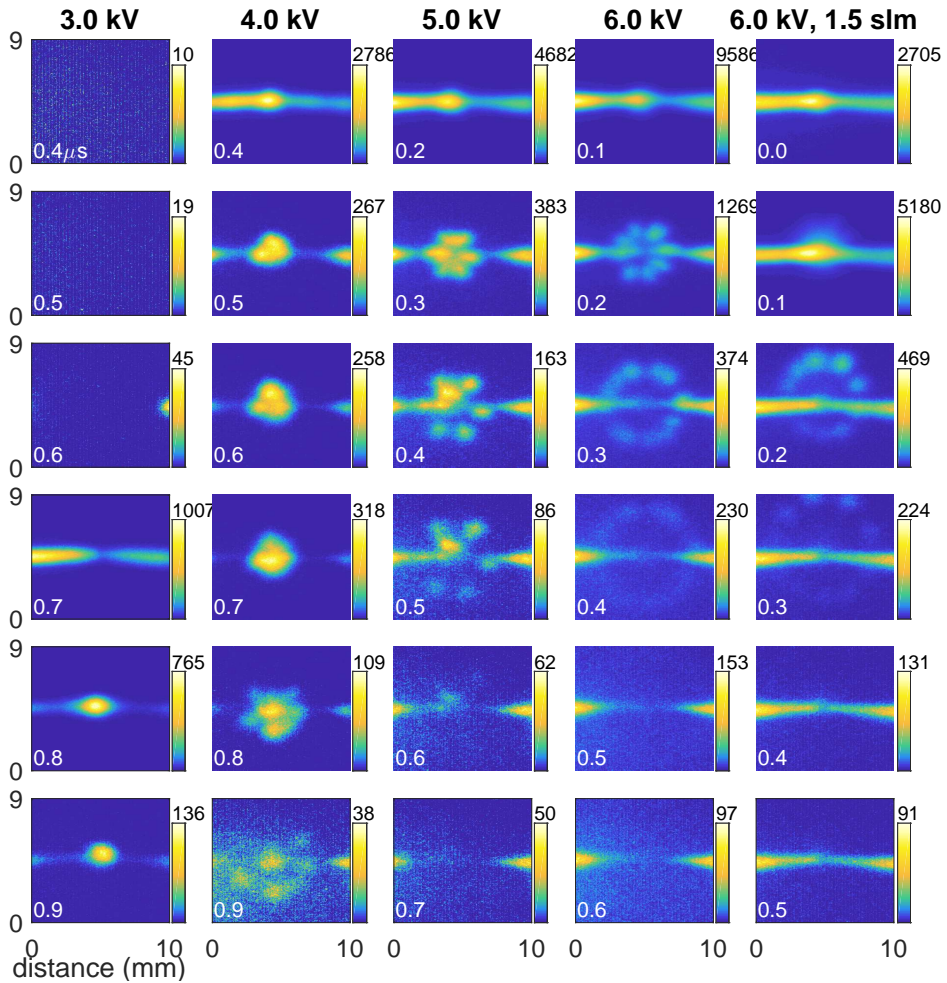


Figure 5.4: The light emission (arb. units) from the perpendicularly impacting ionization waves, generated with different voltage amplitudes. A 5th case is added with 6 kV pulses and a flow of 1.5 slm helium instead of 1.0 slm. Exposure times of 100 ns are used and the time delay (shown in white) is varied and shown during the pulse until maximally  $t_d = 0.9 \mu s$ . Later timescales after the pulse ends ( $> 1.0 \mu s$ ) are shown in figure 5.5. The plasma plume is observed on the left side of the impact and a mirror image is present on the right side. The jet is located 10 mm away from the surface. The lateral dimensions are compensated to show the length scales in the radial  $XY$ -plane, tangential to the surface.

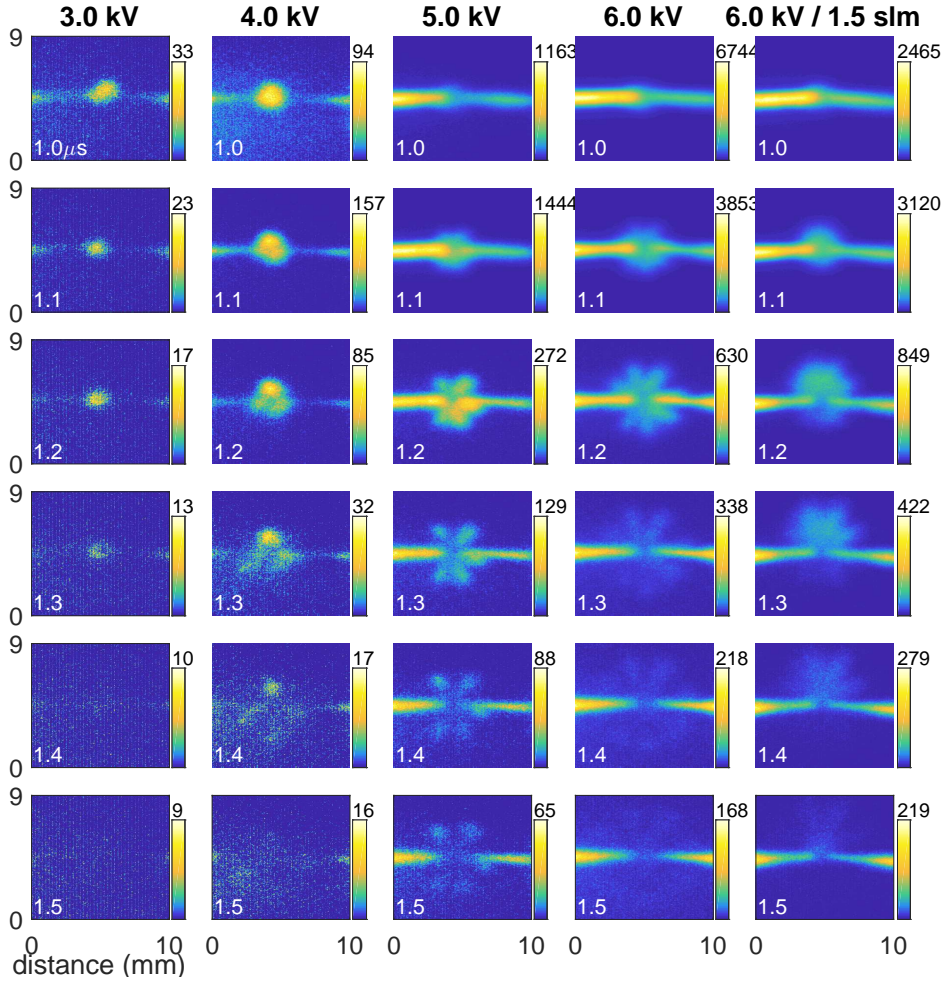


Figure 5.5: The second part of the time-resolved examination of the perpendicular impact of the ionization waves on BSO. The time delay is varied and shown after the pulse has ended, from 1.0 to 1.5  $\mu\text{s}$ , for the different applied voltage amplitudes. For information about the number of acquisition frames per time instance (different per measurement set) see the main text.

measurement with 6 kV pulses (and the “normal” 1.0 slm helium flow), where 20 images are accumulated per frame, but they were averaged only 40 times. From the light emission images, several observations can be made, starting with the dynamics during the high voltage pulse (figure 5.4).

Firstly, the timing of the impact of the ionization waves varies with the applied voltage. For 3 kV the initial impact occurs in between 0.8 and 0.9  $\mu\text{s}$  relative to the rise of the voltage pulse. Since 100 ns exposure times are used the accuracy is less precise than shown previously for the time-resolved imaging on glass. On glass the impact occurred respectively after 850, 400, 225 and 150 ns for the 3, 4, 5 and 6 kV pulses. The initial impacts observed on BSO shown in figure 5.4 relates well with this, which gives a first indication that the dynamics have not been altered significantly by a change of the target.

The second observation concerns the different (surface) patterns that are observed. For the 3 kV amplitude the impact region is small and only increases slightly due to a radial surface propagation. This changes for 4 kV where first a radial expansion is seen until 0.7  $\mu\text{s}$ , after which light emission patterns are shown that indicate the presence of radial surface streamers. Again the temporal behavior matches the behavior observed in figure 5.1. The main difference with the patterns observed before on glass is the spatial length of the patterns. It seems that the surface discharge on glass spreads further than on BSO. This is related to the difference in dielectric constant, which changes the amount of charge that is deposited during the interaction. The permittivity of glass is lower than BSO, meaning that the capacitance is lower as well, which results in less charge lost to the surface. Therefore the ionization wave is able, hypothetically, to propagate further.

The radial streamers appear earlier for higher applied voltages with higher light emissions reaching the detector. The amount of visible branches also seem to increase and it is worth noticing that these patterns are observed while averaging over a large amount of discharge events. This suggest that there is a bifurcation of the surface dynamics, since the stability of the surface branching is quite remarkable. If the surface streamers would have not been reproducible, then the light emission would appear as a disk due to the averaging.

Besides the examination of the influence on different voltage amplitudes, also a 5th case is added in which 6 kV pulses are used while the helium flow is increased from 1.0 slm to 1.5 slm. The patterns that are shown look similar but the timing is slightly different. Again radial surface branching is observed, relatively fast after the initial impact.

For all measurements the highest observed intensity of light emission, either in the impact point or in the plume, decreases quite rapidly in time. This is also present in the images shown on glass in figure 5.1, but less noticeable due to the glow inside the capillary tube.

When the high voltage potential drops, after  $1.0 \mu\text{s}$ , the light intensity briefly increases as shown in figure 5.5, except for the 3 kV pulses. The light emission increases due to the generation of the second (recombination) wave. The drop in high voltage potential at the inner electrode is rapidly noticed at the impact point, proving the existence of a conductive channel left behind the path of propagation by the ionization wave. For higher voltages, light emission increases in intensity in the plume and is seen originating from the surface. The radial streamer patterns are clearly visible, showing a 6 pointed stable star pattern for 5 kV pulses and a 8 pointed star pattern for 6 kV pulses.

The patterns that are observed share great similarities with the patterns that appeared during the pulse. This suggests that the second wave is largely influenced by charge deposition occurring during the first event. This means that the second wave is a back discharge, similar as discussed in other (dielectric) plane configurations.<sup>57,148-150</sup> This is further examined by applying Mueller polarimetry to investigate which electric fields are induced at those time instances.

## 5.2 Time-Resolved Electric Field Patterns

The electric field generated inside a targeted material is examined similarly as done in the previous chapter in section 4.4.3. The time-resolved Mueller matrices are captured at the same relative time instances as the imaging was performed shown in figures 5.4 and 5.5, with the same acquisition settings. This means that the images of the light emission can be used as *dark images* which are subtracted from the intensity images used to build the Mueller matrices. The logarithmic decomposition is applied to retrieve the two linear retardances and eventually equations (5.1) to (5.3) are used to analyze the (linear) birefringent patterns measured with the plasma jet in configuration A and B to retrieve patterns of all the electric field components separately.

The measured Mueller matrices are different than presented before since the electro-optic target is examined at a 45 degree angle. Therefore they will be shown and discussed for two time instances, representing the optical state before impact and after impact. These two examples are part of a larger time-resolved series as will be shown with the final electric field patterns. The examples shown are for the applied voltage amplitude of 4 kV with a helium flow of 1.0 slm.

Figure 5.6 shows the obtained time-resolved imaging Mueller matrices of the BSO material examined at a 45 degree angle while under continuous exposure of the pulsed plasma jet. The top matrix shows the (optical) state of the material

<sup>57</sup>D. M. ORLOV et al. *AIAA J.* 2008 **46**: 3142-3148

<sup>148</sup>S. MASUDA and A. MIZUNO *J. Electrostat.* 1977 **4**: 35-52

<sup>149</sup>G. FONT and W. MORGAN *35th AIAA Fluid Dyn. Conf. Exhib.* 2005 **6**: 4632

<sup>150</sup>J. JÁNSKÝ et al. *J. Electrostat.* 2015 **76**: 238-245

before impact, taken at  $t_d = 0.2 \mu\text{s}$ , without the influence of an external electric field. The second (bottom) image shows the Mueller matrix of the sample after impact has occurred, at  $t_d = 0.7 \mu\text{s}$ . The plasma jet is located on the backside of the electro-optic BSO, corresponding to configuration A facing the iCCD camera. The optical properties that are included in the matrix are entangled and therefore a decomposition is needed for analysis.

For the shown images, the scale in the horizontal direction has been multiplied by a factor of  $\sqrt{2}$  in order to compensate the deformation caused by the tilt of the crystal. By doing so, the shape of the impact point has the same visual size and scale as if the crystal was viewed with an illumination at normal incidence, similar as was done for the imaging of the light emission. Hence, the images correspond to a spatial area of  $16 \times 16 \text{ mm}^2$ . The end of the capillary tube (width 4 mm) is visible on all images, blocking partially the light on the left-hand side.

The Mueller matrices show similarities with the matrices shown in the previous chapter where the BSO was examined at normal incidence. One noticeable difference, however, is that the first row  $\{1, 2 - 4\}$  and column  $\{2 - 4, 1\}$  is not null. This is because of the inclined angle of examination. In this condition the Fresnel coefficients describing the global transmission of the crystal are not equal for polarization state parallel and perpendicular to the tilt angle. This is interpreted as a linear diattenuation property of the sample.

The imaging Mueller matrices share a resemblance with the previous measurements in terms of elements  $\{2 - 4, 2 - 4\}$ , that include the entangled information relating the optical activity and the induced stationary background patterns. To retrieve the actual optical properties a decomposition is necessary to disentangle them.

The logarithmically decomposed matrices  $L_m$  and  $L_u$  are shown in figures 5.7 and 5.8 respectively. As a consequence of the applied decomposition, the off-diagonal elements of the logarithmic matrices are (anti) symmetric and the optical properties are disentangled. A linear diattenuation is visible in the  $L_m$  matrix in the  $0/90$  coordinate system, shown in  $\{1, 2\}$  and  $\{2, 1\}$  with a value of  $0.24 \pm 0.005$  rad.

The circular and linear retardances measured before impact are shown in elements  $\{2, 3\}, \{2, 4\}$  and  $\{3, 4\}$  of  $L_m$  with their respective anti-symmetric counterparts. The patterns of the stationary background birefringent images are slightly different than observed before in chapter 4, which is both due to the changed impact angle of the plasma jet and the propagation direction of the polarized light through the material. The circular retardance, shown in elements  $\{2, 3\}$  and  $\{3, 2\}$  of  $L_m$ , is equal to 0.77 rad and the uncertainty is given in the corresponding  $L_u$  matrix elements by  $\pm 0.18$  rad. This is the largest uncertainty shown in the  $L_u$  matrix. The other uncertainties and depolarization properties (diagonal elements) are close to zero. The uncertainty for  $\Gamma_{l/r}$  is relatively higher than was observed

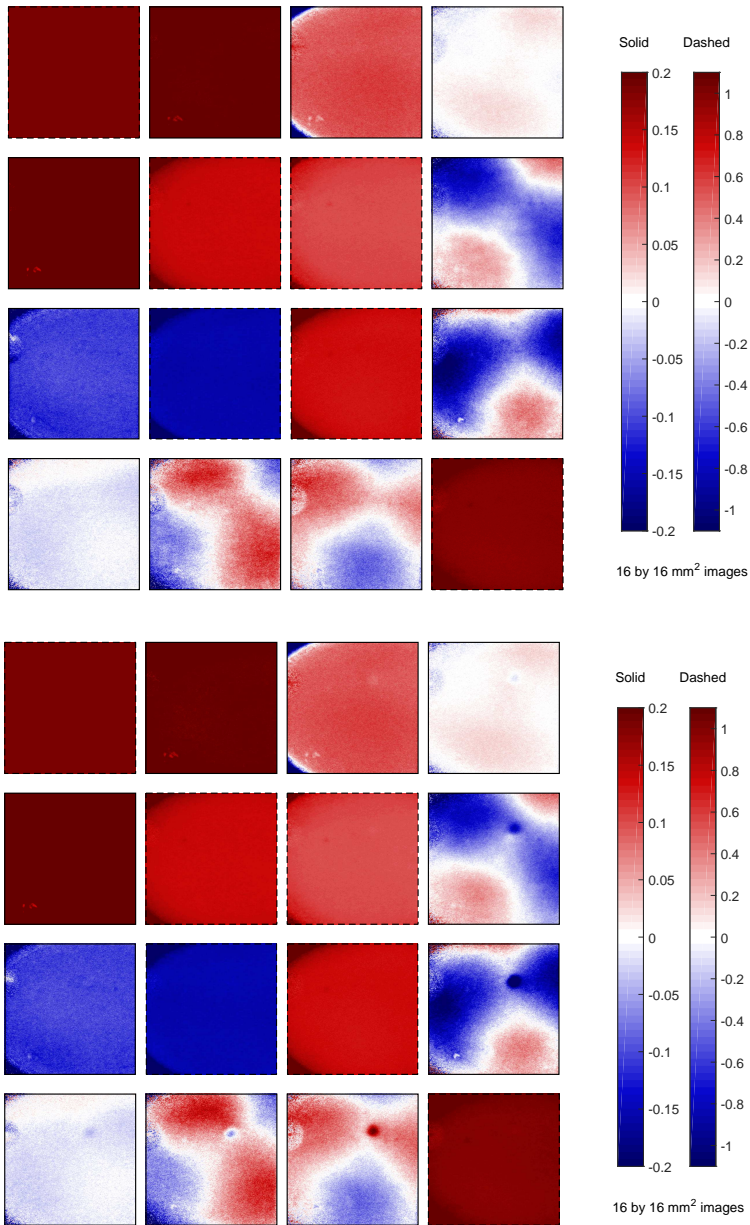


Figure 5.6: Mueller matrices obtained of the electro-optic BSO examined at 45 degrees under perpendicular exposure of guided ionization waves produced using a pulsed plasma jet operated using 4 kV pulses, measured time-resolved and shown before impact  $t_d = 0.2 \mu\text{s}$  (top) and after  $t_d = 0.7 \mu\text{s}$  (bottom). Hence, the second matrix includes the effect of temporally deposited surface charges. The image border (solid or dashed) indicates the colorscale.

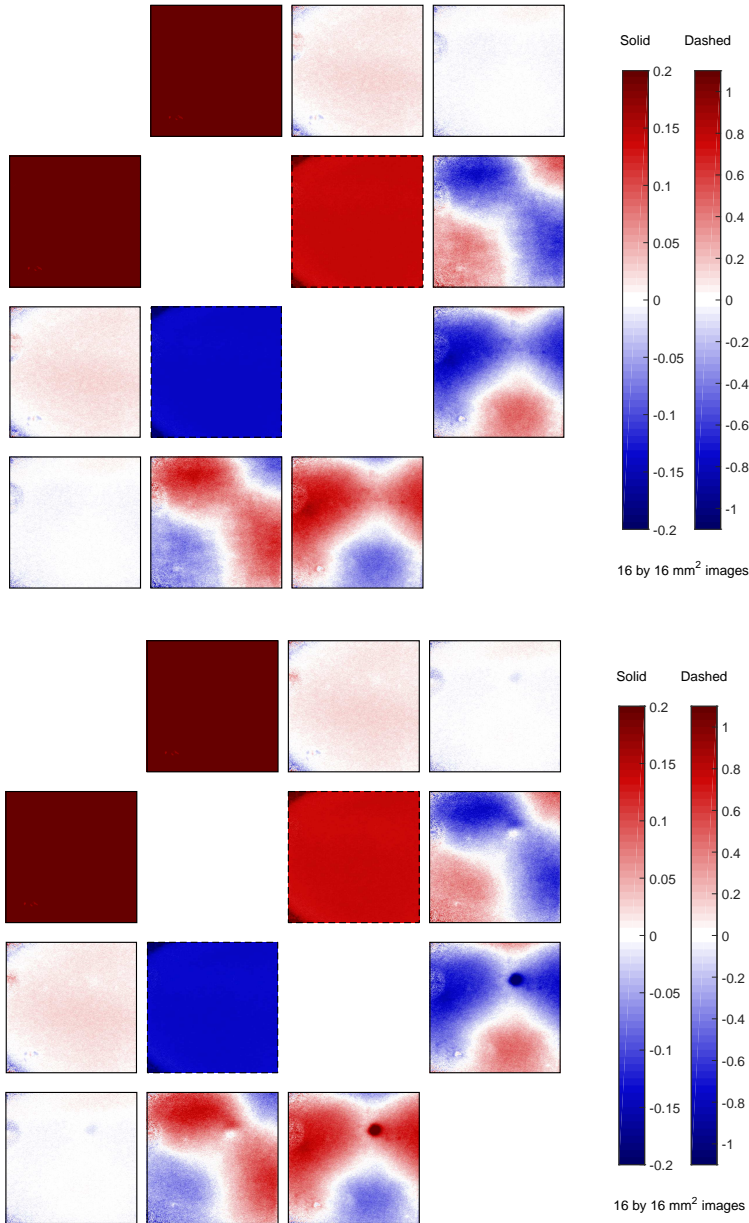


Figure 5.7: Logarithmically decomposed  $L_m$  matrices obtained from the measured Mueller matrices, shown time-resolved for  $t_d = 0.2 \mu s$  (top) and  $t_d = 0.7 \mu s$  (bottom). Now, not all the diattenuation properties are zero, shown in the first column and row. The birefringent properties (remaining elements) share similarities with previously shown matrices from chapter 4, although the patterns induced by the temporally deposited surface charges are slightly different due to the altered impact angle of the jet.

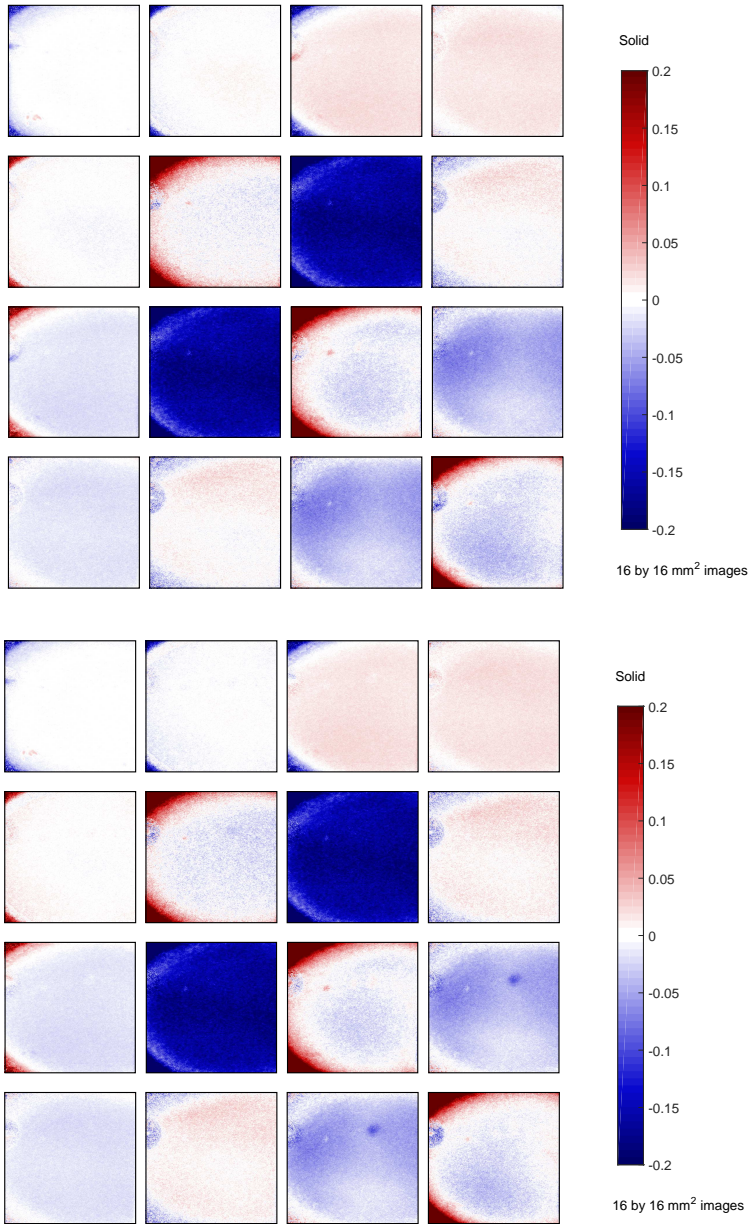


Figure 5.8: Logarithmically decomposed  $L_u$  matrices obtained from the measured Mueller matrices, shown time-resolved for  $t_d = 0.2 \mu\text{s}$  (top) and  $t_d = 0.7 \mu\text{s}$  (bottom). The diagonal elements represent the depolarization properties, while the off-diagonal elements relate to the uncertainty of the diattenuation and retardance.

in the previous chapters, which could be since an additional entanglement with the diattenuation is added to the Mueller matrix.

A change in the linear birefringent patterns is observed due to the temporal charge deposited during the plasma surface interaction in both the coordinate systems. These changes, obtained by simple subtraction of the patterns obtained before and after impact, are defined as  $\Delta\Gamma_{0/90,A}$  and  $\Delta\Gamma_{45/135,A}$ . A second set of measurements has to be done to retrieve  $\Delta\Gamma_{0/90,B}$  and  $\Delta\Gamma_{45/135,B}$  where the plasma jet is located on the other side of the material's surface (configuration B). The images of the electric field patterns can be obtained with the resulting changes in the birefringent patterns using equations (5.1) to (5.3). The time delay  $t_d$  can be varied to study time-resolved the plasma target interaction in terms of all the individual electric field components induced by the charge deposition.

Firstly, this has been applied for a collaborative work with Pedro Viegas and Anne Bourdon to examine a plasma surface interaction both experimentally and numerically. The experimental part, done using the Mueller polarimeter and discussed in section 5.2.1, examines the surface dynamics through imaging of the experienced electric field inside a targeted dielectric material by deposited surface charges during the perpendicular impact of guided ionization waves. The numerical part, done by Pedro Viegas using a fluid model and shown in section 5.2.2, examines a similar surface interaction where the contributions of volume charges and surface charges and the field they induce inside the targeted dielectric material are investigated.

Secondly, the examination is applied to investigate the dependence of the induced electric fields with the voltage amplitude of the constant pulses, complementary to the imaging done in section 5.1.3. This will be shown in section 5.2.3.

### 5.2.1 Electric Field Patterns during Interaction

The time delay relative to the rise of the 4.0 kV high voltage pulse is varied while measuring the Mueller matrix and analyzing the optical properties as shown in the previous section. The same examination is done with the plasma jet on the other side of the targeted crystals and from the comparison of the birefringent patterns, the time-resolved electric field patterns are retrieved. This can be compared phenomenologically with the numerical field calculation for a similar plasma surface interaction done by Pedro Viegas and shown in section 5.2.2.

Figure 5.9 shows the electric field patterns for the individual components measured time-resolved during the impact of the ionization waves generated by the pulsed plasma jet. The individual field patterns shown in each row at a specific time delay  $t_d$  are obtained using equations (5.1) to (5.3) applied to the measurement results with the plasma jet placed on the front and the backside of the target. Only changes induced by surface charge  $\sigma$  deposited during the impact of the ionization wave are visible in the images and any background pattern is not included.

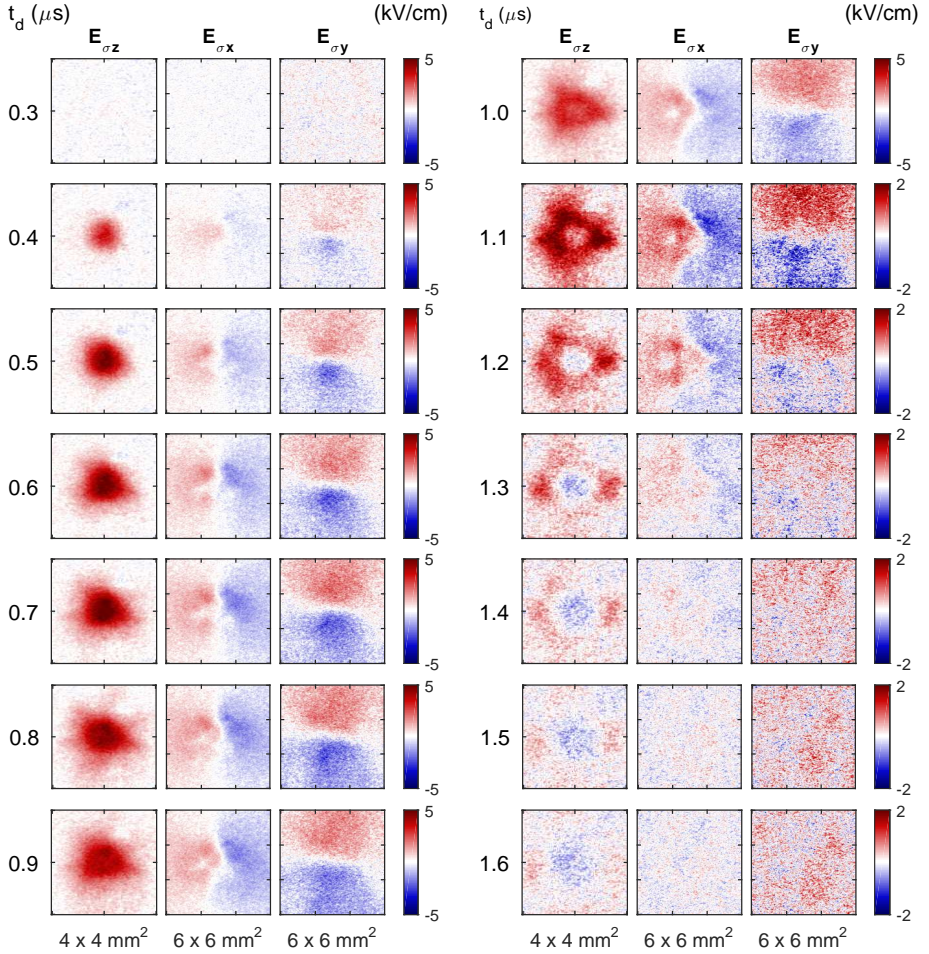


Figure 5.9: The individual electric field components (axial  $E_z$  and radial  $E_x$  and  $E_y$ ) induced inside the inclined BSO material under perpendicular exposure of guided ionization waves produced by the pulsed plasma jet operated using a 1 slm helium flow and a 4 kV voltage amplitude ( $1 \mu\text{s}$  constant pulse with 50 ns rise time, repetition rate 5 kHz). The surface charge  $\sigma$  induced field patterns, shown either as a  $4 \times 4 \text{ mm}^2$  or a  $6 \times 6 \text{ mm}^2$  area, are obtained time-resolved relative to the rise of the voltage pulse.

The lateral dimensions in the horizontal direction are again compensated for the inclined angle and the images show either a  $4 \times 4 \text{ mm}^2$  area or a  $6 \times 6 \text{ mm}^2$  area. The patterns indicating the axial field  $E_z$  are concentrated around the location of the charge deposition and consequently are focused on a smaller area. The radial  $E_x$  and  $E_y$  components spread laterally further outside. This corresponds well with the results obtained in the previous chapter in section 4.4 for BSO and

Felinbo with the AC driven jet at a 45 degree impact.

Similar as before, exposure times of 100 ns are used and the first contact of the ionization wave is shown at  $t_d = 0.4 \mu\text{s}$ . This relates with the moment of impact shown by imaging in figure 5.1 on glass and figure 5.4 on BSO. Branching patterns are observed within the axial  $E_z$  field, occurring at  $t_d = 0.7 \mu\text{s}$ , which also corresponds with both imaging of light emission on glass and BSO. It seems differences between a glass target and a BSO target are limited, even though dielectric constants are different.

Comparison of the electric field patterns with the imaging of light emission for the 4 kV pulses, as shown in the second column of figure 5.4, reveals the resemblances of both the spatial and the temporal evolution. Between 0.4 and 0.7  $\mu\text{s}$  the light emission indicates that there is only a relatively small surface expansion around the impact point. This was shown as well on glass, see figure 5.2(b). The axial and radial electric field patterns show that charge deposition only occurred in these areas. The maximum of the axial field of 5 kV/cm is located in the center while the maximum of the radial fields lies at the edge of the charge deposition.

After 0.7  $\mu\text{s}$  the light emission shows the onset of surface streamers and this becomes also visible in the axial electric field patterns. For the radial electric field patterns this is less noticeable, except that they spread further.

When the pulse ends at 1.0  $\mu\text{s}$ , the light emission increases at the impact point due to the second wave, as shown in figure 5.5. This causes the electric field patterns to change immediately as well, starting in the center of the impact point. The electric field decreases radially in time starting from the impact point and even changes sign at 1.3  $\mu\text{s}$ . The radial change of the electric field pattern coincides with the light emission at the surface. The change of the electric field sign indicates that charge is deposited from opposite (negative) charge. This relates with observations made for the pulsed plasma jet impacting at 45 degree.

As discussed in the previous chapter the electric field values are an average throughout the 0.5 mm thick surface due to deposited surface charge  $\sigma$ . The convolution back to distribution patterns and values of  $\sigma$  is not straightforward and will therefore not be done throughout this work.

## 5.2.2 Comparison with a Numerical Fluid Model

The plasma surface interaction that is studied using Mueller polarimetry is further examined using an axisymmetric numerical fluid model by Pedro Viegas under the supervision of Anne Bourdon at the LPP laboratory at Ecole Polytechnique. Some of his results will be shown here that were obtained in a collaborative work to combine experimental observations obtained from the Mueller polarimeter with numerical results relating the charge propagation describing the ionization waves

near a dielectric target.<sup>151</sup> The main purpose is to gain an understanding of the charge dynamics during the plasma surface interaction and the electric fields they induce. This is important because although the individual electric field components induced by deposited surface charges is uniquely measured using Mueller polarimetry throughout this work, the effect it has on the plasma propagation itself is hard to examine with this technique.

Numerical models have been used in the past to investigate the propagation of ionization waves in the vicinity of different targets.<sup>76,78,79,152</sup> The focus of these works generally lied with the generation of the ionization wave, electric field profile in the plasma plume, production of radical oxygen and nitrogen species, spreading along the surface and the changes induced in the plume by the dielectric constant of the targeted material. The electric fields induced inside the dielectric materials are rarely examined, except by<sup>79</sup>, not to mention the individual electric field components induced by either volume or surface charge in axial and/or radial direction.

The numerical results are obtained using a 2D axisymmetric fluid model in cylindrical coordinates where the charge dynamics are studied following the drift-diffusion equations coupled to the Poisson's equations for the electrons and ions. This method has been used successfully in the past for other investigations of discharge dynamics.<sup>77,153-155</sup> A more detailed explanation of the model used to examine the plasma-target interaction occurring with the plasma jet in the vicinity of (dielectric) targets can be found in the dissertation of Pedro Viegas.

Similar as shown in figure 5.1 a plasma jet is modeled generating ionization waves that impact a 0.5 mm thick glass target at 10 mm distance from the end of the capillary tube. The electrode configuration inside the plasma jet is slightly different than the plasma jet which is used in the experiments. An inner ring is used as powered electrode, while there is no outer grounded ring present. A high constant voltage pulse of 4 kV is applied similar as the experiments, with a rise time of 50 ns. A stationary gas mixing is included using flow calculations for a 1 slm helium flow plus 10 ppm O<sub>2</sub> impurity inside the capillary flowing into a pure O<sub>2</sub> environment. The purpose of this first comparison between Mueller polarimetry and fluid modeling of the discharge is not to compare exact numbers in terms of densities or electric fields, but to discuss the plasma surface interaction phenomenologically by comparing the relative influence of volume and surface

<sup>151</sup>P. VIEGAS et al. *Plasma Sources Sci. Technol.* 2018 [accepted manuscript](#)

<sup>76</sup>Y. SAKIYAMA et al. *J. Phys. D: Appl. Phys.* 2008 **41**: 095204

<sup>78</sup>D. BREDEN and L. L. RAJA *Plasma Sources Sci. Technol.* 2014 **23**: 065020

<sup>79</sup>S. A. NORBERG et al. *J. Appl. Phys.* 2015 **118**: 013301

<sup>152</sup>L. WANG et al. *Phys. Plasmas* 2016 **23**: 103504

<sup>77</sup>F. PECHEREAU et al. *Plasma Sources Sci. Technol.* 2012 **21**: 055011

<sup>153</sup>J. JÁNSKÝ and A. BOURDON *Plasma Sources Sci. Technol.* 2014 **23**: 025001

<sup>154</sup>A. BOURDON et al. *Plasma Sources Sci. Technol.* 2016 **25**: 035002

<sup>155</sup>P. VIEGAS et al. *Plasma Sources Sci. Technol.* 2018 **27**: 025007

charges and the electric fields they induce.

The resulting propagation of the numerical ionization wave shows great similarities with the observations shown in figure 5.1 both with the shape of the ionization front and with the velocity at which it travels. As the ionization wave approaches the dielectric target the axial movement is turned into a radial spread along the surface. In the experiments it has been observed that at a certain moment the isotropic spread initiates radial branching. This cannot be included in this axisymmetrical model. Therefore the high voltage pulse is ended at 800 ns instead of 1  $\mu s$ .

The model allows to track the time-resolved evolution of the charge density and the electric field that is subsequently created. In proximity of the dielectric surface, charge is deposited following charged particle fluxes through electric drift in the axial direction. The influence of volume charge density  $\rho$  and surface charges  $\sigma$  can be examined separately, together with the electric field they induce. A further division can be made of  $\vec{E}_\rho$  and  $\vec{E}_\sigma$  to their axial and radial components.

The spatial distribution of the volume charge density  $\rho$  as a function of time during the plasma surface interaction is shown in figure 5.11, together with the absolute total axial and radial electric field. The surface charge density  $\sigma$  is shown in figure 5.10, for the same time instances during the plasma exposure of the 0.5 mm thick glass. The  $z$ -axis is the initial axis of propagation of the ionization wave perpendicular to the surface of the material but as the interaction continues the discharge spreads along the radial  $r$ -axis along the surface which is defined at  $z = 0$ .

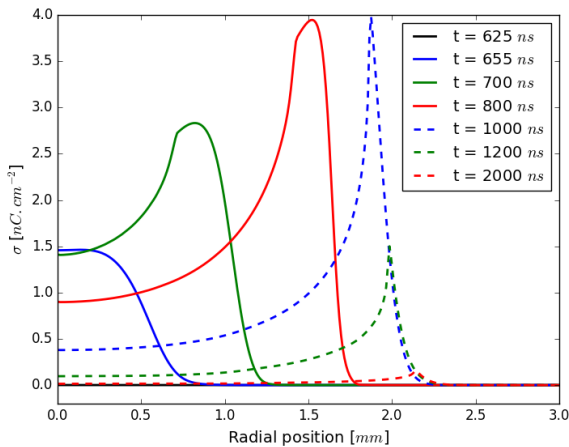


Figure 5.10: The surface charge density  $\sigma$  during the interaction of a guided ionization wave impacting on a glass target, as calculated by Pedro Viegas using an axisymmetrical numerical fluid model.

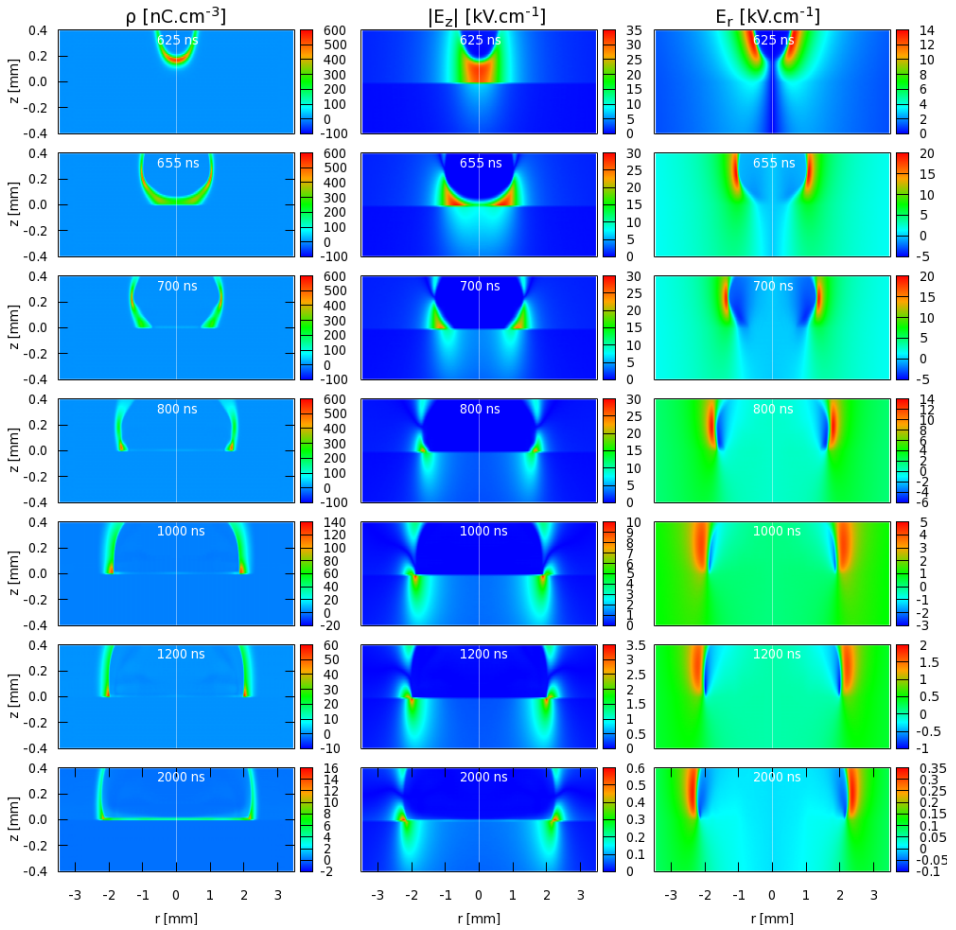


Figure 5.11: The volume charge density  $\rho$  as the (numerical) ionization wave approaches and spreads on the dielectric surface located at  $z = 0$ , together with the absolute electric field in axial and radial direction, as calculated by Pedro Viegas using an axysymmetrical numerical fluid model. The images focus around  $z = 0$ , which is the location of the surface of the glass target which ends at  $z = -0.5$  mm. The ionization wave approaches from the top and spreads radially as it interacts with the dielectric surface.

It shows that the surface gets charged in time during the pulse and then when the potential drops (here at 800 ns) first charges are removed in the center of the impact region. This corresponds well with observations from figure 5.9.

The individual contributions of  $\sigma$  and  $\rho$  to the electric field components in axial and radial direction are separated and shown in figure 5.12. During the interaction the electric field values are higher in the gas phase than inside the target. High

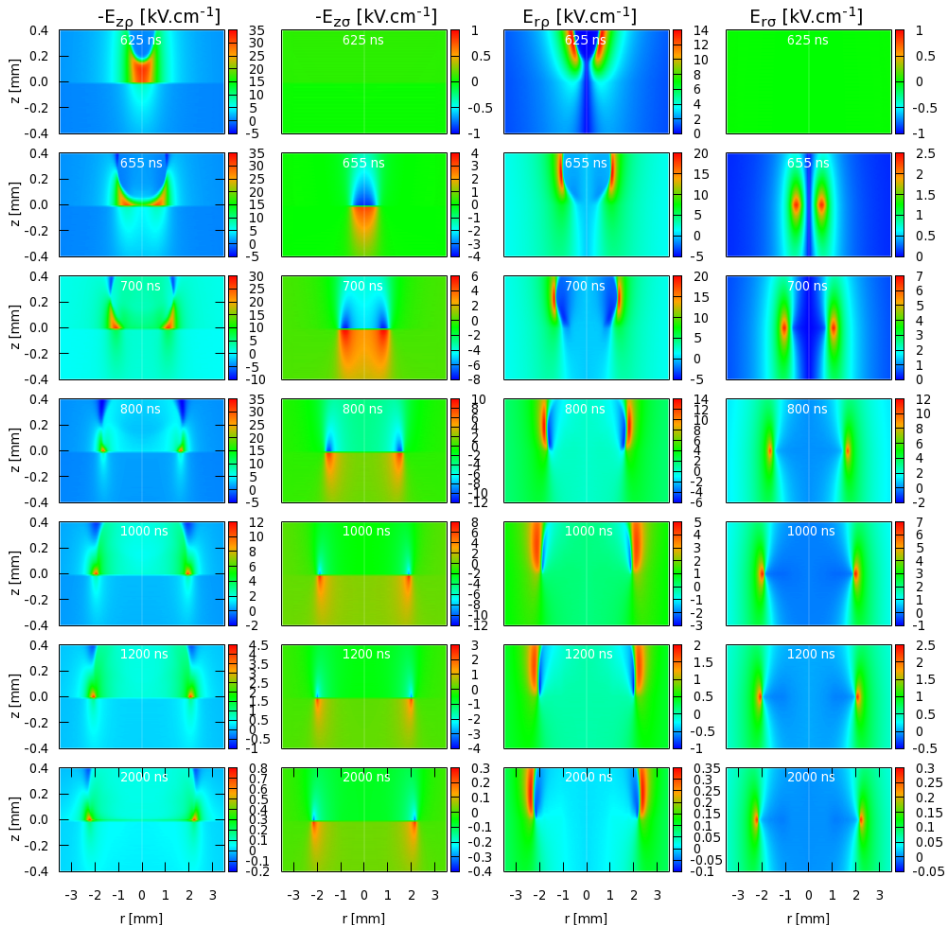


Figure 5.12: The individual electric field contributions caused by  $\sigma$  and  $\rho$  in axial and radial direction as the (numerical) ionization wave approaches and spread on the dielectric surface located at  $z = 0$ , calculated by Pedro Viegas using an axysymmetrical numerical fluid model. The pulse ends after 800 ns which causes removal of surface charge in the center of the impact region.

electric fields in the ionization front due to local charge separation are necessary for the propagation of the discharge. The high values in this region match the experimentally obtained values using Stark shift of forbidden helium lines<sup>66</sup> and using an electro-optic probe.<sup>18,154</sup>

During the radial spreading of the discharge, positive volume charge remains in proximity of the deposited surface charge, which is also of positive polarity. As

<sup>66</sup>A. SOBOTA et al. *Plasma Sources Sci. Technol.* 2016 **25**: 065026

<sup>18</sup>T DARNY et al. *Plasma Sources Sci. Technol.* 2017 **26**: 045008

a result, the total field in front of the surface cancels out. Inside the material however, there is a contribution of the electric field due to both the left-over volume charges and the deposited surface charges, which generate a field in negative axial direction. The influence of electric field induced by the peak volume charge inside ionization front is only present in the proximity of the location of the propagation wavefront. Hence, they are generated locally on short timescales.

The numerical field patterns illustrate very clearly the differences between the electric field components induced by the surface charge as has been shown in the experiments in figure 5.9. The  $E_{z\sigma}$  component relates strongly to the location and profile of the surface charge distribution, while  $E_{r\sigma}$  is highest at the edges of the impact area.

As stated, the electric fields shown in the experimental results due to surface charge are an average value throughout the thickness of the material. Visible in the patterns shown in figure 5.12 is that the  $E_{r\sigma}$  patterns decay faster in the axial direction than  $E_{z\sigma}$ . Consequently, the experienced field is lower in the radial direction throughout the first 0.5 mm thick layer of any sample.

More importantly, the model shows that although the fields that are induced in the gas phase are locally high, the electric field that a target experiences on longer timescales induced by the interaction are lower. This is because the field that is induced in the material for longer timescales comes from surface charges that have been deposited and left-over volume charges that are present in much lower densities than in the front of the ionization wave.

Consequently, the importance of Mueller polarimetry as a diagnostic to examine electro-optic crystals under plasma exposure is stressed since the electric field experienced inside the material due to surface charges can be investigated directly. Lastly, what the model shows is that the total field inside the material will be slightly higher than for instance shown in figure 5.9 due to these left-over volume charges. A different diagnostic has to be used to examine these, e.g. by examining Stark shift of forbidden helium lines. The possibility to selectively examine the electric field induced solely due to surface charge is important for the field of plasma catalysis and applications where electroporation or dielectrophoresis can play a role.

It should be emphasized that the numerical calculations were done on glass, which has a different dielectric constant than BSO. As a result, the interaction is in principle different than observed in the experiments with Mueller polarimetry. Further advances have to be made both experimentally and numerically, to do a more precise comparison where charge patterns and electric field values can be discussed which was at the moment not possible yet.

### 5.2.3 Variation of Voltage Amplitude

The experimental technique is applied to examine the electric field generated by the perpendicular impact of ionization waves produced by the plasma jet operated at different applied voltage amplitudes. This relates to the examination done in the previous chapter in section 4.4.3, where the pulsed plasma jet was operated in the same way but the impact angle was 45 degrees instead of 90 degrees. It was shown there that large surface discharges can be formed behind the initial impact point due to the inclined angle. The electric field that was induced depended on the voltage amplitude and surprisingly lower fields were measured with higher voltage amplitudes, indicating less charge deposition. In this section the examination is repeated but with the plasma jet impacting perpendicularly to see which fields are induced then. The measurements relate to the imaging of light emission as shown in figures 5.4 and 5.5.

The plasma-target interaction as investigated for 4.0 kV high voltage pulses (in section 5.2.2) is also examined time-resolved for voltage amplitudes ranging from 3 to 6 kV, while a constant helium flow of 1 slm is used. With an amplitude of 6 kV an additional measurement is performed with a helium flow of 1.5 slm to do a comparison with the normal flow of 1.0 slm.

The resulting time-resolved electric field patterns resolved axially and radially induced in the BSO materials are shown for the 6 kV pulses (1.0 slm helium) in figures 5.13 and 5.14, while the results for the other measurements (3 kV and 5 kV for 1.0 slm He and 6kV with 1.5 slm He) are shown in appendix A. The measurement procedure was identical as done for the results shown in figure 5.9 for the 4 kV pulses.

The time-resolved induced electric field patterns for the 6 kV pulsed generated ionization waves are split into two figures. Figure 5.13 shows the field patterns during the pulse and figure 5.14 shows the patterns after the high potential has been brought back to zero.

During the pulse, the electric field patterns are easily related to the light emission images obtained before and shown in figure 5.4. The ionization wave impacts relatively early, between 0.1 and 0.2  $\mu\text{s}$  after the rise of the mono-polar pulse. This is because the higher applied voltage induces a higher propagation velocity for the ionization wave. Immediately after impact, a star pattern is observed which corresponds perfectly to the pattern seen with imaging of the light emission.

For 6 kV pulses, the electric field patterns show the occurrence of 8 stable radial surface streamers. Remember that every intensity element (of 16 in total) needed to construct the Mueller matrix consists of 20 accumulations per frame that is averaged 40 times. This means that more than 12000 exposure events have been analyzed to construct the electric field images. The stability of the pattern induced by the surface streamers is remarkable and suggests a bifurcation of the system. Leftover surface charges from the previous cycle play possibly a role, but

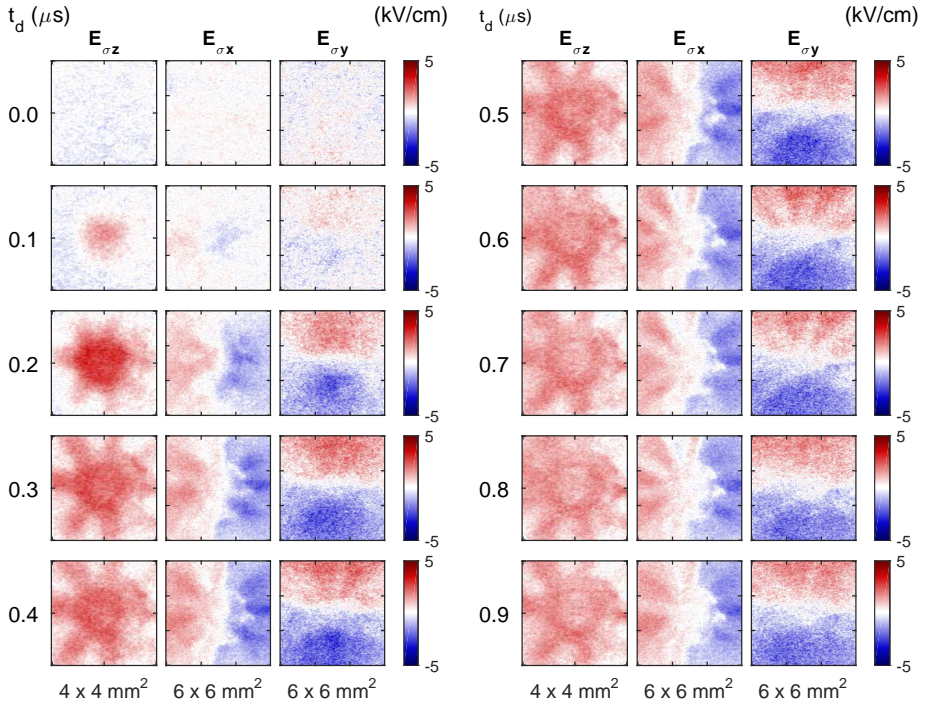


Figure 5.13: Time-resolved electric field patterns (resolved axially and radially) induced inside an electro-optic target by ionization waves impacting perpendicularly. The plasma jet is operated using a 1 slm helium gas flow and  $1 \mu\text{s}$  mono-polar positive voltage pulses of 6 kV in amplitude. The measured fields are shown during the application of the high voltage potential. The fields obtained after the high voltage pulse has ended are shown in figure 5.14.

there is a relatively long time in between the pulses of  $200 \mu\text{s}$ .

During the last part of the high voltage pulse, the electric field patterns are stable, coinciding with an absence of light emission. This indicates that the dynamics at the surface are stable. The stable patterns that are shown relate to an isotropic expansion which forms a ring structure from which 8 streamer branches are initiated. From the fluid model introduced in section 5.2.2 it was found that behind the surface front a stable interaction is formed between the temporarily deposited surface charge and leftover volume charge. The field measured and presented throughout this work only relates to the contribution of the surface charge.

The axial field values have decreased compared to values shown for 4 kV, while the radial field patterns have become slightly larger. This feature was also shown in the previous chapter for the AC driven jet when the voltage was increased. It suggests that the local charge density is reduced, but the total charge deposited

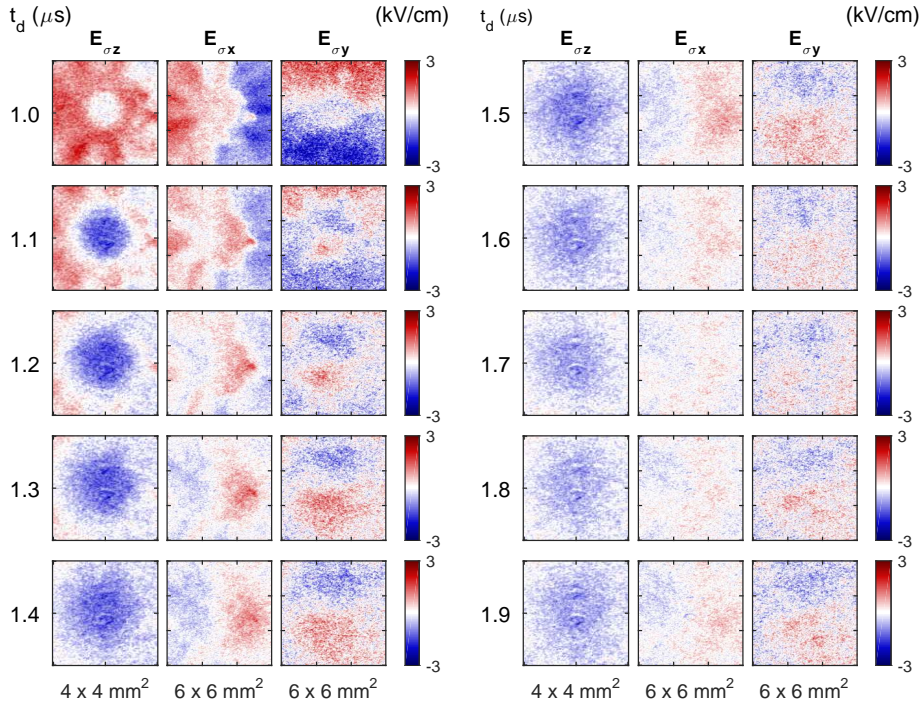


Figure 5.14: Time-resolved electric field patterns obtained after the 6.0 kV high voltage pulse has ended. Similar remarks hold as given for figure 5.13, where the field is shown during the high voltage pulse (i.e.  $t_d < 1.0 \mu\text{s}$ ).

has increased due to an increase of interaction area.

When the high voltage potential is reduced to zero, at  $1.0 \mu\text{s}$ , the stability of the leftover volume charges and surface charges is broken. From imaging it has been seen that a second ionization event is quickly formed which influences the target. Figure 5.14 shows that the electric field patterns change almost instantly as well. From the center of the impact point, the electric field is reduced and field of opposite polarity is seen. The negative axial field patterns show an isotropic pattern, which does not match the light emission shown in figure 5.5 where surface streamers were seen that correspond to the star pattern that was induced during the pulse. This is remarkable because for all the other measurements throughout this thesis the induced electric field pattern always relates to the light emission. This indicates that the dynamics that occur for this second phase of the plasma surface interaction are different, relating to the back discharging that occurs when the so-called recombination wave is initiated as the potential is brought back to zero.

The negative axial fields, induced by negative surface charges, are higher in

value and are seen for longer timescales than for the 4 kV pulses. This can be caused since there is more surface charge deposited during the pulse which influences this back discharging. All the changes that are observed take place on longer timescales than the increase and decrease of the high voltage pulse, which has a rise and fall time of 50 ns.

Besides 4 and 6 kV pulses also the time-resolved electric field patterns have been obtained for 3 kV and 5 kV pulses. Additionally, for 6 kV pulses the helium flow has increased from 1.0 to 1.5 slm. All of these results, shown for each time delay varied during and after the interaction, can be found in the appendix A. From each time-resolved set for each applied voltage amplitude the resulting patterns from one specific time delay are shown in figure 5.15 during the positive half period. The time delays chosen resemble either the highest (axial) electric field or the typical pattern that is induced during that specific time-resolved series.

The electric field in the center of the impact point is shown in figure 5.16 as a function of time during the interaction for the different applied voltage amplitudes. The shown values are an average in the center of the impact point over a  $0.5 \times 0.5 \text{ mm}^2$  area ( $20 \times 20 \text{ px}^2$ ). The error bar indicates the standard deviation in this area.

Both figure 5.15 and 5.16 show that the axial field is highest when operating the plasma jet with 4.0 kV high voltage pulses. The maximal electric field in the impact point decreases when higher voltage amplitudes are used. This is related with the shape of the surface charge density which induces  $E_{\sigma z}$ . When the voltage is higher than 4 kV the maximum electric field value is not in the center but in a ring around the impact point. Also these values are lower than 5 kV/cm. Radial streamer patterns are observed that initiate from this ring.

When the helium flow is increased from 1.0 to 1.5 slm the electric field decreases further and the ring structure is enlarged. The lowering of the electric field could be a result of the new gas mixing that has decreased the oxygen density along the plasma plume, which influences the processes important for the shape of the ionization wave, e.g. Penning ionization or electron detachment.<sup>146,156</sup>

The ring shape could mean that the higher applied voltage has caused the ionization wave to turn the axial propagation in a radial spread on a further distance from the target than with a lower voltage. It has been observed before that the diameter of the angularly shaped ionization wave in the plasma plume region become larger for higher applied voltages,<sup>147</sup> which could relate to the change in the patterns as shown in figure 5.15.

The appearance of surface streamers indicates that the peak volume charge density must be higher with higher applied voltages. This relates to findings presented in literature for a different pulsed plasma jet where the reduced electric field increases with the applied voltage amplitude.<sup>147</sup> Another reason why the vol-

<sup>156</sup>Y. SAKIYAMA et al. *Appl. Phys. Lett.* 2010 **96**: 041501

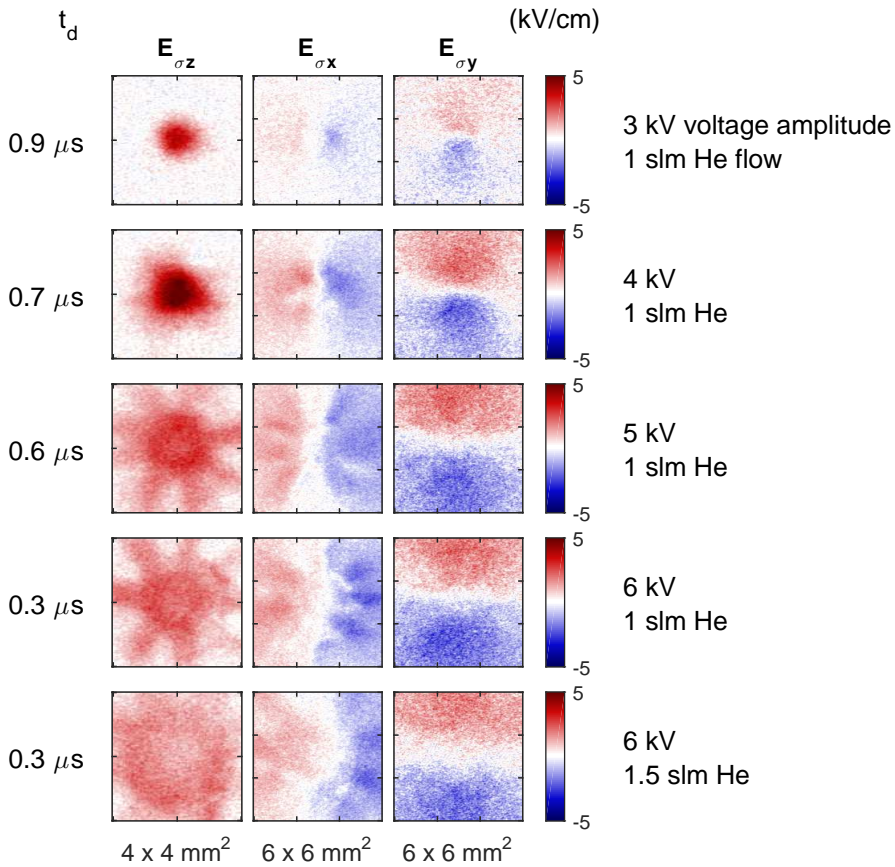


Figure 5.15: The individual components of the electric field patterns obtained at a specific time delay  $t_d$ , relative to the rise of the voltage pulse, while varying the voltage amplitude. Each time delay is part of a time-resolved measurement series, which is shown either in this chapter or in appendix A. The plasma jet is in all cases impacting at 90 degrees at 10 mm from the target.

ume charge density is likely to be higher is because the ionization waves travel faster since the impact at the surface occurs earlier in time.

Even though volume charge densities are likely to be higher with an increasing voltage amplitude, the axial electric field values inside the material due to the surface charges seem to decrease. Only the total area of the plasma surface interaction increases which results in an increase of the radial field values. This has been observed as well in the last chapter in section 4.4 when the AC sine wave was substituted with the constant high voltage pulses, impacting at 45 degrees.

The decrease in axial electric field values indicates that less charge is locally

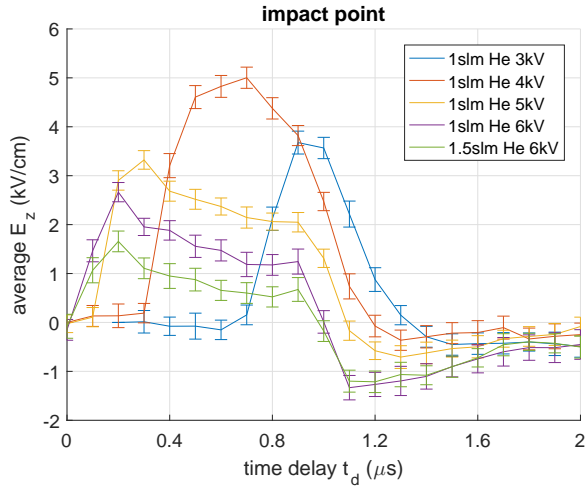


Figure 5.16: The axial electric field averaged in the center of the impact point as a function of time during the high voltage pulse ( $0 \leq t_d \leq 1.0 \mu\text{s}$ ) and after ( $t_d > 1.0 \mu\text{s}$ ) for different voltage amplitudes. The changes are much slower than the increase / decrease of the constant high voltage pulse (50 ns).

deposited during the plasma interaction. This is possible since the interaction time has decreased because the ionization waves propagate faster over the surface.

Negative axial electric field values are observed in the impact point after the pulse has ended at  $t_d = 1.0 \mu\text{s}$  for higher applied voltages. Also the polarity of the radial electric field patterns is reversed. This indicates that charge is deposited of opposite sign, i.e. negative surface charges. The rapid decrease back to zero of the applied potential has caused this. More negative charge is deposited for higher pulse amplitudes. This suggests that the back discharging that occurs after the pulse has ended is influenced by the total amount of charge that has been deposited during the pulse. This corresponds with the observed increase of light emission during this recombination wave at  $t_d = 1.0 \mu\text{s}$  shown in figure 5.5.

### 5.3 Summary and Perspectives

- A plasma target interaction has been investigated for a pulsed plasma jet impacting perpendicularly on a dielectric surface. This is done through imaging of light emission, which reveals the ionization wave propagation, and with Mueller polarimetry (at a 45 degree angle) applied to BSO to capture the electric field. Due to the inclined angle of examination of the electro-optic target, all the individual electric field components are obtained simultaneously. This is done time-resolved during and after the interaction as a function of voltage amplitude for the pulsed plasma jet.
- Imaging of light emission in the gas phase indicates that the ionization waves propagate with a higher velocity and consequently impact the surface earlier for higher applied voltage amplitudes. The spreading on the dielectric surface also changes, indicating two sequential stages. Initially, an isotropic spreading is observed after which a stable radial streamer pattern is formed. These star-shaped patterns occur for higher applied voltage amplitudes both on glass and BSO, but the length scales are different since the dielectric constants are not the same. The electric field patterns induced during the high voltage pulse show great resemblance with the imaging of light emission.
- The formation of the stable star-shaped patterns at higher voltages, together with the increased propagation velocity, suggests that the volume charge densities have increased. The induced electric field patterns inside the targeted material, however, suggest that locally less surface charge is actually deposited during the interaction since the maximum axial electric field values decrease from 5.0 to 2.6 kV/cm when the voltage is increased. This relates to the results obtained in section 4.4.3 with the pulsed plasma jet impacting at 45°. Surface charge densities have decreased during the plasma interaction since the interaction time has decreased due to the faster propagation. However in total, there is more charge deposited on the surface since the interaction area has increased. This influences the back discharging that occurs when the high potential reduces back to zero, which even deposits negative charges.
- In a collaborative work a comparison is made with a numerical axisymmetric fluid model by Pedro Viegas to follow the volume and surface charge densities in time during the interaction and the individual electric field components they generate. This is done for a fixed voltage amplitude of 4 kV. It has been found that the electric field which a material experiences during a plasma interaction is determined by two effects. On short time scales relatively high electric fields are generated in the vicinity of the ionization front, due to peak volume charges. On longer time scales, the induced electric field

is lower since it is induced by surface charges that are deposited by the impact and left-over volume charges in the vicinity of the material.

- The time-resolved examination of the electro-optic material includes the subtraction of the observed stationary *background* patterns to only focus on the electric field. However, even though the patterns are not related to the electric field, they are still induced by the plasma surface interaction. Therefore more investigation has to be done to understand their origin and meaning. This will be the subject of the next chapter.

## References

- [18] T DARNY, J.-M. POUVESLE, V PUECH, C DOUAT, S DOZIAS, and E. ROBERT. *Plasma Sources Sci. Technol.* **26**: 045008, 2017. DOI: [10.1088/1361-6595/aa5b15](https://doi.org/10.1088/1361-6595/aa5b15) (see pp. 4, 146, 181)
- [57] D. M. ORLOV, G. I. FONT, and D. EDELSTEIN. *AIAA J.* **46**: 3142–3148, 2008. DOI: [10.2514/1.37514](https://doi.org/10.2514/1.37514) (see pp. 17, 98, 135)
- [60] M. TESCHKE, J. KEDZIERSKI, E. FINANTU-DINU, D. KORZEC, and J. ENGMANN. *IEEE Trans. Plasma Sci.* **33**: 310–311, 2005. DOI: [10.1109/TPS.2005.845377](https://doi.org/10.1109/TPS.2005.845377) (see pp. 20, 125)
- [66] A. SOBOTA, O GUAITELLA, G. B. SRETENVIĆ, I. B. KRSTIĆ, V. V. KOVAČEVIĆ, A OBRUSNÍK, Y. N. NGUYEN, L ZAJÍČKOVÁ, B. M. OBRADOVIĆ, and M. M. KURAICA. *Plasma Sources Sci. Technol.* **25**: 065026, 2016. DOI: [10.1088/0963-0252/25/6/065026](https://doi.org/10.1088/0963-0252/25/6/065026) (see pp. 20, 102, 146, 179, 183)
- [76] Y. SAKIYAMA, D. B. GRAVES, and E. STOFFELS. *J. Phys. D. Appl. Phys.* **41**: 095204, 2008. DOI: [10.1088/0022-3727/41/9/095204](https://doi.org/10.1088/0022-3727/41/9/095204) (see pp. 22, 143)
- [77] F. PECHEREAU, J. JÁNSKÝ, and A. BOURDON. *Plasma Sources Sci. Technol.* **21**: 055011, 2012. DOI: [10.1088/0963-0252/21/5/055011](https://doi.org/10.1088/0963-0252/21/5/055011) (see pp. 22, 143)
- [78] D. BREDEN and L. L. RAJA. *Plasma Sources Sci. Technol.* **23**: 065020, 2014. DOI: [10.1088/0963-0252/23/6/065020](https://doi.org/10.1088/0963-0252/23/6/065020) (see pp. 22, 143)
- [79] S. A. NORBERG, E. JOHNSEN, and M. J. KUSHNER. *J. Appl. Phys.* **118**: 013301, 2015. DOI: [10.1063/1.4923345](https://doi.org/10.1063/1.4923345) (see pp. 22, 89, 143)
- [144] X. LU and M. LAROSSI. *J. Appl. Phys.* **100**: 063302, 2006. DOI: [10.1063/1.2349475](https://doi.org/10.1063/1.2349475) (see p. 125)
- [145] Z. XIONG, X. LU, Y. XIAN, Z. JIANG, and Y PAN. *J. Appl. Phys.* **108**: 103303, 2010. DOI: [10.1063/1.3511448](https://doi.org/10.1063/1.3511448) (see p. 125)
- [146] G. V. NAIDIS. *J. Phys. D. Appl. Phys.* **44**: 215203, 2011. DOI: [10.1088/0022-3727/44/21/215203](https://doi.org/10.1088/0022-3727/44/21/215203) (see pp. 125, 151)
- [147] J. JARRIGE, M. LAROSSI, and E. KARAKAS. *Plasma Sources Sci. Technol.* **19**: 065005, 2010. DOI: [10.1088/0963-0252/19/6/065005](https://doi.org/10.1088/0963-0252/19/6/065005) (see pp. 128, 151)
- [148] S. MASUDA and A. MIZUNO. *J. Electrostat.* **4**: 35–52, 1977. DOI: [10.1016/0304-3886\(77\)90107-3](https://doi.org/10.1016/0304-3886(77)90107-3) (see p. 135)
- [149] G. FONT and W. MORGAN. *35th AIAA Fluid Dyn. Conf. Exhib.* **6**: 4632, 2005. DOI: [10.2514/6.2005-4632](https://doi.org/10.2514/6.2005-4632) (see p. 135)
- [150] J. JÁNSKÝ, D. BESSIÈRES, J. PAILLOL, and F. LEMONT. *J. Electrostat.* **76**: 238–245, 2015. DOI: [10.1016/j.elstat.2015.05.028](https://doi.org/10.1016/j.elstat.2015.05.028) (see p. 135)

- 
- [151] P. VIEGAS, E. SLIKBOER, A. OBRUSNIK, Z BONAVENTURA, A. SOBOTA, E. GARCIA-CAUREL, O. GUAITELLA, and A. BOURDON. *Plasma Sources Sci. Technol.* accepted manuscript, 2018. DOI: [10.1088/1361-6595/aadcc0](https://doi.org/10.1088/1361-6595/aadcc0) (see p. 143)
- [152] L. WANG, Y. ZHENG, and S. JIA. *Phys. Plasmas* **23**: 103504, 2016. DOI: [10.1063/1.4964482](https://doi.org/10.1063/1.4964482) (see p. 143)
- [153] J. JÁNSKÝ and A. BOURDON. *Plasma Sources Sci. Technol.* **23**: 025001, 2014. DOI: [10.1088/0963-0252/23/2/025001](https://doi.org/10.1088/0963-0252/23/2/025001) (see p. 143)
- [154] A. BOURDON, T. DARNY, F. PECHEREAU, J.-M. POUVESLE, P. VIEGAS, S. ISÉNI, and E. ROBERT. *Plasma Sources Sci. Technol.* **25**: 035002, 2016. DOI: [10.1088/0963-0252/25/3/035002](https://doi.org/10.1088/0963-0252/25/3/035002) (see pp. 143, 146)
- [155] P. VIEGAS, F. PÉCHEREAU, and A. BOURDON. *Plasma Sources Sci. Technol.* **27**: 025007, 2018. DOI: [10.1088/1361-6595/aaa7d4](https://doi.org/10.1088/1361-6595/aaa7d4) (see p. 143)
- [156] Y. SAKIYAMA, D. B. GRAVES, J. JARRIGE, and M. LAROSSI. *Appl. Phys. Lett.* **96**: 041501, 2010. DOI: [10.1063/1.3298639](https://doi.org/10.1063/1.3298639) (see p. 151)



# Chapter 6

## Temperature Profiles Induced by the Plasma Jet Interaction

### Contents

---

<b>6.1 Optical Effects Induced by Temperature</b> . . . . .	<b>160</b>
6.1.1 The Background Structure . . . . .	160
6.1.2 The Photo-Elastic Effect . . . . .	161
6.1.3 Temperature Induced Strain . . . . .	163
<b>6.2 Calibration of the Coupling Constants</b> . . . . .	<b>164</b>
6.2.1 Procedure to Retrieve the Temperature Pattern . . . . .	166
6.2.2 Calibration through Variation of Applied Voltage . . . . .	168
<b>6.3 Summary and Perspectives</b> . . . . .	<b>175</b>
<b>References</b> . . . . .	<b>176</b>

---

This chapter investigates the dependence of the electro-optic BSO crystal on externally delivered heat and the resulting inhomogeneous temperature distribution inside the material. The birefringence this induces is caused by internal strain, following the photo-elastic effect (also called elasto-optic effect). The first part of this chapter shows the relation between the temperature (gradient) and the induced birefringence, i.e. the stationary *background* as has been mentioned in the previous chapters but systematically subtracted to obtain the electric field results. The second part shows how the measured birefringence can be used to determine the temperature pattern inside the material using a fitting procedure. Lastly, a calibration is performed by using the proposed fitting procedure on the birefringent background patterns measured while operating the AC plasma jet at different voltage amplitudes.

## 6.1 Optical Effects Induced by Temperature

### 6.1.1 The Background Structure

The birefringent patterns observed in the previous chapters, reshown in figure 6.1 and referred to as “background”, are stationary in time and can therefore not be caused by a surface charge induced electric field since this is time dependent. Through subtraction of the birefringent patterns obtained before and after impact the *background* is easily removed to be able to focus only on changes induced by charge deposition during the plasma interaction. This has been done in the previous chapters as well as in other works.<sup>86,87</sup> However, no explanation of the occurrence of the background has been given.

It will be shown here that this background structure is induced by a temperature effect inside the material. The BSO material is potentially thermo-optic, although this has never been investigated thoroughly,<sup>157</sup> which made this idea plausible. The observed patterns, however, shared no resemblance to a temperature distribution. According to the thermo-optic effect, the birefringent pattern that should be observed would relate to the temperature distribution linearly, in a similar way as the electric field has induced the birefringent pattern relating to the location of the deposited surface charges.

A second option related to an indirect effect of the temperature is internal stress due to a temperature gradient inside the material, causing a birefringent pattern to arise. Accordingly, the birefringence can be related to the stress through the photoelastic effect which is then coupled to a temperature gradient.

Several miscellaneous tests were done (not shown in detail in this thesis), which gave the convincing arguments to pursue this hypothesis. They include measurements of the Mueller matrix of BSO under different conditions of exposure without a discharge present. Firstly, a metal rod was heated in the vicinity of the surface of the crystal. Secondly, different gas flows were applied to create different inhomogeneous temperature profiles. Lastly, when the semi-spherical golden electrodes were used, as shown in chapter 3, to apply a potential difference to the ITO coated regions on the surface for a homogeneous electric field, an inhomogeneous birefringent pattern was created as a result. This pattern shows similarities with the patterns induced by the other miscellaneous tests as well as the time-constant *background* field observed when exposing the electro-optic target to the plasma jet, as shown in figure 6.1.

The possibility to use the measured linear birefringent patterns to investigate the temperature of the BSO crystal under plasma exposure is very interesting for the investigation of plasma-target interactions. First of all, the temperature is

---

<sup>86</sup>E. SLIKBOER et al. *Plasma Sources Sci. Technol.* 2016 **25**: 03LT04

<sup>87</sup>E. SLIKBOER et al. *Plasma Sources Sci. Technol.* 2017 **26**: 035002

<sup>157</sup>M. R. R. GESUALDI et al. *J. Optoelectron. Adv. Mater.* 2011 **13**: 643–647

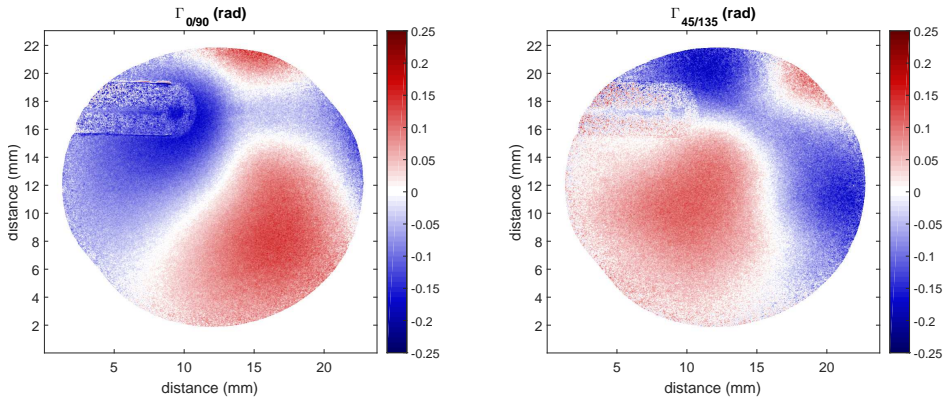


Figure 6.1: The two stationary *background* birefringent patterns for the 0/90 degree coordinate system and the diagonal 45/135 degree system. The measurements are obtained through examination of the BSO crystal at normal incidence while under plasma exposure with the plasma jet horizontally at 45 degrees, 7 mm away from the target, operated using 2 kV voltage amplitude at 30 kHz AC frequency with a 1000 sccm helium flow. The capillary tube of the plasma jet is clearly visible blocking part of the patterns.

clearly important when temperature-sensitive targets are used – e.g. polymers for surface functionalization or biological targets, ranging from *in-vitro* cell cultures to *in-vivo* living patients that undergo medical treatment – since burning has to be prevented.<sup>12</sup> Additionally, some chemical processes related to nitrification can be altered within a relatively small range of temperature.<sup>158</sup> This will be elaborated in the next chapter, where the temperature induced by the plasma jet is investigated for different operating frequencies. Information is gained simultaneously about the electric field induced inside the target since Mueller polarimetry is applied to the examined BSO target.

### 6.1.2 The Photo-Elastic Effect

A similar analytical approach is followed to obtain the relation between the birefringence and the externally induced temperature gradient, as taken when deriving the electric field dependence in the previous chapters.

The case is examined for the investigation of the BSO crystal at normal incidence. This reduces the index ellipsoid to a two-dimensional ellipse, via intersection with the plane wave determined by the propagation direction of the light, as

<sup>12</sup>K.-D. WELTMANN et al. *Contrib. to Plasma Phys.* 2009 **49**: 631–640

<sup>158</sup>S. PFEIFFER et al. *J. Biol. Chem.* 1997 **272**: 3465–3470

shown by equation (3.5). The normal incidence ellipse in the XY-plane is perturbed by external anisotropies  $\Delta\eta_1$ ,  $\Delta\eta_2$  and  $\Delta\eta_6$ .

$$x^2 \left( \frac{1}{n_o^2} + \Delta\eta_1 \right) + y^2 \left( \frac{1}{n_o^2} + \Delta\eta_2 \right) + 2xy\Delta\eta_6 = 1. \quad (3.5 \text{ revisited})$$

To derive which retardance is induced when polarized light travels through the material, the refractive index has to be examined along the appropriate axis of the polarization state of the light. The change in refractive index  $\Delta n$  observed in that coordinate system relates to the retardance according to  $\Gamma = \frac{2\pi d}{\lambda} \Delta n$ , with thickness  $d$  and wavelength  $\lambda$ .

For the retardance observed in the 0/90 degree optical system the change in refractive index depends only with  $\Delta\eta_1$  and  $\Delta\eta_2$ , see equation (3.8). This is derived using equation (3.5), by finding the radii respectively when  $x \rightarrow 0$  and  $y \rightarrow 0$ , as shown in chapter 3.

$$\Delta n_{0/90} = \pm \frac{1}{2} n_o^3 (\Delta\eta_1 - \Delta\eta_2) \quad (3.8 \text{ revisited})$$

The change in refractive index in the 45/135 deg optical system depends on only  $\Delta\eta_6$ , see equation (3.9). This is obtained by finding the diagonal axis of the two-dimensional ellipse.

$$\Delta n_{45/135} = \pm n_o^3 \Delta\eta_6 \quad (3.9 \text{ revisited})$$

The externally induced anisotropies  $\Delta\eta_i$  are coupled to the source of the birefringence, e.g. electric field, stress or temperature, through the use of optical tensors. The electro-optic tensor was used for the coupling between  $\Gamma$  and  $\vec{E}$ , but for temperature  $T$  induced strain the photo-elastic tensor  $\vec{P}$  is used multiplied with the strain vector  $\vec{S}$ , see equation (6.1). The photo-elastic tensor for a cubic crystal with symmetry point group 23, like BSO, depends on 4 non-zero constants, i.e.  $p_{11}$ ,  $p_{12}$ ,  $p_{21}$  and  $p_{44}$ .<sup>40,123</sup> Consequently  $\Delta\eta_1$  and  $\Delta\eta_2$  depend on a combination of  $S_{1-3}$ , while  $\Delta\eta_6$  scales with  $S_6$ , see equation (6.2).

---

<sup>40</sup>C. MALGRANGE et al. 2014 ISBN: 978-94-017-8992-9

<sup>123</sup>R. C. POWELL 2010 ISBN: 978-1-4419-7597-3

$$\begin{pmatrix} \Delta\eta_1 \\ \Delta\eta_2 \\ \Delta\eta_3 \\ \Delta\eta_4 \\ \Delta\eta_5 \\ \Delta\eta_6 \end{pmatrix} = \bar{\mathbf{P}} \cdot \vec{S} = \begin{pmatrix} p_{11} & p_{12} & p_{21} & 0 & 0 & 0 \\ p_{21} & p_{11} & p_{12} & 0 & 0 & 0 \\ p_{12} & p_{21} & p_{11} & 0 & 0 & 0 \\ 0 & 0 & 0 & p_{44} & 0 & 0 \\ 0 & 0 & 0 & 0 & p_{44} & 0 \\ 0 & 0 & 0 & 0 & 0 & p_{44} \end{pmatrix} \cdot \begin{pmatrix} S_1 \\ S_2 \\ S_3 \\ S_4 \\ S_5 \\ S_6 \end{pmatrix} \quad (6.1)$$

$$= \begin{pmatrix} p_{11} \cdot S_1 + p_{12} \cdot S_2 + p_{21} \cdot S_3 \\ p_{21} \cdot S_1 + p_{11} \cdot S_2 + p_{12} \cdot S_3 \\ p_{12} \cdot S_1 + p_{21} \cdot S_2 + p_{11} \cdot S_3 \\ p_{44} \cdot S_4 \\ p_{44} \cdot S_5 \\ p_{44} \cdot S_6 \end{pmatrix} \quad (6.2)$$

### 6.1.3 Temperature Induced Strain

The strain vector  $\vec{S}$  is defined by gradients in the displacement vector  $\vec{u} = (u_x, u_y, u_z)$ ,<sup>40</sup> shown by equation (6.3). The components of the displacement vector are coupled linearly to the temperature gradients using constant  $\alpha$ , to describe temperature gradient induced strain, e.g.  $u_x \propto \partial T / \partial x$ .

The materials under exposure of the plasma are relatively thin,  $d = 0.5$  mm, compared to the lateral dimensions of the crystals ( $30 \times 30$  mm<sup>2</sup>). As a consequence, gradients in the  $z$  direction (perpendicular to the surface) can be neglected. Therefore the strain vector components  $S_{3-5}$  are zero, see equation (6.3).

$$\vec{S} \equiv \begin{pmatrix} \partial u_x / \partial x \\ \partial u_y / \partial y \\ \partial u_z / \partial z \\ \frac{1}{2}(\partial u_y / \partial z + \partial u_z / \partial y) \\ \frac{1}{2}(\partial u_x / \partial z + \partial u_z / \partial x) \\ \frac{1}{2}(\partial u_y / \partial x + \partial u_x / \partial y) \end{pmatrix} \propto \alpha \begin{pmatrix} \partial^2 T / \partial x^2 \\ \partial^2 T / \partial y^2 \\ \partial^2 T / \partial z^2 \\ \partial^2 T / \partial y \partial z \\ \partial^2 T / \partial x \partial z \\ \partial^2 T / \partial x \partial y \end{pmatrix} = \alpha \begin{pmatrix} \partial^2 T / \partial x^2 \\ \partial^2 T / \partial y^2 \\ 0 \\ 0 \\ 0 \\ \partial^2 T / \partial x \partial y \end{pmatrix} \quad (6.3)$$

The resulting linear birefringence  $\Gamma$  in the 0/90 deg optical system and the diagonal 45/135 deg system are finally obtained through substitution of the derived relations. This is shown in equations (6.4) and (6.5), where the  $\pm$  sign and constants  $\alpha$  and  $p_{ij}$  are contracted to form constants  $\gamma_{1-3}$ . This is done since both the coupling constant  $\alpha$  and the photo-elastic constants for BSO are not well investigated and reported in literature. Only one reference for some of the photo-elastic constant has been found.<sup>159</sup> This means it is more reliable to combine them and

<sup>159</sup>W. MARTIENSSEN and H. WARLIMONT 2005 ISBN: 978-3-540-44376-6

calibrate the newly defined  $\gamma_{1-3}$  instead.

$$\begin{aligned}
 \Gamma_{0/90} &= \pm \frac{2\pi d}{\lambda} \frac{1}{2} n_o^3 (S_1 \cdot (p_{11} - p_{21}) + S_2 \cdot (p_{12} - p_{11})) \\
 &= \pm \frac{2\pi d}{\lambda} \frac{1}{2} \alpha n_o^3 \left( \frac{\partial^2 T}{\partial x^2} \cdot (p_{11} - p_{21}) + \frac{\partial^2 T}{\partial y^2} \cdot (p_{12} - p_{11}) \right) \\
 &\equiv \frac{2\pi d}{\lambda} n_o^3 \left( \gamma_1 \frac{\partial^2 T}{\partial x^2} + \gamma_2 \frac{\partial^2 T}{\partial y^2} \right) \tag{6.4}
 \end{aligned}$$

$$\begin{aligned}
 \Gamma_{45/135} &= \pm \frac{2\pi d}{\lambda} \alpha n_o^3 p_{44} \frac{\partial^2 T}{\partial x \partial y} \\
 &\equiv \frac{2\pi d}{\lambda} n_o^3 \gamma_3 \frac{\partial^2 T}{\partial x \partial y} \tag{6.5}
 \end{aligned}$$

An analysis of order of magnitude reveals that the  $\gamma$  calibration coefficients should be approximately  $\pm 5 \cdot 10^{-12} \text{ m}^2/\text{K}$ , based upon the estimations shown in equation (6.6).

$$0.2[\text{rad}] = \frac{2\pi \cdot 0.0005[\text{m}]}{530 \cdot 10^{-9}[\text{m}]} \cdot 2.54^3 \cdot \gamma \cdot \frac{10[\text{K}]}{(0.005[\text{m}])^2} \tag{6.6}$$

More information about  $\gamma_{1-3}$  is obtained by investigating the derivatives of an assumed symmetrical Gaussian temperature profile, as shown in figure 6.2. The isotropic distribution of temperature, with a maximum amplitude of 10 °C and standard deviation of 0.5 cm, is shown for a  $2 \times 2 \text{ cm}^2$  area together with the first and second derivatives to  $x$  and  $y$ . The pattern shown by  $\frac{\partial^2 T}{\partial x \partial y}$  already shares great similarities with one of the background birefringent patterns, as the derived equations (6.5) predicts. A comparison with figure 6.1 demonstrates that  $\gamma_3$  has to be positive.

The other birefringent pattern is observed when a combination of  $\frac{\partial^2 T}{\partial x^2}$  and  $\frac{\partial^2 T}{\partial y^2}$  is taken, according to equation (6.4). A difference between the two second derivatives is necessary, instead of a sum, indicating that  $\gamma_1$  has to be negative and  $\gamma_2$  positive. A non-symmetrical background pattern can be induced when there is a (small) difference in magnitude between  $\gamma_1$  and  $\gamma_2$ , as shown in figure 6.3. The pattern arising for the case where  $|\gamma_1| < |\gamma_2|$  resembles the measured birefringent pattern.

## 6.2 Calibration of the Coupling Constants

The derived relations, equations (6.4) and (6.5), between the measured birefringence and the temperature distribution can be used to investigate the stationary *background* patterns. Unfortunately, an inversion of the derived relations is not

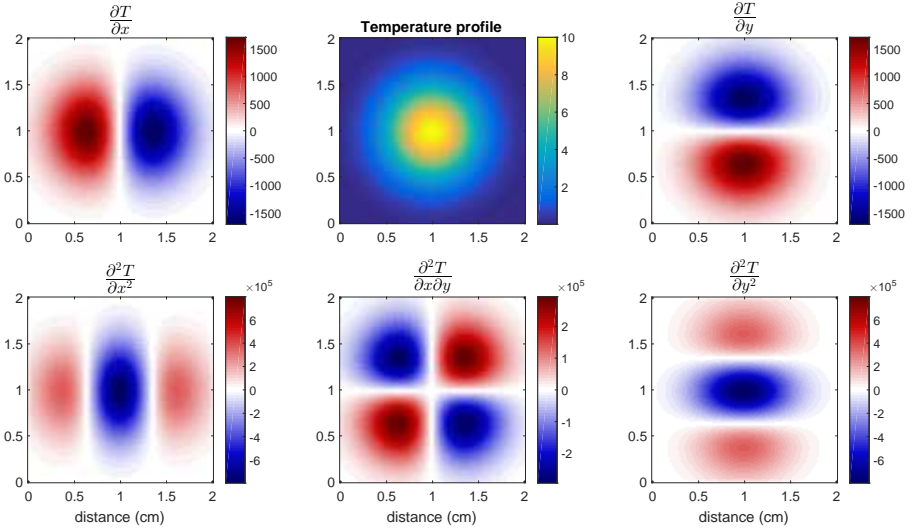


Figure 6.2: The first and second derivatives of a isotropic Gaussian temperature distribution, with an amplitude of 10 °C and standard deviation of 0.5 cm, shown for a  $2 \times 2$  cm<sup>2</sup> area.

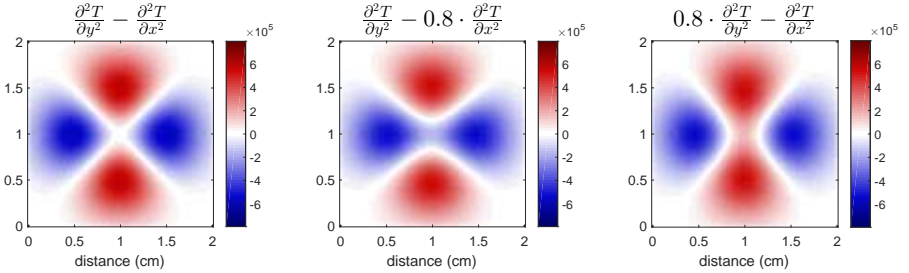


Figure 6.3: The resulting patterns arising when taking the difference between  $\frac{\partial^2 T}{\partial y^2}$  and  $\frac{\partial^2 T}{\partial x^2}$ . Three cases are shown, relatively when  $|\gamma_1| = |\gamma_2|$ ,  $|\gamma_1| < |\gamma_2|$  and  $|\gamma_1| > |\gamma_2|$ .

trivial, since this would involve partial integration of the measured birefringent patterns, while boundary conditions are not fixed.

A different approach is followed where a temperature profile is numerically created for which the second derivatives match the one measured, determined by the derived equations. This requires a calibrated value of  $\gamma_{1-3}$ . Consequently, a second method of determining the temperature distribution inside the material is needed to perform this calibration.

For this purpose, the temperature profile induced by a plasma jet in a targeted

material is investigated using a GaAs dielectric temperature probe sensor. This probe, consisting of a  $100\ \mu\text{m}$  small crystal on the end of a glass fiber, is used to scan the temperature pointwise along a fixed grid on the backside of a  $0.5\ \text{mm}$  thick glass under exposure of a plasma jet operated in similar conditions. The probe has also been tested on the backside of BSO (targeted in similar conditions) to make sure that the induced temperature is the same for the different targets.

The resulting temperature profiles will be compared with the numerical profiles obtained using a fitting procedure to match the measured birefringent patterns using Mueller polarimetry. In the next section, this fitting procedure is first introduced after which it is applied to calibrate  $\gamma_{1-3}$ . This is done using different background birefringent patterns measured under exposure of the plasma jet operated at different voltage amplitudes.

### 6.2.1 Procedure to Retrieve the Temperature Pattern

A simple iterative procedure is followed in *MATLAB* to obtain a temperature profile for which the second derivatives match the ones obtained from the birefringent patterns using Mueller polarimetry. First, the measured birefringent patterns, named  $\Gamma_{pol,0/90}$  and  $\Gamma_{pol,45/135}$ , are rescaled to a  $250 \times 250\ \text{px}^2$  area. This allows the algorithm / procedure to be applicable for almost all measurements and reduces computational cost. Most measurements have a *region of interest* consisting of a circular area with radius length in between 250 and 400 px.

A mask is created to remove the outer edges where noise levels are significantly higher as well as the area where the capillary tube of the plasma jet is blocking the light. The  $250 \times 250\ \text{px}^2$  area is located central to a larger domain (e.g.  $440 \times 440\ \text{px}^2$ ) in which the temperature profile is created numerically.

During each iteration of the fitting procedure an elliptical area  $T_g$  is randomly chosen with location coordinates  $X_r$  and  $Y_r = \text{randi}(440)$  and semi half axis  $wr_1$  and  $wr_2 = \text{randi}(200)$ , according to the following code.

```

1 Tg=zeros(440,440);
2 for i=1:440
3     for j=1:440
4         if sqrt((i-Yr)^2/wr1^2+(j-Xr)^2/wr2^2)<1
5             Tg(i,j)=1;
6         end
7     end
8 end

```

The area randomly indicated where  $T_g = 1$  will be the proposed change in temperature, but first it is smoothed three times using a Gaussian filter with a width of 25 px. This creates a Gaussian-like trial temperature profile with a maximum amplitude of 1 and no abrupt edges. The latter is important since second derivatives are taken to calculate the birefringent outcome.

```

9  for i=1:3
10 Tg=imgaussfilt(Tg,25);
11 end
12 Tg=Tr*Tg;
    
```

$T_g$  is multiplied with a randomly chosen *temperature gradient amplitude*, defined by  $T_r = \pm 0.05 \cdot 2^{randi(8)-4}$  with minimal value  $T_r = \pm 0.0063$  and maximally  $T_r = \pm 0.8$ . An example is shown in figure 6.4. This proposed temperature profile is added to the profile  $T_n$  built during the previous iterations  $T_{try} = T_n + T_g$ , which is used to calculate the linear birefringence. This is done using the *gradient* function with  $10^{-3}/sc$  the inner pixel distance. Often  $sc \approx 12$  px/mm after rescaling the measured birefringent patterns. Constants  $dd = 0.5$  mm,  $lamb = 530$  nm and  $n_0 = 2.54$  are predetermined while  $gamma1$  to  $gamma3$  are selected from a calibration procedure.

```

13 [px,py]=gradient(T_try, 1e-3./sc);
14 [pxx,pxy]=gradient(px, 1e-3./sc);
15 [pyx,pyy]=gradient(py, 1e-3./sc);
16 LB=2*pi*dd/lam*n0^3*gamma3*pxy;
17 LBp=2*pi*dd/lam*n0^3*(gamma1*pxx+gamma2*pyy);
18 N_1=sum(sum(MSK.*abs(LB-LB_0)));
19 N_2=sum(sum(MSK.*abs(LBp-LBp_0)));
    
```

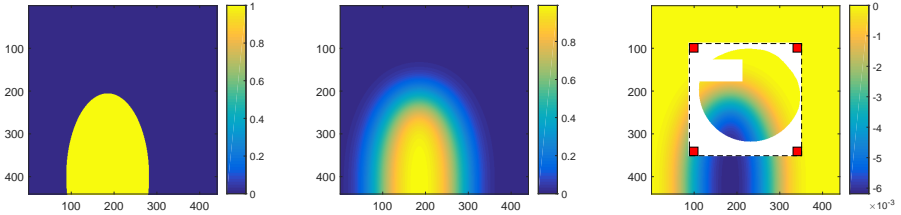


Figure 6.4: The left image shows an example of an initially chosen elliptical area, with  $Y_r = 399$ ,  $X_r = 186$ ,  $wr_1 = 193$  and  $wr_2 = 96$ . After applying the Gaussian filter three times it is smoothed and shown in the central image. Multiplication with  $T_r$  gives the image shown on the right ( $T_r = -0.0063$ ). This image also shows the measurement domain (within the black dashed border), together with the mask shown in white and 4 red squared areas indicating where the average corner temperatures are calculated.

A comparison is made with the measured birefringence and if a better match is obtained  $T_{try}$  is accepted and a new iteration is started. The acceptance protocol is determined by quantities  $N_1$  and  $N_2$  that are simply the cumulative absolute pixelwise difference between the newly found linear birefringence  $LB$  and  $LBp$  with  $LB_0 = \Gamma_{pol,0/90}$  and  $LBp_0 = \Gamma_{pol,45/135}$  using only pixels *within* the region defined by the mask  $MSK$ . When the new values of  $N_1$  and  $N_2$  are lower than their values in the previous cycle, the randomly proposed change in temperature profile is accepted.

Only one additional condition needs to be fulfilled, based upon the average temperature value on the corner edges of the region of interest (red squares in figure 6.4). A higher temperature profile is expected in the top right compared to the bottom left due to the orientation of the plasma jet and the buoyancy action. This condition has to be fulfilled during every iteration. Since  $T_r$  is allowed to be negative the overall / absolute temperature range is not controlled. After a certain amount of iterations the entire temperature profile is shifted in order that the minimum edge temperature in the bottom left corner is equal to zero, i.e. defined as the ambient room temperature.

The iteration steps are repeated 5000 times. An example of the outcome is shown in figure 6.5. No significant improvement to the fitting procedure with the temperature profile is obtained when a higher number of iteration steps is taken. The fitting procedure is restarted and repeated at least 10 times to check if a consistent temperature profile is obtained. The average maximum temperature is calculated from the repetitive fitting outcomes, together with the standard deviation. For the example shown in figure 6.5 values of  $\gamma_1 = -4 \cdot 10^{-12}$ ,  $\gamma_2 = 5.4 \cdot 10^{-12}$  and  $\gamma_3 = 10.8 \cdot 10^{-12} \text{ m}^2/\text{K}$  are used. The next section focuses on the determination of these calibration values.

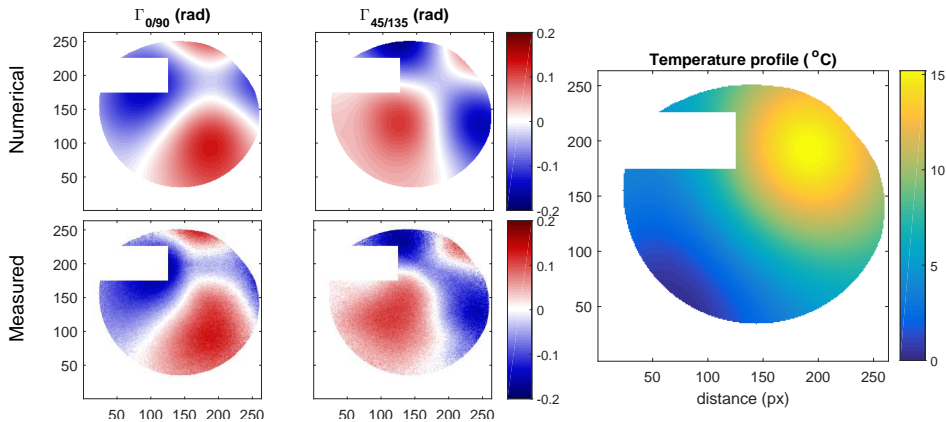


Figure 6.5: The obtained result of the fitting procedure algorithm. After 5000 alterations of a temperature profile have been tested, of which 721 have been accepted as improvement in this example, a temperature profile is obtained shown on the right for which the birefringent outcome matches the measured patterns, shown in the left images. This profile should correspond to the elevation of temperature compared to ambient conditions.

## 6.2.2 Calibration through Variation of Applied Voltage

Birefringent patterns induced by different temperature profiles will be analyzed to validate the proposed fitting procedure and determine which values of  $\gamma_{1-3}$  have

to be used. By operating the AC plasma jet at different applied voltage amplitudes, the amount of heat delivered to the target is varied and as a consequence different temperature patterns are formed.

A second technique, using a GaAs temperature probe sensor, is applied to map the temperature on the backside of a glass target in order to match the temperature profiles obtained from the fitting procedure using the measured birefringent patterns with the Mueller polarimeter in similar plasma exposure conditions.

The plasma jet is oriented horizontally at a 45 degree impact angle with a 7 mm distance between the end of the capillary and the impact point. The jet is powered with AC sine waves using a 30 kHz frequency and a helium gas flow of 1 slm.

The mapping of the temperature using the GaAs probe sensor follows a predefined grid where the temperature is measured in each point for a small time period (approximately 1-3 seconds) before going to the following grid point. A motorized translation stage is used to automatize the mapping and also to place the 100  $\mu\text{m}$  temperature probe right at the surface (backside) of the targeted glass sample. A glass target is used instead of the electro-optic BSO target due to the relatively long total measurement time. It is verified that similar maximum temperature values are observed regardless whether a glass or BSO target is used, with similar thicknesses of 0.5 mm.

The temperature pattern induced by the plasma jet in the targeted material will be examined for 4 different applied AC voltage amplitudes, i.e. 0, 1.0, 1.5 and 2.0 kV. With 0 kV applied voltage only the helium gas flow is present, while 1.0 kV initiates a discharge, but this discharge is limited between the electrodes. Using a 1.5 kV voltage amplitude a plasma plume is present creating a single impact point. Lastly, with 2.0 kV a surface discharge is visible by eye prolonging behind the impact point on the targeted material.

The characteristic voltage-current waveforms are shown in figure 6.6. With an increase of AC voltage amplitude, the current peak, indicating the charging underneath the grounded ring around the dielectric capillary, also increases in amplitude and occurs earlier in time. This indicates that more power has been delivered into the plasma and higher temperatures are expected.

Figure 6.7(a) shows the temperature profile obtained with the probe sensor, measured when operating the plasma jet using the 2.0 kV voltage amplitude. Theoretically, the GaAs temperature sensor is able to measure temperatures with an accuracy of 0.1  $^{\circ}\text{C}$  since it examines the shift of the band edge of the crystal, which is temperature dependent. Due to variations in the ambient conditions the uncertainty in the temperature measurements is slightly higher, approximately  $\pm 1$   $^{\circ}\text{C}$ .

A maximum increase of temperature is observed of approximately 15 degrees Celsius, relative to the room temperature of 25 degrees. The maximum induced

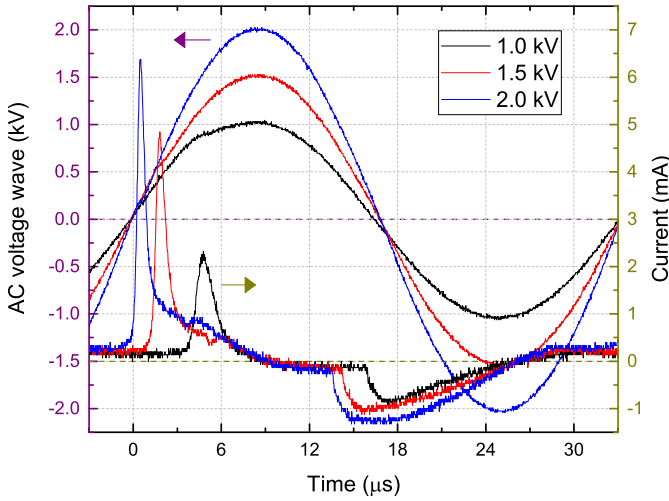


Figure 6.6: The applied AC voltage sine waves used to power the plasma jet, shown for 1.0, 1.5 and 2.0 kV. The resulting current waveform are shown as well, with the characteristic peak in the beginning of the positive half period and a dip shortly after, indicating the propagation of the ionization wave towards the target.

temperature decreases when a lower applied voltage amplitude is used, see figure 6.7(b), since the dissipated power by the plasma is reduced. With the absence of any discharge present, i.e. shown by an applied voltage of 0 kV, there is still a temperature increase of approximately 5 degrees Celsius. This is due to the helium in air mixing and will be investigated in the next chapter.

The maximum increase in temperature as a function of applied voltage, as shown in figure 6.7(b), is used for calibration of the fitting procedure to retrieve the temperature profile from the measured birefringent patterns.

The birefringent patterns obtained using Mueller polarimetry are shown in figure 6.8 (left columns) for the 4 different applied voltage amplitudes. They are obtained by measuring the Mueller matrix of the exposed BSO material before the ionization waves have impacted the surface. Therefore no effect due to surface charge induced electric field is present with the birefringent patterns. The patterns relate to the previously named *background* structures that were deliberately removed in the previous chapters to focus only the electric field.

To guarantee that only anisotropies induced by external exposure of the crystal are measured, the BSO is also measured when no external influence is present. The birefringent patterns obtained in this case should be zero, but will always contain some systematic small deviation from zero. These non-zero residual birefringent patterns are subtracted from the patterns obtained during exposure to

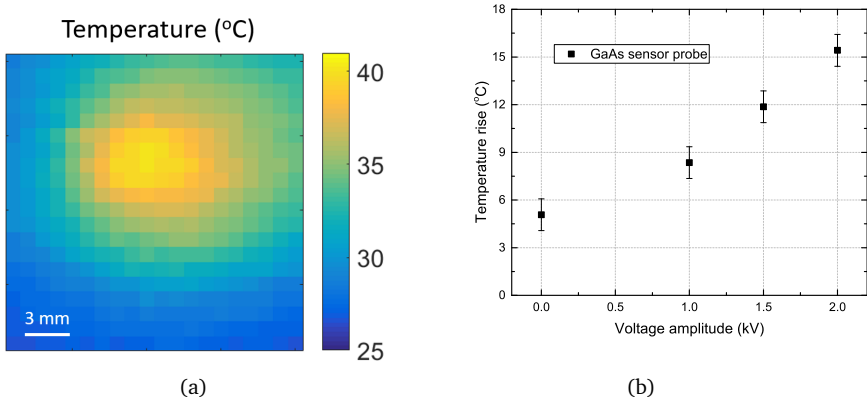


Figure 6.7: The mapped temperature pattern (6.7(a)) using the GaAs temperature probe sensor on the backside of a 0.5 mm thick glass with the plasma jet impacting horizontally on the left hand side at a 45 degree angle at 7 mm distance, with a 1 slm helium flow and 2.0 kV AC sine wave of 30 kHz frequency. The maximum induced temperature compared to room conditions (25 °C) as a function of voltage (6.7(b)) is used to calibrate the fitting procedure for the birefringent patterns obtained using Muller polarimetry.

only examine the externally induced anisotropies.

The fitting procedure is applied to retrieve the temperature distributions that induced the birefringent patterns for the four different applied voltages. The matched numerical birefringent patterns, shown in the right columns of figure 6.8, show great similarities with the measured patterns indicating that the used values of  $\gamma_1 = -4 \cdot 10^{-12}$ ,  $\gamma_2 = 5.4 \cdot 10^{-12}$  and  $\gamma_3 = 10.8 \cdot 10^{-12} \text{ m}^2/\text{K}$  are accurate. Each fitting case consists of 5000 iterations and is repeated 14 times for consistency, of which the averaged outcome is shown.

In addition to the linear birefringences, and perhaps more importantly, the obtained temperature profiles also match with the profiles mapped using the temperature probe. This is shown in figure 6.9 for the 4 different applied voltage amplitudes, using the fixed values of  $\gamma_{1-3}$ .

Table 6.1 shows the outcome of the maximum temperature increase as a function of voltage amplitude for different values of  $\gamma_{1-3}$ . The maximum induced temperature deviates from the probe values when the  $\gamma_{1-3}$  values are respectively 40% decreased or increased. The uncertainties shown come from the standard deviation in the outcome of the repeated fitting procedures.

With this calibration and the resulting temperature profiles shown in figure 6.9 it has been shown that the fitting procedure works accurately to numerically create a temperature profile for which the second derivatives match the ones observed within the linear birefringent patterns obtained with Mueller polarimetry.

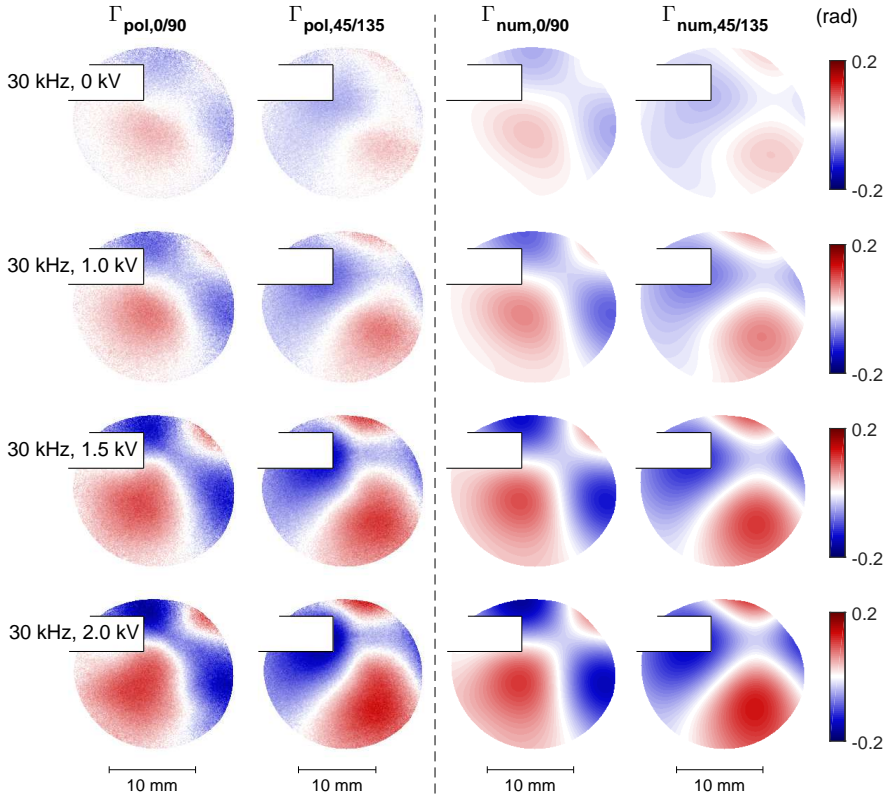


Figure 6.8: The birefringent patterns ( $\Gamma_{pol,0/90}$  and  $\Gamma_{pol,45/135}$ ) measured using Mueller polarimetry while applying different voltage amplitudes are shown in the left two columns. The profiles obtained from the fitting procedure ( $\Gamma_{num,0/90}$  and  $\Gamma_{num,45/135}$ ) are shown on the right. For information about the used settings in both the measurement and the fitting procedure see the text. The first row (30 kHz, 0.0 kV) shows the birefringent patterns when only a helium flow is present.

The temperature profile is fixed even though boundary conditions are difficult to impose. This is possible because of the added boundary conditions with respect to the corner temperatures within the numerical domain and the chosen signs of the  $\gamma_{1-3}$  calibration factors.

An important aspect of the measurement and the fitting procedure is the lateral dimensions of the patterns that are investigated. A temperature profile is created with the assumption that the average temperature in the bottom left corner is equal to ambient conditions and hence the maximum temperature is obtained relative to this. For this reason, the measurements have been performed with the plasma jet located not in the center of the *region of interest*, but towards the upper

Table 6.1: Maximum temperature increase observed for different voltage amplitudes, ranging from 0 kV to 2.0 kV. The GaAs temperature probe sensor is used for calibration of the fitting procedure of the birefringent patterns obtained using Mueller polarimetry. Different values of  $\gamma_{1-3}$  have been tested to match the resulting maximum increase in temperature with the temperature observed with the probe. The fitting procedure is repeated 14 times for each case consisting of 5000 iterations, with the uncertainty indicating the standard deviation in the outcomes relative to the averaged value.

Voltage amplitude	$T_{probe}$	Temperature from Mueller polarimetry (°C)					
(kV)	$\pm 1$ (°C)	settings $\gamma_{1-3}$ ( $10^{-12} \text{ m}^2/\text{K}$ )					
		$\gamma_1 = -4.0$	$-2.4$	$-5.60$			
		$\gamma_2 = 5.4$			$3.2$	$7.6$	
		$\gamma_3 = 10.8$					$6.5$
0.0	5.1	$5.1 \pm 0.8$	$5.9 \pm 0.9$	$4.3 \pm 0.5$	$5.6 \pm 0.7$	$4.2 \pm 0.6$	$5.2 \pm 0.7$
1.0	8.4	$9.2 \pm 1.0$	$10.2 \pm 0.9$	$8.1 \pm 0.7$	$9.9 \pm 1.1$	$7.6 \pm 0.6$	$9.6 \pm 0.8$
1.5	11.9	$12.4 \pm 1.0$	$14.5 \pm 1.8$	$11.5 \pm 1.0$	$15.5 \pm 1.1$	$11.0 \pm 0.9$	$14.3 \pm 1.2$
2.0	15.4	$15.9 \pm 1.1$	$17.5 \pm 1.6$	$14.2 \pm 1.2$	$18.9 \pm 2.1$	$13.3 \pm 1.3$	$18.1 \pm 1.9$
							$15.1$

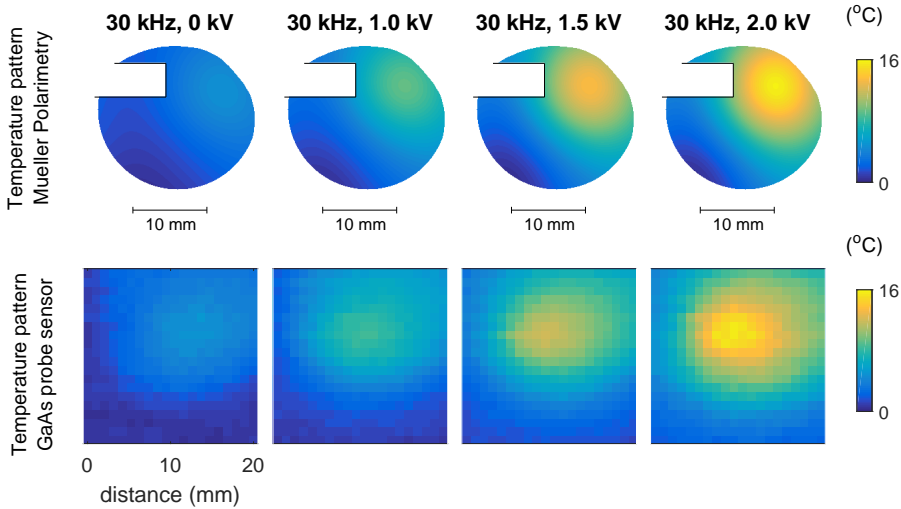


Figure 6.9: The resulting temperature profiles obtained using the fitting procedure (top row) for different voltage amplitudes. It shows great resemblances with the mapped profiles obtained with the GaAs temperature probe (bottom row) in similar conditions.

right corner. When this boundary condition is not fulfilled a “floating” temperature is obtained to an unknown boundary point.

From the mapped profiles using the temperature probe, it is shown that with the limited heating provided by the plasma jet the measurement (and resulting numerical) domain are large enough. However, when a significantly larger spreading is expected in the material, a larger view has to be used in order to examine a maximum temperature increase relative to ambient conditions. If that is not possible, the absolute temperature increase observed from the fitting procedure cannot be trusted. Luckily even then the technique can be applied and used to investigate the homogeneity / spreading of the temperature distribution within the measurement domain.

## 6.3 Summary and Perspectives

- The photo-elastic effect is followed to derive analytically a relation between the linear birefringence and the temperature gradient induced strain inside the electro-optic BSO material under external exposure. It turns out that the birefringent background patterns, which were systematically removed in the previous chapters to focus on the transient electric fields, relate to the second spatial derivatives of the temperature profile scaling with calibration factors  $\gamma_{1-3}$ .
- An iterative fitting procedure is introduced to numerically build a temperature profile for which the second derivatives match the birefringent patterns measured using Mueller polarimetry.
- By operating the plasma jet with different voltage amplitudes a variation in the temperature distribution is induced, which is used for calibrating  $\gamma_{1-3}$ . For this purpose, a second method of investigating the temperature profile is applied, by mapping pointwise the temperature on the backside of a glass target under plasma exposure using a dielectric GaAs temperature probe sensor.
- The temperature pattern and the maximum increase in temperature are compared for the profiles obtained through mapping with the probe and obtained from the numerical fitting procedure applied to the measured birefringent background patterns. This resulted to the calibrated values of  $\gamma_1 = -4 \cdot 10^{-12}$ ,  $\gamma_2 = 5.4 \cdot 10^{-12}$  and  $\gamma_3 = 10.8 \cdot 10^{-12} \text{ m}^2/\text{K}$ .
- As a result, the fitting procedure can be used to examine the temperature profile inside the electro-optic BSO in addition to the electric field investigation. This is beneficial for the investigation of the plasma surface interactions for temperature sensitive targets.
- Even though both the electric field and the temperature (gradient) induce a birefringence, in practice they are easily separated in a measurement for two reasons. Firstly, the electric field pattern is time-dependent on a sub- $\mu\text{s}$  scale, while temperature profiles become stable over time during the (continuous) plasma exposure. Secondly, the patterns induced by the temperature gradient are much larger and do not reflect the observable shape of the discharge on the surface, while the electric field does.
- The fitting procedure / algorithm allows to retrieve the temperature profile within 1 or 2 degrees of accuracy. With conventional techniques using diagnostics in the gas phase this is not possible, which makes Mueller polarimetry a great tool for the characterization of this important aspect of low temperature plasma interactions.

## References

- [12] K.-D. WELTMANN, E. KINDEL, R. BRANDENBURG, C. MEYER, R. BUSSIAHN, C. WILKE, and T. VON WOEDTKE. *Contrib. to Plasma Phys.* **49**: 631–640, 2009. DOI: [10.1002/ctpp.200910067](https://doi.org/10.1002/ctpp.200910067) (see pp. 3, 17, 20, 21, 161, 179)
- [40] C. MALGRANGE, C. RICOLLEAU, and M. SCHLENKER. *Symmetry and Physical Properties of Crystals*. Dordrecht: Springer Netherlands, 2014. ISBN: 978-94-017-8992-9 DOI: [10.1007/978-94-017-8993-6](https://doi.org/10.1007/978-94-017-8993-6) (see pp. 12, 55, 57, 88, 162, 163)
- [86] E. SLIKBOER, O. GUAITELLA, and A. SOBOTA. *Plasma Sources Sci. Technol.* **25**: 03LT04, 2016. DOI: [10.1088/0963-0252/25/3/03LT04](https://doi.org/10.1088/0963-0252/25/3/03LT04) (see pp. 22, 53, 79, 80, 83, 95, 96, 160, 181)
- [87] E. SLIKBOER, E. GARCIA-CAUREL, O. GUAITELLA, and A. SOBOTA. *Plasma Sources Sci. Technol.* **26**: 035002, 2017. DOI: [10.1088/1361-6595/aa53fe](https://doi.org/10.1088/1361-6595/aa53fe) (see pp. 22, 53, 80, 83, 96, 101, 102, 160)
- [123] R. C. POWELL. *Symmetry, Group Theory, and the Physical Properties of Crystals*. vol. 824 Lecture Notes in Physics New York, NY: Springer New York, 2010. ISBN: 978-1-4419-7597-3 DOI: [10.1007/978-1-4419-7598-0](https://doi.org/10.1007/978-1-4419-7598-0) (see pp. 54, 162)
- [157] M. R. R. GESUALDI, C. JACINTO, A. A. ANDRADE, T. CATUNDA, and M. MURAMATSU. *J. Optoelectron. Adv. Mater.* **13**: 643–647, 2011. (see p. 160)
- [158] S. PFEIFFER, A. C. F. GORREN, K. SCHMIDT, E. R. WERNER, B. HANSERT, D. S. BOHLE, and B. MAYER. *J. Biol. Chem.* **272**: 3465–3470, 1997. DOI: [10.1074/jbc.272.6.3465](https://doi.org/10.1074/jbc.272.6.3465) (see pp. 161, 178)
- [159] W. MARTIENSSSEN and H. WARLIMONT. *Springer Handbook of Condensed Matter and Materials Data*. Springer Berlin Heidelberg, 2005. ISBN: 978-3-540-44376-6 DOI: [10.1007/3-540-30437-1](https://doi.org/10.1007/3-540-30437-1) (see p. 163)

# Simultaneous Investigation of Temperature and Electric Field

## Contents

---

<b>7.1</b>	<b>Relevance for Plasma Target Interaction . . . . .</b>	<b>178</b>
<b>7.2</b>	<b>Increase Temperature and Electric Field . . . . .</b>	<b>179</b>
7.2.1	Dependency on the Operating Frequency of the Jet . . . . .	179
7.2.2	Gas Flow Dynamics . . . . .	183
<b>7.3</b>	<b>Background Images from Previous Measurements . . . . .</b>	<b>185</b>
7.3.1	Influence of a Controlled Environment with the AC-driven Plasma Jet . . . . .	186
7.3.2	Voltage Amplitude of the Pulsed Plasma Jet . . . . .	189
<b>7.4</b>	<b>Summary and Perspectives . . . . .</b>	<b>191</b>
	<b>References . . . . .</b>	<b>192</b>

---

This chapter will show the application of Mueller Polarimetry for the simultaneous investigation of the temperature and electric field induced in the electro-optic BSO crystal by the AC-driven plasma jet. This relies on the derivation, calibration and verification of the fitting procedure done in the previous chapter which allows to numerically build a temperature profile based upon the measured birefringent (background) patterns. The effect of the operating frequency of the plasma jet is examined for the induced plasma target interaction. Additionally, the temperature profile in the plume of the plasma jet is examined using the GaAs probe to investigate the heat transfer that takes place. Lastly, the fitting procedure is applied to the background images obtained during the electric field measurements presented in chapter 4 to study the influence of a controlled environment and the voltage amplitude for the pulsed plasma jet impacting at an 45 degree angle.

## 7.1 Relevance for Plasma Target Interaction

The heat transferred during a plasma-target interaction and the consequent temperature increase of a sample is an important parameter when exposing materials to a discharge. The reason for this is that generally every treated surface has a particular heat sensitivity. Most commonly melting or deformation, for instance of polymers, should be prevented for the treated materials. To this purpose, non-equilibrium plasmas are widely used for application purposes, instead of thermal plasma. However, despite having a difference between the heavy particle temperature and electron temperature of several orders of magnitude, it could still occur that gas temperatures get elevated by several hundreds of degrees depending on the plasma source and environment.

As stated before, the atmospheric pressure filamentary discharges investigated throughout this work have various applications, ranging from biomedical treatment, to plasma catalysis and surface functionalization. The melting temperature of different plastics differ over several hundreds of degrees Celsius, but most of them become moldable already at several tens of degrees above room temperature. For biomedical purposes it is clear that heating of a sample should remain low, to prevent burning, whether it involves the treatment of a living patient or an *in-vitro* culture study.

Not only to prevent burning or melting of the sample has the target's temperature to be controlled. There are known chemical processes of molecules that change reactivity / stability over a small temperature range, with possible consequences for certain plasma applications. For instance, the reaction constant of aqueous *peroxynitrite* changes completely over just a 40 degrees temperature range.<sup>158,160</sup> This means that pathways of reactive oxygen and nitrogen species (RONS) could change as well, which is important for plasmas interacting with the surrounding air and liquids.<sup>68</sup>

Plasma-liquid interactions have regained recently significant attention due to the biomedical applications and the emerging field of *plasma agriculture*. When a discharge is in contact with a liquid surface, species produced in the gas phase dissolve and become part of an intricate combination of processes<sup>161,162</sup> that ultimately change the pH levels of the liquid, together with predominantly nitrite, nitrate and H<sub>2</sub>O<sub>2</sub> concentrations.<sup>70</sup>

The temperature of plasma jets similar to the one used throughout this work has been investigated in the past. For two different RF-driven plasma jets, gas tem-

---

<sup>158</sup>S. PFEIFFER et al. *J. Biol. Chem.* 1997 **272**: 3465–3470

<sup>160</sup>R. KISSNER and W. H. KOPPENOL *J. Am. Chem. Soc.* 2002 **124**: 234–239

<sup>68</sup>D. B. GRAVES *J. Phys. D. Appl. Phys.* 2012 **45**: 263001

<sup>161</sup>P. BRUGGEMAN and C. LEYS *J. Phys. D. Appl. Phys.* 2009 **42**: 053001

<sup>162</sup>P. LUKES et al. *Plasma Sources Sci. Technol.* 2014 **23**: 015019

<sup>70</sup>A. LINDSAY et al. *J. Phys. D. Appl. Phys.* 2015 **48**: 424007

peratures have been found ranging from 63 °C<sup>12</sup> to several hundreds of degrees.<sup>163</sup> Earlier work done on the same AC kHz-driven plasma jet as used in this work revealed a relatively low gas temperature of 35°C,<sup>66</sup> which matches the temperature values from the profiles shown in chapter 6 used for the calibration of the fitting procedure. Lastly, it has been shown that the working mode of a micro-scaled reference jet greatly influences the gas temperature<sup>164</sup>.

Generally, there are various techniques to estimate the gas or heavy particle temperature in a discharge, e.g. via Raman or Rayleigh scattering,<sup>165</sup> using rotational lines from optical emission spectroscopy,<sup>166</sup> quantitative Schlieren,<sup>167</sup> optical probes or through the observed Doppler broadening of meta-stable species. All these measurements allow for the investigation of the gas temperature in the plume of the plasma jet. No literature has been found where the temperature distribution *inside* a targeted material under exposure of a plasma jet is investigated.

Mueller polarimetry will be applied to examine simultaneously with the electric field which temperature the electro-optic BSO crystal has under exposure of the plasma jet. Not only the maximum temperature is obtained but also the temperature distribution throughout the material. The influence of the operating frequency of the AC sine wave is the subject of the examination. In the last part, the background images are examined that were obtained in chapter 4, but not shown, during the electric field measurements when examining the influence of a controlled environment and the voltage amplitude of the pulsed plasma jet impacting at 45 degree.

## 7.2 Increase in Temperature and Electric Field Induced by the Plasma Jet

### 7.2.1 Dependency on the Operating Frequency of the Jet

The Mueller matrix of the BSO crystal is measured twice during continuous operation of the AC plasma jet, right before and after the impact of the ionization waves on the surface. This is done by changing the time delay settings of the acquisition at the iCCD camera relative to an external trigger relating to the repetitive generation event of the ionization wave at the powered electrode. Each frame needed to build the intensity matrix is collected according to this time delay. When a delay  $t_d = 1 \mu\text{s}$  is used the generated ionization wave in that voltage period has not

<sup>12</sup>K.-D. WELTMANN et al. *Contrib. to Plasma Phys.* 2009 **49**: 631–640

<sup>163</sup>S. ZHANG et al. *J. Phys. D. Appl. Phys.* 2013 **46**: 205202

<sup>66</sup>A. SOBOTA et al. *Plasma Sources Sci. Technol.* 2016 **25**: 065026

<sup>164</sup>S. KELLY et al. *J. Phys. D. Appl. Phys.* 2015 **48**: 444002

<sup>165</sup>A. F. H. VAN GESSEL et al. *Plasma Sources Sci. Technol.* 2012 **21**: 015003

<sup>166</sup>P. J. BRUGGEMAN et al. *Plasma Sources Sci. Technol.* 2014 **23**: 023001

<sup>167</sup>A. SCHMIDT-BLEKER et al. *J. Phys. D. Appl. Phys.* 2015 **48**: 175202

left the capillary tube yet. A time delay  $t_d = 8 \mu s$  is used to measure the Mueller matrix while temporal charge deposition due to the impact of the ionization wave has occurred, similarly to the experiments described in the previous chapters.

Likewise, the exposure time of each frame is  $1 \mu s$  and each element of the intensity matrix is obtained 200 times and averaged to reduce noise levels. The total acquisition time of the two measured Mueller matrices is approximately 3 minutes and is done at least 10 minutes after the plasma jet has been turned on to reach stable plasma operation conditions.

The Mueller matrices are examined using the logarithmic decomposition to obtain the two linear birefringent patterns before and after impact. The difference present due to the impact is used to calculate the electric field (as shown in chapters 4-5), while the patterns before impact are used to obtain the temperature distribution using the fitting procedure (shown in chapter 6).

The obtained electric field and temperature induced in the electro-optic BSO crystal under exposure of the AC driven plasma jet for different operating frequencies is shown in figure 7.1. The plasma jet is oriented horizontally at a 45 degree impact angle with a 7 mm distance between the end of the capillary tube and the impact point. A helium gas flow of 1 slm is applied and the electric field and temperature are obtained during a simultaneous measurement series at a fixed applied operating frequency of the AC sine wave with an amplitude of 2.0 kV. The operating frequency is varied from 20 to 50 kHz.

The images in the first and second row of fig 7.1 show the axial electric field pattern and the temperature distribution with similar spatial scales. The axial electric field concentrates around the area where charge deposition has taken place. Since this occurs at a smaller spatial scale a zoomed-in image of the axial electric field pattern is added as the third row.

The operating AC frequency changes the plasma surface interaction both in terms of the electric field due to surface charge and the temperature increase of the target. The investigation ranges from 20 kHz to 50 kHz, which is identified as the linear operating regime of this AC-driven plasma jet. In this frequency range there is a single current peak with a reproducible amplitude at each period. Both higher and lower operating frequencies outside of this range cause an unstable mode of the generation of ionization waves. This is monitored through the current measured at the grounded electrode.

Hypothetically, when the frequency is too low, there is too much time in between the ionization events for a stable reproducible generation of the ionization waves, since densities of left-over charges and/or metastables from the previous discharge have decreased. An operating frequency which is too high causes aperiodical behavior. The role that left-over charges, pre-ionization and metastable play in the generation and dynamics of the ionization waves has been discussed

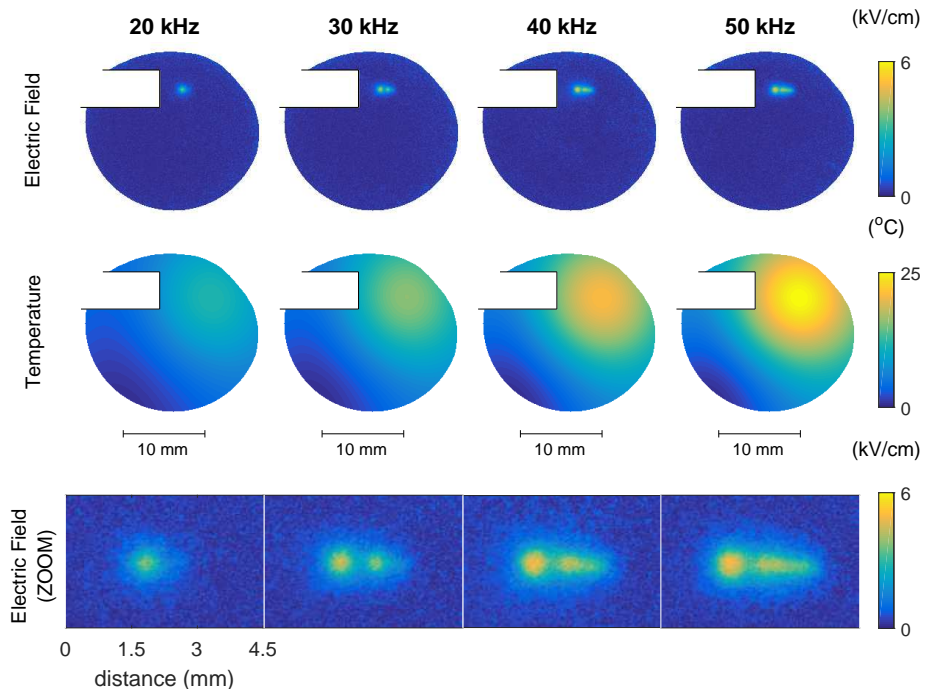


Figure 7.1: The (axial) electric field and temperature pattern induced by the plasma jet in the electro-optic BSO material measured using Mueller polarimetry, for different operating frequencies of the plasma jet. A constant voltage amplitude is used of 2.0 kV, with a helium flow of 1 slm while the horizontally mounted jet is at 7 mm from the target.

frequently in literature.<sup>18,74,86,168</sup> The influence of the gas temperature is usually not considered but could also play a role in the stabilization of the plume structure because of its possible influence in the He/air mixing and the large difference of density between the two gases.

The electric field pattern evolves from a single impact point pattern at 20 kHz operating frequency to an elongated pattern at higher frequencies. With a higher operating frequency there is less time in between the ionization events meaning that densities of leftover charge and / or metastables will be elevated which is non-negligible and can influence and contribute to the deposition of subsequent charges on the crystal. For instance, they can account for an easier generation of the ionization wave along the path of propagation. Consequently, the ionization

<sup>18</sup>T DARNY et al. *Plasma Sources Sci. Technol.* 2017 **26**: 045008

<sup>74</sup>A SOBOTA et al. *J. Phys. D. Appl. Phys.* 2009 **42**: 015211

<sup>86</sup>E. SLIKBOER et al. *Plasma Sources Sci. Technol.* 2016 **25**: 03LT04

<sup>168</sup>J.-P. BOEUF et al. *J. Phys. D. Appl. Phys.* 2013 **46**: 015201

wave will transfer more charge during the plasma surface interaction. When more charge is deposited on the surface, higher (axial) electric fields are measured and the ionization wave is able to propagate longer distances along the surface of the dielectric target. This creates the *tail*-like structure behind the originally single impact point region in the direction of the helium flow (towards the right). The maximum (axial) electric field value in the impact point increases from  $3.8 \pm 0.2$  kV/cm to  $5.1 \pm 0.2$  kV/cm as a function of operating frequency.

Also the temperature of the target increases with higher operating frequency of the plasma jet. The maximum temperature in the impact point increases from  $11.7 \pm 0.9$  °C for 20 kHz to  $25 \pm 2$  °C for 50 kHz, see figure 7.2. The figure shows a temperature of  $4.8 \pm 0.5$  °C when no plasma is generated, indicated by an applied frequency of 0 kHz. This is induced solely due to the helium-in-air mixing as was shown already in the previous chapter when the voltage amplitude was 0 kV. Since no plasma is generated there is also no impact and as a result no electric field generated inside the material.

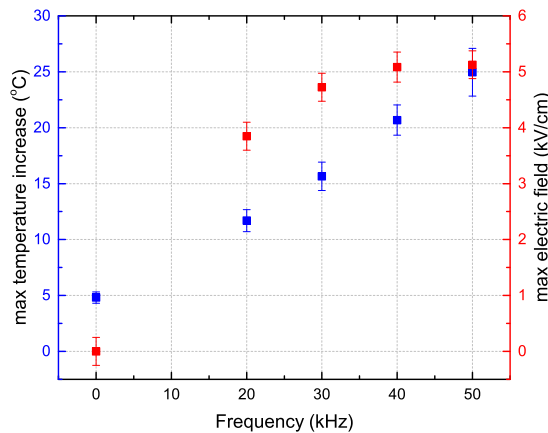


Figure 7.2: Maximum temperature increase (blue) and maximum (axial) electric field values in the impact point as a function of operating frequency of the AC driven jet.

The increase of temperature observed as a function of operating frequency relates to the power dissipated by the plasma jet. It has been shown with the same jet as the one used in this work, that when the plasma jet is operated using the 30 kHz frequency sine waves with a 2.0 kV amplitude an average power of 0.2 W is dissipated.<sup>67</sup> Since a flow of 1000 sccm helium is used this means the heating can maximally induce an average temperature increase of the displaced helium gas of 23.1 °C, using a heat capacity for helium of 3.12 kJ/(kg K) and a

<sup>67</sup>A SOBOTA et al. *Plasma Sources Sci. Technol.* 2014 **23**: 025016

density of  $0.1664 \text{ kg/m}^3$ . The difference with the measured value at 30 kHz can be explained by energy losses due to heating of the capillary walls, chemistry inside the discharge and the observed radiation from the plasma.

For higher frequencies the number of ionization waves generated per time interval increases linearly. Since the frequency is varied within the linear operating regime, the amount of heat generated per each ionization wave is expected to remain constant. Thus the total heat delivered per time interval will increase linearly as well and consequently the maximum temperature observed in a target, as is shown in figure 7.2.

### 7.2.2 Gas Flow Dynamics

The temperature profiles measured inside the target under plasma exposure arise from heat transferred to the surface. To examine this further the GaAs temperature probe, used in the previous chapter for calibrating the fitting procedure, is used to map the temperature profile within the plasma plume.

A vertical grid is chosen along the axis of the horizontally mounted plasma jet, starting at the edge of the capillary tube. A motorized translation stage is used to automatically change the position of the  $100 \mu\text{m}$  sized sensor along the grid while capturing the local temperature.

Figure 7.3 shows the resulting temperature profiles for two cases. The first (top image) involves the freely expanding plasma plume generated using a 2.0 kV voltage amplitude with 30 kHz AC frequency and 1 slm helium gas flow. The second (bottom) image shows the temperature plume for a 1 slm helium gas flow when no voltage is applied (i.e. without a plasma present). The temperature is corrected for the ambient room temperature to only show the resulting change.

Surprisingly the highest temperature is not measured at the exit of the capillary, close the electrodes, but further downstream in the direction of the gas flow. This has only been reported before once,<sup>66</sup> while often the assumption is made of highest temperatures at the exit of the capillary.

At 7 mm distance from the end of the capillary, i.e. the location where previously the BSO target was placed, a temperature amplitude is observed similar as shown inside the targeted material. This means that the heating mechanisms are not significantly influenced by the presence of a target.

Right at the exit of the capillary a temperature increase is measured of  $10 \text{ }^\circ\text{C}$  for the plasma plume, while the increase for the gas plume is  $0 \text{ }^\circ\text{C}$ . The observed increase of approximately  $7 \text{ }^\circ\text{C}$  further downstream within the gas plume originates from the gas mixing that occurs, since a similar *decrease* of  $7 \text{ }^\circ\text{C}$  is observed at the surroundings close to the edge of the capillary, see figure 7.3(b). A decrease in temperature of the surrounding gas is also observed around the plasma plume, but less significant.

The origin of this heat exchange caused by the mixing of the (gas) jet with

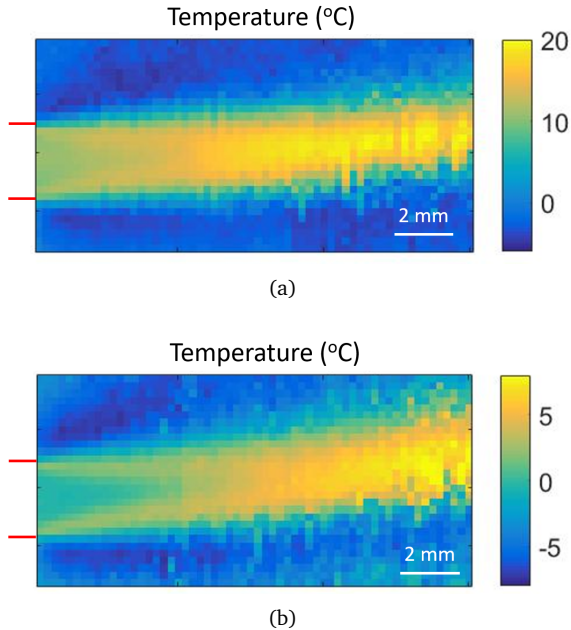


Figure 7.3: The mapped temperature profile relative to ambient conditions using the GaAs probe sensor for the freely expanding plasma plume (2 kV, 30 kHz and 1 slm helium flow) shown in figure 7.3(a) and the gas plume (0 kV / 0 kHz and 1 slm helium flow) in figure 7.3(b). The location of the exit of the capillary tube is indicated in red.

the surroundings is not well understood. First of all, most investigations of heat exchange between gas flows from jets occur either at different pressures or with significantly higher velocities. At atmospheric pressure with an average outlet velocity of only 2.4 m/s, no previous literature has been found showing this heat exchange resulting from the helium-in-air mixing.

A key component of this heat exchange could be related to the density and / or specific heat difference between helium and air. When the temperature profile in the plume of different gas jets is examined the heat exchange changes, as shown in figure 7.4. The use of a gas similar as the environment, i.e.  $O_2$ ,  $N_2$  or *dry air*, lacks the heat exchange as observed when using (the same amount of) helium gas.

The temperature profile induced by argon-in-air gas mixing has the heat exchange reversed. The core of the gas jet cools down while the environment increases slightly in temperature. This suggests the importance of relative density or specific heat since argon is heavier than air and has a lower specific heat, while helium is lighter with a higher specific heat. The reversed effect observed with an argon flow is less significant than with the helium gas flow. The heat exchange clearly creates or follows a boundary mixing layer starting at the edges of the capillary tube located on the left-hand side.

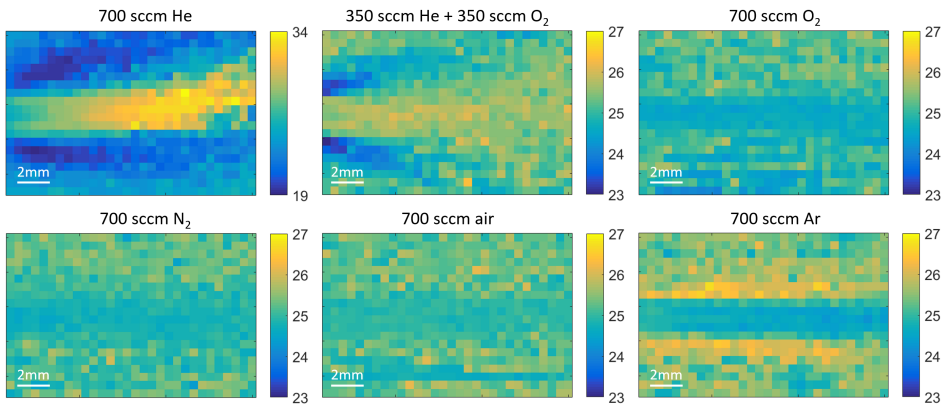


Figure 7.4: The mapped temperature profiles for different gas flows (helium, helium + oxygen, oxygen, nitrogen, dry air and argon) using the GaAs probe sensor. The ambient conditions are  $\approx 25$  °C. The end of the capillary is located on the left-hand side.

## 7.3 Background Images from Previous Measurements

In the previous chapters several electric field investigations have been shown. The background birefringent images have not been used yet, but will be discussed in this section. Unfortunately, at the time of those measurements the algorithm to retrieve the temperature profile from the background images was not working yet.

As a result, measurements with the polarimeter were performed to optimize the electric field measurements. This means that the plasma jet was oriented in a way that the impact region was central to the images that were obtained. This is not ideal for the use of the algorithm to retrieve the temperature patterns since the boundary condition is not guaranteed, i.e. the bottom left corner is most likely not equal to room temperature. Additionally, in some cases a broken piece of BSO was used. This is not causing a problem for the electric field measurements but for the temperature algorithm the entire background has to be seen with the biggest *field-of-view* as possible.

As a consequence, the algorithm can only be used to retrieve a so-called *floating* temperature pattern, relative to the temperature in the bottom left corner of the images which is unknown. Still some results will be shown, for the backgrounds obtained while investigating the influence of the controlled environment with the AC jet and measurements done with the pulsed jet at 45 degree impact, because relative trends in the temperature can still be discussed.

### 7.3.1 Influence of a Controlled Environment with the AC-driven Plasma Jet

In chapter 4 section 4.4.2, electric field measurements were performed where the AC driven plasma jet and the targeted BSO material were placed in a glass cell to control and determine the influence of the environmental gas. The obtained electric field patterns were shown and discussed but the constant *background* images were not. These were subtracted from the linear birefringence in order to obtain the electric field results.

Figure 7.5 shows the linear birefringent patterns ( $\Gamma_{0/90}$  and  $\Gamma_{45/135}$ ) obtained *before* the impact of the ionization waves for the different examined environmental gasses (dry air, O<sub>2</sub>, N<sub>2</sub> and CO<sub>2</sub>). The fitting procedure is applied and the resulting temperature distribution is shown together with the electric field patterns. The measurements were obtained within a series of axial electric field examinations (BSO) for which some results were shown and discussed in figure 4.12. In figure 4.12 two cases were shown, i.e. 1.5 slm He with a 2.4 kV amplitude and 0.7 slm He with a 1.6 kV amplitude. A different case is shown in figure 7.5, where a 2.0 kV amplitude is used and a 1.0 slm helium flow. This case has similar operating parameters as used before for the temperature examination of the AC driven jet in open air. Since the operating parameters are similar, the temperature induced by the AC driven jet in the dry air environment is expected to be very similar to the temperature observed in open air, shown e.g. in figure 7.1 (30 kHz sine waves are used).

However it is not, indicated by a maximum temperature increase of  $5.3 \pm 0.7$  °C instead of  $15.7 \pm 1.3$  °C. This is a direct consequence of the failure to comply with the boundary condition that the bottom left corner of the examined images represent the ambient room temperature. As a result a *floating* temperature is obtained, without a reference point. It should be pointed out that the sign of the background images is reversed compared to the images shown before. Because of this the calibration factors  $\gamma_{1,2,3}$  are corrected in sign, not value, to retrieve properly the (positive) temperature profiles.

For all the measurements done to examine the influence of the controlled environmental gas a floating temperature is obtained, as shown in figure 7.5. Although the absolute temperature values cannot be trusted, what can be seen is that the induced temperature for the dry air environment is slightly lower than for O<sub>2</sub>, N<sub>2</sub> and CO<sub>2</sub> with a 2.5 % admixture of O<sub>2</sub>. This is not only visible in the fitted temperature patterns but also in the amplitudes of the linear birefringent patterns.

The reason why the temperature profile is slightly different could be related to a change in chemistry that occurs since the helium gas mixing has changed. Figure 7.5 shows also the corresponding (axial) electric field components ( $E_z$ ), which relates to the patterns observed in chapter 4 in figure 4.12. A diffuse electric field is seen for CO<sub>2</sub>, while evidence of a more filamentary discharge is seen for the N<sub>2</sub>

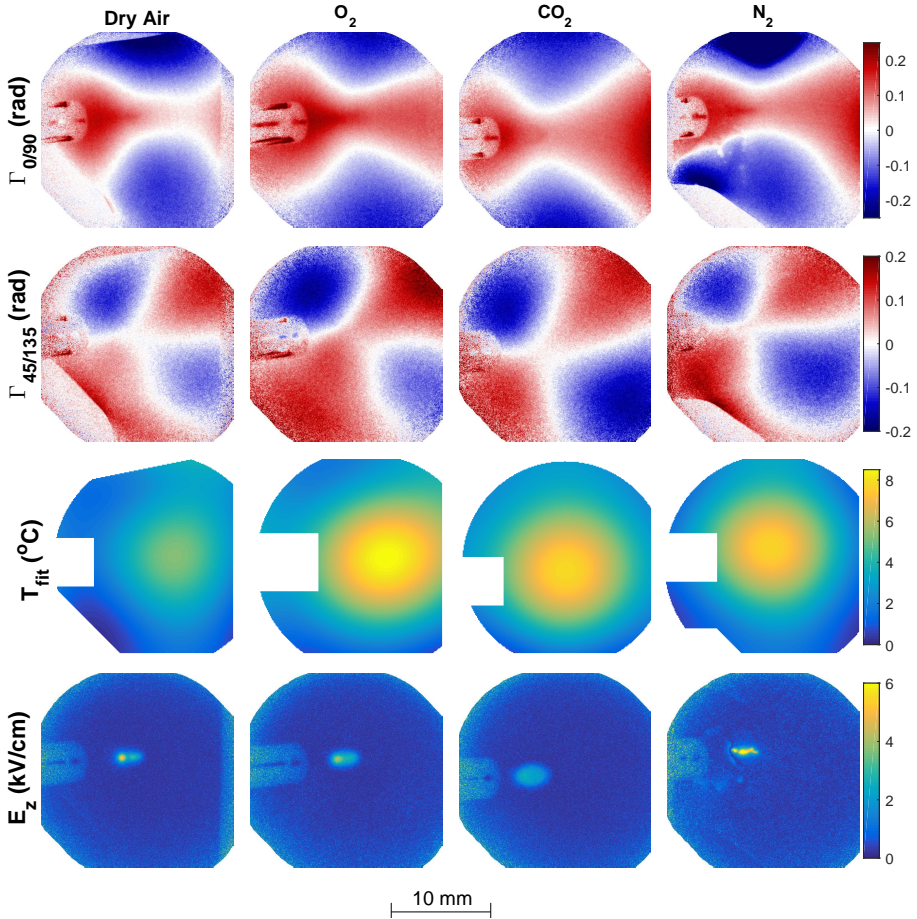


Figure 7.5: The two linear birefringent pattern ( $\Gamma_{0/90}$  and  $\Gamma_{45/135}$ ) obtained before the impact of the ionization waves propagation in different controlled environmental gasses, i.e. dry air, O<sub>2</sub>, N<sub>2</sub> and CO<sub>2</sub> with 2.5 % O<sub>2</sub>. The AC plasma jet is located 7 mm from the target and operated with a 1.0 slm helium flow and 2.0 kV voltage amplitude. The fitting procedure / algorithm is applied to retrieve the temperature profile, which is shown in the third row. Electric field patterns are obtained by using the change in linear birefringence after the impact of the ionization waves.

environment. To get the correct temperature profiles the experiments need to be redone, where the impact of the plasma jet is located more towards the top right corner, to be able to comply with the boundary condition of the fitting procedure / algorithm.

Secondary to the study on the influence of the environmental gas, also the influence of voltage and helium gas flow was simultaneously studied in chapter

4. For the controlled dry air environment, figure 7.6 shows the resulting background images, while the helium flow and AC voltage amplitude is varied. These measurements were part of the axial electric field examination presented in figure 4.10.

It was shown in figure 4.10 that the axial electric field patterns do not change significantly when varying the flow (between 700 sccm and 1500 sccm) or the AC voltage amplitude (between 1.6 and 2.4 kV). The patterns get elongated with higher flows and the maximum axial electric field value slightly decreases, suggesting a slightly reduced local surface charge density. The radial fields showed to be more influential, probably due to changes in the total amount of charge deposition.

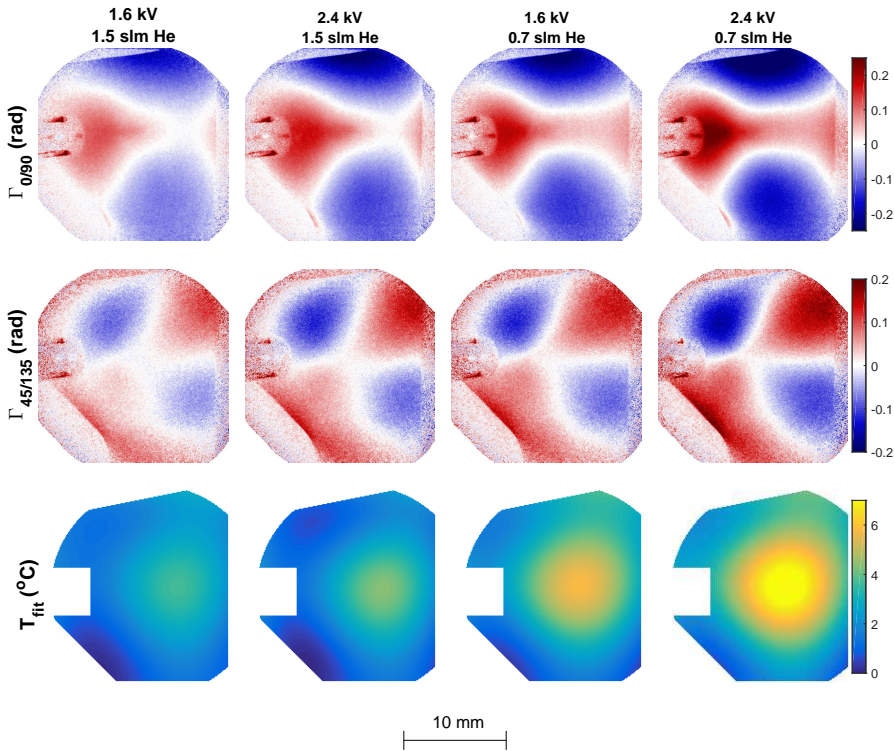


Figure 7.6: The background linear retardances  $\Gamma_{0/90}$  and  $\Gamma_{45/135}$  for the dry air environment in the cases of 700 and 1500 sccm helium flow and an AC voltage amplitude of 1.6 and 2.4 kV. The corresponding (axial) electric field patterns are shown in figure 4.10. The measurements are ordered based on the fitted value of temperature.

It can be seen in figure 7.6 that both the amplitudes of the birefringent patterns and the resulting temperature fit depend on the operating parameters of the

plasma jet. Similar as before the temperature amplitudes are obtained relative to an unknown boundary temperature, making them not very useful in absolute number. However compared to the measurement shown in figure 7.5 for dry air (2.0 kV and 1.0 slm He) a trend can be observed. When the helium flow is increased, the temperature decreases, while with an increase of voltage amplitude the temperature increases as well.

The latter relates to an increase of input power to the system. The volume of gas in which the power is dissipated depends on the gas flow. This means that with higher gas flows the heat produced by the jet is distributed over a larger gas volume which lowers the gas temperature.

Figures 7.5, 7.6 and 4.10 indicate the large amount of information that can be gained using the birefringent patterns obtained by analyzing optically electro-optic targets under plasma exposure using Mueller polarimetry. Images of the electric field patterns and the temperature distribution in different condition help to assess the plasma surface interactions that occur for the AC-driven plasma jet.

#### 7.3.2 Voltage Amplitude of the Pulsed Plasma Jet

For the examination done with the pulsed plasma jet impacting the BSO material at 45 degrees for different voltage amplitudes, chapter 4 section 4.4.3, the background images were subtracted to evaluate time-resolved the electric field. Figure 7.7 shows these linear birefringent patterns for the examined mono-polar 1  $\mu$ s high voltage pulses of 3 - 6 kV in amplitude. The distance between the capillary and the target is 10 mm and a helium flow of 1.0 slm is used.

In section 4.4.3 it was shown with time-resolved imaging of the light emission and the electric field patterns induced inside the targeted BSO material, that the surface discharge behind the impact point strongly depends on the voltage amplitude. The ionization waves travel faster and further along the targeted surface with higher voltage amplitudes. Surface streamers are observed at 5 or 6 kV, while the plume shows still repetitive behavior.

The temperature, shown in figure 7.7, also shows great dependence with the voltage amplitude. For these measurements, the impact of the plasma jet was located more towards the top right compared to the measurements performed with the AC jet in controlled environments. This makes the temperature values more reliable since the bottom left corner is more easily related to the ambient conditions. As a result, the temperature values are more comparable to the AC driven jet shown in figure 7.1, although they are still lower.

The reason why the temperatures are lower could be simply because of the failure to comply with the boundary condition, however it can also be related to the change of repetition frequency of the ionization waves. With the pulsed plasma jet a frequency of 5 kHz is used, while the AC driven jet operated between 20 and 60 kHz.

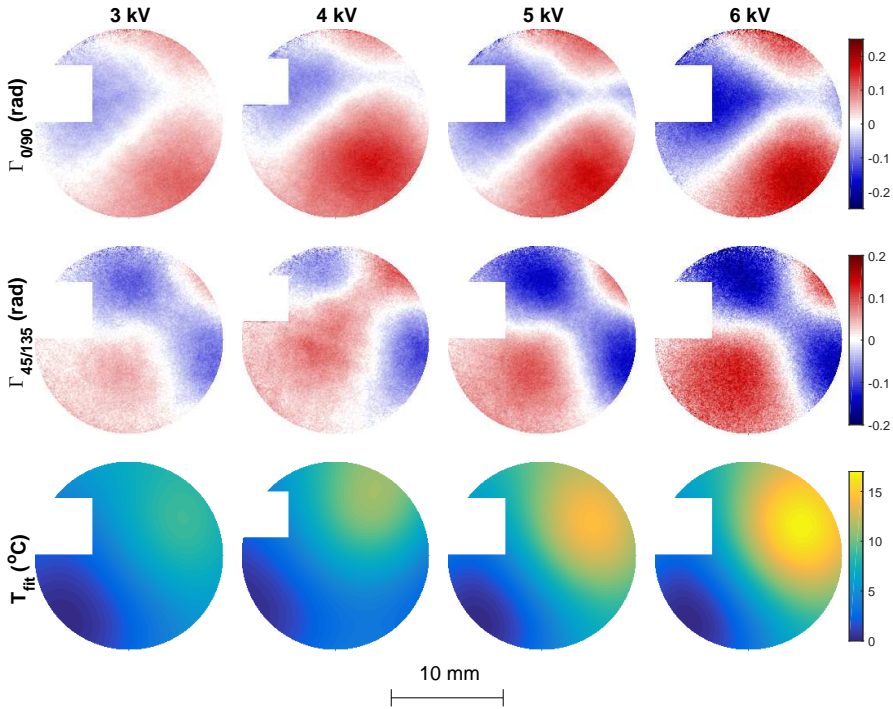


Figure 7.7: The linear birefringent patterns ( $\Gamma_{0/90}$  and  $\Gamma_{45/135}$ ) induced by the pulsed plasma jet operated at different voltage amplitudes. The fitted temperature profiles are shown in the last row. The corresponding time-resolved imaging of light emission and (axial) electric field is shown in chapter 4 section 4.4.3.

It is shown in figure 7.7 that the temperature increases with the voltage amplitude. This relates to observations made earlier, which is explained by an increase of input power into the system.

As stated, it is important to know the conditions to which targets are exposed to as a function of the operating parameters of the plasma jet. Mueller polarimetry applied to electro-optic materials under similar plasma exposures as used in applications is a unique tool to determine this. The variations of temperature that are detected for this plasma jet are just of a few degrees, which are clearly distinguishable using this optical diagnostic technique. Additionally, when a background structure is detected using a simpler diagnostic method, e.g. a basic Sénarmont setup, it is impossible to know whether it is a real birefringence signal or any other alteration of the light intensity. Therefore it would not have been possible to confidently interpret it as the birefringence resulting from a temperature gradient and not another optical effect. The fact that all the optical properties are detected with Mueller polarimetry does give this possibility.

## 7.4 Summary and Perspectives

- Mueller polarimetry is applied to simultaneously investigate the electric field and temperature to which targets are exposed to during a plasma surface interaction. Both the electric field and temperature change as a function of the operating frequency of the plasma jet. The linear operating regime of the AC plasma jet is identified between 20 to 50 kHz for the generation of stable repetitive ionization waves. The maximum temperature increases linearly from  $11.7 \pm 0.9$  °C to  $25 \pm 2$  °C within this frequency regime. Without a discharge present there is an increased temperature of  $4.5 \pm 0.5$  °C. The maximum (axial) electric field value increases from  $3.8 \pm 0.2$  kV/cm to  $5.1 \pm 0.2$  kV/cm. The shape of the surface patterns evolves from a single point impact to an elongated structure indicating a surface discharge was initiated behind the impact point.
- The temperature profile in the plasma plume, using the GaAs temperature probe, reveals that the maximum of the temperature is not close to the electrodes but further downstream. A heat exchange caused by the helium-in-air mixing is found inducing an elevation of the temperature in the plume while the surroundings cool down slightly. This effect is opposite when a heavier gas like argon is used, suggesting that the relative density and/or specific heat to the surroundings is an important factor. This helium-in-air heat exchange is responsible for the slightly elevated temperature of the target when no plasma is present.
- The fitting procedure / algorithm can normally only be applied when a boundary condition is fulfilled, meaning a reference temperature point is needed. Normally, the bottom left corner is assumed to be at room temperature since mild increases of temperature are assumed and the helium flows towards the top right. This boundary condition is not fulfilled when measurements are done with the plasma jet in the center of the images, meaning that the absolute temperature values cannot be trusted since a *floating* temperature is obtained towards an unknown temperature boundary point.
- Still trends can be compared, as has been shown using measurements that were done in chapter 4 for the influence of a controlled environment (AC jet) and the voltage amplitude of the pulsed jet. For different environments the temperature profile does not seem to change significantly, while the shape of the electric field patterns did. For the pulsed plasma jet, the electric field pattern got elongated with higher applied voltage amplitudes while the maximum field values slightly decreased. From the birefringent background patterns it has been shown that the temperature increases due to the increase of input power.

## References

- [12] K.-D. WELTMANN, E KINDEL, R BRANDENBURG, C MEYER, R BUSSIAHN, C WILKE, and T VON WOEDTKE. *Contrib. to Plasma Phys.* **49**: 631–640, 2009. DOI: [10.1002/ctpp.200910067](https://doi.org/10.1002/ctpp.200910067) (see pp. 3, 17, 20, 21, 161, 179)
- [18] T DARNY, J.-M. POUVESLE, V PUECH, C DOUAT, S DOZIAS, and E. ROBERT. *Plasma Sources Sci. Technol.* **26**: 045008, 2017. DOI: [10.1088/1361-6595/aa5b15](https://doi.org/10.1088/1361-6595/aa5b15) (see pp. 4, 146, 181)
- [66] A. SOBOTA, O GUAITELLA, G. B. SRETENović, I. B. KRSTIĆ, V. V. KOVAČEVIĆ, A OBRUSNÍK, Y. N. NGUYEN, L ZAJÍČKOVÁ, B. M. OBRADOVIĆ, and M. M. KURAICA. *Plasma Sources Sci. Technol.* **25**: 065026, 2016. DOI: [10.1088/0963-0252/25/6/065026](https://doi.org/10.1088/0963-0252/25/6/065026) (see pp. 20, 102, 146, 179, 183)
- [67] A SOBOTA, O GUAITELLA, and A ROUSSEAU. *Plasma Sources Sci. Technol.* **23**: 025016, 2014. DOI: [10.1088/0963-0252/23/2/025016](https://doi.org/10.1088/0963-0252/23/2/025016) (see pp. 20, 182)
- [68] D. B. GRAVES. *J. Phys. D. Appl. Phys.* **45**: 263001, 2012. DOI: [10.1088/0022-3727/45/26/263001](https://doi.org/10.1088/0022-3727/45/26/263001) (see pp. 21, 178)
- [70] A. LINDSAY, C. ANDERSON, E. SLIKBOER, S. SHANNON, and D. GRAVES. *J. Phys. D. Appl. Phys.* **48**: 424007, 2015. DOI: [10.1088/0022-3727/48/42/424007](https://doi.org/10.1088/0022-3727/48/42/424007) (see pp. 21, 178, 204)
- [74] A SOBOTA, A LEBOUVIER, N. J. KRAMER, E. M. VAN VELDHUIZEN, W. W. STOFFELS, F MANDERS, and M HAVERLAG. *J. Phys. D. Appl. Phys.* **42**: 015211, 2009. DOI: [10.1088/0022-3727/42/1/015211](https://doi.org/10.1088/0022-3727/42/1/015211) (see pp. 22, 181)
- [86] E. SLIKBOER, O. GUAITELLA, and A. SOBOTA. *Plasma Sources Sci. Technol.* **25**: 03LT04, 2016. DOI: [10.1088/0963-0252/25/3/03LT04](https://doi.org/10.1088/0963-0252/25/3/03LT04) (see pp. 22, 53, 79, 80, 83, 95, 96, 160, 181)
- [158] S. PFEIFFER, A. C. F. GORREN, K. SCHMIDT, E. R. WERNER, B. HANSERT, D. S. BOHLE, and B. MAYER. *J. Biol. Chem.* **272**: 3465–3470, 1997. DOI: [10.1074/jbc.272.6.3465](https://doi.org/10.1074/jbc.272.6.3465) (see pp. 161, 178)
- [160] R. KISSNER and W. H. KOPPENOL. *J. Am. Chem. Soc.* **124**: 234–239, 2002. DOI: [10.1021/ja010497s](https://doi.org/10.1021/ja010497s) (see p. 178)
- [161] P. BRUGGEMAN and C. LEYS. *J. Phys. D. Appl. Phys.* **42**: 053001, 2009. DOI: [10.1088/0022-3727/42/5/053001](https://doi.org/10.1088/0022-3727/42/5/053001) (see p. 178)
- [162] P LUKES, E DOLEZALOVA, I SISROVA, and M CLUPEK. *Plasma Sources Sci. Technol.* **23**: 015019, 2014. DOI: [10.1088/0963-0252/23/1/015019](https://doi.org/10.1088/0963-0252/23/1/015019) (see p. 178)
- [163] S. ZHANG, W. VAN GAENS, B. VAN GESSEL, S. HOFMANN, E. VAN VELDHUIZEN, A. BOGAERTS, and P. BRUGGEMAN. *J. Phys. D. Appl. Phys.* **46**: 205202, 2013. DOI: [10.1088/0022-3727/46/20/205202](https://doi.org/10.1088/0022-3727/46/20/205202) (see p. 179)

- 
- [164] S. KELLY, J. GOLDA, M. M. TURNER, and V. SCHULZ-VON DER GATHEN. *J. Phys. D. Appl. Phys.* **48**: 444002, 2015. DOI: [10.1088/0022-3727/48/44/444002](https://doi.org/10.1088/0022-3727/48/44/444002) (see p. 179)
- [165] A. F. H. VAN GESSEL, E. A. D. CARBONE, P. J. BRUGGEMAN, and J. J. A. M. VAN DER MULLEN. *Plasma Sources Sci. Technol.* **21**: 015003, 2012. DOI: [10.1088/0963-0252/21/1/015003](https://doi.org/10.1088/0963-0252/21/1/015003) (see p. 179)
- [166] P. J. BRUGGEMAN, N. SADEGHI, D. C. SCHRAM, and V. LINSS. *Plasma Sources Sci. Technol.* **23**: 023001, 2014. DOI: [10.1088/0963-0252/23/2/023001](https://doi.org/10.1088/0963-0252/23/2/023001) (see p. 179)
- [167] A. SCHMIDT-BLEKER, S. REUTER, and K.-D. WELTMANN. *J. Phys. D. Appl. Phys.* **48**: 175202, 2015. DOI: [10.1088/0022-3727/48/17/175202](https://doi.org/10.1088/0022-3727/48/17/175202) (see p. 179)
- [168] J.-P. BOEUF, L. L. YANG, and L. C. PITCHFORD. *J. Phys. D. Appl. Phys.* **46**: 015201, 2013. DOI: [10.1088/0022-3727/46/1/015201](https://doi.org/10.1088/0022-3727/46/1/015201) (see p. 181)



# Investigation of Plasma Interacting with a Complex Surface using Depolarization

## Contents

---

<b>8.1 Complex Plasma Surface Interactions . . . . .</b>	<b>196</b>
8.1.1 Test Case: Plasma Impact on Onion Cells . . . . .	197
8.1.2 Experimental Setup and Procedure . . . . .	198
<b>8.2 Material Evolution during Target Interaction . . . . .</b>	<b>202</b>
8.2.1 Dewetting by Plasma Impact . . . . .	202
8.2.2 Mapping Before and After Exposure . . . . .	204
8.2.3 Electric Field Through Onion Cells . . . . .	208
8.2.4 Outlook and Discussion . . . . .	218
<b>8.3 Summary and Perspectives . . . . .</b>	<b>220</b>
<b>References . . . . .</b>	<b>221</b>

---

This chapter investigates the use of Mueller polarimetry to examine plasma surface interactions occurring with complex samples. A combined measurement of the sample with the electro-optic BSO material allows to visualize the electric field generated through the complex sample while measurements before and after plasma exposure identify material changes due to the interaction. The coupling between the measured electric field and the changes in the material (through depolarization and transmission) offers a unique way to examine in-situ the plasma surface interaction. This has been applied to a test case where a single layer of onion cells is exposed to the plasma jet.

## 8.1 Complex Plasma Surface Interactions

The optical technique and examples shown in the previous chapters illustrate the unique way Mueller polarimetry can investigate plasma surface interactions by determining the electric fields and temperature induced *inside* a targeted material. Usually, diagnostics only allow for the examination of these quantities in the surrounding of the sample and an extrapolation to the target has to be made. For the temperature this is not a problem but for the electric field it was shown that the electric fields inside targets are lower than in the volume phase of the discharge. It is important to know the quantities that the material actually experiences during the plasma surface interaction in order to couple the observed changes in the material of the targeted samples to the discharges that have caused them.

This can simply be done by applying the same discharge to the electro-optic targets under examination of the Mueller polarimeter as was used to *treat / modify* a target. The (spatial) changes observed in the targeted sample, either by eye or determined with another diagnostic, can afterwards be related to the electric field and temperature pattern induced in the electro-optic targets. However, when a different target is used than during an application, the subsequent plasma surface interaction could be altered in an unknown way due to for instance a change in dielectric constant of the targeted material. Hence, it would be more interesting if the examination of the material can be done at the same time as the electric field and temperature are identified generated during the interaction. This chapter investigates the possibilities of Mueller polarimetry to do exactly that.

The main idea is to couple the complex material that is to be exposed to the plasma environment with the electro-optic BSO crystal. Mueller polarimetry (in transmission) allows for the optical characterization of the combined sample, similarly as done before. Repetitive changes in the retardance of the combined sample can be contributed to the electro-optic behavior of BSO, while depolarization is added through light scattering as the light propagates through the complex sample. Mueller polarimetry combined with the logarithmic decomposition allows for the decoupling / separation of these two quantities. This allows, hypothetically, to investigate surface changes of the sample while simultaneously the electric field is determined. However, this increases the complexity of Mueller polarimetry as a diagnostic tool.

In the remainder of this chapter an example will be given of such an examination, by exposing onion cells to the plasma jet. The focus lies with the new measurement procedure that is needed, the data treatment which becomes more delicate and the primary observations that can be made.

### 8.1.1 Test Case: Plasma Impact on Onion Cells

The example which will be explored consists of a single epidermal cell layer of an onion (*Allium cepa*). The layered vegetable offers ideal testing opportunities for several reasons. Firstly, a single cell layer can be extracted rather easily, see figure 8.1, from either the outer-facing side or the core-facing side of an onion layer. Naturally, this offers easy and cheap repetition possibilities.



(a)



(b)

(c)

Figure 8.1: An example of the extraction of the single epidermis cell (outer-facing) layer of an onion. The cells offer a cheap and simple test case for the use of Mueller polarimetry to examine more complex plasma surface interactions.

Secondly, the cells of an onion are rectangular and relatively large with a length between 100 and 300  $\mu\text{m}$ . This allows visualization of the cells even with a simple lens focusing configuration. Precisely for this reason, high school students often use the single skin cell layer in biology classes as an exercise for the determination of cell structures, including the cell walls, nucleus, cytoplasm and vacuoles.

For the non-thermal atmospheric pressure plasma community the onion cells could provide an interesting test case as well. As stated, non-thermal plasmas (e.g. jets or DBDs) have been used for biomedical applications and agricultural purposes. The onion cell layer provides easy monitoring at both macroscopic scale and cellular level meaning that the induced plasma interaction can be examined in a way that other biomedical / biological samples do not allow that easily. This could enhance the research to the effects that the so-called *plasma cocktail* (e.g.

reactive oxygen and nitrogen species, electric fields, charged species, heat and (UV) radiation) has on these types of targets.

This chapter will investigate the interaction between the guided ionization waves generated by the non-thermal AC plasma jet and a single onion cell layer by applying Mueller polarimetry. The cell layer is combined with the electro-optic BSO crystal to examine the induced electric fields. The purpose of the test case is not to investigate in depth the interaction between the onion cells and the discharges but rather to show how the investigation works and how this new diagnostic technique offers interesting ways to examine the plasma surface interaction for complex samples.

### 8.1.2 Experimental Setup and Procedure

The experimental setup and the measurement procedure are slightly changed in order to investigate interactions between surface discharges and more complex surfaces using Mueller polarimetry. This is indicated by figure 8.2, which shows the setup of the *sample-area* of the polarimeter, i.e. in between the PSA and PSG as shown in chapter 2.

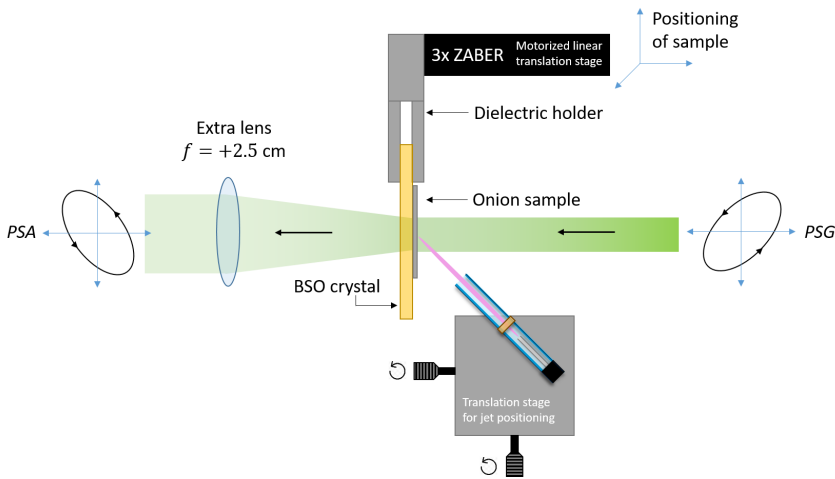


Figure 8.2: The adapted experimental setup (top view) shown of the Mueller polarimeter in between the *Polarizer State Generator* (PSG) and *Polarizer State Analyser* (PSA), including an additional lens and the translation stages to position both the sample (BSO crystal with onion cells) and the plasma jet. The other parts of the polarimeter remain the same as presented in chapter 2.

Firstly, an additional lens is added between the PSA and the location of the sample. This is necessary to increase the numerical aperture of the system which allows the detection of scattering of the light as it interacts with the complex

sample (onion cells). The polarization of scattered light is in general different than that of non-scattered light. When the two types of contributions combine incoherently in the camera to form an image, they contribute to produce Mueller matrices with a given degree of depolarization.

Both the plasma jet and the dielectric holder for the targeted samples are placed on translation stages. Due to the addition of the extra lens, the numerical aperture has increased but the *field-of-view* has decreased. This is not disadvantageous since a smaller field of view provides a higher image resolution for a constant number of pixels of the camera. Consequently, smaller details inside the onion cells can be studied. The spatial resolution increases from approximately 40 pixels per mm to 500 px/mm. The translation stages are advised since the position of the sample and the plasma jet have to be controlled more precisely for focusing and ensuring that the impact area of the plasma jet is within the smaller field-of-view of the iCCD camera.

Similar as before is the positioning of the plasma jet at a 45 degree impact angle with a 7 mm gap between the end of the capillary and the surface of the target. Also the operating parameters are the same by using 30 kHz sine waves with 2.0 kV amplitude to generate the ionization waves while a helium flow of 1 slm is used.

In order to investigate plasma surface interactions for more complex samples the Mueller polarimeter will be used as follows. The sample that is to be examined under plasma exposure is placed on top of the electro-optic BSO material. The Mueller matrix of the combined sample is measured using the polarimeter following two approaches.

The first approach is to simply measure the optical properties of the combined sample while there is no active plasma interaction. In this case there is no need for a time-resolved acquisition. A mapping of the sample can be done by combining multiple measured Mueller matrices while positioning the sample along a predefined grid using three ZABER *motorized linear translation stages* on which the holder of the sample is placed. The discharges have to be absent since only the holder is moved as shown in the setup. After the mapping, the motorized stages allow for a very precise return of the sample to the original position. The mapping gives the opportunity to look at larger spatial scales, which is necessary because of the reduced *field-of-view* due to the added lens to capture more depolarizing properties.

The Mueller matrices will predominantly be influenced by the optical response of the complex sample when no discharges are present, since the electro-optic BSO only has circular birefringent properties when it is under no external influence. This has been shown in chapter 3.

The second approach does include the plasma interaction and therefore incorporates induced optical properties for the BSO material. The Mueller matrix of the

combined sample is obtained during the plasma interaction, triggered before and after the impact of the ionization waves, in order to investigate the electric field induced through the sample into the electro-optic BSO. The measured retardance will have contributions of both the BSO material (with a static circular birefringence and time-dependent linear birefringence induced by the electric field) and the complex sample, however only repetitive time-resolved changes are expected in BSO related to the induced electric field.

The physical scenario of the described experiments is characterized by at least two different characteristics timescales. The shorter one ( $\mu\text{s}$  timescale) is related to the interaction of a single plasma wave to the sample, which e.g. induces electric field due to deposited surface charges. This process can be followed according to the second method. The longer characteristic time (minutes) is related to the surface modifications induced due to long exposure to the plasma jet. Processes happening at this second time scale (the evolution of the targeted material) can be monitored using the first measurement method.

A combination of the two approaches is used to complement each other to investigate the plasma surface interactions occurring with more complex targets. An example is shown in figure 8.3. The first approach is repeated before and after plasma exposure to retrieve a larger overview of the optical state of the combined sample. During the plasma exposure the time-resolved measurements should allow for the investigation of the electric field since they focus on the repetitive changes induced externally. Two time-resolved measurements are needed (before and after impact) to see differences induced by the temporal charge deposition.

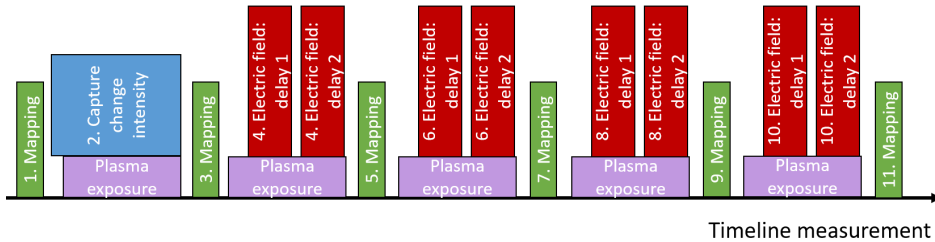


Figure 8.3: An example of the experimental procedure to investigate more complex plasma surface interactions with the Mueller polarimeter to either do a mapping before and after plasma exposure or acquire time-resolved measurements during the exposure. The same sample is used throughout this timeline with the impact of the plasma jet at a fixed location.

Naturally, non-repetitive changes of the complex sample are part of the investigation as well, since the plasma interaction is expected to either *modify*, *change* or *treat* the sample in a certain way. Ideally, this can be monitored using the first approach before and after the plasma interaction has been applied. During the plasma interaction, when the second approach is applied, the evolution of the

sample should be not significant to allow the determination of the induced electric fields.

The second approach of the investigation during plasma exposure only works when the non-repetitive changes (evolution) of the sample are not dominant within the acquisition of the time-resolved matrices. When they are dominant, the measured intensity matrices cannot be related to a physically realizable Mueller matrix related to the properties of the sample. This is simply due to the fact that the sample properties were non constant and modified significantly during the measurement. Therefore, the repetitive changes in birefringence due to the induced electric field cannot be identified.

It has been observed in some initial tests that significant and rapid changes happen during the first plasma exposure of new samples, as will be shown in the next section, most likely due to water displacement or evaporation. Consequently, during the first plasma exposure it is beneficial to monitor time-resolved the change of intensity reaching the iCCD camera, while the liquid crystals are in neutral position. This does not give any polarimetric information, but simply allows to see physical changes of the combined sample. After the first plasma exposure the targeted sample is still expected to change during the interaction, but the evolution of the sample will take place on longer time scales. This causes significantly less problems for the construction of the Mueller matrices and the extraction of the optical properties from which the electric field is obtained.

As usual, a calibration of the PSG and PSA is done, after which the combined sample (BSO + onion cells) is placed in front of the lens to create a sharp image at the iCCD camera. A mapping is done before plasma is applied to measure the Mueller matrix of the sample at 9 different locations which are combined to create a large field of view around the initially chosen spot where the plasma impact will take place.

When a plasma exposure is initiated, first the sample is left for 120 seconds in order for the temperature inside the material to become stable. The gradients induced by the inhomogeneous temperature profile induce a birefringence as well (as has been shown in chapter 6), thus they have to be stable in order to be able to subtract them and only look at changes induced by the electric field before and after impact. The acquisition of each time-resolved Mueller matrix takes between 115 and 130 seconds, depending on the acquisition parameters. In total, including the stabilizing time for the temperature and the acquisition of the time-resolved matrices the sample is exposed to the discharges for 8 minutes. After that, the plasma jet is turned off and a sequential mapping of the combined sample is repeated. The mapping approach takes approximately 12 minutes to be completed. Since the motorized linear translation stages return the sample after the mapping to the original position (with  $\mu\text{m}$  accuracy), a new plasma exposure with time-resolved Mueller imaging can be done with the plasma jet impacting at the same

point. The Mueller matrices that are measured with both approaches are analyzed with the logarithmic decomposition to retrieve the transmission, linear birefringence, and depolarization.

## 8.2 Material Evolution during Target Interaction

An example is shown in this section illustrates the results that can be obtained when using Mueller polarimetry to investigate optically the combined signature of BSO and a complex sample under plasma exposure. To this purpose a single cell layer of an onion is used. The examination follows the experimental timeline as shown in figure 8.3.

### 8.2.1 Dewetting by Plasma Impact

Firstly, significant changes are observed during the initial plasma exposure on a new sample, as has been stated in previous sections. This is shown in figure 8.4. The outer facing cells of the third layer of an onion are carefully mounted on the BSO crystal (without any coverslip). Before plasma exposure the cell structure is clearly visible when capturing the intensity reaching the iCCD camera (top left image). The transmission seems relatively high, but since the liquid crystals of the PSG and PSA are in neutral state it is not clear which polarization state is passing through both the material as well as reaching the iCCD camera. For visualization of the changes occurring during initial plasma exposure this is not a problem.

Acquisitions are done frequently to visualize the changes when the interactions starts. Every acquisition consists of 50 frames each with an exposure time of  $10 \mu\text{s}$  to accumulate enough light reaching the detector. It takes approximately 0.8 seconds to acquire the 50 frames and another 0.7 seconds to save the image. Figure 8.4 shows every third image saved with the corresponding time of acquisition in blue. The 1 slm flow of helium is initiated manually at  $t = 15 \text{ s}$ , while the plasma starts to be applied from  $t = 45 \text{ s}$ .

Between  $t = 15$  and  $t = 45$  seconds the gas flow of 1 slm helium does not seem to induce much change for the intensity reaching the iCCD camera. It is only when the plasma is generated and the ionization waves start impacting the surface after  $t = 45$  seconds that a change is observed. From  $t = 67.6$  seconds a local decrease in intensity is observed which spreads radially as the exposure continues. It takes approximately 100 seconds to spread along the  $1.5 \times 1.5 \text{ mm}^2$  images as shown in figure 8.4. The plasma jet is impacting at a 45 degree angle and in this case it is positioned at the right-hand side (not to be confused with the previous chapters in which the plasma jet was placed on the left-hand side).

The changes that are observed for the intensity reaching the detector are most probably related to the presence of a liquid thin layer which becomes unstable un-

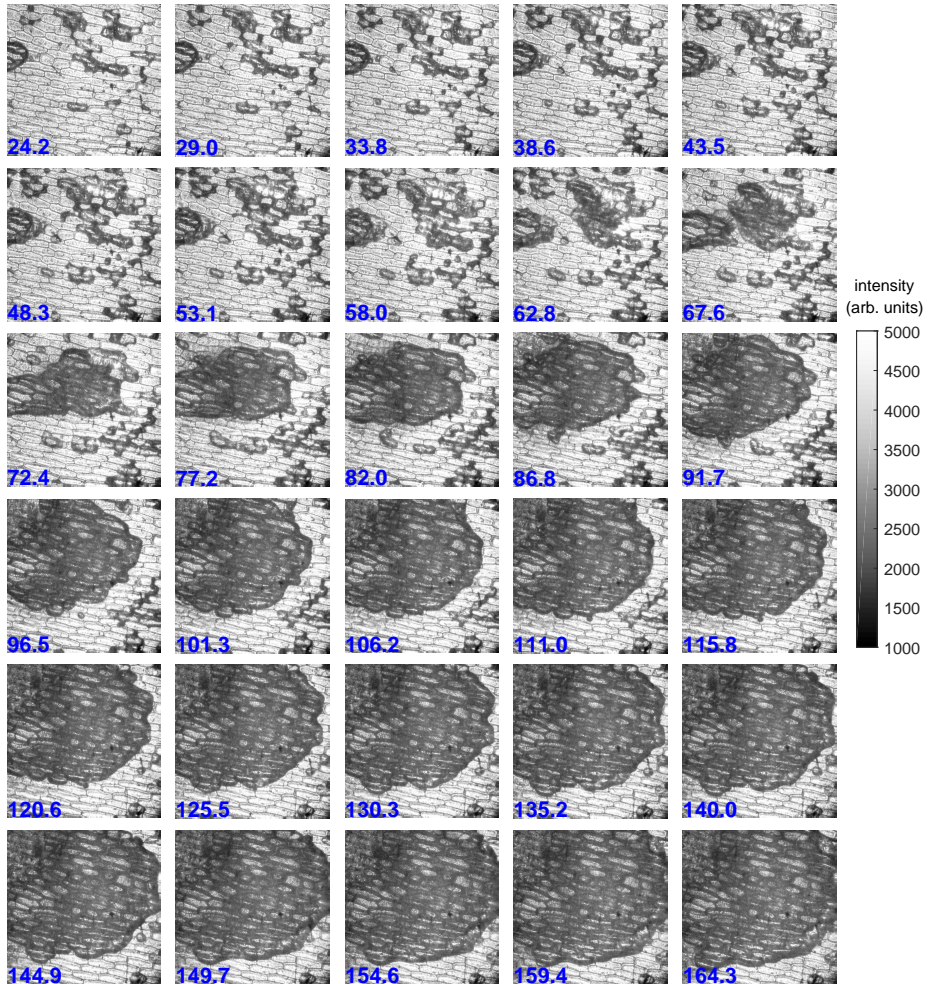


Figure 8.4: Intensity reaching the iCCD camera during the first moments of plasma exposure to a new onion sample. Gas flow (1 slm helium) is started at  $t = 15$  sec, while the voltage (2kV, 30 kHz sine wave) is applied at  $t = 45$  sec which initiates the plasma impact. The jet is located on the right hand side, meaning the impact direction is towards the left. The time-resolved intensity images (time stamp in seconds in blue) are  $1.5 \times 1.5$  mm<sup>2</sup> in size. The liquid crystals are in neutral state and every acquisition (50 frames average) took less than 1 second.

der plasma exposure. Changes in a thin liquid film under exposure of a plasma jet have been observed before,<sup>169</sup> which were related to a change in surface tension that induced Marangoni flows. These changes are different than when applying only a gas jet to the liquid thin layer, which can also deform the surface.<sup>170</sup> Additionally, by the deposition of surface charge it is possible to influence a thin liquid layer through dielectrophoresis.<sup>135</sup> This could play an important role since the dewetting is only observed when the plasma jet is turned on and not when only the gas flow is turned on. Dewetting and rupture of thin films have also been studied using infrared laser spots,<sup>171,172</sup> where it has been found that the energy and spot size greatly influence the timing, occurrence and velocity of the dewetting.

The unstable liquid front spreads radially outwards away from the impact region. This effect has only been observed for *new* and “*fresh*” onion cell samples. The spreading does not return after the plasma exposure has been ended and it is neither present for onion cell samples that have been exposed to room conditions for a duration of time. This suggests that the plasma is not deforming the liquid thin layer, but rather causing a dewetting through evaporation. Evaporation of water vapor due to the presence of a plasma jet has been shown numerically,<sup>70</sup> which predicts consequently that this causes a cooling of the liquid of approximately 10 degrees over 200  $\mu\text{m}$  at the interface. The thickness of the onion cells is approximately 5–10  $\mu\text{m}$ .

The local evaporation of the liquid thin layer causes significant changes of the sample during the plasma exposure. This would render the possibility to apply time-resolved Mueller polarimetry to investigate the electric field non-valid. However, the evaporation only occurs during the first minutes of the interaction between the discharges and the targeted sample. As a result, Mueller polarimetry can be applied afterwards. First, the results are shown with the mapping (approach 1) done before and after the plasma exposure. Afterwards the results obtained with the second approach are shown, where electric field patterns are obtained during the interaction.

## 8.2.2 Mapping Before and After Exposure

The mapping of the combined sample is done before and after plasma exposure for two reasons. Firstly, mapping allows to examine a greater area of the exposed sample by measuring the Mueller matrix while positioning the sample at a fixed grid around the impact area of the plasma jet. This gives information on

---

<sup>169</sup>C. W. J. BERENDSEN et al. *J. Phys. D. Appl. Phys.* 2015 **48**: 025203

<sup>170</sup>C. W. BERENDSEN et al. *J. Colloid Interface Sci.* 2013 **407**: 505–515

<sup>135</sup>C. W. J. BERENDSEN et al. *Soft Matter* 2013 **9**: 4900–4910

<sup>171</sup>H. M. J. M. WEDERSHOVEN et al. *Appl. Phys. Lett.* 2014 **104**: 054101

<sup>172</sup>H. M. J. M. WEDERSHOVEN et al. *Phys. Rev. Appl.* 2015 **3**: 024005

<sup>70</sup>A. LINDSAY et al. *J. Phys. D. Appl. Phys.* 2015 **48**: 424007

the changed state (evolution) of the targeted material, by examining the transmission, linear birefringence, and depolarization. The second reason is to verify whether the results from the second approach (time-resolved measurements during the interaction) are valid. This has to be done since those measurements are done in-situ and material changes of the sample during the acquisition can cause errors since they are not repetitive. This could lead to the appearance of optical properties that are non-physical or inaccurate.

In this example the mapping is performed using a  $3 \times 3$  Cartesian grid with 1.5 mm distance between the positions. The central image represents the location of the impact region. The ZABER motorized translation stages are used to precisely position the sample to the grid points to allow a precise combination of the results to create a map of the examined area with an increased field of view of  $4.9 \times 4.9$  mm<sup>2</sup>. Spatial points at the edge of each measurement are averaged with the corresponding points of the neighboring measurements.

Figure 8.5 shows the relative transmission, total linear retardance and depolarization of the combined sample before and after certain plasma exposures. Hence the BSO is not influenced by temperature and electric field, meaning the optical properties are dominated by the targeted sample on top of the electro-optic BSO, i.e the onion cell layer. The 9 maps are shown in full scale in the appendix B which reveals the high resolution obtained by the mapping procedure.

The transmission is obtained from the first element of the measured Mueller matrix (used to normalize the Mueller matrix) and is relative to the transmission of air. After the logarithmic decomposition is applied, the total linear retardance is calculated by the square root of the sum of  $\Gamma_{0/90}$  and  $\Gamma_{45/135}$  squared. The diagonal elements of the  $L_u$  matrix are used to examine the total depolarization, by taking the square root of the sum of the diagonal elements squared and dividing it by 3.

The transmission of the sample before any plasma exposure (shown in the top-left map of figure 8.5 and figure B.3) clearly shows the unperturbed onion cell layer. After 8 minutes of treatment the transmission map has changed drastically, see figure B.4. In the impacted area the transmission has decreased significantly and further dewetting of the thin liquid layer is observed towards the upper left corner. This is consistent with the helium flow, since the plasma jet is located on the right-hand side and lighter helium will move upwards due to buoyancy forces. The onion cells in the bottom and right part of the mapped area seem to be unaffected. This changes when the plasma exposure time is increased. After 48 minutes of exposure the major part of cells are dried indicated by a modified transmission.

The decrease of the transmission has spread radially away from the impact region and inside the impact region a new spatial structure has appeared, which shows the membranes of the onion cells. It will be shown with the electric field

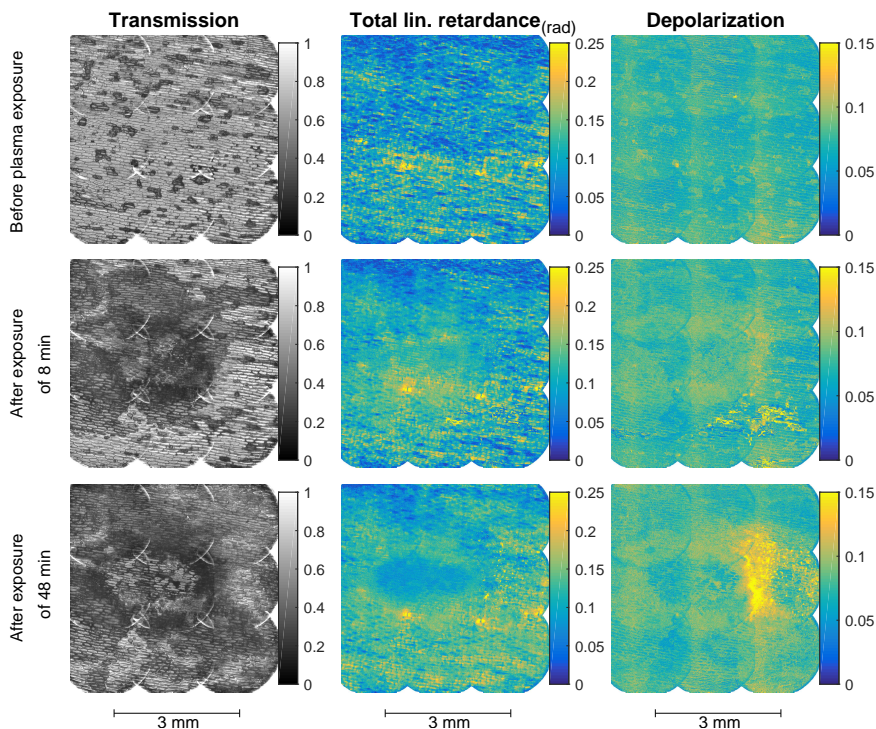


Figure 8.5: The mapped transmission, total linear retardance and depolarization obtained before and after plasma exposure. The results correspond to the same sample as will be used in section 8.2.3. The center of the  $4.9 \times 4.9 \text{ mm}^2$  maps relates to the impact point. The 9 individual maps are shown in full view in the appendix, see figure B.3 to B.11.

patterns that the total impact region relates to both the impact point and the additional *tail* that formed due to the surface discharge “behind” the impact point.

The total linear retardance of the combined sample is shown in the second column of figure 8.5 and in the appendix in figures B.6 to B.8. Since there was no plasma exposure during the acquisition of the Mueller matrices, the linear retardance is caused fully by the onion cells. The structure and orientation of the cell membranes can cause a linear retardance due to the alignment of the molecules forming them.

This specific sample does not have high retardance properties and the effect of the dewetting has only caused minor changes. These minor changes are probably related to a change in focus and / or light propagation through the sample. After 48 minutes of plasma exposure the linear retardance has decreased in the impact region. This is an indication that etching has occurred and that the onion cell layer

has become thinner or smoother. Additionally, some small peaks with a relatively high retardance are observed on the right side of the impact point.

The depolarization, shown in the right column of figure 8.5 and in the appendix in figures B.9 to B.11, shows similar behavior as the total linear retardance. After 8 minutes of plasma exposure there is in the bottom area of the mapped images an increase in depolarization. This is most probably related to the local dewetting of the onion cell sample. After 48 minutes a significant increase in depolarization is observed on the right side of the impact region. This pattern is also observed with the time-resolved measurements during the plasma exposure (approach 2), as will be shown in the next section. The fact that it is also detected after the exposure means it is not a false representation caused by the acquisition of the intensity elements while the sample is changing under exposure.

At present we do not have any plausible explanation for the occurrence of this pattern of high depolarization. Further experiments and measurements with other techniques such as polarimetric microscopy may help to elucidate the origin of it. The location of the increased depolarization is only on the right side of the impact region, on the side where the plasma jet is located. This matches the location of the blackening that was observed on BSO (without an additional complex material) for the plasma jet in a controlled nitrogen environment, shown in chapter 4 section 4.4.2 in figure 4.12. The blackening of the BSO in the nitrogen environment and the depolarization peaks on onion cells are different material changes, but the location where they occur relative to the impact point makes it plausible that they share a similar cause.

The impact region itself has a lower depolarization, while an outer ring region is observed right at the edge of the impact region (where the transmission has decreased significantly) for which the depolarization has increased to approximately 0.1. The decrease of depolarization in the center of the impact area can be related to the etching of the onion cells. Due to the etching the amount of scattered light decreases, thus increasing the amount of direct light reaching the camera. This is supported by the fact that the transmission has increased in the impact zone after it initially got “blackened”.

The slight increase of depolarization in a ringed region all around the impact point (so not the area with high depolarization) can be related to a severe dewetting of the cells. In general, water present in the cells can act as a matching refractive index medium between the air and the cell membranes and organelles. The effect of the index matching is a decrease of the scattering level since it is proportional to the difference of refractive indexes between different media. Once the water has disappeared, the optical contrast between the air and the cell components becomes large and thus the scattering level. An increase in scattering results to a decrease of the transmission and an increase of the depolarization since the relative weight of the direct light, which is fully polarized, is decreased

in comparison to the scattered light component.

To relate the observed changes in the material to the plasma interaction, the second approach of examination is applied, where time-resolved measurements are done during the interaction to capture the electric field to which the onion cells are exposed to.

### 8.2.3 Electric Field Through Onion Cells

#### Mueller matrices and logarithmic decomposition

After the first plasma exposure of 8 minutes and a sequential second mapping of the optical state of the combined sample, a new plasma exposure is started to investigate time-resolved changes caused by the electric field. First the sample is left for 120 second after the plasma jet has been initiated (1 slm helium flow and 2.0 kV amplitude sine wave at 30 kHz) for the temperature profile to become stable. This makes it possible to subtract the retardance background generated by temperature gradient induced strain.

After the two minutes of stabilizing time the Mueller polarimeter is used to measure two Mueller matrices during the plasma exposure (before and after impact) using the external trigger relative to the rise of the positive half period of the high voltage sine wave. A delay of  $7 \mu\text{s}$  is used to measure the optical state of the combined sample after the ionization waves have impacted and charge deposition has taken place inducing electric fields. For the optical state when temporal surface charges are not present a time delay of  $28 \mu\text{s}$  is used. This is at the end of the voltage cycle where the charges have recombined and no electric fields are induced. In the investigations presented in the previous chapters a time delay of  $1 \mu\text{s}$  was used but now the exposure time is increased from 1 to  $3 \mu\text{s}$ . Therefore it is better to look at a time delay of  $28 \mu\text{s}$  to make sure not to be too close to the impact event of the ionization waves and the subsequent temporal deposition of charge. The increased exposure time is used to increase the accumulated light intensity, while the total acquisition time of the intensity matrix remains between 115 and 130 seconds. Each element of the intensity matrix is obtained via averaging of 500 frames before going to the sequential next element by switching the combined states of the liquid crystals. When both Mueller matrices (before and after impact) have been acquired, the plasma exposure is stopped after a total time of 8 minutes. This accumulates to the total *treatment* time of the sample.

Figure 8.6 shows the two obtained Mueller matrices of the combined sample (BSO with onion cells) under plasma exposure, before (bottom matrix) and after impact (top matrix) which results in the temporal deposition of surface charge. The onion cell layer used in this example was taken again from the outer facing cells of the third onion layer (same sample as used for the results shown in figure 8.5 but different than used for figure 8.4) and the results are shown during the

sixth time the same location was under exposure of the plasma jet. That means the total plasma exposure of the combined sample during the acquisition of the optical state was in between 43 and 48 minutes. A visualization of what occurred during earlier exposures is shown later.

The Mueller matrices share some characteristics with the matrices shown in the previous chapters, since again BSO is part of the examination done at normal incidence. As a result, the elements in the first column and row, elements  $\{1, 2-4\}$  and  $\{2-4, 1\}$ , are close to zero except element  $\{4, 1\}$  which will be discussed later. The first element  $\{1, 1\}$  is unity due to normalization of the matrices by dividing each element by the transmission. The transmission is shown in figure 8.7.

The transmission shows the spatial structure of the onion on top of the BSO material. Normally, the BSO material with a thickness of 0.5 mm has a transmission compared to air between 0.65 and 0.70. The transmission of the combined sample is lowered at some locations to 0.15, because light has been scattered out due to the presence of the onion cells, while other regions show transmission equal to only BSO (0.67). This suggests that in those regions there is no onion cell layer present anymore. In the center of the images an almost circular region is identified where the transmission is approximately 0.54. This region is found to be the impact region of the ionization waves, by visualization of the induced electric field as will be shown later. In this region the transmission is not equal to BSO meaning that there is still organic material present. Cell walls do show indications that etching has taken place since they appear much thinner than the cell walls around them, see for instance the cells in the upper left corner of the image.

The transmission is relative to the calibration, i.e. air, which is done using the same acquisition settings in terms of exposure time and number of acquired frames for averaging. During the time of acquisition of both time-resolved Mueller matrices (each takes approximately 120 sec) the samples have changed slightly because of the plasma interaction with the onion cells. In order to highlight the changes that occurred during this plasma exposure a relative change in transmission is evaluated by taking the ratio between the two measured transmissions. The changes that are observed are present around a circular region which is identified as the impact area of the discharges. The relative transmission image shows that the transmission of the sample changed during this exposure of 8 minutes most noticeably in the area surrounding the impact point of the plasma with the cells. This area appears in red meaning that the transmission has decreased. This phenomenon is referred to as '*blackening*' of the sample.

The Mueller matrices in figure 8.6 include non-zero off-diagonal elements, similarly as was shown in the previous chapters when only BSO was under exposure of the plasma jet. There is no (anti) symmetry present between the off-diagonal elements since the optical properties are entangled. The logarithmic decomposition is applied and separated in  $L_m$  and  $L_u$  as was done before to extract the

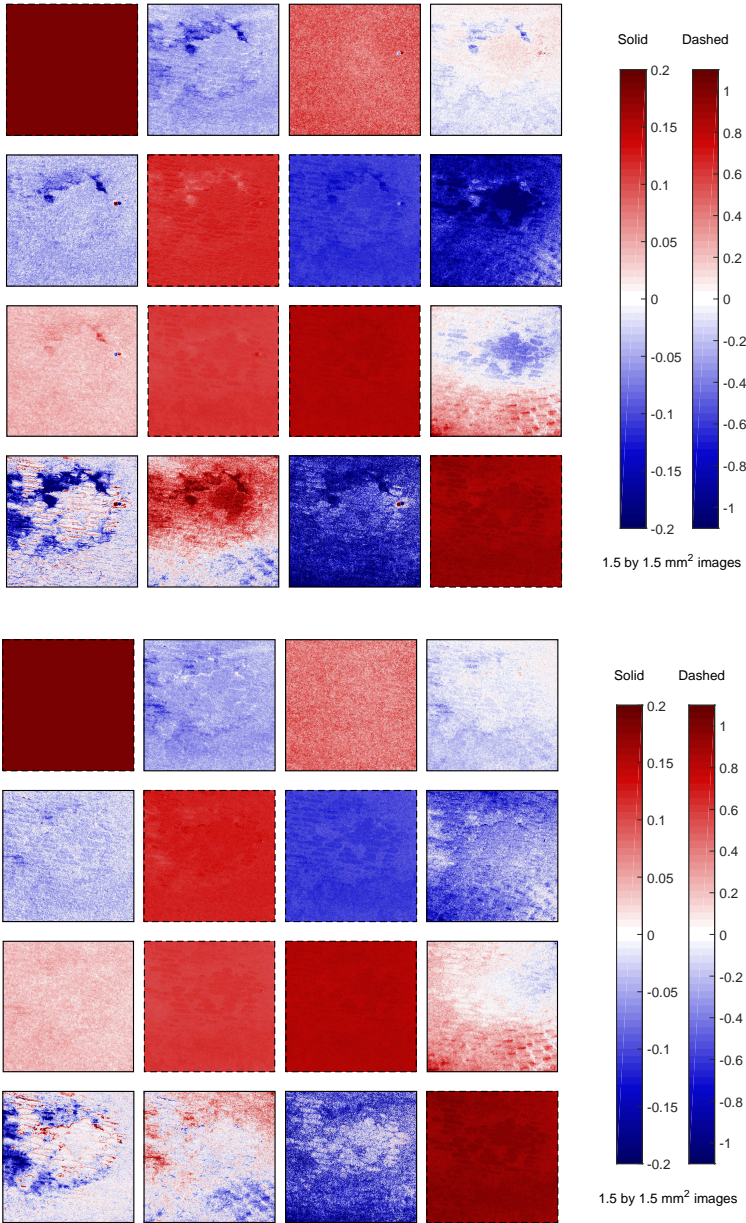


Figure 8.6: The time-resolved Mueller matrices of the combined sample (BSO + onion cells) under exposure of the AC-driven plasma jet, shown before impact of the ionization waves in the bottom matrix and after impact in the top matrix. The border of the matrix elements (shown  $1.5 \times 1.5 \text{ mm}^2$ ) indicates the colorscale. The guided ionization waves produced by the plasma jet are impacting from the right hand side moving towards the left. The influence of temporal charge deposition is included in the top matrix.

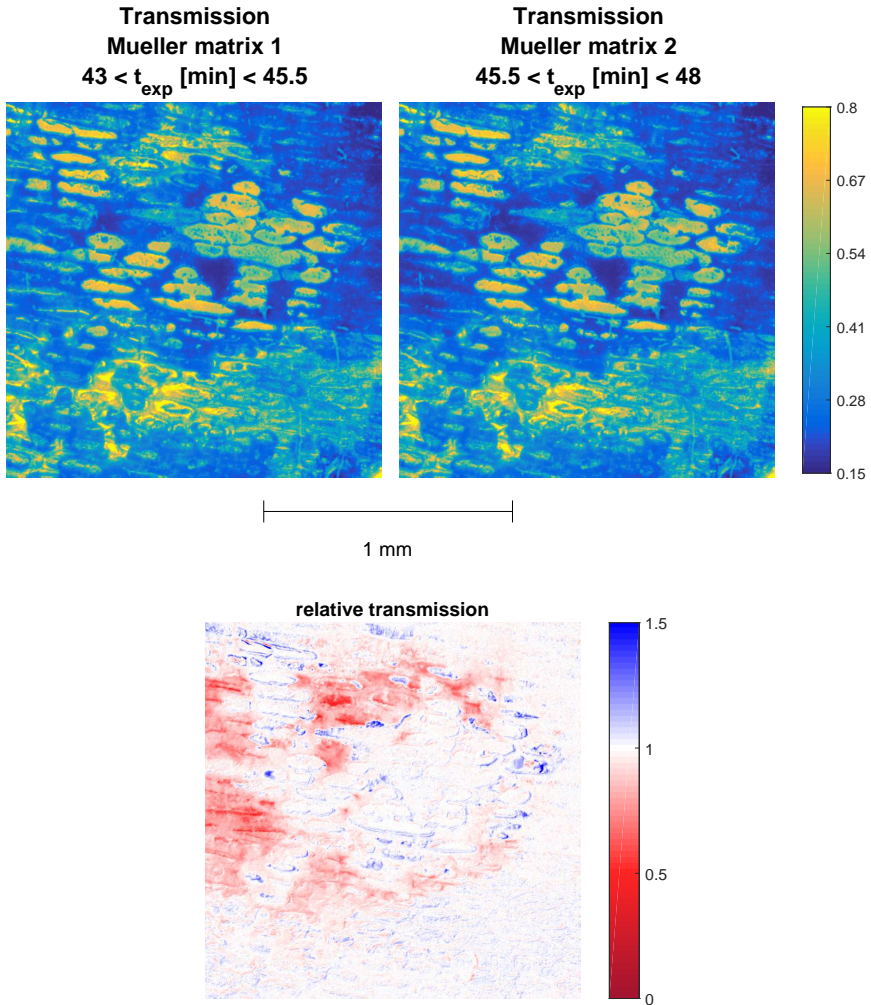


Figure 8.7: Transmission obtained from the two Mueller matrices measured time-resolved after impact (Mueller matrix 1,  $t_d = 7 \mu\text{s}$ ) and before impact (Mueller matrix 2,  $t_d = 28 \mu\text{s}$ ). The total accumulated time the sample has been under exposure is denoted by  $t_{exp}$  in minutes. The relative transmission between the time-resolved measurements is simply obtained by division between the transmission of the second matrix by the transmission of the first matrix.

optical properties. The resulting logarithmically decomposed matrices are shown in figures 8.8 and 8.9.

Due to the separation of the optical properties, the  $L_m$  matrix is symmetric again for the first row and column, while anti-symmetric from the remaining elements. A spatial pattern related to circular diattenuation seems to be present,

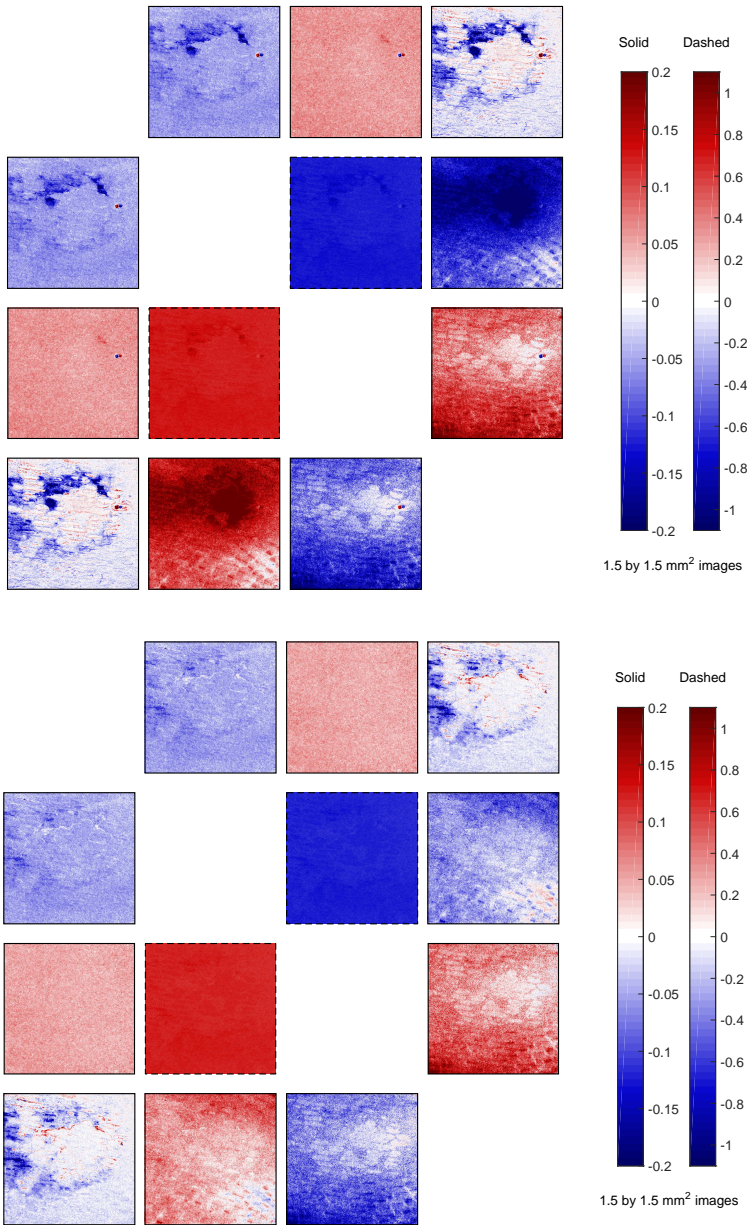


Figure 8.8: The logarithmically decomposed  $L_m$  matrices of the combined sample (BSO + onion cells) under exposure of the AC-driven plasma jet, obtained before impact (bottom matrix) and after (top), showing the diattenuation and birefringent properties. Similar remarks as in figure 8.6 are applicable.

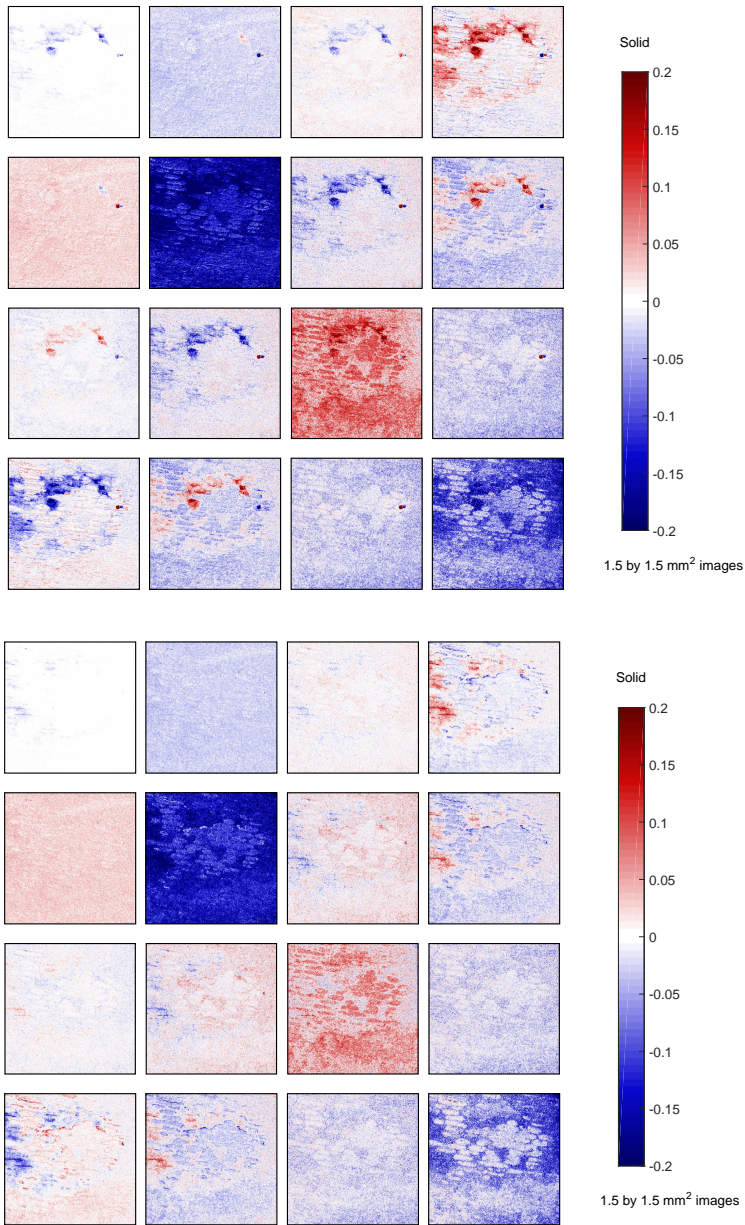


Figure 8.9: The logarthimically decomposed  $L_u$  matrices of the combined sample (BSO + onion cells) under exposure of the AC-driven plasma jet, measured before impact (bottom matrix) and after (top). Depolarization properties are shown in the diagonal elements, while the off-diagnoal elements relate to uncertainties in the optical properties.

see elements  $\{1, 4\}$  and  $\{4, 1\}$ , both before and after impact. This comes partially from the non-zero  $\{4, 1\}$  element observed in the Mueller matrix. However the same spatial pattern is present in the  $L_u$  matrix for the same elements. The pattern matches with the relative transmission, which confirms in fact that it is a false presentation of an optical property, solely present because the intensity matrix elements were captured while the sample was undergoing change due to the interaction. Similar spatial patterns are present in all the  $L_u$  elements as a result. This indicates that the optical properties in these areas have to be examined with care.

The diagonal elements of the  $L_u$  matrices represent the depolarization properties of the combined sample. Element  $\{3, 3\}$  appears slightly positive which is non-physical since all the depolarization properties should be smaller than zero by definition. This is also present when the combined sample is moved to a location where only BSO is present where it is measured as reference. The non-physical positive offset of the second depolarization element can therefore be compensated by taking the difference with the reference. Also the first and third element are compensated, since the reference shows already slightly negative values for only BSO. The same is observed when the sample is removed completely and air is measured.

The  $L_m$  matrices show the presence of a strong circular retardance,  $\{2, 3\}$  and  $\{3, 2\}$ , due to the rotatory power of BSO, as was observed in the previous chapters. The linear retardances,  $\{2 - 3, 4\}$  and  $\{4, 2 - 3\}$ , are present as well which is a combined effect from the onion and the BSO under external influence (induced electric field and temperature induced stress). This means that temperature gradient induced stress is present in both matrices as well as electric field induced anisotropy for the top matrix measured after impact of the ionization waves when the charges are present. The effect of the electric field due to surface charges is clearly visible by comparing element  $\{2, 4\}$  in both matrices. The linear retardances induced by the impact of the ionization waves are used to calculate the electric field, as will be specified in the next section.

### **Electric field and depolarization**

The two logarithmically decomposed matrices  $L_m$  and  $L_u$  obtained before and after the impact of the ionization waves are used to visualize the transient electric field generated inside the BSO material and the depolarization caused by the onion, shown in figure 8.10. The electric field is calculated similarly as before using equation (3.29) by taking the difference before and after impact of the linear retardance in both coordinate systems. Similar as for the mapping, the total depolarization is calculated as one-third of the square root of the sum of the three compensated diagonal elements, of the  $L_u$  matrix, squared. The resulting total depolarization, shown in figure 8.10, is calculated using the second  $L_u$  matrix.

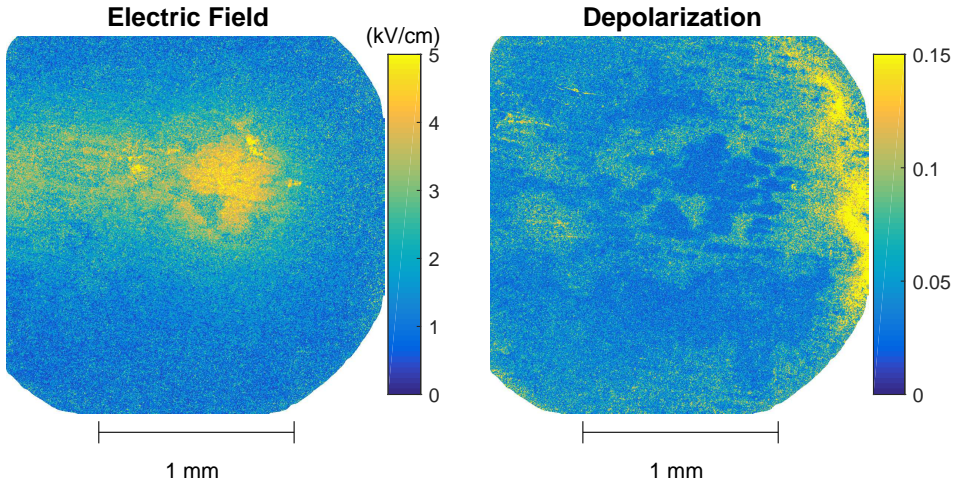


Figure 8.10: The obtained electric field pattern (kV/cm) from the change in linear retardances before and after impact using the logarithmically decomposed time-resolved matrices. The total depolarization is calculated using the second  $L_u$  matrix, relative to the reference measurement of unperturbed BSO without the onion sample present.

The electric field shows a similar pattern as observed before. Since the plasma jet is positioned on the right-hand side, rather than the left-hand side as before in the previous chapters, the pattern is flipped. The highest values of approximately 5 kV/cm are observed in the impact point. Lower fields are measured “behind” the impact point on the left side in the direction of the helium flow. This so-called *tail* is caused by a surface propagation of the discharge. The electric field relates to the axial field perpendicular to the surface of the sample. The spatial structure of the onion cell layer is visible in the electric field pattern, lowering the electric field where depolarization is higher ( $\sim 0.08$ ).

The spatial profile of the total depolarization relates with the transmission shown in figure 8.7. The patterns shown in figure 8.10 show the entire field-of-view of the iCCD camera, which is larger than the previously shown area of  $1.5 \times 1.5 \text{ mm}^2$ . The similarities between the transmission and the depolarization are understandable since they both relate to the thickness of the material.

The total depolarization shows an increased edge on the right side of the image with a value of 0.15. Since the depolarization is calculated from the time-resolved measurements during plasma exposure, it can be caused by the non-constant acquisition of the intensity images. A comparison with the optical properties measured before and after the plasma exposure is necessary to examine this. This pattern is also visible in figure 8.5 which as discussed means that it is physical and not induced by an error since the Mueller matrices are measured while the sample

is evolving.

The electric field and total depolarization are obtained from the time-resolved matrices shown before. As previously stated, those are obtained during the 6th exposure of 8 minutes of the same sample to the plasma jet. Figure 8.11 shows the obtained results for the relative transmission, electric field and depolarization during all the different exposures that were done at the same onion cell sample.

During the first exposure to the plasma to this onion sample, the time-resolved matrices were directly acquired, instead of capturing the change in intensity reaching the iCCD camera as was done in section 8.2.1. As a result, the dewetting of the thin layer, as shown in figure 8.4, is still continuously spreading radially outwards. These significant changes that occur during the acquisition of the intensity elements can cause major errors in the interpretation of polarimetric effects. This can contribute to an enhancement of the depolarization values, see for instance the lower right corner of the depolarization image taken during the first plasma exposure. This is simultaneously observed with a non-physical value of the electric field (because there is no plasma in that area). The time-resolved measurements were taken in the last 5 minutes of each of the 8 minute exposure periods, meaning the changes in the center of the impact region is minimal, while they are largest at the edge due to the radial spread. This is observable in the relative transmission as well as the electric field and depolarization.

Starting from the second plasma exposure, the dynamical changes in the sample structure and consequent optical response are less abrupt, as shown by the relative transmission. Inside the impact point region where the electric field is highest, there is a small increase in relative transmission during the second plasma exposure. This suggests (partial) removal of the onion cell layer creating a higher transmission. Around the impact region there is a gradual decrease. This tendency is present and keeps constant along the entire the measurement sequence of 6 plasma exposures.

The increased depolarization at the upper right edge of the images observed during the last 25 minutes of plasma exposure is not present in the relative transmission images. This already suggests that it is not a false value due to changes during the acquisition of the intensity elements but rather a slow change of the sample occurring over longer time scales. This was confirmed by the mapping done, shown in the previous section, before and after the individual plasma exposure series of 8 minutes.

Results obtained when using different onion cell layers show repetitive and comparative features, see figures B.1 and B.2 in the appendix. Although different onion samples are tested from different inner layers it is shown that the electric field pattern is retrieved through the (partially) depolarizing complex sample. This is only possible because Mueller polarimetry is applied and the logarithmic decomposition allowed to separately examine these two quantities.

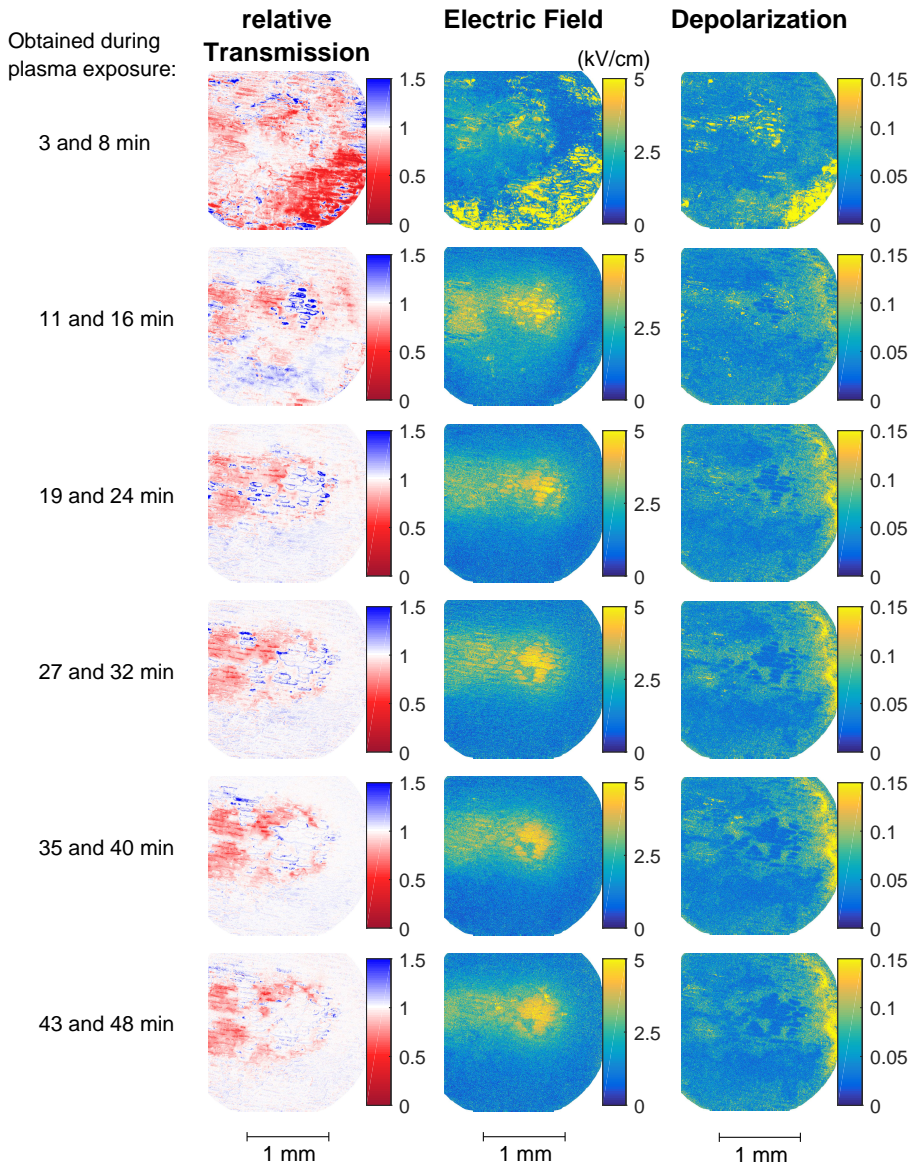


Figure 8.11: The relative transmission, electric field and total depolarization obtained during different exposures of the same combined sample (BSO + onion cells). The relative transmission and electric field are obtained using the differences between the two time-resolved matrices. The depolarization is shown for the second matrix, in that exposure series, relative to the reference BSO.

## 8.2.4 Outlook and Discussion

Figures 8.10 and 8.11 show it is possible to measure electric fields in the electro-optic BSO in combination with an organic complex sample like a cell layer from an onion. Mueller polarimetry allows for this investigation because all the optical properties are part of the examination. The unknown transmission of the combined sample together with the depolarization properties due to scattering render it difficult or even impossible to investigate the linear retardance with a simpler setup like for instance the Sénarmont setup.

Also for Mueller polarimetry changes of the sample during the acquisition of the time-resolved matrices can become a problem if they are not taken into account. For this purpose, the sample should always be investigated before and after exposure as well as during exposure. For the preliminary study discussed in this chapter the acquisition of the time-resolved Mueller matrices took approximately 120 seconds per matrix. This is partially because short exposure times are taken meaning that multiple frames per intensity element are needed for averaging. The design of this Mueller polarimeter used in the course of this dissertation was done for the sole purpose to be able to acquire time-resolved measurements relative to an external trigger event (i.e. to measure the electric field in the electro-optic crystals without an additional sample which can evolve in a different time scale on top of it). The optical design of the polarimeter can be adjusted in the future to measure the full Mueller matrix at a faster rate. This would improve the quality of the measurements since changes of the sample during the acquisition of the intensity elements would become less influential.

The onion cell sample was chosen as a test case to show the use of Mueller polarimetry to investigate electric fields through the targeted sample while material changes are examined simultaneously due to the exposure of the plasma jet. Through transmission, linear retardance and depolarization measured before and after plasma exposure (approach 1) it has been observed that the plasma surface interaction at the onion cell layer has caused 4 different categories of change of the material due to the impact. Thanks to the electric field measurements (approach 2) these can be related to the location of the (surface) discharge, charged species and the value of electric field.

The first category is inside the impact point, where the electric field is highest and etching seems to be the most influential during early exposures. Secondly, in the *tail*-region caused by the surface discharge propagating behind the impact point the electric field values are slightly lower. This indicates less surface charge. The optical properties have changed in two ways. First a “*darkening*” is observed, i.e. lowering of the transmission and increase of depolarization, while on longer timescale etching seems to reverse this process.

The third region is located around the total impact zone. There the electric field is zero, meaning there are no surface charges present. In this region there is

only a darkening of the sample. The fourth identified region happens only on the right side of the impact zone and is characterized by sharp depolarization peaks that have appeared. Since no electric field is present this cannot have been caused by charged species. This fourth region appears not with every examined onion cell layer. Only when the onion cell layer is taken from the outer facing side of the onion peel it could appear and not with the cell layer from the core-facing side.

Mueller polarimetry does not give any information about the physical-chemical processes that are related to the darkening of the samples. For that investigation other techniques have to be used, for instance examination of the changes in the chemical composition of the sample. However, thanks to the examination done of the combined sample including the BSO material, Mueller polarimetry has allowed for the spatial identification with regard to the induced electric field. This new diagnostic approach opens new ways to couple material changes induced during a plasma surface interaction to the characteristics of the discharge itself in terms of the induced electric field by temporarily deposited surface charge. Naturally, this is not limited to the study of plasma-onion interaction but can theoretically be applied to many different types of targets.

### 8.3 Summary and Perspectives

- The use of Mueller polarimetry has been shown for the examination of plasma surface interactions occurring for more complex targeted samples. This is done through optical characterization of a combined sample of the complex material with the electro-optic crystal.
- Mueller polarimetry combined with the logarithmic decomposition allows for the examination of the electric field through detection of the changes in the linear retardance, while material changes of the targeted sample are monitored through transmission and depolarization.
- A single epidermal cell layer of an onion was used as an example to study the complex plasma surface interaction as a function of the induced electric field. Different regions of the targeted material were found depending on the impact region, deposition of charge and induced electric field, causing etching and a *darkening* of the sample.
- Complementary diagnostic methods are necessary for a deeper chemical understanding of the changes that were induced, but the proof-of-principle of the use of this new diagnostic approach has been shown.
- The approach is believed to be interesting for the plasma community as well as the field of functional materials / surfaces, since the evolution of a sample under plasma exposure can be monitored in-situ while the electric field is measured at the same time.

---

## References

- [70] A. LINDSAY, C. ANDERSON, E. SLIKBOER, S. SHANNON, and D. GRAVES. *J. Phys. D. Appl. Phys.* **48**: 424007, 2015. DOI: [10.1088/0022-3727/48/42/424007](https://doi.org/10.1088/0022-3727/48/42/424007) (see pp. 21, 178, 204)
- [135] C. W. J. BERENDSEN, C. J. KUIJPERS, J. C. H. ZEEGERS, and A. A. DARHUBER. *Soft Matter* **9**: 4900–4910, 2013. DOI: [10.1039/c3sm27944h](https://doi.org/10.1039/c3sm27944h) (see pp. 97, 204)
- [169] C. W. J. BERENDSEN, E. M. VAN VELDHUIZEN, G. M. W. KROESEN, and A. A. DARHUBER. *J. Phys. D. Appl. Phys.* **48**: 025203, 2015. DOI: [10.1088/0022-3727/48/2/025203](https://doi.org/10.1088/0022-3727/48/2/025203) (see p. 204)
- [170] C. W. BERENDSEN, J. C. ZEEGERS, and A. A. DARHUBER. *J. Colloid Interface Sci.* **407**: 505–515, 2013. DOI: [10.1016/j.jcis.2013.06.011](https://doi.org/10.1016/j.jcis.2013.06.011) (see p. 204)
- [171] H. M. J. M. WEDERSHOVEN, C. W. J. BERENDSEN, J. C. H. ZEEGERS, and A. A. DARHUBER. *Appl. Phys. Lett.* **104**: 054101, 2014. DOI: [10.1063/1.4863318](https://doi.org/10.1063/1.4863318) (see p. 204)
- [172] H. M. J. M. WEDERSHOVEN, C. W. J. BERENDSEN, J. C. H. ZEEGERS, and A. A. DARHUBER. *Phys. Rev. Appl.* **3**: 024005, 2015. DOI: [10.1103/PhysRevApplied.3.024005](https://doi.org/10.1103/PhysRevApplied.3.024005) (see p. 204)



# General Conclusions and Perspectives

## Method

Mueller polarimetry is examined for the first time as a novel optical diagnostic for the investigation of plasma surface interactions. The general approach presented throughout this work, to examine optically active materials under plasma exposure, allows for an *in-situ* characterization of several aspects of the interaction that are important for plasma applications regarding modification or treatment of temperature sensitive targets. The focus is on the identification of the spatially and time-dependent electric fields experienced by the targeted surfaces, as well as the inhomogeneous temperature profiles induced by the plasma interaction.

Mueller polarimetry is closely related to ellipsometry which has been used significantly in the past to examine plasma surface interactions. Ellipsometry has been applied mostly in reflection to examine changes occurring in materials in a (low-pressure) plasma environment, regarding e.g. thin-film growth, etching processes and modifications to the refractive index or surface energy. These examinations focused on the material side and information on the plasma side had to be obtained from modeling or “plasma”-diagnostics. For the relatively stable plasmas and ideal flat surfaces of thin films used in these low-pressure environments, this approach has had success. However, at atmospheric pressure different challenges are present that demanded a new approach.

The plasmas generated at atmospheric pressure are usually filamentary in nature, characterized by short time scales ( $\approx \mu\text{s}$ ), relatively small dimensions (mm - cm), high gradients in species' densities, and locally high inhomogeneous electric fields. As a consequence, the determination of the characteristics of the plasma environment during the interaction with a target can prove to be a demanding task. Extrapolation of measured plasma parameters towards the target is riskier

since for instance the plasma sheath is highly collisional at elevated pressures. Additionally, the role that dielectric targets play in alterations of the dynamics of ionization waves is not well understood.

The approach taken in this work shows how optically active targets can be examined with Mueller polarimetry to directly investigate the conditions to which targets are exposed to *during* an interaction with plasma. This optical diagnostic technique relates to ellipsometry but it follows the more general Stokes formalism which includes depolarization of the polarized light due to the interaction with the sample. The technique is applied in transmission to examine certain aspects of the plasma interactions (e.g. electric field, temperature or stress) that are induced *inside* the targeted material.

In order to do this *in-situ* examination of a plasma-surface interaction an unconventional Mueller polarimeter has been built, to be able to measure time-resolved Mueller matrices. Usually, the technique is applied to examine static samples, but that would not be very informative when dealing with transient discharges. The time-resolved results shown throughout this thesis have been examined to investigate the differences that are induced by the plasma impact. Depending on the operating mode of the plasma jet, a plasma impact ( $< 1\mu\text{s}$ ) occurs repetitively every  $33\mu\text{s}$  (AC mode 30 kHz) or  $200\mu\text{s}$  (pulsed mode 5 kHz). This means that the acquisition was done to examine repetitively induced optical changes occurring in these timescales. This was possible because the detection with the iCCD camera was controlled together with the orientations of the liquid crystals to an external trigger event. This trigger event is related to the repetitive generation of the discharges. Hence, all the frames needed to acquire the time-resolved Mueller matrices were done sequentially during separate discharge events.

Most examinations in this work were done to examine changes induced by temporally deposited surface charges during the interaction by comparing the optical state of the material before and after the impact of the ionization waves. Additionally for the pulsed plasma jet, the time delay relative to the trigger event determining the examination of the time-resolved Mueller matrix has been varied to obtain also the change of the optical state *during* the plasma-surface interaction with 100 ns temporal resolution.

The main restriction of the temporal acquisition of the time-resolved Mueller matrices is the jitter in the discharges, which is low for *guided* ionization waves created with this particular jet (ns range). Since the frames needed to build the Mueller matrices are obtained during different voltage periods, the technique is only applicable to examine continuous, repetitive plasma exposures. The interaction occurring with a singular (arbitrarily propagating) filament has additional challenges since all the required frames need to be obtained within a small window of exposure. Luckily, most discharges applied in practice for treatment or

---

modification of temperature sensitive targets are applied continuously and appear to have a repetitive character.

With the investigation of the spatial and temporal charging occurring with a mono-polar positively pulsed jet, a comparison has been made with a two-dimensional numerical fluid model. This phenomenological comparison shows that during the interaction of guided ionization waves produced by a plasma jet and a dielectric target the electric field inside the target is induced following two sequential effects. First, the propagation of the ionization front in the vicinity of the surface induces on short timescales relatively high electric fields due to a locally high volume charge density. Then behind the ionization front, due to deposition of surface charge and left-over volume charge densities, the electric fields induced inside the dielectric target are relatively low but remain at much longer timescales. The electric fields induced during the last phase are examined with Mueller polarimetry when electro-optic targets are used. This is because only the field caused by deposited surface charge is measured following the Pockels effect.

Electro-optic crystals like BSO, have been used by some other groups in the past where the electric field is used to estimate surface charge densities deposited during a certain interaction. In this work, electro-optic crystals have been used to investigate the electric field directly. BSO examined at normal incidence with the Mueller polarimeter allows for the detection of the axial  $E_z$  field. Additionally, new approaches have been formulated to identify and obtain individual images of the separate electric field components (axially and radially resolved) induced inside the target. This is either done by examining the BSO crystal at oblique incidence or by using a different electro-optic material, Fe:LiNbO<sub>3</sub>, which has a different symmetry point group. Analytic relations between the induced birefringent properties and the externally applied electric field are necessary to predict and choose which material should be used to examine a desired aspect of the plasma surface interaction. This has been shown in this work by deriving the relations for the different examined cases by coupling anisotropy induced changes in the index ellipsoid to the polarization state of the propagating light beam.

## Electric Fields

The examined electric fields caused by the impact of the ionization waves generated by the pulsed plasma jet operated for various voltage amplitudes have shown interesting pattern formations indicating the surface interaction. When the pulsed plasma jet impacts the targeted surface at a 45 degree angle, large surface discharges are observed behind the initial impact point for higher applied voltages. When the jet impacts perpendicularly, radial surface streamers are observed that create a stable star-shaped pattern.

Both the elongated surface discharge at a 45 degree angle and the symmetric surface streamer patterns indicate that the volume charge densities (or reduced

electric field) in the head of the ionization wave in the gas phase must be higher with higher applied voltages. This is suggested also by imaging of the light emission of the propagating ionization wave. Surprisingly, the values of the axial electric field measured inside the targeted material seem to decrease when the voltage amplitude is increased from 3 to 6 kV. At 45 degree impact, in the impact point it decreases from 6 to  $4.5 \pm 0.5$  kV/cm, while it decreases from 4 to  $2.0 \pm 0.5$  kV/cm right next to the impact point. For the perpendicular impact, a similar decrease with higher applied voltage amplitude is observed (from 5.0 to 2.6 kV/cm) as well as for the AC driven plasma jet.

These values correspond to the axial electric field, which indicates that the local surface charge density has decreased. This means that the time-integrated flux of charged species towards the targeted surface has decreased, even though most likely more charge is present in the head of the ionization wave. This is explained since the propagation velocity of the ionization wave along the surface has increased with the voltage amplitude. Correlation between imaging of light emission and the induced electric field patterns shows that charges are only deposited in the vicinity of the ionization wave, where light emission occurs. After the ionization wave has passed the electric fields are stable. When the ionization waves propagate faster there is less time to deposit charges on the surface. This shows stability of adsorbed charges and negligible recombination in the quasi neutral channel left behind the ionization front, until the applied voltage potential at the inner electrode changes. This initiates a so-called recombination wave or back discharge.

Since the ionization wave travels faster with higher applied voltage amplitudes, the interaction time with the surface has decreased and less charge has been deposited locally. The total charge that is deposited has increased since a larger area of the surface is part of the interaction. The latter is observed when monitoring the radial electric field patterns, both measured with Fe:LiNbO<sub>3</sub> and BSO examined at an oblique angle. The radial values increase while the interaction area becomes elongated because they depend on all the charges that are deposited, not just the local surface charge density.

This examination towards the influence of voltage amplitude to the surface flux, charge deposition and induced electric field (both axial and radial) shows the potential that Mueller polarimetry has to examine optically active targets for the investigation of plasma surface interactions.

## Temperature Investigation

During the investigation of the electric fields induced by the plasma in the targeted electro-optic sample, a constant background field was observed within the birefringent patterns. Analysis has shown that these images were induced by local temperature gradients that create an internal pressure distribution causing bire-

---

fringent properties through the elasto-optic effect. By following the same analytical approach, a relation was obtained between the birefringence and the second derivative of the temperature distribution. This allowed a fitting procedure / algorithm to be constructed to create numerically a temperature profile for which the second derivatives match the measured birefringent patterns.

Consequently, the temperature profile can be detected with Mueller polarimetry during the same *in-situ* investigation of the plasma-surface interaction when the electric field is examined. This simultaneous imaging has never been done before and has been applied in this work to investigate the influence of the operating frequency of the AC driven plasma jet.

It has been shown that the operating frequency, varied from 20 to 50 kHz, influences the temperature induced in the targeted material. Using the calibrated fitting procedure the temperature profiles can be retrieved from the birefringent background patterns with high accuracy. The maximum increased temperature above room conditions for the examined operating frequencies ranges from  $11.7 \pm 0.9$  to  $25.0 \pm 2.0$  °C. This is caused by an increase of ionization events since a higher operating frequency is used. It is important to know the temperature distribution accurately since these types of discharges are applied to temperature sensitive materials, e.g. polymers and living tissues. Additionally, there are unstable chemical processes that depend strongly on the temperature in this range, i.e. nitrification through peroxyxynitrite in liquids. Other (plasma) diagnostics will not have this accuracy.

The limitation of the fitting procedure using the background birefringent patterns is that only relative temperature differences are detected, so usually the bottom left corner of the images has to be room temperature to get absolute changes. It has been shown that even when this is not the case, and a relative temperature is obtained to an unknown boundary, still trends and relative changes in the temperature can be discussed.

This has been done for measurements performed in a controlled environment with the AC driven jet and for measurements with the pulsed jet at 45 degree impact. Since Mueller polarimetry is applied to examine optically electro-optic targets, information is obtained simultaneously of electric field and temperature.

In a controlled environment the surrounding gas is varied (dry air, O<sub>2</sub>, N<sub>2</sub> and CO<sub>2</sub> with 2.5 % O<sub>2</sub>) where it has been shown that the electric field patterns change since the propagating character of the ionization waves is altered. The temperature differences seem to be negligible. In a N<sub>2</sub> environment the surface discharges show a more filamentary surface propagation compared to dry air and O<sub>2</sub>. This probably means that electron attachment to oxygen is an important mechanism for the prevention of surface filaments. This is observed even more strongly in the predominant CO<sub>2</sub> environment where the most diffuse plasma interaction is seen. Then there is no difference between the impact point and the tail like surface

discharge behind it, and the (axial) electric field values are more homogeneous.

Larger temperature differences are observed for the pulsed plasma jet impacting at 45 with an increase in voltage amplitude. Unfortunately, the measurements were not performed under ideal conditions for the temperature examination, meaning absolute numbers are not obtained in this case. But the increase in temperature with voltage amplitude is seen as well for the AC driven jet, where the temperature increases above room temperature from  $9.2 \pm 1.0$  to  $15.9 \pm 1.1$  °C while the AC voltage goes from 1.0 to 2.0 kV. This is explained by an increase in input power towards the system. Even without the presence of a plasma with only helium flow, there is a small increase in temperature in the targeted sample of approximately  $5.1 \pm 0.8$  °C above room conditions. This is caused by an unusual heat exchange observed for the helium-in-air mixing where the surrounding air cools slightly while the helium core heats up. This is related to the density and / or specific heat of helium compared to air since for a heavier argon gas flow the opposite heat exchange is observed.

The newly developed diagnostic approaches regarding the imaging of the individual electric field components and the temperature distribution relate to the investigation of the birefringent properties. These properties are identified within the Mueller matrix in addition to the diattenuation and depolarization, by following the logarithmic decomposition. Although the latter two properties are not directly used for these approaches it is a big advantage that they are examined as well. With different diagnostics where only birefringent properties are identified it would have been impossible to say if the background birefringence, which was related to the temperature, was indeed a birefringence or maybe a shadow effect caused by diattenuation and / or depolarization.

## Complex Targets

Depolarization becomes more important when examining more complex targets. It has been shown in the last chapter that Mueller polarimetry can be applied to examine a combined sample consisting of a complex organic target with the well-characterized electro-optic materials. When the optical properties are examined under plasma exposure, the birefringence can be used to determine the electric field while changes in the depolarization relate with changes induced inside the complex sample due to e.g. etching or surface modification. This provides unique possibilities to directly relate the experienced electric field to the observed changes (evolution) in a targeted material.

This examination has been applied for a test case consisting of a single layer of onion cells. The spatial images of the electric field induced during the plasma surface interaction have been obtained as well as the depolarization which can be used to identify the state of the targeted sample. Different regions have been identified related to the charge deposition and the resulting experienced fields.

---

Different spatial surface modifications can be coupled to this. Although other diagnostic techniques are needed to quantify the surface modifications themselves, it is a unique possibility to couple them *in-situ* to the plasma interaction through electric field measurements.

The test case has proven the principle of the examination and since depolarization and birefringence are examined, the full use of Mueller polarimetry is shown. This opens the way to apply the same examination to other materials that are more commonly used for plasma treatment, e.g. polymer surfaces or even biological or biomedical samples.

Besides the possibility to apply this new diagnostic technique to examine plasma surface interactions for other temperature sensitive targets in terms of experienced electric field, it can be applied to examine other aspects of an interaction as well. Different materials can be used to exploit other optically active effects, regarding e.g. magnetic fields or pressure. The same analytical approach can be used as shown in this work, where external anisotropies are coupled to the measured birefringence. The external anisotropies are related to the optically active effect through the use of optical tensors, as has been used with the electro-optic tensor and the elasto-optic tensor in this work. Not only different targets can be examined, but also the application of this diagnostic can be easily used for other surface discharges as well besides ionization waves generated by jets, e.g. (surface) DBDs.

Although this work presents the first investigation of plasma surface interactions using Mueller polarimetry, significant progress has been made to the examination of the electric field patterns and temperature distributions. Trends in surface charge densities and total charge have been mentioned but no absolute patterns or values have been shown. This is because a relation between the measured fields and the surface charge properties has to be examined first in the future before any convolution can be made. Lastly, a start has been made to couple the examinations to more complex targets, by using depolarization as an indication of the material evolution under plasma exposure. Further testing is needed as well as a coupling to other diagnostic methods to quantify the surface modifications that are observed, but it provides an exciting approach to examine surface modification directly as a function of experienced electric fields.

---

# Appendix A

## Time Resolved Individual Electric Field Components

Figures A.1 to A.5 show the time-resolved electric field patterns obtained in axial and radial direction during and after the plasma surface interaction for different applied voltage amplitudes for a jet impacting perpendicular (at  $90^\circ$ ) of the BSO. When an amplitude is used of 5.0 or 6.0 kV, the figures either relate to the electric field patterns during the plasma pulse ( $0 \leq t_d \leq 1.0 \mu\text{s}$ ) or after ( $t_d > 1.0 \mu\text{s}$ ), while for 3.0 kV all the results are shown in the same figure.

The time-resolved electric field patterns are obtained following the same procedure as explained in section 5.1.2 used to obtain the results shown in figure 5.9 when applying the 4.0 kV voltage amplitude.

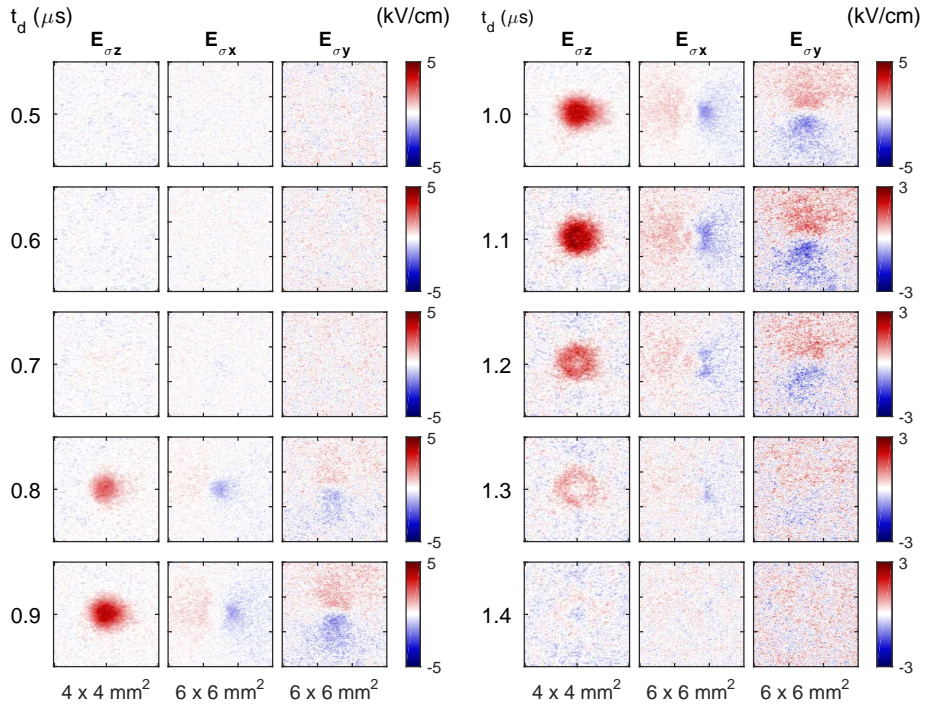


Figure A.1: Time-resolved electric field patterns when operating the pulsed plasma jet using 1000 He and 3 kV voltage amplitude. The jet impacts perpendicularly and is located at 10 mm from the surface. The results have been obtained following the same approach as explained in chapter 4.

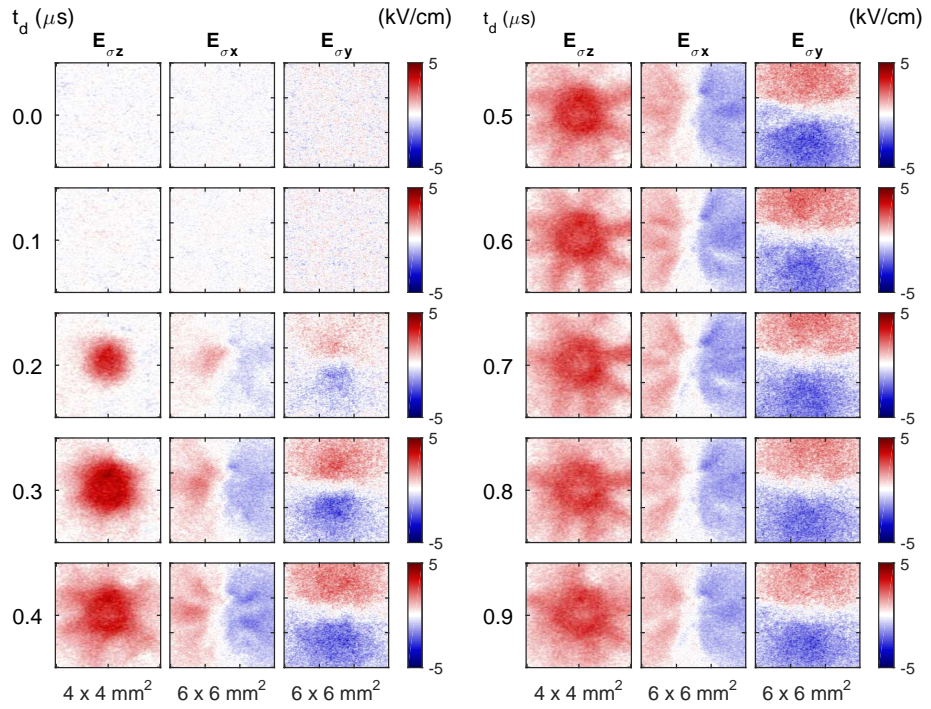


Figure A.2: Time-resolved electric field patterns when operating the pulsed plasma jet using 1000 He and 5 kV voltage amplitude, during the pulse. Similar remarks hold as for fig A.1.

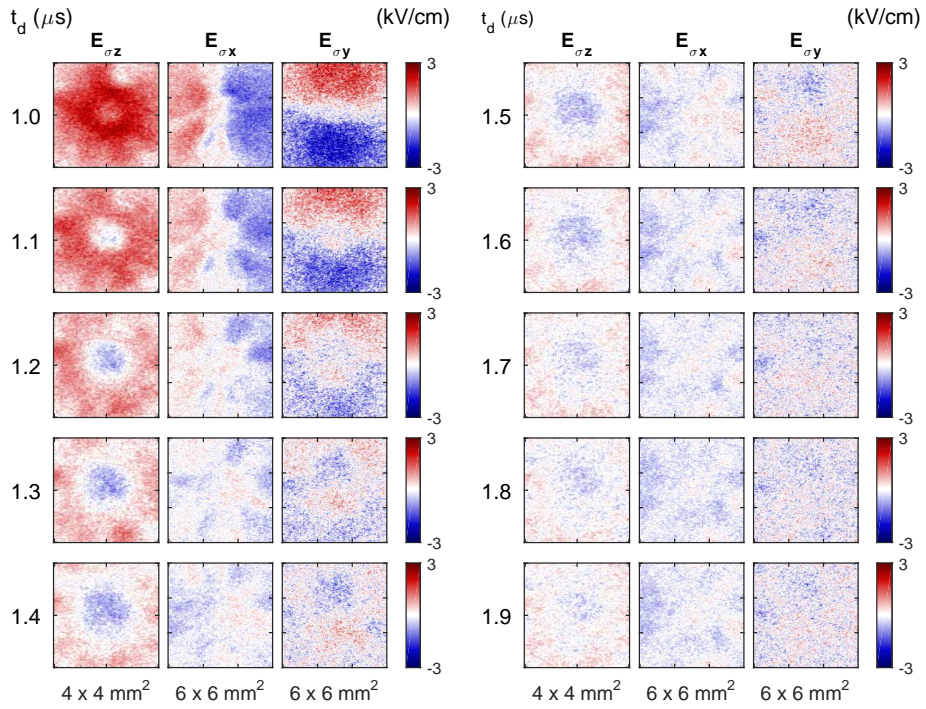


Figure A.3: Time-resolved electric field patterns when operating the pulsed plasma jet using 1000 He and 5 kV voltage amplitude, after the pulse. Similar remarks hold as for fig A.1.

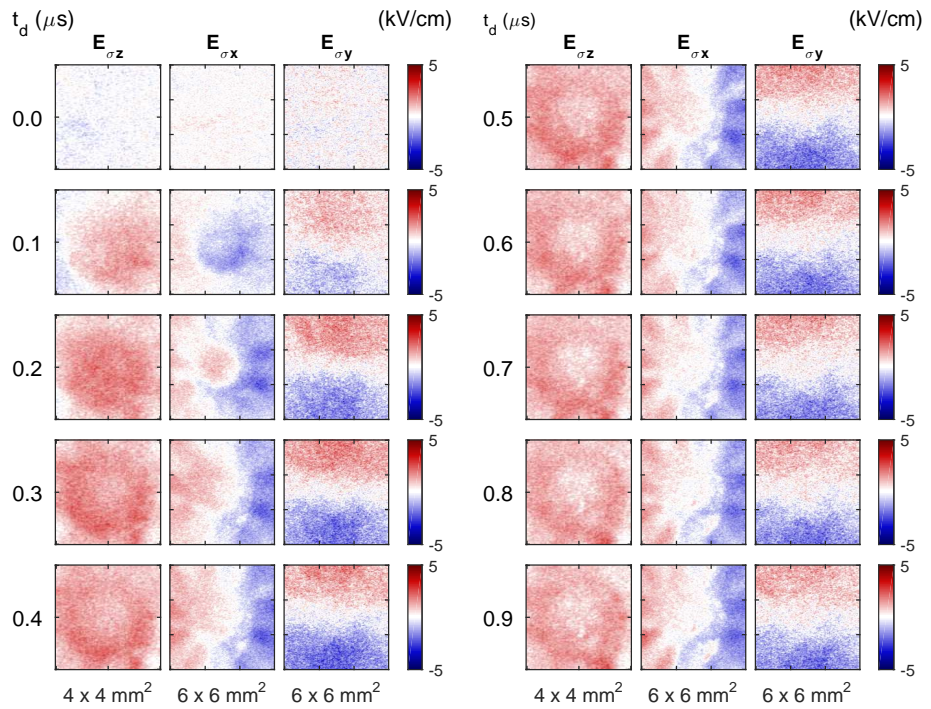


Figure A.4: Time-resolved electric field patterns when operating the pulsed plasma jet using 1500 He and 6 kV voltage amplitude, during the pulse. Similar remarks hold as for fig A.1.

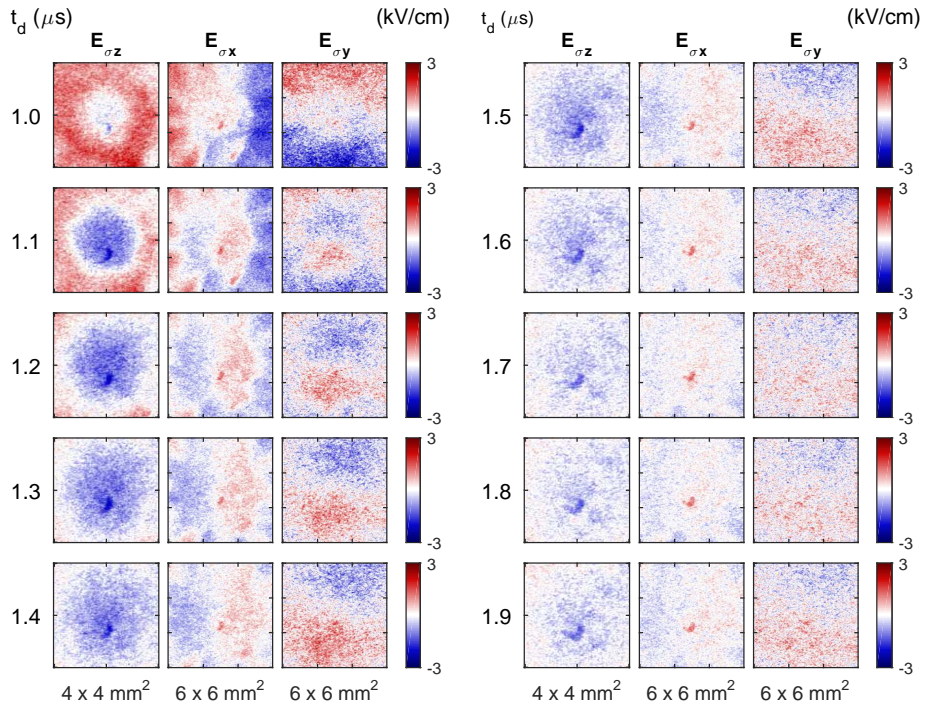


Figure A.5: Time-resolved electric field patterns when operating the pulsed plasma jet using 1500 He and 6 kV voltage amplitude, after the pulse. Similar remarks hold as for fig A.1.

# Appendix **B**

## Additional Figures from Complex Surface Interactions

This appendix shows additional figures that were obtained and partially discussed in chapter 8. Figures B.1 and B.2 shows additional examination that were performed on different single cell onion layers. It shows the reproducibility of the results obtained with Mueller polarimetry to optically examine complex samples coupled to electro-optic targets for the simultaneous investigation of depolarization (indicating the evolution of the sample under plasma exposure) and electric field.

Figures B.3 till B.10 show in full scale the mapped images of transmission, linear retardance and depolarization that were shown in figure 8.5.

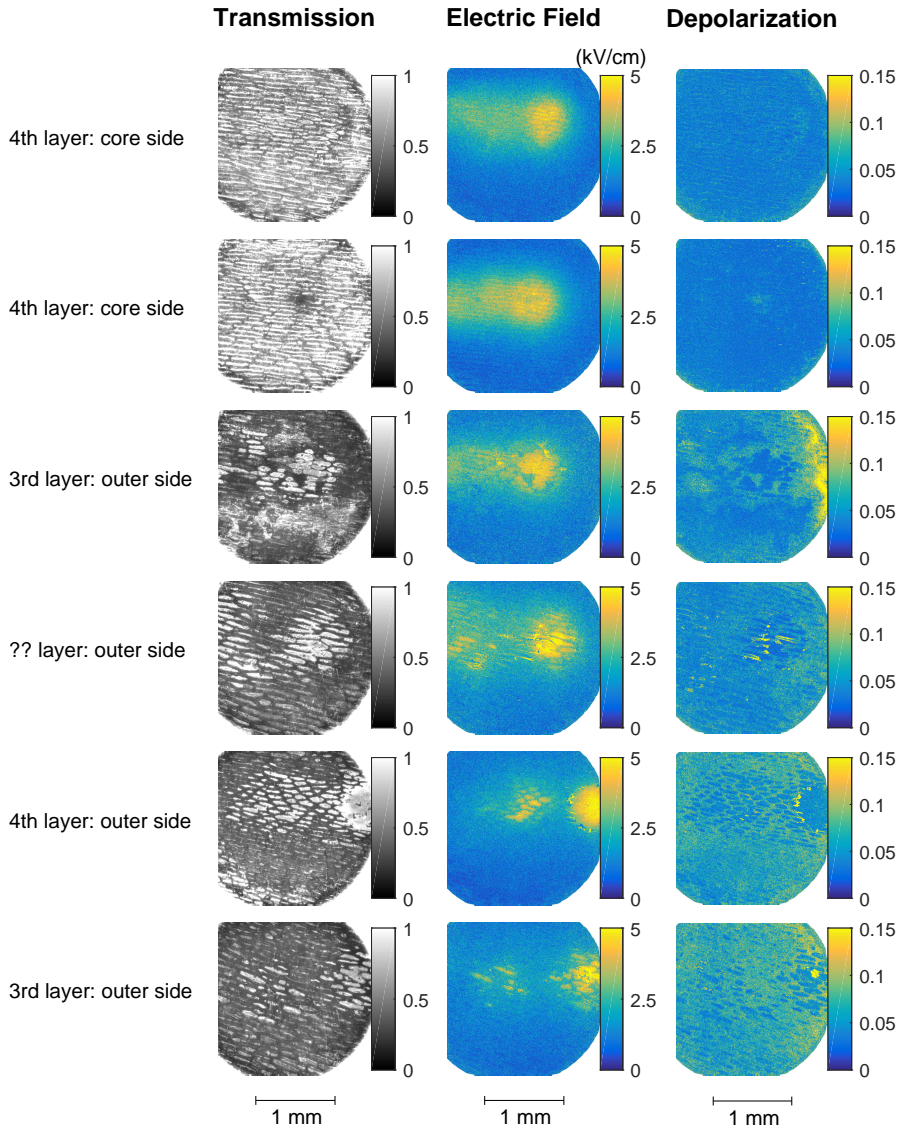


Figure B.1: Repetitive results shown for multiple samples, taking from different onion layers, show comparable results in changes of transmission and depolarization caused by the long-term impact of the ionization waves, which is indicated by the simultaneously obtained electric field pattern. More results are shown in figure B.2.

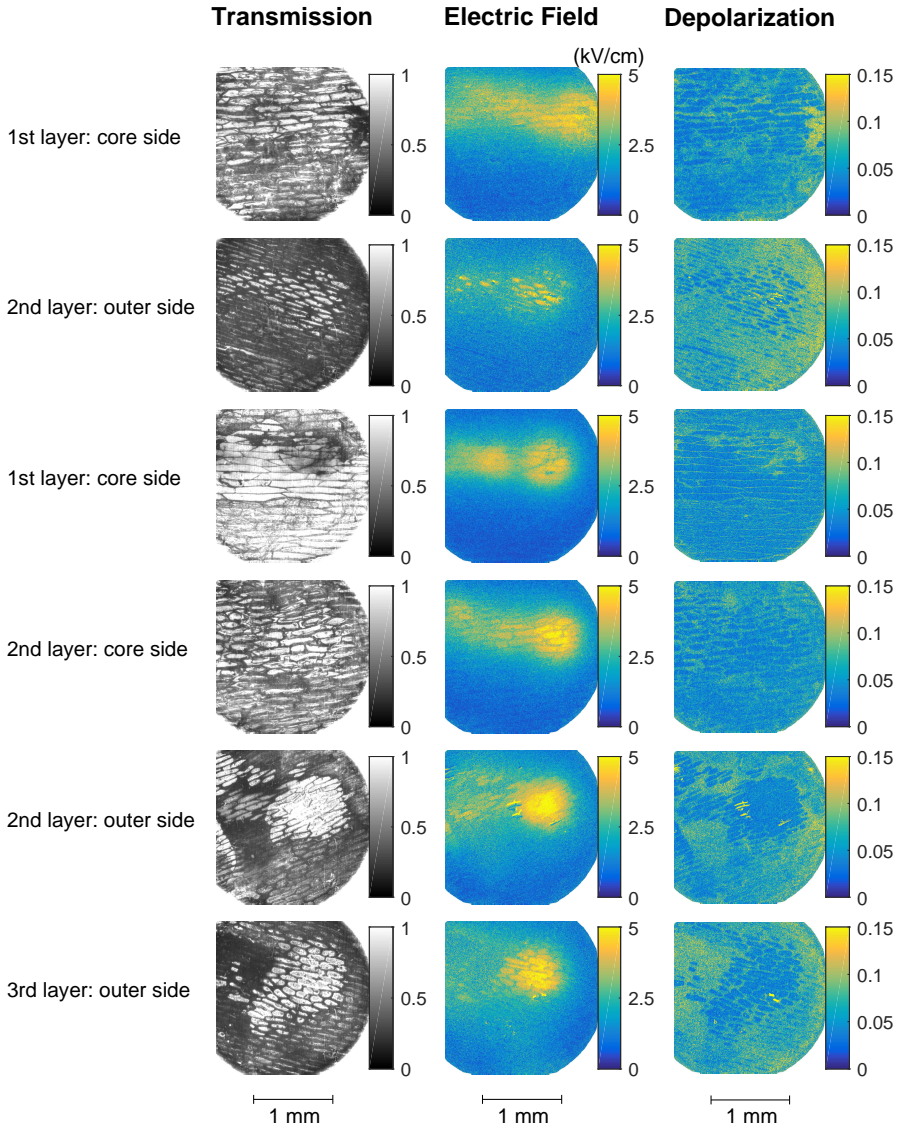


Figure B.2: Similar as figure B.1, here are shown comparable repetitive results, taking from different onion layers, showing changes of transmission and depolarization caused by the long-term impact of the ionization waves, which is indicated by the simultaneously obtained electric field pattern.

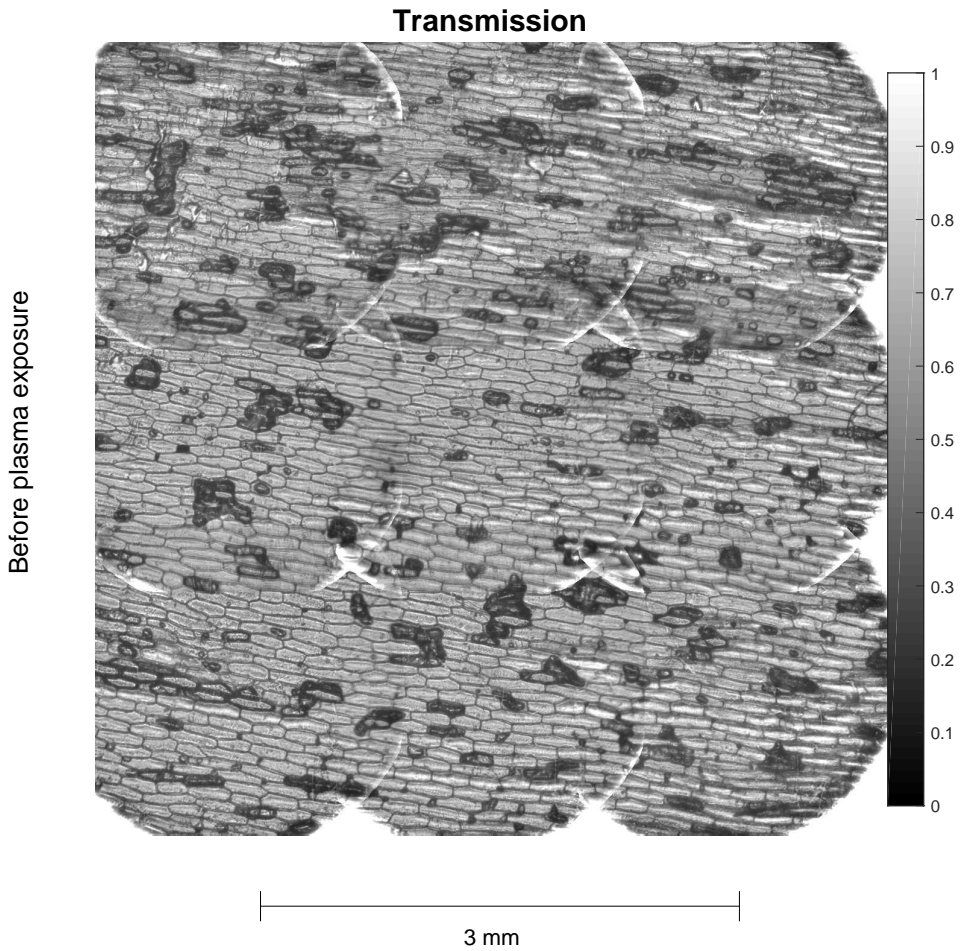


Figure B.3: The mapped transmission relative to air of the combined sample (BSO + onion cells) before any plasma exposure has been applied. This figure is part of figure 8.5, but shown in full scale.

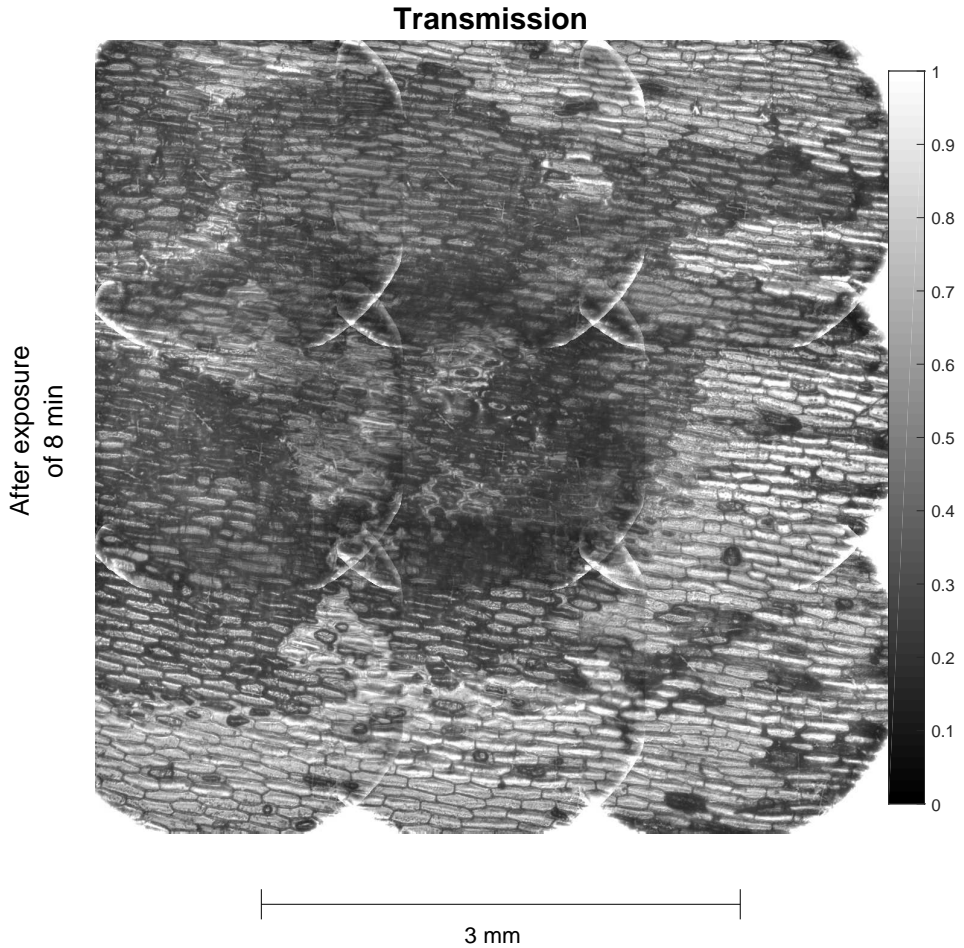


Figure B.4: The mapped transmission relative to air of the combined sample (BSO + onion cells) after 8 minutes of plasma exposure. The ionization waves generated by the plasma jet (2 kV amplitude 30 kHz sine waves and 1 slm helium flow) have impacted in the center of the map, while moving from the right side to the left. This figure is part of figure 8.5, but shown in full scale.

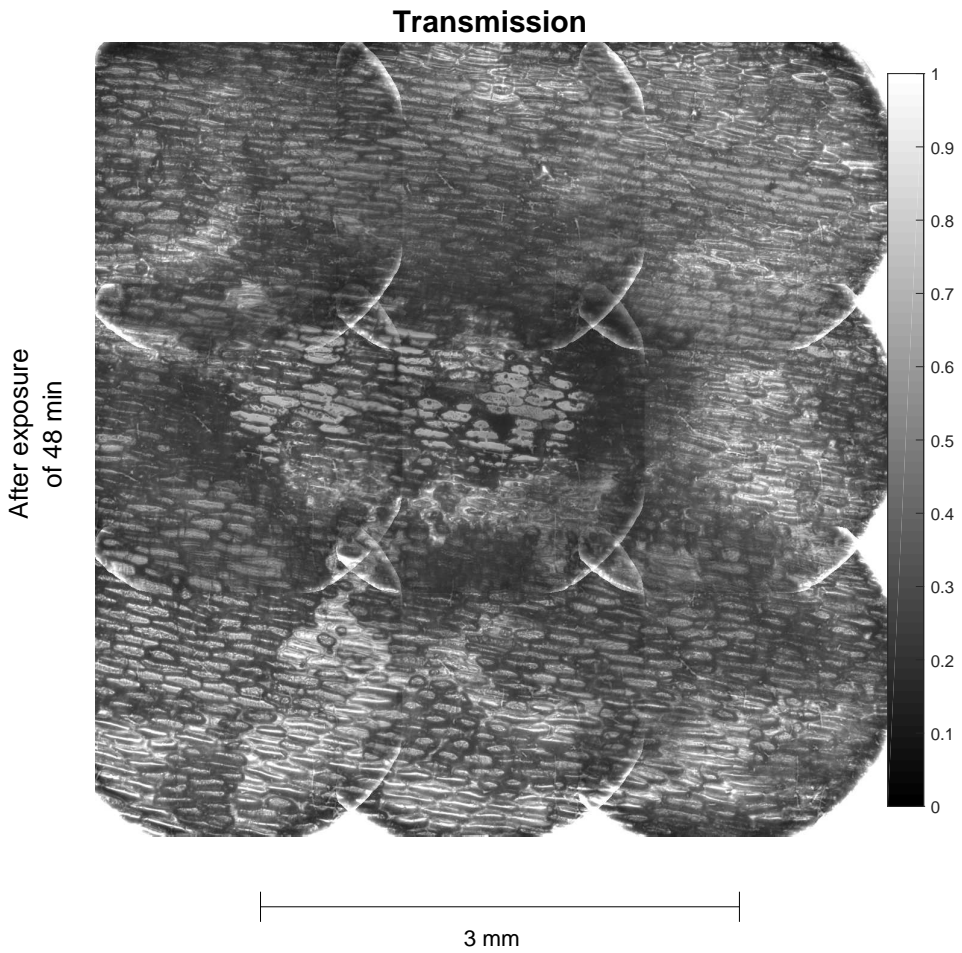


Figure B.5: The mapped transmission relative to air of the combined sample (BSO + onion cells) after 48 minutes of plasma exposure. This figure is part of figure 8.5, but shown in full scale.

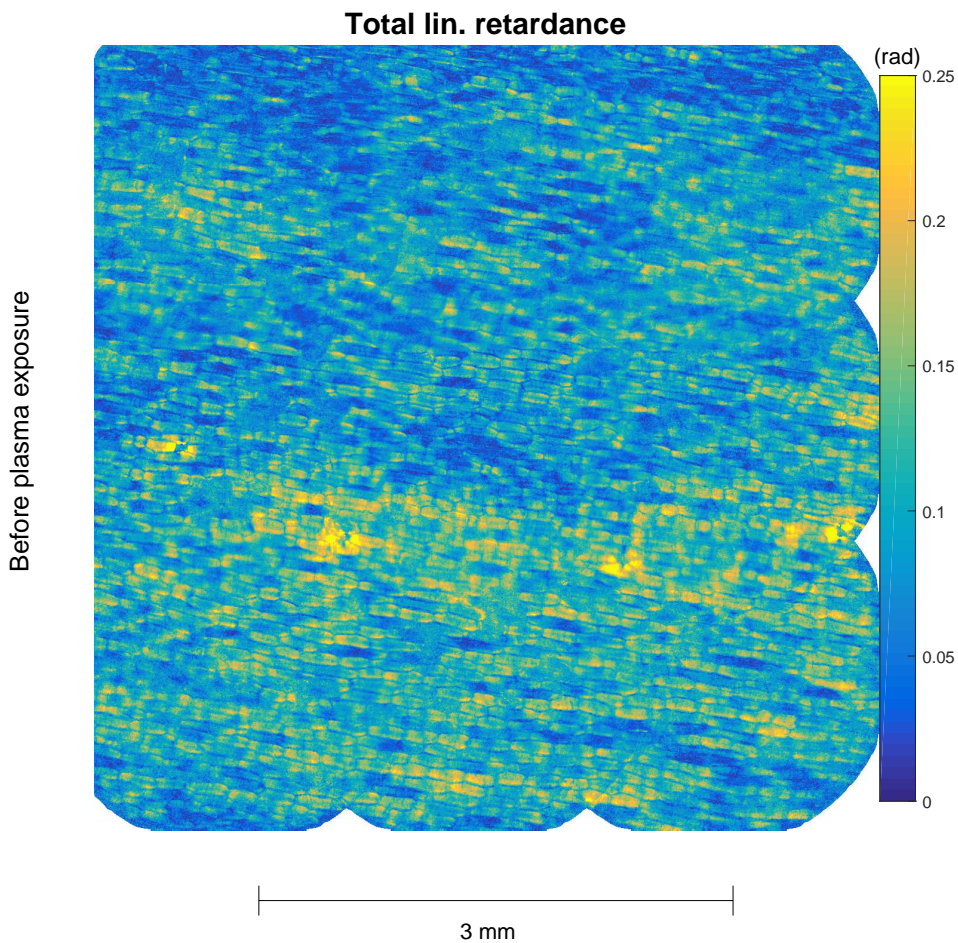


Figure B.6: The mapped linear retardance of the combined sample (BSO + onion cells) before any plasma exposure has been applied. This figure is part of figure 8.5, but shown in full scale.

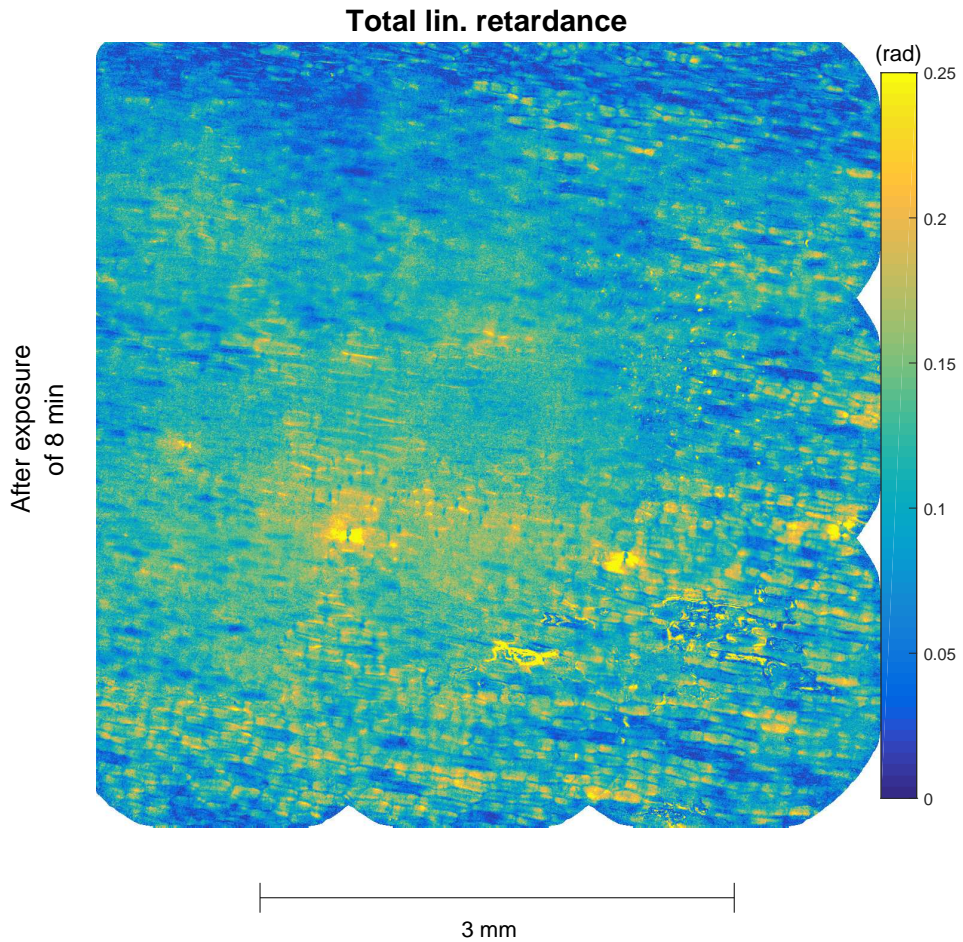


Figure B.7: The mapped linear retardance of the combined sample (BSO + onion cells) after 8 minutes of plasma exposure. This figure is part of figure 8.5, but shown in full scale.

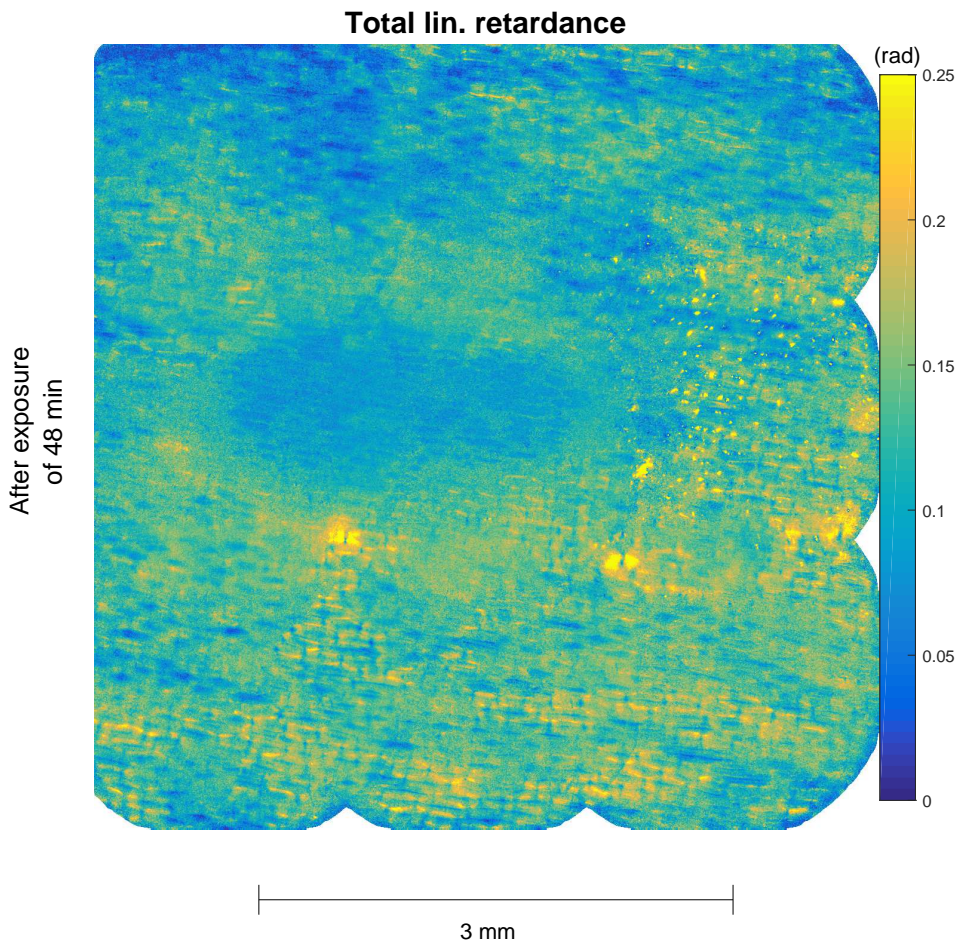


Figure B.8: The mapped linear retardance of the combined sample (BSO + onion cells) after 48 minutes of plasma exposure. This figure is part of figure 8.5, but shown in full scale.

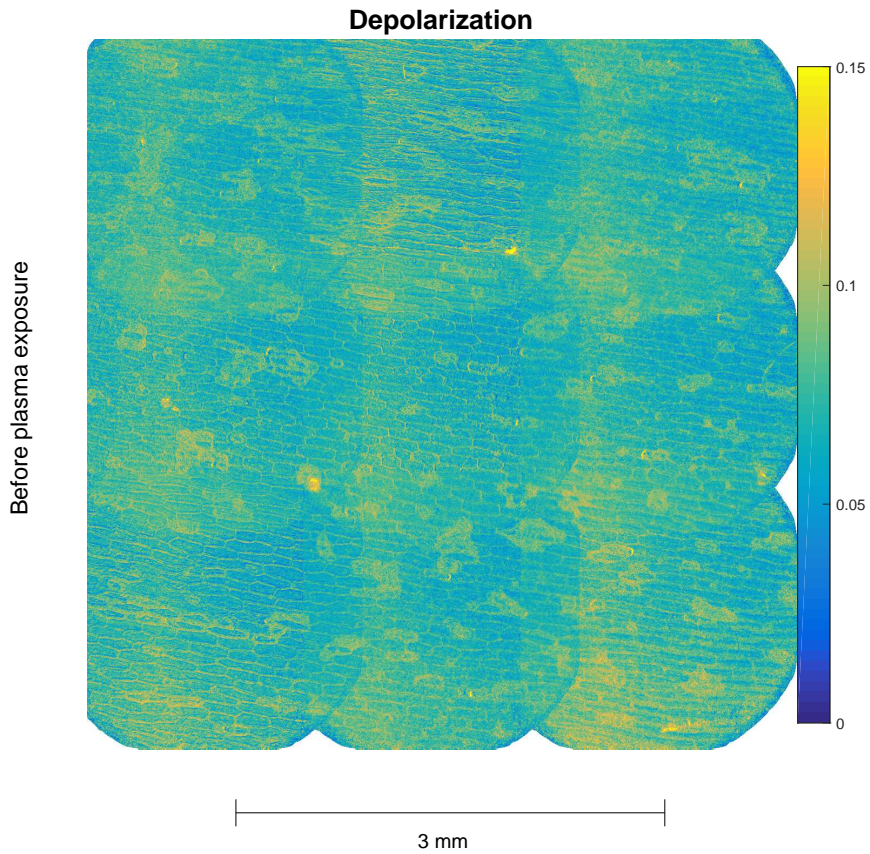


Figure B.9: The mapped total depolarization of the combined sample (BSO + onion cells) before any plasma exposure has been applied. This figure is part of figure 8.5, but shown in full scale.

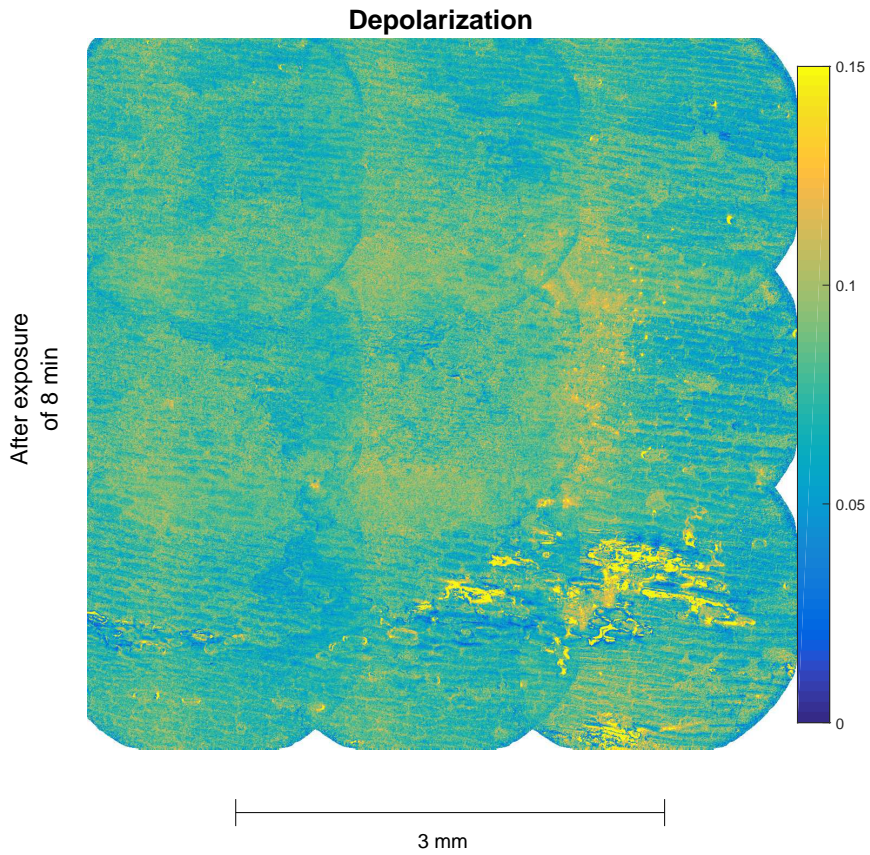


Figure B.10: The mapped total depolarization of the combined sample (BSO + onion cells) after 8 minutes of plasma exposure. This figure is part of figure 8.5, but shown in full scale.

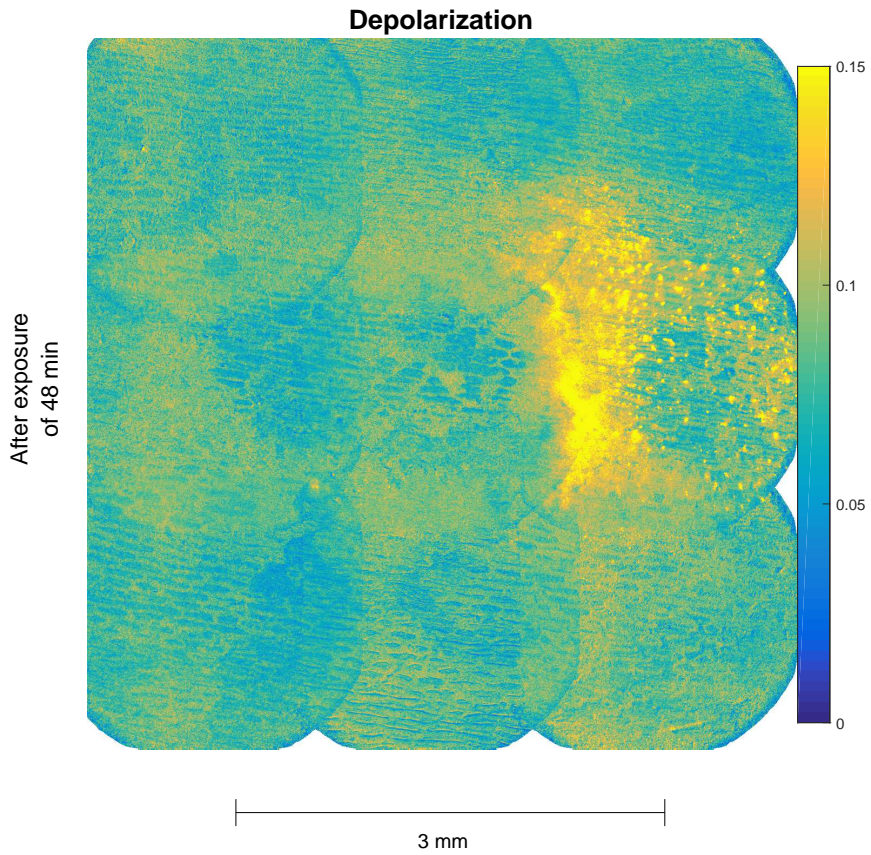


Figure B.11: The mapped total depolarization of the combined sample (BSO + onion cells) after 48 minutes of plasma exposure. This figure is part of figure 8.5, but shown in full scale.

# Curriculum Vitae

## Elmar Slikboer

**22 April, 1992**

Born in Schijndel, the Netherlands.

**2004 - 2010**

Secondary education (VWO) at the Elde College in Schijndel, the Netherlands.

**2010 - 2013**

Bachelor of Science at the department of Applied Physics at the Eindhoven University of Technology (TU/e), the Netherlands.

**2013 - 2015**

Master of Science at the department of Applied Physics at the TU/e. Master thesis (12 months) done under supervision of dr. A. Sobota. External internship (5 months) under supervision of prof.dr. D.B. Graves at University of California, Berkeley, the United States.

**2015 - 2018**

PhD candidate for a joint project between the TU/e and École Polytechnique (as part of Université Paris-Saclay) in Palaiseau, France. The results are presented in this thesis and the work is done under supervision of dr. A. Sobota and prof.dr.ir. G.M.W. Kroesen at *the Elementary Processes in Gas Discharges* group at the TU/e and under supervision of dr. O. Guaitella and dr. E. Garcia-Caurel at École Polytechnique in respectively *le laboratoire de physique des plasmas* and *le laboratoire de physique des interfaces et des couches minces*.

---

## List of Publications

- [7] *April 2018*      **Investigation of a Plasma-Target Interaction through Electric Field Characterization examining Surface and Volume Charge Contributions: Modeling and Experiment**  
[DOI: 10.1088/1361-6595/aadcc0](https://doi.org/10.1088/1361-6595/aadcc0)  
*Pedro Viegas, Elmar Slikboer, Adam Obrusník, Zdenek Bonaventura, Ana Sobota, Enric Garcia-Caurel, Olivier Guaitella and Anne Bourdon*
- [6] *February 2018*    **Imaging Axial and Radial Electric Field Components in Dielectric Targets under Plasma Exposure**  
[DOI: 10.1088/1361-6463/aaad99](https://doi.org/10.1088/1361-6463/aaad99)  
*Elmar Slikboer, Ana Sobota, Olivier Guaitella and Enric Garcia-Caurel*
- [5] *January 2018*    **The Effect of Liquid Target on a Nonthermal Plasma Jet – Imaging, Electric Fields, Visualization of Gas Flow and Optical Emission Spectroscopy**  
[DOI: 10.1088/1361-6463/aaa288](https://doi.org/10.1088/1361-6463/aaa288)  
*Vesna Kovačević, Goran Sretenović, Elmar Slikboer, Olivier Guaitella, Ana Sobota, Milorad Kuraica*
- [4] *November 2017* **Electric Field and Temperature in a Target induced by a Plasma Jet Imaged using Mueller Polarimetry**  
[DOI: 10.1088/1361-6463/aa9b17](https://doi.org/10.1088/1361-6463/aa9b17)  
*Elmar Slikboer, Ana Sobota, Olivier Guaitella and Enric Garcia-Caurel*
- [3] *February 2017*    **Charge Transfer to a Dielectric Target by Guided Ionization Waves using Electric Field Measurements**  
[DOI: 10.1088/1361-6595/aa53fe](https://doi.org/10.1088/1361-6595/aa53fe)  
*Elmar Slikboer, Enric Garcia-Caurel, Olivier Guaitella and Ana Sobota*
- [2] *May 2016*        **Time-resolved Electric Field Measurements During and After the Initialization of a kHz Plasma Jet – from Streamers to Guided Streamers**  
[DOI: 10.1088/0963-0252/25/3/03LT04](https://doi.org/10.1088/0963-0252/25/3/03LT04)  
*Elmar Slikboer, Olivier Guaitella and Ana Sobota*
- [1] *August 2015*     **Momentum, Heat and Neutral Mass Transport in Convective Atmospheric Pressure Plasma-Liquid Systems and implications for aqueous targets**  
[DOI: 10.1088/0022-3727/48/42/424007](https://doi.org/10.1088/0022-3727/48/42/424007)  
*Alexander Lindsay, Carly Anderson, Elmar Slikboer, Steven Shannon and David Graves*

---

## List of Conferences Attended

- November 2018*  
**Oral** Student Excellence Award Finalist: **Coupling Induced Changes of Complex Samples to the Experienced Electric Field During a Plasma-Surface Interaction using Mueller Polarimetry**  
*Elmar Slikboer, Ana Sobota, Enric Garcia-Caurel and Olivier Guaitella*  
at 71th Annual Gaseous Electronics Conference (GEC), Portland, USA
- July 2018*  
**Poster** **Diagnostics of Targets under Plasma Exposure using Mueller Polarimetry**  
*Elmar Slikboer, Ana Sobota, Enric Garcia-Caurel and Olivier Guaitella*  
Europhysics Conference on the Atomic and Molecular Physics of Ionized Gases (ESCAMPIG), Glasgow, United Kingdom
- March 2018*  
**Oral** **Mueller Polarimetry for Plasma Diagnostics: Imaging of Electric Fields in Dielectric Targets**  
*Elmar Slikboer, Olivier Guaitella, Ana Sobota and Enric Garcia-Caurel*  
Journées Imagerie Optique Non Conventionnelle (JIONC) - 13ème édition  
Paris, France
- February 2018*  
**Poster** **Advances in Pockels Polarimetry for Electric Field and Temperature Measurements using Atmospheric Pressure Plasma Jet**  
*Elmar Slikboer, Kishor Acharya, Enric Garcia-Caurel, Ana Sobota and Olivier Guaitella*  
at the PLAS@PAR Scientific Days, UPMC, Paris, France
- February 2018*  
**Oral** **Simultaneous Diagnostic of Temperature and Electric Field Patterns in Dielectric Targets**  
*Elmar Slikboer, Enric Garcia-Caurel, Ana Sobota and Olivier Guaitella*  
les journées scientifiques de l'EDOM, Institut d'Optique Graduate School  
Saclay, France
- November 2017*  
**Oral** **Simultaneous Diagnostic of Temperature Distribution and Electric Field induced in Dielectric Target by Atmospheric Pressure Plasma Jet**  
*Elmar Slikboer, Enric Garcia-Caurel, Ana Sobota and Olivier Guaitella*  
at 70th Annual Gaseous Electronics Conference (GEC), Pittsburgh, USA

---

July 2017

Poster

**Tangential and Normal Electric Field Imaging using Mueller Ellipsometry for kHz driven Atmospheric Jet in Controlled Environment**

*Elmar Slikboer, Enric Garcia-Caurel, Ana Sobota and Olivier Guaitella*  
at International Conference on Phenomena in Ionized Gases (ICPIG)  
Estoril, Portugal

June 2016

Oral

**Characterization of Bismuth Silicon Oxide Crystals Using Imaging Mueller Ellipsometry**

*Elmar Slikboer, Sang Hyuk Yoo, Olivier Guaitella, Ana Sobota and Enric Garcia-Caurel*  
at 7th International Conference on Spectroscopic Ellipsometry (ICSE-7)  
Berlin, Germany

# Acknowledgements / Remerciements / Dankwoord

This thesis has been the results of three years of work I did at three different labs. I am very happy that I was able to be part of the already existing collaboration between my three supervisors Olivier Guaitella, Enric Garcia-Caurel, and Ana Sobota. This allowed me to do research at two great universities (Eindhoven University of Technology and École Polytechnique) within the groups *le Laboratoire de Physique des Plasmas (LPP)*, *le Laboratoire de Physique des Interfaces et des Couches Minces (LPICM)* and *Elementary Processes in Gas Discharges (EPG)*.

I have enjoyed a lot the research that I was doing and I owe the biggest thanks to Ana, Enric, and Olivier: you have helped me to build the project as it is today, but also allowed me to find my own direction within it. Luckily, the (bi)monthly skype meetings between all four of us were there to keep everyone informed and steer me back on tracks whenever I strayed too far. What impressed me perhaps most throughout these years, besides your knowledge on plasma physics and Mueller polarimetry, is the contagious enthusiasm you all showed for the project. I always enjoyed sending updates by email whenever I had some because often there were quickly replied with joyful phrases of surprise, success, disbelief or new ideas. Of course, sometimes I had to share also some bad news, like when some crystals ended up in multiple pieces (not my fault), dark images were forgotten to be subtracted (oops) or some previously shown results turn out to be something completely else. However even then, your response always helped me forward so thank you for all the help!

Of course, I am also grateful to all the other members of the three labs helping me on a technical or administrative level. Whether the communication went in

---

English, French, Dutch or by hands, in the end we always managed to book flights for conferences, create glass mounts needed for new experiments or get some incomprehensible paperwork done!

When I started my PhD, Mueller polarimetry was new to me and it took some time figuring it out. Luckily Thomas (Sang Hyuk), you were always around and never too busy to make time to answer my random questions. The experiences I made on your setup was crucial for me to later build my own polarimeter, so thanks! Additionally, the discussions with obviously Enric and also the other members of *AOP* and in particular with Razvigor were very insightful and I learned a lot from it. Besides the work part, I am happy there was a great group of people around to have lunch with, do Christmas activities, celebrate birthdays, watch football and predict the Eurocup games. So Chiara, Anna, Edoardo, Luka, Alfredo, Alba, Loïc, Arthur, Federico, and Sang Hyuk: thanks! Lastly, also thanks to Pere for organizing amazing barbecues every summer!

Building my own setup meant moving back to the plasma labs where I was given my own space in the mezzanine in the lab of Olivier. By coincidence, this happened to be the place where a couch was located together with a fridge that was usually filled with some beers or wine. The good-results-on-friday-beer-rule was definitely a good motivator so I owe a big thanks to that. For me it was always great fun to see or listen to the dynamics in the lab, regarding the various people that were working beneath the mezzanine and their habits relating to organizing things, keeping the lab clean and the (un)willingness to share space/tools (the last one might have been me). I would like to thank Kishor for his work during his master internship and I am happy that I was able to help you a bit since you definitely helped me with the measurements that you did. Within the plasma labs there are too many people to thank individually but specifically Olivier, Ana, Ana Sofia, Abhyuday, Pedro, Marija, and Marlous: thanks to you it has been an amazing time, whether it was for discussing results, having lunch, preparing a presentation, going to a conference or just grabbing a drink. Unfortunately, there was not enough time to play a game of basketball but who knows in the future what will happen!

During my stay at LPP and LPICM, I first lived on the campus of Polytechnique at Palaiseau. Although some practical struggles were there due to the location and the absence of for instance a supermarket, I am still very happy with my time there since I was able to meet a lot of people and make great friends. Perhaps climbing the stairs from Lozère in the middle of the night after going to Paris creates a specific bond. Luckily that part was only in the beginning because then I moved to Cité Universitaire. I want to thank everybody that made my time in Paris so nice by discovering the city together, trying to find cheap bars using the MisterGoodBeer-app, going to museums for free, enjoying the foodtrucks in front of Mk2 before seeing a movie and just sitting at the riverside enjoying the summer. Also playing

---

tennis and making trips to for instance la Loire valley/Tours, Deauville, Lille, and Rome were really nice. So thanks to Daniel, Dory, Ali, Jose, Nico, Cris, Kevin, Marcia, Jessica, Vince, Karla, Mayssa, Soraya, Tim, Fausto, Seray, Varunesh, Eva, Vladimir, Enrico, Grégoire, Claudia, and Ana Rita.

Natuurlijk wil ik ook iedereen uit Nederland bedanken, met name mijn familie en vrienden in Schijndel en omstreken. Het was altijd een plezier om jullie te ontvangen in Parijs, ook al betekende dat dat ik dan voor de zoveelste keer maar weer naar de Eifeltoren of de Sacre Couer mocht gaan. Gelukkig was het ook altijd gezellig om weer terug in Nederland te zijn en vonden jullie het ook geen probleem (hoop ik) om tijd voor mij vrij te maken. Zo hebben we ook genoeg andere activiteiten kunnen doen zoals de stedentrips naar London, Dublin en Gent. Ook aan mijn vakantie naar Iran met Bronya en Ramon, New York met Frank en Pukkelpop met Stijn en Erwin denk ik natuurlijk terug met plezier! Die afleidingen waren natuurlijk nodig zodat ik me daarna weer vol op mijn onderzoek kon richten, dus bedankt: pap, mam, Bronya, Ramon, Jordy, Falco, Frank, Erwin, Stijn, Bas, Harold, Aron, Tommy, Remko, Gijs, Marjan, Richard, Jolanda, Koen T., Koen A., Anouk, Wessel, Babs en Calvin. En vanwege al jullie onvoorwaardelijke steun is het jullie vergeven dat ik telkens maar weer mocht uitleggen dat lasers and plasma's niet hetzelfde zijn.

Lastly, I want to firstly thank prof.dr.ir. Erwin Kessels, prof.dr. François Goudail and prof.dr. Ronny Brandenburg to be a member of my jury committee and making the time to read, assess and judge my thesis. Secondly, thanks to prof.dr.ir. Gerrit Kroesen to be my official promotor and to arrange and organize the joint agreement of this PhD project between the TU/e and École Polytechnique / Paris-Saclay, with obviously the help of Olivier, Enric and Ana.

Thanks to all  
Merci à tous  
Bedankt allemaal

Elmar

---

**Titre** : L'Étude des Interactions Plasma-Surface en utilisant la Polarimétrie de Mueller

**Mots clés** : Jet plasma à pression atmosphérique, Polarimétrie de Mueller, Interaction plasma-surface, Champ électrique, Température, Dépolarisation

**Résumé** :

Cette thèse examine une nouvelle méthode de diagnostic optique pour l'étude des interactions plasma-surface, appelée polarimétrie de Mueller. A partir des matrices de Mueller mesurées, les cibles optiquement actives exposées au plasma sont caractérisées en termes de diatténuation, de biréfringence et de dépolarisation. Cela permet d'obtenir des images résolues en temps de différents effets induits par le plasma sur la surface. Cette technique est appliquée pour étudier l'interaction entre une surface diélectrique et des ondes d'ionisation guidées générées par un jet de plasma non thermique à pression at-

mosphérique dans la gamme kHz. Les champs électriques axiaux et radiaux transitoires induits par les charges de surface déposées ont été déterminés en examinant des cibles électro-optiques. Le profil de température à l'intérieur du matériau cible a également été obtenu à partir de la structure des images de biréfringence sur des temps longs. Enfin, le potentiel de cette technique pour l'étude in situ d'échantillons complexes exposés à un plasma est démontrée en examinant l'évolution de la dépolarisation tout en caractérisant simultanément le champ électrique induit par le plasma.

**Title** : Investigation of Plasma Surface Interactions using Mueller Polarimetry

**Keywords** : Atmospheric pressure plasma jet, Mueller polarimetry, Plasma surface interactions, Electric field, Temperature, Depolarization

**Abstract** :

This thesis examines a novel optical diagnostic method called Mueller polarimetry for the investigation of plasma surface interactions. From the measured Mueller matrices, optically active targets under plasma exposure are characterized in terms of diattenuation, birefringence, and depolarization. This allows for the time-resolved imaging of specific aspects of the induced surface interaction. The technique is applied to study the surface interaction occurring for guided ionization waves generated by a non-thermal khz-driven plasma jet at at-

mospheric pressure. The axial and radial electric field patterns induced by temporarily deposited surface charges are obtained by examining electro-optic targets. Additionally, the temperature profile inside the targeted material was retrieved also from the birefringence by analysing the background pattern. Lastly, the potential for in-situ surface analysis is shown by examining the evolution in depolarization that occurs with more complex samples under exposure while characterizing the plasma interaction in terms of the induced electric field.



